

QCD Studies at LHC using CMS Detector

A Thesis

Submitted to the
Tata Institute of Fundamental Research, Mumbai
for the degree of Doctor of Philosophy
in Physics

by

Suvadeep Bose

Department of High Energy Physics
Tata Institute of Fundamental Research
Mumbai

September, 2009

To

My parents

and

My wife

Acknowledgements

I would like to take the opportunity to acknowledge the invaluable and indispensable guidance of Prof. Sunanda Banerjee, with whom I have worked for five long years. It was an association which resulted in this thesis. He has been an advisor not only for the physics topics I have worked with but in general most of the decisions I have taken during these last five years. It was a pleasure working with him.

I sincerely thank Dr. Monoranjan Guchait and Dr. Gobinda Majumder, my local guides at TIFR, who introduced me to particle physics research. My work got benefited through the collaboration I had with them. They were ever approachable for any sort of discussion from detector physics to computing techniques. Personally I had great time with them.

During the course of my work TIFR always offered a pleasant atmosphere and all the facilities I needed. I express my gratitude to all the professors in my graduate school at TIFR and all the members of the Experimental High Energy Physics - Prof. Atul Gurtu, Prof Tariq Aziz, Prof. Kajari Mazumdar, Dr. Sudhakar Katta. My first project work in INO under the guidance of Prof. N. K. Mondal was my first exposure to experimental particle physics. Towards the end of my Ph.D. Prof. Aziz helped me a lot as the DHEP chairperson. I appreciate the help I received from Prof. Sreerup Raychaudhuri for the theoretical aspects of the thesis.

My warm thanks go to Mr. P. V. Deshpande for maintaining the computing system in our group in good shape all along. He always extended his helping hands whenever I had problems with the computers. Ms Minal Rane and Mr. Suresh T. Divekar at the EHEP office were always co-operative.

I would like to thank TIFR for partially supporting my travel to Fermilab and CERN on different occasions. I acknowledge the financial support of India-CMS collaboration for supporting my stay at CERN during test beam experiment. DHEP was kind enough to partially sponsor the schools and conferences I attended during my Ph.D.

In the latter half of my Ph.D. I was stationed at Fermilab. I am thankful to the LHC Physics Centre (LPC) at Fermilab to support my two years of stay there.

I am grateful to Dan Green and Lothar Bauerdick who arranged fund for my stay there. I sincerely acknowledge the help I received from Ms Terry Grozis and Ms Terry

Read whose help made my stay easier in a new country. I must mention Ms. Melissa Clayton Lang, at the Fermilab Visa Office, who helped me out with the technicalities of US Visa system, always with a smile.

During my stay at Fermilab, I had the fortune to work with Shuichi Kunori and Nikos Varelas who advised me on two major topics I worked on. I am thankful to have them as my well wishers too. A simple plot, even if it is wrong, can tell a thousand things - learned this lesson from Shuichi. And Nikos made me realize the importance of working within a time frame in order to reach a goal. Their ever-encouraging attitude always ushered me with confidence. But the one person whom I am indebted to in more than one ways is Kostas Kousouris. He has truly been a friend, philosopher and guide for me for the last couple of years of my Ph.D., not only for academics but in personal life as well.

I cherished my stay at TIFR Experimental High Energy Physics group with my friends Nikhil, Arun, Abinash, Garima, Seema, Anirban and Devdatta. I thank my other friends in TIFR for their smiles and company in hard times - Ajay, Amit, Aniket, Manjusha, Suresh, Basudev, Navodit, Kadir, Rakesh, Vandna, Shanta, Shamik, Naren, Sarang, Bhargav, Ravi .. to name a few.

I must mention my friends at Fermilab - Sudhir, Shubhendu, Amit, Shilpee, Pelin, Agata, Cosmin, Stefan, Ingo, Francisco, Gena who made my stay all the more enjoyable in a new country. I must specially mention my housemates Youn, Chiyong and their lovely son Thomas with whom we stayed like a family for almost a year.

Going down memory lane, the excitement of the first year graduate course work at TIFR, the nights at Mac Rajan with a plateful of *maggi* and *chai* at 1 a.m., the night-long discussions before assignment deadlines, the long walks after dinner on the sea-shore, the Sunday dine-outs, the 10:40 round trip in TIFR bus, the late night taxis after movie show... I owe a lot to those sweet memories. I also owe a lot to the city of Mumbai where I learned to become a complete human being through love, hate, loss and joy.

I also enjoyed the cultural atmosphere at TIFR that helped me to breathe out from the academic world. The amateur music association (AMA) which I was a part of, made me nurture my interest in classical music.

Last but not the least, it is difficult to emphasise my gratitude towards the people closest to my heart. I would like to thank my parents for their belief in me and for always being there for me. To conclude, I would like to mention the love and support I got from Pratima without her I would not have achieved what I have today, for she is not only my wife but my best friend too.

SYNOPSIS

Title of the Thesis	:	QCD Studies at LHC using CMS Detector
Name of the Candidate	:	Suvadeep Bose
Registration Number	:	PHYS-071
Degree	:	Doctor of Philosophy
Subject	:	Physics
Thesis Supervisor	:	Prof. Sunanda Banerjee
Institution	:	Tata Institute of Fundamental Research

Synopsis

In the present understanding of particle physics, the elementary building-blocks of matter comprise of spin- $\frac{1}{2}$ fermions and their antiparticles. The particles can be grouped into three families, each containing two quarks, one charged lepton and one neutrino. Interactions are explained in the Standard Model by imposing *local gauge symmetries* on the fields. These symmetries require the existence of vector fields. The photon and the W^\pm and Z^0 bosons are responsible for the electroweak interaction, and the gluons are the carriers of the strong interaction. Quantum Chromodynamics (QCD) is the theory of strong interaction between particles carrying colour quantum number.

One additional particle, the scalar Higgs boson (H^0), is predicted to exist, but has not yet been observed conclusively. The Higgs field introduces a *spontaneously broken symmetry* into the Standard Model, thereby offering an explanation for the non-zero masses of the W^\pm and Z^0 bosons. It also accounts for the mass terms in the Dirac Lagrangian, but does not predict the masses of the individual fermions.

The Large Hadron Collider (LHC) [1] is being built as the world's largest and most powerful accelerator and collider. It is designed to collide protons at a centre of mass energy of 14 TeV with a nominal luminosity of $10^{34} \text{ cm}^{-2}\text{s}^{-1}$. At the start-up LHC will run at a reduced luminosity ($10^{31} \text{ cm}^{-2}\text{s}^{-1}$) and reduced centre of mass energy (10 TeV). Protons being composite particles, a wide range of centre of mass energy can be probed and the high luminosity makes it possible to observe rare phenomena occurring with very small probabilities to be recorded with convincing statistics.

The Compact Muon Solenoid (CMS) [2] is one of the two general purpose detectors to be used at the LHC. The main physics goal of the CMS is to look for the Higgs boson and/or to look for signatures of any new physics which may be unravelled at TeV energy scale. The design of the CMS detector is optimized to look for these signatures over a wide range of energy. The CMS calorimeter system consists of two kinds of detectors - Electromagnetic Calorimeter (ECAL), a crystal calorimeter, to detect and measure energy of electron and photon and Hadron Calorimeter (HCAL), a sampling calorimeter, to absorb all hadrons and measure their energies.

The electromagnetic calorimeter (ECAL) consists of lead tungstate crystals which provide good energy and position resolution for electrons and photons. The radiation length (X_0) of lead tungstate crystals is 0.89 cm. In the barrel the ECAL provides a total of $26 X_0$. The CMS hadron calorimeter (HCAL) consists of a barrel (HB) and an endcap (HE) detector. It uses plastic scintillator as the active material and a copper alloy as the absorbing material which has an interaction length (λ_0) of 16.4 cm. Granularity of the readout of HCAL is 0.087×0.087 in pseudo-rapidity (η) and azimuthal angle (ϕ) for the

barrel. The digitization of the analog signal is done at the beam crossing frequency of 40 MHz by QIE chips (Charge(Q) Integration(I) range Encoding(E)).

In proton-proton collisions, interactions take place between the partons of the colliding protons. In the cases where the scattering is hard (large momentum transfer), the scattered partons will hadronize into highly collimated bunches of particles that will be measured in the calorimeter as high transverse momentum (p_T) jets. The study of the high p_T jets is useful as a test of QCD and to look for physics beyond the Standard Model. Since parton scattering is practically an elementary QCD process, the jet distributions can be calculated from first principles, provided that reasonable hadronization modelling is available. Also, their production is sensitive to the strong coupling constant α_S and precise knowledge of the jet cross section can help to reduce the uncertainties of the parton distribution functions (PDFs) of the proton. High p_T jets are furthermore sensitive to new physics (e.g. quark compositeness, resonances). Given the high reach in p_T at the LHC, current limits can be improved and discoveries are possible even at the startup.

High p_T jets will be measured primarily in the CMS calorimeters. Therefore, a precise measurement of this process needs a good understanding of the CMS calorimeter. A number of test beam experiments are performed to understand various aspects of the calorimeter system.

Test Beam Analysis

A slice of the CMS calorimeter is tested at the H2 test beam area of CERN with different beams of momenta ranging between 1 GeV/c and 300 GeV/c in the summer of 2007. Test Beam 2007 studies the CMS endcap system which consists of Hadron Endcap (HE), Electromagnetic Endcap (EE) and the Preshower detector (ES). The preshower detector is tested in the test beam for the first time in this experiment. Very Low Energy (VLE) beam line provides beams of momenta between 1 and 9 GeV/c with good rate using a secondary target (T22). Identification of particle type is accomplished by time of flight counters (TOF), Cerenkov counters (CK) and muon veto counters. High energy beam line covers a momentum range from 10 to 300 GeV/c for hadrons through secondary particle production at the T2 target. For electrons/positrons, the range is 10 to 150 GeV/c.

The Test Beam 2007 data are reconstructed using the standard CMS software package, CMSSW. Two kinds of data are analyzed - one is with HCAL alone setup and the other is data from the combined HCAL, ECAL and ES detector system. The absolute energy scale for the combined calorimeter setup is studied. The response and resolution of the hadron calorimeter are measured.

Response and Resolution

Identification of individual particle is done by a combination of the beam line elements, e.g. Cerenkov counters, time of flight counters and the muon veto counters. Figure 1

demonstrates the use of time of flight (TOF) counters to identify pions from kaon and protons in the beam.

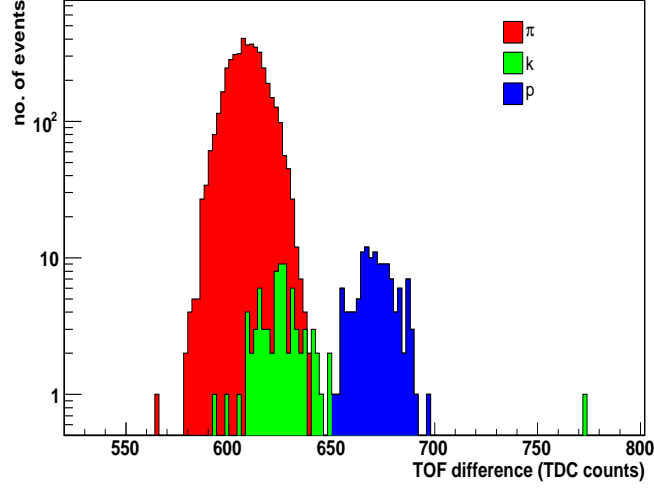


Figure 1: Particle identification using time of flight (TOF) counters for 6 GeV/c positive beam. The time of flight difference is plotted in the units of TDC counts. Protons are well separated from pions and kaons for this beam momentum.

The interactions of pions in the calorimeter results in a hadronic shower which develops longitudinally with the depth of the calorimeter and spreads laterally in the neighbouring towers of the central tower where beam is shot. Signals in adjacent towers of HCAL are summed up for HE. Signals from 5×5 crystals are summed up to get the total signal in the ECAL.

To obtain the energy scale for HCAL, the average signal produced by 50 GeV/c π^- in the HCAL is made to correspond to 50 GeV. The HCAL can also be calibrated using electrons such that the signal produced by 50 GeV/c electron beam in the HCAL becomes 50 GeV. The ratio of these two scale factors essentially gives the π/e for HCAL at 50 GeV/c incident momentum and it characterizes the performance of the calorimeter in terms of the linearity of response and the resolution for hadrons. The π/e is measured to be 0.836 for CMS HCAL at 50 GeV/c in the test beam experiments. The energy scale for ECAL is obtained using 50 GeV/c electrons with the signal measured in 5×5 crystals. The response of the calorimeter is measured as a ratio of the reconstructed energy in the combined calorimeter system to the nominal beam energy. Left hand side plot in Figure 6.20 shows the energy response for the combined calorimeter in the endcap and barrel region. The response is observed to be the same for both the regions except for higher energies where the response from endcap is more as the absorber in the endcap has more material thickness.

The resolution of the calorimeter is measured as the ratio of the RMS of the combined energy distribution to the reconstructed energy. The resolution of the HE+EE combined

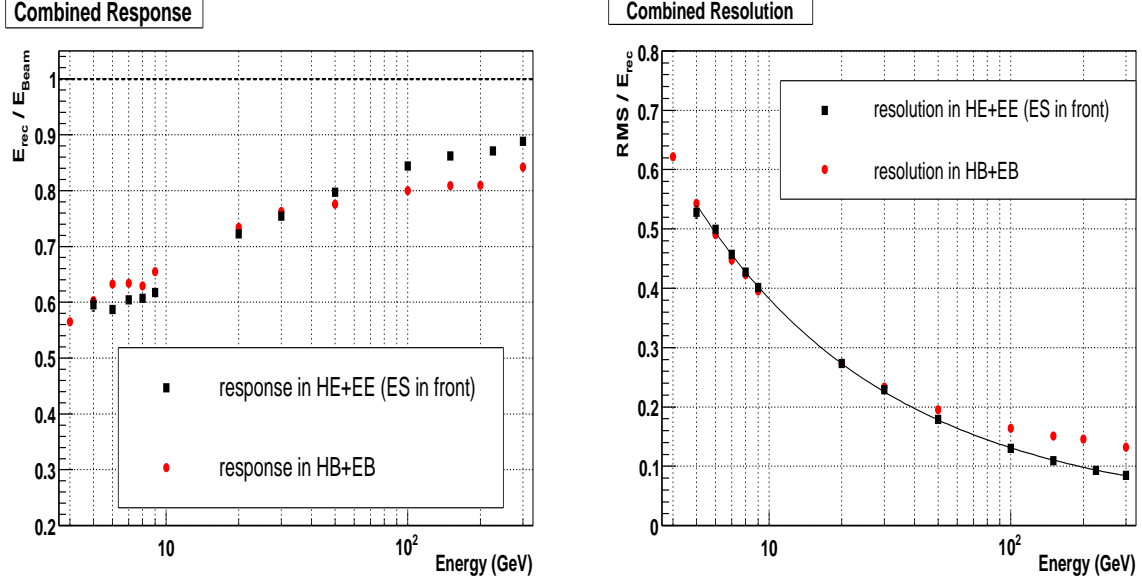


Figure 2: Response and resolution of the combined ECAL + HCAL system (with preshower in front) measured as the ratio of energy measured to the beam momentum for π^- beam. Here HCAL is calibrated using 50 GeV/c electron beam. For the barrel part the beam was shot at $i\eta$ tower 7 and for the endcap the beam was shot at $i\eta$ tower 19.5.

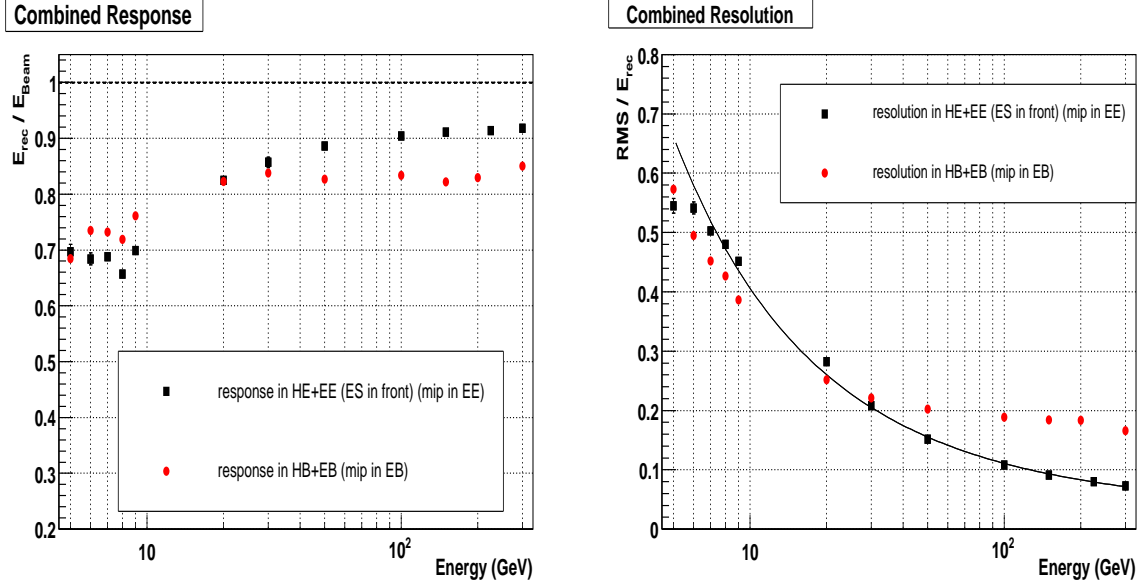


Figure 3: Response and resolution of the combined ECAL + HCAL system (with preshower in front) with pion beams where the pion gives an MIP like signal in the EE. The response is defined as the ratio of the measured energy to the beam momentum and here the HCAL is calibrated using 50 GeV/c electron beam.

setup is fitted with a resolution function

$$\frac{\sigma}{E} = \frac{a}{\sqrt{E}} \oplus b$$

and the fit to the resolution plot (right hand side plot in Figure 6.20) gives the stochastic term $a = 116.9\%$ and the constant term $b = 1.4\%$. For the HB+EB combined setup the respective terms are $a = 111.5\%$ and $b = 8.6\%$ [3]. Energy resolution is found to be the same for barrel and endcap detectors at lower energies after noise suppression but at higher energies resolution is better in the endcap.

Beam Profile and MIP fraction

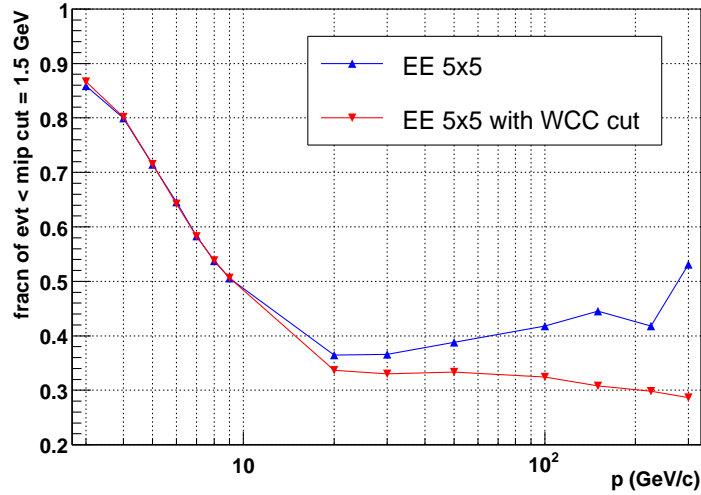


Figure 4: MIP fraction (fraction of events where energy measured in the ECAL ≤ 1.5 GeV) as a function of beam momenta.

ECAL being positioned in front of the HCAL provides an additional material budget of $1.1\lambda_0$. As a result, 67% of hadrons starts interacting with the ECAL before reaching the HCAL. The rest of the hadron shower deposits a small amount of energy in the ECAL due to the presence of minimum ionizing particle (MIP). The response and resolution are plotted in Figure 6.21 for events which give a MIP signal in the EE by the same procedure as for Figure 6.20. Figure 6.21 represents the response and resolution for the HCAL alone system without ECAL in front.

Due to a gap between the two super crystals as used in the test beam 2007 there is some leakage of the beam through ECAL depending on its impact point and they deposit more energy in the HCAL. Figure 6.22 shows the effect of the gap and the MIP-fraction after the gap is masked out. It is crucial to look for potential gaps in the material of the modules used as such phenomenon leads to mis-leading energy response measurement in the combined calorimeter system. With increasing energy the electromagnetic part of the

hadron shower increases and as a result the MIP fraction decreases with increasing beam momentum as is shown in Figure 6.22.

Conclusion from Test Beam Analysis

Energy response and resolution of hadrons are measured for the endcap detector of CMS and are compared with similar measurements done with the barrel detector. The endcap detector shows better response and resolution for higher energy beams due to smaller leakage in the system. MIP-fraction is also measured and it shows the same characteristics as in the barrel, namely a small drop off at the high energy end.

QCD Studies in CMS

The signatures of hadronic events are a large number of particles observed in the final states and large visible energy measured in the detector. The hadronic events are characterized by two, three or more jet topology, corresponding to zero, one or more hard gluon radiations. Study of multi-jet events allows a test of the validity of the QCD calculations to higher order and a probe of the underlying QCD dynamics. The topological distributions of these multi-jet events provide sensitive tests of the QCD matrix element calculations.

Jet reconstruction and event selection

The Monte Carlo sample used for these analysis consists of simulated QCD di-jet events at $\sqrt{s} = 10$ TeV in pp collisions. They are produced by the PYTHIA [4] event generator which is based on leading order (LO) matrix elements of $2 \rightarrow 2$ processes matched with a parton shower to describe multi-jet emission due to initial and final state radiation. The events are passed through a full GEANT4 [5] based simulation of the CMS detector. For the present analysis calorimeter jets are used. These jets are reconstructed with the Seedless Infrared Safe Cone algorithm (SISCone) [6] of radius $R = 0.5$ after applying “SchemeB” energy thresholds [7]. In order to construct a jet composite objects of HCAL cells and ECAL crystals are first constructed and they are called calorimeter towers (CaloTowers). The jet finding algorithm is applied on these towers to reconstruct calorimeter jets or raw CaloJets. The same jet finding algorithms is also applied to stable particles generated by event generators such as PYTHIA to reconstruct particle jets or GenJets. For both calorimeter jets and particle jets, the minimum reconstructed jet p_T is 1 GeV/c. The energies and directions of the raw calorimeter jets are corrected to the particle level by applying jet corrections.

Events are preselected by requiring the jets in these events to stay within a region of $|\eta| < 3.0$ (within the endcap region of the CMS calorimeter) which is considered specially suitable for early data analysis. Events are selected based on the following conditions:

- leading jet p_T above 110 GeV/c
- p_T of non-leading jets above 50 GeV/c
- inclusive 3-jet and 4-jet samples are selected. This means that at least 3 jets are required in the system passing the first two criteria for the 3-jet study and at least 4 jets are required in the system passing the first two criteria for 4-jet study.

For early measurements the luminosity condition, $L = 1 \cdot 10^{31} \text{ cm}^{-2}\text{s}^{-1}$ is used. The analysis with multi-jets depends strongly on the choice of triggers. The analysis is performed with single jet trigger as this will provide sufficient statistics for these measurements. The High Level Trigger (HLT) is chosen to be single jet with 80 GeV threshold (HLT80) since this trigger will have a small prescale factor of 10. The inefficiency of that single jet trigger is rather small for the offline selection criteria chosen in this study.

In CMS, jets are reconstructed primarily from calorimeter information. They can also be reconstructed using charged tracks which will give independent reconstruction results and must be compared to the jets reconstructed from calorimeter information. Track jets are reconstructed by selecting charged tracks from general tracks and applying specific jet algorithm on the collection. These reconstructed detector level jets are compared with particle level jets.

Study of Multi-jet Topological variables

In order to study the three and four parton final states a class of observables is defined. A study of these observables is made using samples of simulated hadronic events within the CMS detector.

The topological variables used in this study are defined in the multi-jet (parton) centre-of-mass system (CM). The topological properties of the three-parton final state can be described in terms of five variables. Two of these variables are the scaled energies of any two out of the three final state partons. The other variables define the spatial orientation of the planes containing the three partons and the total CM energy of the 3-parton system.

It is convenient to introduce the notation $1 + 2 \rightarrow 3 + 4 + 5$ for the three-parton process. Here, the numbers 1 and 2 refer to incoming partons while the numbers 3, 4 and 5 label the outgoing partons, ordered in descending energies in the parton CM frame, i.e., $E_3 > E_4 > E_5$. For simplicity, E_i ($i = 3, 4, 5$) are often replaced by the scaled variables x_i ($i = 3, 4, 5$), which are defined by $x_i = 2E_i/\sqrt{\hat{s}}$, where $\sqrt{\hat{s}}$ is the centre-of-mass energy of the hard scattering process. The angles that fix the event orientation can be chosen to be (i) the cosine of the polar angle of parton 3 with respect to the beam ($\cos\theta_3$) and (ii) the angle between the plane containing partons 1 and 3 and the plane containing partons 4 and 5 (ψ) [86].

To define a four-parton final state in its centre-of-mass system, eight independent parameters are needed. One of these variables is the CM energy of the 4-parton system, two variables will define the overall event orientation while the remaining variables fix the internal structure of the four-parton system. The four partons are ordered in descending energy in the parton CM frame and are labelled from 3 to 6. The variables include the scaled energies (x_i , with $i = 3, \dots, 6$), the cosines of polar angles ($\cos \theta_i$, with $i = 3, \dots, 6$) of the four jets. Here three angular variables characterizing the orientation of event planes are investigated. These are the Bengtsson-Zerwas angle (θ_{BZ}) [88], Nachtmann-Reiter angle (θ_{NR}) [89] and the angle defined by Korner, Schierholz and Willrodt, ϕ_{KSW} [85].

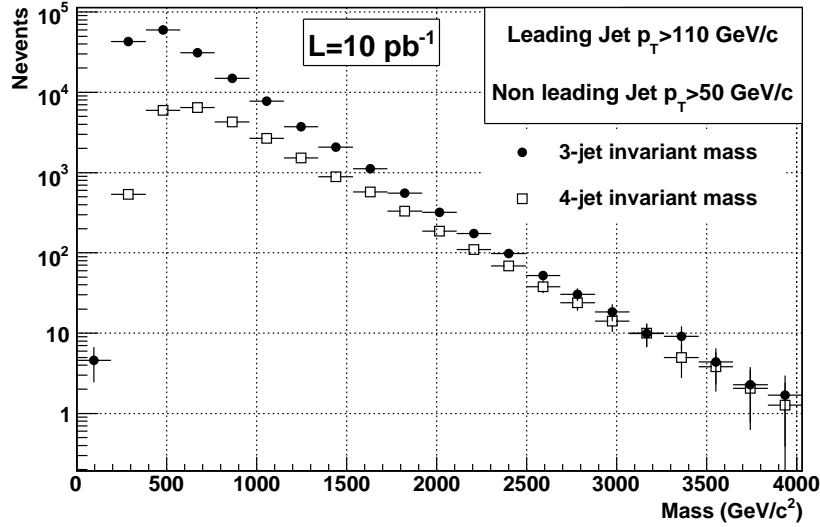


Figure 5: Distribution of invariant mass of the 3- and 4-jet events as expected from integrated luminosity of 10 pb^{-1} .

The detector effect on these variables is studied by smearing the jet energy and direction with estimated values of energy and position resolution. A first estimate of the expected dominant systematic uncertainty at the start up data taking, resulting from limited knowledge of the jet energy scale and event selection is made. Finally the sensitivity of the chosen observables to distinguish models of QCD multi-jet production is shown.

The invariant mass distribution of the three (four) highest p_T jets in case of 3(4)-jet events is shown in Figure 7.5. The effect of the jet energy resolution is studied by applying smearing on jet energy to generator level jets and comparing these to the jets which are not smeared. If the chosen smearing function is the right one, then one expects to get the detector level jets by smearing the particle level jets. The jets are smeared by taking care of (1) energy resolution, and (2) position resolution (which affects η and ϕ measurements). After the smearing, the jets are reordered in p_T . The jet resolution parameters are obtained from a di-jet sample using tag-probe method as would be done

with the real data.

The effect of position resolution is studied by smearing of the angular variable (η) and the azimuthal angle (ϕ). The distributions from the smeared jets are then compared to those from unsmeared jets.

After the studies of the individual effect of energy, η and ϕ resolutions, the combined smearing effect is studied. It is worthwhile to see whether a simple Gaussian smearing of energy, η , ϕ of the jets can reproduce the detector effects as observed in the calorimeter jets after corrections. In Figure 7.14 the top left plot shows the energy fraction of the most energetic jet for inclusive 3-jet final state. The top right plot shows the ψ angle in the 3-jet case. Bottom left plot shows the energy fraction of the 4th leading jet in the inclusive 4-jet final state. The Bengston-Zerwas angle is shown as the bottom right plot.

In each of the figures the following quantities are examined: ratio of detector level jets to the particle level jets; effect of only energy smearing; effect of only η smearing; effect of only ϕ smearing; effect of combined smearing.

As can be seen from the plots, the dominating contribution due to detector correction comes from the energy resolution of the jets which is well within $\pm 10\%$ for all the variables. The effect of position resolution which is reflected in the smearing of η and ϕ is found to be negligible. The combined smearing which is dominated by effect of energy smearing underestimates the overall detector effects which is obtained from the ratio of detector level and generator level distribution. From the ratio plots of the detector level jets to the combined smeared generator level jets it is clear that the combined smearing only partially explains the overall detector effect. The difference between the two is attributed to systematic uncertainty for unfolding detector correction.

The leading source of systematic uncertainty in QCD data analysis is the limited knowledge of the jet energy scale (JES). The JES uncertainty at start up is expected to be $\pm 10\%$ based on the best educated guess [92]. Changing the JES correction within its uncertainty changes the jet shapes as jets migrate between p_T bins. However, jet shapes vary slowly with jet p_T . So the net effect on the shape distributions is expected to be small. To determine the impact on the jet shapes, the p_T of the jets are changed by $\pm 10\%$. The systematic uncertainty due to JES is between 3% and 4% for the multijet variables studied. In order to demonstrate the sensitivity of hadronic multi-jet distributions to different models of multi-jet production, the distributions obtained from the corrected calorimeter level measurements are unfolded to particle level distributions using a bin-by-bin correction factor from the generator and detector level information. These distributions are then compared with the generator level predictions as obtained from different event generators that contain different models of QCD multi-jet production, PYTHIA, MADGRAPH[13] and HERWIG[14]. Figure 7.20 shows four such comparisons. The error bars show the statistical fluctuation as expected from a measurement with an

integrated luminosity of 10 pb^{-1} . The shaded bands show the total uncertainty which is a sum of statistical uncertainty and systematic uncertainty added in quadrature. The systematic uncertainties come from the jet energy scale and the unfolding of the detector level distributions to particle level. For the scaled energy of the most energetic jet in inclusive 3-jet final state, the expected distribution with total uncertainty, as shown on the top left plot in Figure 7.20, can distinguish different event generators. The top right plot shows the ψ angle for which expected data can also distinguish between generators. For the two plots in the bottom, the Nachtmann-Reiter angle and the Bengtson-Zerwas angle, expected data will not be able to distinguish among the event generators clearly. However, these distributions are sensitive to relative colour factors for different multi-parton vertices and all the models shown in these figures use the same set of colour factors. So these distributions will be able to test basic characteristics of QCD calculations.

Study of Global Event Shape variables

The jet properties of hadronic events are investigated using the global event shape variables. These event shape variables have been widely used to study QCD dynamics, especially at e^+e^- and ep colliders. These collinear and infrared safe variables, like thrust (T) [15, 16], heavy jet mass (ρ), total and wide jet broadening (B_T , B_W) [17, 18], are utilized to study the characteristic topology of the hadronic events. These variables are linear in momentum and hence infrared safe. This enables a more complete calculation of the respective distributions in perturbation theory. For e^+e^- annihilation predictions are available up to next-to-next-to-leading order (NNLO) in α_s [19]. Also the re-summation of large logarithms has been carried out up to the next-to-leading-logarithmic approximation (NLLA) [20]. This has been exploited for the experimental determination of fundamental parameters of QCD, in particular the strong coupling constant. In this study a simulation study of a class of event-shape variables as proposed in [21] is presented.

Figure 8.2 shows four of the central transverse event shape variables - Thrust, Major, total and wide jet broadenings. In the plots the measurements using corrected calorimeter jets as expected to be measured with 10 pb^{-1} of integrated luminosity are compared to the particle level jets. Also measurements using only charged particles at detector level and generator level are compared. Good agreement among all the four measurements is seen for all these variables. Figure 8.4 shows the transverse event shape distributions as expected from a measurement based on an integrated luminosity of 10 pb^{-1} . The shaded bands indicate the total uncertainty which is a sum of statistical uncertainty and systematic uncertainty added in quadrature. The systematic uncertainty is calculated in a similar way as done for multi-jet variables in Figure 7.20. The expected distributions with total uncertainty can distinguish different event generators.

Conclusion from QCD Analysis

Prospect of studies of global event shape variables as well as multi-jet variables in pp collision at a centre-of-mass energy of 10 TeV is presented for integrated luminosity of 10 pb^{-1} . Procedure for selecting the data sample, unfolding the data from detector effect and estimation of systematic uncertainties are established. These studies will enable to tune QCD event generators and will distinguish different hadronic models.

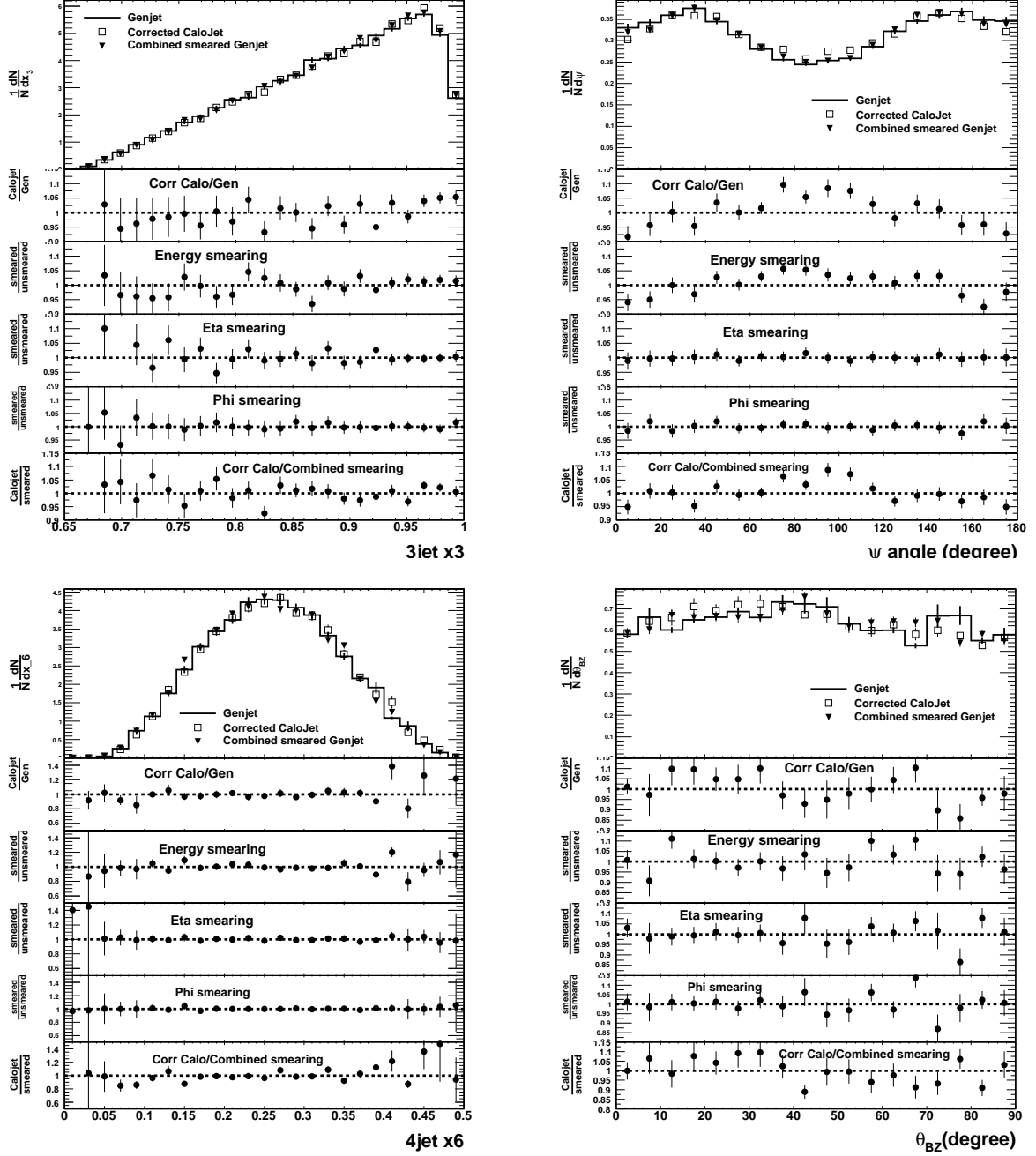


Figure 6: The effect of smearing of Genjets on the multi-jet distributions. The top left shows the energy fraction of the hardest jet in inclusive 3-jet final states. The top right plot shows the ψ angle in 3-jet case. Bottom left plot shows the energy fraction of the 4th leading jet for inclusive 4-jet final state. The Bengston-Zerwas angle is shown in bottom right plot. In each of the figures the histograms from top to bottom are as follows: distributions with Genjets, corrected Calojets and combined smeared Genjets; ratio of corrected Calojets to Genjets; ratio of smeared and unsmeared Genjets with only energy smearing; ratio of smeared and unsmeared Genjets with only η smearing; ratio of smeared and unsmeared Genjets with only ϕ smearing; ratio of corrected Calojets and smeared Genjets with combined energy+ η + ϕ smearing.

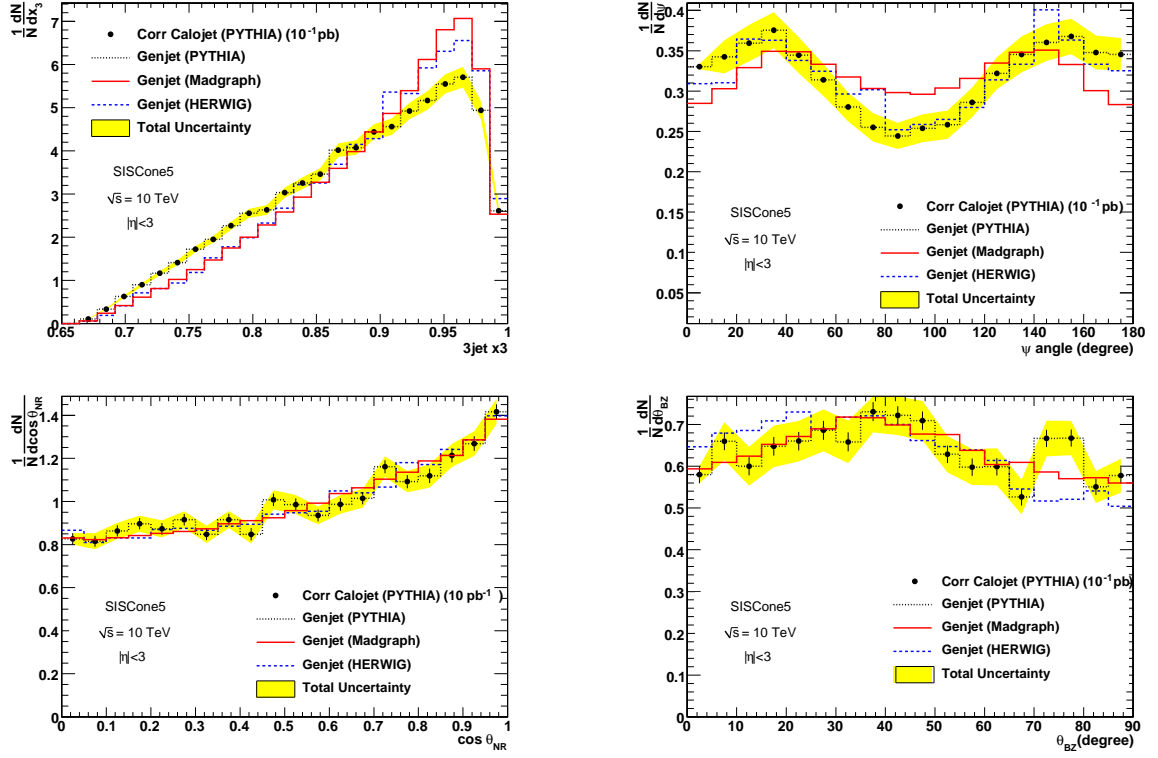


Figure 7: Multi jet distributions as they are expected to be measured with an integrated luminosity of 10 pb^{-1} and unfolded to particle level, compared to different event generator models. The top left plot shows the energy fraction of the most energetic jet in inclusive 3-jet final state. The top right plot shows the ψ angle in the 3-jet case. Bottom left plot shows the Nachtmann-Reiter angle. The Bengtson-Zerwas angle is shown in bottom right plot. The error bars reflect the statistical uncertainty and the yellow bands show the total uncertainty which is a sum of statistical uncertainty and systematic uncertainty (from jet energy scale and from unfolding correction) added in quadrature.

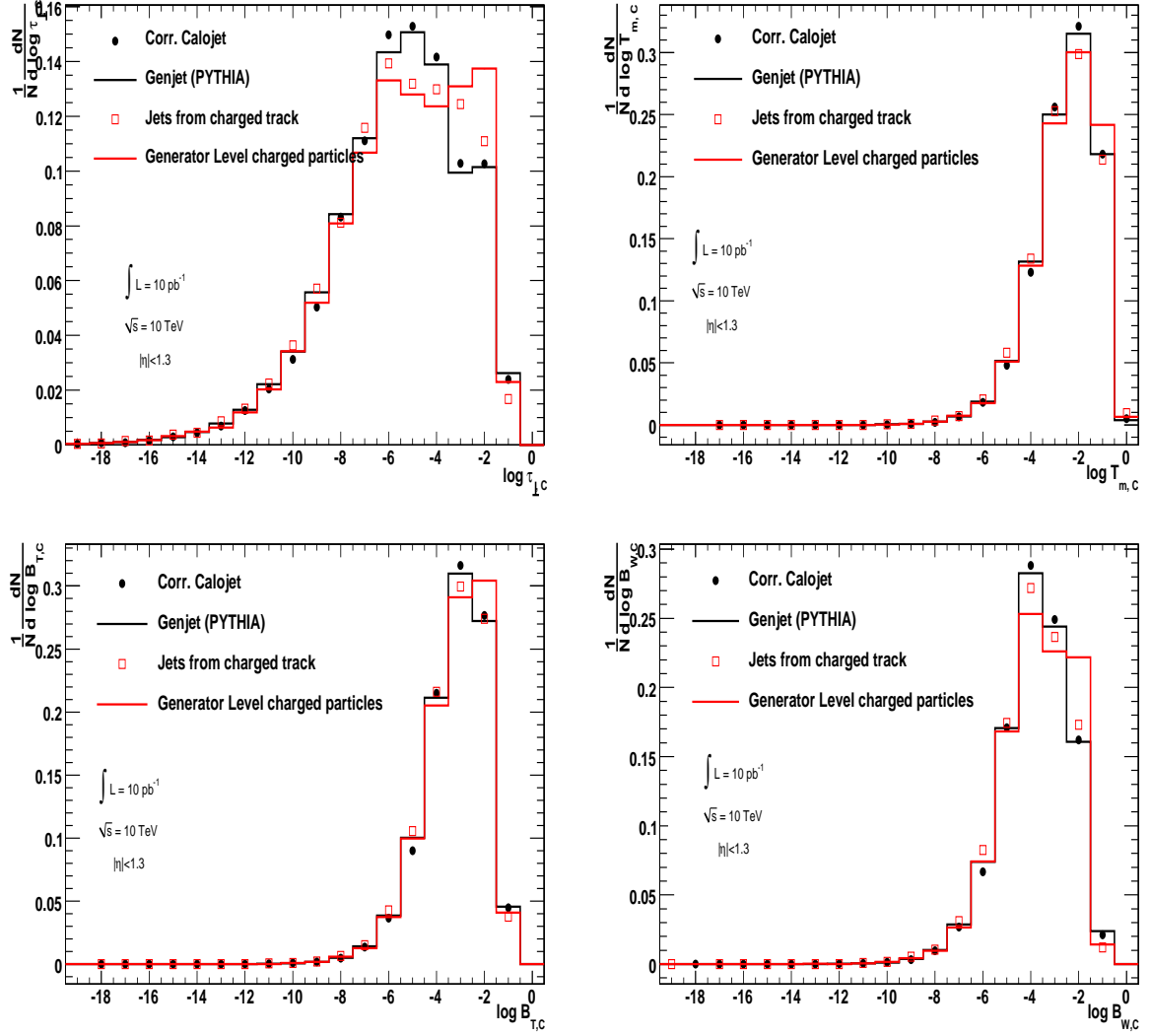


Figure 8: Global transverse event shape distributions for particle level and detector level jets. The black dots represent the measurements from corrected calorimeter jets as expected from 10 pb^{-1} data. The black lines show distributions using particle level jets (obtained from all stable charged and neutral particles). The open red circles and red lines show measurements using track jets at detector and at generator level.

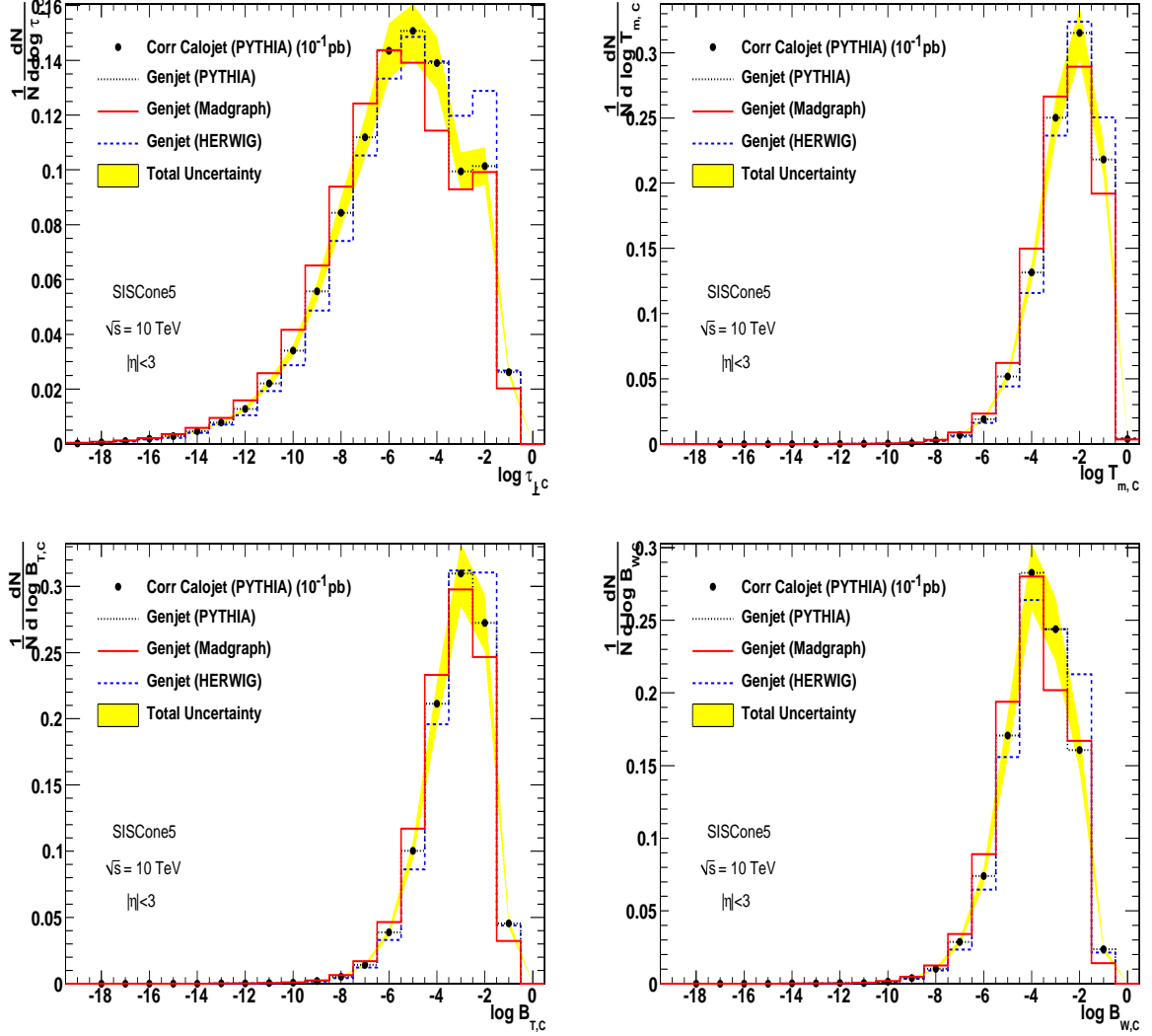


Figure 9: Global transverse event shape distributions as they are expected to be measured with an integrated luminosity of 10 pb^{-1} from pp data at 10 TeV centre-of-mass energy and unfolded to particle level. These are compared to predictions of different event generators. The top left figure shows the distribution for transverse thrust. The top right plot shows the distribution for transverse major. Bottom left and right plots show the distributions for total and wide jet broadenings. The error bars reflect the statistical uncertainty and the yellow band shows the total uncertainty which is a sum of statistical uncertainty and systematic uncertainty (from jet energy scale and from unfolding correction) added in quadrature.

Bibliography

- [1] The Large Hadron Collider: Conceptual Design, CERN/AC/95-05(LHC), 1995 and LHC Design Report, CERN 2004-003 (2004)
- [2] The CMS Collaboration, Technical Proposal, CERN/LHCC 94-39 (1994).
- [3] S. Abdullin, *et al.*, *The CMS Barrel Calorimeter Response to Particle Beams from 2 to 300 GeV/c*, European Physical Journal **C60** (2009) 359.
- [4] T. Sjostrand *et al.*, “*PYTHIA 6.4 Physics and Manual*”, hep-ph/0603175.
- [5] S. Agostinelli *et al.*, Nuclear Instruments and Methods **A506** (2003) 250; J. Allison *et al.*, IEEE Transactions on Nuclear Science **53** (2006) 278.
- [6] G. P. Salam, “*A Practical Seedless Infrared Safe Cone Algorithm*”, hep-ph/0705.2696.
- [7] R. Demina *et al.*, “*Calorimeter Energy Thresholds for Jet Reconstruction in CMS*”, CMS NOTE-2006/020.
- [8] S. Abachi *et al.*, “*Studies of topological distributions of inclusive three and four jet events in $\bar{p}p$ collisions at $\sqrt{s} = 1800\text{GeV}$ with the D0 detector.*”, Physical Review **D53**, No. 11 (1996) and the references therein.
- [9] M. Bengtsson and P. M. Zerwas, Physics Letters **B208** (1988) 306.
- [10] O. Nachtmann and A. Reiter, Zeitschrift für Physik **C16** (1982) 45.
- [11] B. Adeva *et al.*, *A test of QCD based on 4-jet events from Z^0 decays.*, Physics Letters **B248** (1990) 227.
<https://twiki.cern.ch/twiki/bin/view/CMS/CSA08AnaJets>.
- [12] CMS Collaboration, “*Plans for Jet Energy Corrections at CMS*”, CMS-PAS-JME-007-002.
- [13] See, for example, <http://madgraph.phys.ucl.ac.be/>
<https://twiki.cern.ch/twiki/bin/view/CMS/MadGraphCMSPage>.

- [14] M. Bahr, S. Gieseke, and M. H. Seymour, “*Simulation of multiple partonic interactions in Herwig++*”, JHEP **07** (2008), hep-ph/0803.076.
- [15] S. Brandt *et al.*, Physics Letters **12** (1964) 57.
- [16] E. Fahren, Physical Review Letters **39** (1977) 1587.
- [17] S. Catani *et al.*, Physics Letters **B295** (1991) 269.
- [18] Yu. L. Dokshitzer *et al.*, Journal of High Energy Physics **01** (1998) 11.
- [19] A. Gehrmann-De Ridder, T. Gehrmann, E. W. N. Glover and G. Heinrich, JHEP **0712** (2007) 094 [arXiv:0711.4711].
- [20] A. Banfi, G. P. Salam and G. Zanderighi, JHEP 0201 (2002) 018 [hep-ph/0112156].
- [21] A. Banfi, G. P. Salam and G. Zanderighi, JHEP 0408 (2004) 62 [hep-ph/0407287] .

Contents

Bibliography	xvii
Contents	i
List of Figures	v
List of Tables	ix
1 Introduction	1
1.1 Standard Model	2
1.2 Quantum Chromodynamics	3
1.2.1 The QCD Lagrangian	4
1.2.2 Renormalization and Running of α_S	7
1.2.2.1 Renormalization	7
1.2.2.2 Energy Dependence of α_S	8
1.2.2.3 Asymptotic Freedom and Confinement	8
1.2.2.4 The Λ Parameter	9
1.3 Cross Section for Hadron Collisions	10
1.3.1 Cross Section	10
1.3.2 Elastic Electron-Proton Scattering	11
1.3.3 Deep-inelastic Scattering and PDFs	12
1.3.4 Hadroproduction	14
1.4 Outline of the Thesis	17
2 LHC Machine and CMS Experiment	19
2.1 LHC Machine	19
2.2 CMS Detector	22
2.2.1 Tracker	24
2.2.2 Calorimeter	26
2.2.2.1 Electromagnetic Calorimeter	26
2.2.2.2 Preshower Detector	29

2.2.2.3	Hadron Calorimeter	29
2.2.3	Magnet	37
2.2.4	Muon Chambers	38
2.2.5	Trigger and Data Acquisition System	39
2.2.5.1	Level-1 Trigger	40
2.2.5.2	High Level Trigger	42
3	Simulation and Reconstruction	44
3.1	Event Generation	45
3.1.1	Modelling Perturbative QCD	48
3.1.2	Non-Perturbative Aspects of QCD	50
3.1.2.1	Fragmentation Process	50
3.2	Detector Simulation with Geant4	52
3.2.1	Treatment of Particles in Simulation	52
3.2.2	Electromagnetic Processes	54
3.2.3	Hadronic Processes	54
3.2.4	Physics Lists	55
3.3	Event Reconstruction	56
3.3.1	Track Reconstruction	56
3.3.2	Jet Reconstruction	57
3.3.2.1	Calorimeter Jet Reconstruction	59
3.4	CMS Simulation and Reconstruction Software	59
4	Jets and Event Selection	61
4.1	Jets in Hadron Colliders	61
4.2	Jet Definition	61
4.2.1	Jet Algorithms	62
4.3	Jet Energy Scale	67
4.4	Corrections to Calorimetry Jets	67
4.4.1	Offset Correction	69
4.4.2	Relative Corrections	69
4.4.3	Absolute Correction	70
4.4.4	Optional Corrections	70
4.4.4.1	Electromagnetic Energy Fraction	70
4.4.4.2	Jet Flavour	71
4.4.4.3	Underlying Event	71
4.4.4.4	Parton Level	71
4.5	Event Selection	71
4.5.1	Monte Carlo Sample	71

4.5.2	Event Selection for Calorimeter Jets	73
4.5.2.1	Event Clean-up	73
4.5.2.2	Trigger Selection	73
4.5.2.3	Offline Selection	75
4.5.3	Event Selection for TrackJets	75
4.5.3.1	Track Selection	75
4.5.3.2	Jet reconstruction from charged tracks	76
4.5.3.3	Trigger selection	77
4.5.3.4	Offline selection	77
5	Test Beam Experimental Setup	78
5.1	Introduction	78
5.2	Experimental Setup	78
5.2.1	TB2006 Calorimeter Setup	78
5.2.2	TB2007 Calorimeter Setup	80
5.2.3	Electronics and Data Acquisition	82
5.3	H2 Beam Line	83
5.4	Beam Line Counters and Particle Identification	84
5.4.1	Beam Line Counters	84
5.4.2	Beam Cleaning	85
5.4.3	Particle Identification	89
5.5	Detector Calibration	93
6	Test Beam Analysis	97
6.1	TB2006	97
6.1.1	Longitudinal Shower Profiles	98
6.1.2	Calibration with Electron Beam	100
6.2	TB2007	100
6.2.1	Reconstruction	102
6.2.2	Noise Levels in EE and HE	102
6.2.2.1	Noise in EE	102
6.2.2.2	Noise in HE	104
6.2.2.3	Noise in ES	104
6.2.3	MIP Studies in ECAL	106
6.2.4	Energy Measurements	107
6.2.4.1	HCAL Alone Setup	107
6.2.5	Energy Measurements in Combined Calorimeter System HE+EE . .	112
6.2.5.1	Beam Profile and MIP Fraction	115
6.2.6	Energy Measurements in the Preshower Detector	120

7	Multi-jet Studies	122
7.1	Multi-jet Topological Variables	122
7.1.1	3-parton Variables	123
7.1.2	4-parton Variables	124
7.2	Invariant mass of 3- and 4-jet system	126
7.3	Multi-jet Topological Distributions	127
7.3.1	Topologies of Three-Jet Events	127
7.3.2	Topologies of Four-Jet Events	129
7.4	Detector Effects	132
7.4.1	Energy Resolution	132
7.4.2	Position Resolution	132
7.4.2.1	Resolution in Eta	132
7.4.2.2	Resolution in Phi	134
7.4.3	Combined Effect of Energy and Position Resolution	134
7.5	Systematic Uncertainty	135
7.6	Sensitivity to Jet Algorithm	136
7.7	Sensitivity to Different Event Generators	137
7.7.1	Parton Shower versus Matrix Element	137
7.7.1.1	MADGRAPH Production	138
7.7.1.2	Comparison between PYTHIA and MADGRAPH	139
7.7.2	Sensitivity to Colour Coherence	141
7.7.3	Comparison between PYTHIA and HERWIG	141
7.8	Results	143
8	Study of Global Event Shape Variables	146
8.1	Global Event Shape Variables	146
8.2	Event Shape Variables in Hadronic Collisions	149
8.3	Systematic Uncertainty	150
8.4	Results	151
9	Conclusion	154
	Bibliography	156

List of Figures

1	Particle identification using time of flight (TOF) counters for 6 GeV/c positive beam. The time of flight difference is plotted in the units of TDC counts. Protons are well separated from pions and kaons for this beam momentum.	iv
2	Response and resolution of the combined ECAL + HCAL system (with preshower in front) measured as the ratio of energy measured to the beam momentum for π^- beam. Here HCAL is calibrated using 50 GeV/c electron beam. For the barrel part the beam was shot at $i\eta$ tower 7 and for the endcap the beam was shot at $i\eta$ tower 19.5.	v
3	Response and resolution of the combined ECAL + HCAL system (with preshower in front) with pion beams where the pion gives an MIP like signal in the EE. The response is defined as the ratio of the measured energy to the beam momentum and here the HCAL is calibrated using 50 GeV/c electron beam.	v
4	MIP fraction (fraction of events where energy measured in the ECAL \leq 1.5 GeV) as a function of beam momenta.	vi
5	Distribution of invariant mass of the 3- and 4-jet events as expected from integrated luminosity of 10 pb^{-1}	ix
6	The effect of smearing of Genjets on the multi-jet distributions.	xiii
7	Comparison of expected multi jet distributions to different event generators.	xiv
8	Event shape distributions at particle and detector level.	xv
9	Comparisons of different Event shape distributions as they are expected to be measured with different event generators.	xvi
1.1	Basic vertices in QCD describing quark-gluon and gluon self couplings. . .	7
1.2	Running of the strong coupling constant.	9
1.3	Distribution of $xf(x)$ (where $f(x)$ is the parton distribution function) as a function of the momentum fraction x at $\mu^2 = 10 \text{ GeV}^2$ for different partons.	14
1.4	The parton model description of a hard scattering process in a hadron-hadron collision.	15

2.1	Overview of the CERN Accelerator Complex. The hadron beams are accelerated by several successive facilities to the LHC injection energy of 450 GeV before being accelerated in the LHC to higher energies.	20
2.2	An overview of the CMS detector.	23
2.3	Layout of the CMS Tracker showing various components of the detector. .	25
2.4	Cross sectional view of the CMS detector with approximate dimensions and positions.	27
2.5	Grouping of layers of the barrel and the endcap hadron calorimeter in the (r, z) plane. Different groupings are shown in different colours.	31
2.6	A schematic view of HCAL readout electronics.	34
2.7	Quarter-view of the CMS detector. The muon system is labeled.	38
2.8	General architecture of CMS DAQ system.	40
2.9	Level-1 trigger components.	41
3.1	Schematic overview of showering and hadronization.	46
3.2	String representation of a $q\bar{q}g$ system.	51
3.3	Schematic diagram of cluster fragmentation.	53
3.4	Visualization of Jets - from particle level to the detector level.	58
4.1	Infrared and collinear safety.	63
4.2	Schematics of Seedless Infrared Safe Cone Algorithm.	66
4.3	Schematic overview of the factorised multi-level jet correction in CMS. . .	68
4.4	Relative and absolute corrections on calorimeter jets.	70
4.5	Distribution of the MET/ ΣE_T for simulated QCD events and the Cosmic data. .	74
4.6	Determination of efficiency of single jet HLT trigger for Calojets.	75
4.7	Track selection.	76
4.8	Determination of efficiency of single jet HLT trigger for track jets.	77
5.1	Calorimeter setup in the 2006 test beam	79
5.2	Calorimeter setup in the 2007 test beam	80
5.3	Design and readout schemes of HE modules used in the test beam setup and in the CMS setup.	81
5.4	EE super-crystal as used in the 2007 test beam.	82
5.5	The two planes and a ladder of the preshower detector in 2007 test beam. .	83
5.6	A Schematic diagram to show the location of secondary target T22 and the VLE beam line	84
5.7	A schematic view of beam line elements showing the location of detectors used for beam cleaning and particle identification.	86
5.8	Signal and pedestal distributions in the four trigger scintillators.	87

5.9	Signal distributions for the trigger scintillator - S4.	87
5.10	Pulse height distributions in the beam halo counters.	88
5.11	Beam profiles measured by wire chamber C at different beam energies. . .	89
5.12	Pulse height distributions in the front and the back muon veto counters. .	90
5.13	Pressure in the Cerenkov counters as a function of pion energy.	90
5.14	Signals in two Cerenkov counters - CK2, CK3.	91
5.15	Time of flight measurement for different beam momenta.	92
5.16	Calibration of Time of Flight Detector.	93
5.17	Time of flight measurement for different beam momenta.	94
5.18	Calibration of preshower detector.	95
6.1	Using Cerenkov counters for beam cleaning.	98
6.2	Longitudinal shower profiles of electrons and pions.	99
6.3	Shower depth as a function of incident beam energy.	100
6.4	Calibration of hadron barrel.	101
6.5	Correlation between the calibration constants from electron and muon data.	101
6.6	Energy distribution in 10 time slices for HE.	102
6.7	Noise in EE super-crystals.	103
6.8	Energy contained in a matrix of N×N crystals surrounding the central crystal in the super-module	104
6.9	Noise in hadron endcap (HE).	105
6.10	Noise in the preshower detector.	105
6.11	MIP signal in the ECAL for π^- beam.	106
6.12	Illustration of the beam spot position in the HE towers geometry.	107
6.13	Calibration of HE towers.	108
6.14	Total energy measured in the two depths of HE.	109
6.15	Total energy measured in the two depths of HE with beam cleaning cuts applied.	109
6.16	Total energy measured in HE.	110
6.17	Response and resolution of HCAL alone system.	111
6.18	Energy shared between HE towers and EE crystals.	113
6.19	Total energy measured in the combined HCAL+ECAL system.	113
6.20	Response and resolution of the combined ECAL + HCAL system (with the preshower in front).	114
6.21	Response and resolution of the combined ECAL + HCAL system with MIP in EE.	116
6.22	MIP fraction as a function of beam momenta.	118
6.23	Wire Chamber hits and energy weighted occupancy in the EE crystals. . .	118
6.24	Beam profile for EE and HE as a function of Wire chamber y hits.	119

6.25	Cut on the wire chamber y position to mask the gap between EE super-modules.	120
6.26	Beam spot in the two planes of preshower detector.	121
6.27	Energy measured in the preshower detector.	121
7.1	Feynman diagrams for 3 parton final state.	122
7.2	Feynman diagrams for 4-parton final state.	123
7.3	An Illustration of the three-jet angular variables.	123
7.4	An Illustration of the four-jet angular variables.	125
7.5	Invariant mass of 3-jet and 4-jet final states.	126
7.6	Particle level distributions of scaled energies of three jets.	127
7.7	Particle level distributions of scaled energies of three jets with higher leading jet threshold.	127
7.8	Particle level distributions of the angular variables for three jets.	128
7.9	Particle level distributions of the angular variables for three jets with higher leading jet threshold.	128
7.10	Particle level distribution of scaled energies of four jets.	129
7.11	Particle level distribution of scaled energies of four jets with higher leading jet threshold.	130
7.12	Particle level distributions of the angular variables for four jets.	130
7.13	Particle level distributions of the angular variables for four jets with higher leading jet threshold.	131
7.14	The effect of smearing of Genjets on the multi-jet distributions.	133
7.15	The effect of uncertainty in the jet energy scale on the multi-jet distributions.	136
7.16	Distribution of multi-jet distributions for different jet algorithms.	138
7.17	Multi jet distributions from generator level jets obtained using PYTHIA and MADGRAPH.	140
7.18	Effect of Angular Ordering for multijet distributions.	142
7.19	Multi jet distributions from generator level jets obtained using PYTHIA and HERWIG.	143
7.20	Comparison of expected multi jet distributions to different event generators.	144
8.1	Illustration of the thrust axis.	147
8.2	Event shape distributions at particle and detector level.	151
8.3	The effect of jet energy scale on the event shape distributions.	152
8.4	Comparisons of different Event shape distributions as they are expected to be measured with different event generators.	153

List of Tables

1.1	The fermion sector of the Standard Model.	2
2.1	Parameters for the Large Hadron Collider relevant for the peak luminosity operation.	22
3.1	Energy thresholds (in GeV) for calorimeter noise suppression “Scheme B”. Σ EB and Σ EE refer to the sum of ECAL energy deposits associated with the same tower in the barrel and in the endcap respectively.	59
4.1	Details of the MC samples used in the present analysis.	72
4.2	Trigger table proposed for $L = 10^{31} \text{ cm}^{-2} \text{ s}^{-1}$	74
4.3	Number of events passing the prescale for two HLT trigger paths.	74
5.1	Peak positions of pion from negative and positive beams.	93
5.2	Peak positions of pion from negative and positive beams.	95
5.3	Beam composition in the hadron beam of the negatively charged low energy beams.	95
5.4	Beam composition in the hadron beam of the positively charged low energy beams.	96
5.5	The combination of detectors used in identifying particle types in the test beam setup.	96
6.1	Response for HCAL alone system.	110
6.2	Resolution for the HCAL alone system.	111
6.3	Response for HCAL+ECAL (ES in front) with HCAL calibrated using 50 GeV/c electron.	115
6.4	Resolution for HCAL + ECAL (ES in front) with HCAL calibrated using 50 GeV/c e^-	116
6.5	Response for HCAL+ECAL (ES in front) with MIP in EE and with HCAL calibrated using 50 GeV/c electron.	117
6.6	Response for HCAL+ECAL (ES in front) with MIP in EE with HCAL calibrated using 50 GeV/c electron.	117

7.1	Average statistical uncertainties for 3-jet and 4-jet variables.	131
7.2	RMS (in %) of the ratio of the smeared and generator level distributions for different multi-jet variables.	135
7.3	RMS (in %) of the ratio of distributions when jet p_T 's are increased or decreased by 10% with respect to the default distribution.	137
7.4	RMS (in %) of the ratio of distributions for Corrected and Generated jets for the four jet algorithms - Siscone5, Siscone7, KT4 and KT6.	139
7.5	Details of the MADGRAPH Fall08 MC samples used in the present analysis. . .	139
7.6	RMS (in %) of the ratio of distributions for corrected jets obtained from the two Monte Carlo samples using MADGRAPH and PYTHIA event generators. . . .	141
7.7	RMS (in %) of the ratio of distributions for generator level distributions for different multi-jet variables without and with angular ordering effects in the PYTHIA Monte Carlo.	141
7.8	RMS (in %) of the ratio of distributions for generator level jets obtained using HERWIG and PYTHIA event generators.	144
8.1	RMS (in %) of the ratio of distributions when jet p_T is increased or decreased by 10% with respect to the default distribution.	153

Chapter 1

Introduction

At one time there were believed to be four fundamental particles - electron, photon, proton and neutron. These were not only sufficient to explain the physical and chemical properties of matter that we encounter in everyday life, the processes inside the Sun and stars, the prospectives of condensed matter and plasma, the physics of reactors, etc.

However the dense packing of like-charged mutually repelling protons in the small core of an atom called nucleus led physicists to seek for an understanding of the forces of strong interaction between the nucleons: an interaction strong enough to overcome the electrostatic repulsions between protons at distances (10^{-15} m), smaller than the radius of the nucleus *i.e.* an interaction with a lifetime $\sim 10^{-23}$ sec.

The idea of global isospin invariance, that proton and neutron are two components of an isospin doublet, had been proposed the same year neutron was discovered (1932), and the hypothesis that the carrier of this nucleon force is the π meson was proposed by Yukawa in 1934. It was realized that a triplet of π -mesons must exist (1938): π^+, π^0, π^- (π^0 is the first particle predicted on the basis of internal symmetry). But the experimental connection between the mesotron (discovered in cosmic ray by two groups: Anderson and Neddermeyer, and Street and Stevenson, in 1937) with the theoretically wanted triplet of pi mesons was unclear.

Three discoveries in 1947 marked the beginning of our current knowledge about the understanding the matter. Powell *et al.* at Bristol discovered two particles of mass between electron and proton masses in cosmic rays by exposing photographic emulsions on mountain tops. These particle were later designated as pion (π^+) and muon (μ^+) (for the preceding ten years they “coexisted as mesotron”). Also strange particles were discovered around same time by Rochester and Butler as they saw two V^0 decay events in cloud chamber photographs. These discoveries started the process of shifting high energy physics from its cosmic ray cradle to the huge detectors in today’s big accelerator.

In 1948, the first man-made charged pions were produced and the neutral ones were discovered in 1950. The first man-made kaons and hyperons were produced in 1954. By

the end of 1960, the list of strongly interacting or decaying particles discovered had grown to hundreds.

In 1961 the “Eightfold Way” was invented by Gell-Mann and Ne’eman, and the discovered mesons (spin-0, 1 bound states) and baryons (spin- $\frac{1}{2}$ bound states) started to get explained in terms of a model of 3 quarks (u, d, s) with fractional values of baryonic number and electric charge. The next decade witnessed the transformation of our understanding of the nature of strong interaction: from the phenomenological Quark Model (1964) to QCD or Quantum ChromoDynamics - a local field theory based on the non-abelian group SU(3) of internal gauge symmetry of colour degrees of freedom.

1.1 Standard Model

The Standard Model of particle physics, formulated in a period 1964 - 1973, is a theory which describes the fundamental particles and their interactions. According to this model, all matter is built from a small number of fundamental spin 1/2 particles, namely six leptons and six quarks. For each of these particles, which are called fermions according to their half-integer spin, an antiparticle exists which has the same properties as the corresponding particle but the signs of its internal quantum numbers are reversed.

	1st family	2nd family	3rd family
leptons	$\begin{pmatrix} \nu_e \\ e \end{pmatrix}$ $\begin{matrix} < 3 \text{ eV} \\ 0.511 \text{ MeV} \end{matrix}$	$\begin{pmatrix} \nu_\mu \\ \mu \end{pmatrix}$ $\begin{matrix} < 0.19 \text{ MeV} \\ 106 \text{ MeV} \end{matrix}$	$\begin{pmatrix} \nu_\tau \\ \tau \end{pmatrix}$ $\begin{matrix} < 18.2 \text{ MeV} \\ 1.777 \text{ GeV} \end{matrix}$
quarks	$\begin{pmatrix} u \\ d \end{pmatrix}$ $\begin{matrix} \sim 7 \text{ MeV} \\ \sim 3 \text{ MeV} \end{matrix}$	$\begin{pmatrix} c \\ s \end{pmatrix}$ $\begin{matrix} \sim 1.2 \text{ GeV} \\ \sim 115 \text{ MeV} \end{matrix}$	$\begin{pmatrix} t \\ b \end{pmatrix}$ $\begin{matrix} \simeq 175 \text{ GeV} \\ \sim 4.25 \text{ GeV} \end{matrix}$

Table 1.1: The fermion sector of the Standard Model.

The four fundamental interactions between particles are described by the exchange of integer spin mediators which are called bosons: the photon for the electromagnetic force, two W bosons and the Z boson for the weak interaction and eight gluons for the strong interaction. Gravity takes a special position in this context as it is not included in the Standard Model and its predicted mediator, the graviton, has not been observed to date.

Three of the six leptons carry a charge of $-e$ and each can be paired with a neutral lepton, the neutrino, to form three families. These consist of the electron, the muon and the tau with their corresponding neutrino. Characteristic for each family is a quantum number called the electron, muon or tau number, which is conserved by all interactions. However, the mass eigenstates of the neutrinos differ from their energy eigenstates lead-

ing to experimentally observed oscillations between different flavours. Obviously, these oscillations do not conserve the family specific lepton numbers but only their sum. An overview of the three lepton families is given in Table 1.1.

The six quarks carry a fraction of $\frac{2}{3}$ or $-\frac{1}{3}$ of the elementary charge and can also be grouped into three families. Each quark flavour has an own quantum number which is conserved by all interactions except the weak force. This violation is a result of the difference between the mass eigenstates of the quarks and the eigenstates of the weak interaction. The two representations are connected by the Cabibbo-Kobayashi-Maskawa (CKM) matrix which makes flavour changes without conservation of the dedicated quantum number become possible. An overview of the different quark flavours is presented in Table 1.1.

With the Δ^{++} resonance, a spin 1/2 particle consisting of three up quarks has been observed. The three quarks are in the same state and an additional quantum number is required to preserve the Pauli principle. This quantum number is called the colour-charge and can adopt three values of red(R), green(G) and blue(B). All particles observed to date are colour-neutral, which indicates that quarks do not exist as free particles. The colour disappears if a colour and its anti-colour are combined. This is possible for a bound state of a quark and an anti-quark, which is called meson. Baryons are RGB bound states of three quarks. These two strongly interacting bound quark states are called hadrons.

The Standard Model is a local quantum field theory. The Lagrangian of the theory is invariant under a $SU(3)_C \otimes SU(2)_L \otimes U(1)_Y$ transformation. The field content of the Standard Model consists of a set of massless gauge fields, spin 1/2 fermions and massive gauge bosons. The gauge bosons are spin 1 vector fields. Gauge fields are G_μ^a ($a = 1, 2, \dots, 8$), W_μ^i ($i = 1, 2, 3$) and B_μ corresponding to the symmetry groups $SU(3)_C$, $SU(2)_L$, $U(1)_Y$ respectively. The known matter fields in the fermionic sector are spin $\frac{1}{2}$ fermion: quarks and leptons. The charged leptons take part in electromagnetic and weak interactions whereas the neutral leptons take part only in weak interaction. Some of the physical gauge bosons are massive, although gauge invariance requires them to be massless. Spontaneous symmetry breaking (SSB) was introduced as a mechanism to generate masses of the massive gauge bosons and the massive fermions.

1.2 Quantum Chromodynamics

Quantum Chromodynamics (QCD)[1, 2, 3, 4, 5, 6, 7, 8] is a gauge theory which describes the strong interactions of the spin- $\frac{1}{2}$ quarks and spin-1 gluons, collectively known as partons through the exchange of an octet of massless vector gauge bosons, the gluons, using similar concepts as known from Quantum Electrodynamics, QED[9]. QCD, however, is more complex than QED because quarks and gluons, the analogues to electrons and

photons in QED, are not observed as free particles but are confined inside hadrons. QCD is based on an exact internal symmetry with non-abelian SU(3) group structure. Two main properties of the theory are asymptotic freedom and confinement. Asymptotic freedom [100, 101] tells us that the effective coupling decreases logarithmically at short distances (at high momentum transfer) making the partons quasi-free so that perturbative calculation stands relevant at that scale. Confinement, implies that the coupling strength α_s , the analogue to the fine structure constant α in QED, becomes large in the regime of large-distance or low-momentum transfer interactions.

Within QCD, the phenomenology of confinement and of asymptotic freedom is realized by introducing a new quantum number, called “colour charge”. Quarks carry one out of three different colour charges, while hadrons are colourless bound states of 3 quarks or 3 antiquarks (“baryons”), or of a quark and an anti-quark (“mesons”). Gluons in contrast to photons which do not carry (electrical) charge by themselves, have two colour charges. This leads to the process of gluon self interaction, which in turn, through the effect of gluon vacuum polarization, produce an anti-screening of the bare QCD charges, giving rise to asymptotic freedom and colour confinement.

The perturbative calculation of a process requires the use of Feynman rules describing the interactions of quarks and gluons which can be derived from the effective Lagrangian density of the interaction.

1.2.1 The QCD Lagrangian

In QCD the six quark flavours are represented by quantum fields $q = \{u, d, s, c, b, t\}$, which behave identically, apart from their differing masses, and do not directly interact with one another. The quark fields have an extra degree of freedom known as colour; each of the three components q_a ($a = 1, 2, 3$) is a Dirac spinor. Treating them as non-interacting fermion fields, the Dirac Lagrangian would therefore become

$$\mathcal{L} = \sum_a \bar{q}_a (i\gamma^\mu \partial_\mu - m) q_a \quad (1.1)$$

Under a unitary “phase transformation” applied to the three-component colour vector q , it becomes

$$q_a \rightarrow q'_a = \sum_b \Omega_{ab} q_b \equiv \sum_b \exp \left[\frac{ig_S}{2} \sum_A \alpha^A \lambda_{ab}^A \right] q_b \quad (1.2)$$

where the 3×3 Hermitian matrices λ^A ($A = 1, 2, \dots, 8$) are the generators of the Lie group SU(3), and α^A are eight arbitrary constants. The Lagrangian given in Equation (1.1) is invariant under this global transformation, due to the unitary property of the Ω matrices; this is analogous to the invariance of the Dirac Lagrangian under the phase transforma-

tion $\psi \rightarrow \psi' = \psi e^{iq\phi}$.

The global colour transformation demonstrates the conservation of colour in a non-interacting theory, but does not introduce any physical dynamics. The theory of QCD is derived by requiring the invariance of the Lagrangian under *local* SU(3) colour transformations: instead of choosing the same unitary matrix, $\Omega = \exp[i \sum_A \alpha^A \lambda^A]$, at all points in space and time, the coefficients α^A are space-time dependent, giving

$$q_a \rightarrow q'_a = \sum_b \Omega_{ab}(x) q_b \equiv \sum_b \exp \left[\frac{ig_S}{2} \sum_A \alpha^A(x) \lambda_{ab}^A \right] q_b \quad (1.3)$$

Substituting this transformed quark field into Equation (1.1), the Lagrangian is found no longer to be invariant, because the space-time derivatives act on the coefficients $\alpha^A(x)$. To restore the invariance of the Lagrangian, the partial derivative ∂_μ should be first replaced with a *covariant derivative*

$$(D_\mu)_{ab} = \partial_\mu \delta_{ab} + \frac{ig_S}{2} \sum_A \mathcal{A}_\mu^A \lambda_{ab}^A, \quad (1.4)$$

where the eight *gauge fields* \mathcal{A}^A are introduced, each with four space-time components μ ; the free parameter g_S is a coupling constant. The Lagrangian now becomes

$$\mathcal{L} = \sum_{a,b} \bar{q}_a (i\gamma^\mu D_\mu - m)_{ab} q_b \quad (1.5)$$

$$\equiv \sum_a \bar{q}_a (i\gamma^\mu \partial_\mu - m) q_a + \frac{ig_S}{2} \sum_{a,b} \sum_A \bar{q}_a (\gamma^\mu \mathcal{A}_\mu^A) \lambda_{ab}^A q_b \quad (1.6)$$

In the last line, \mathcal{L} has been decomposed into two contributions: the first is the Dirac Lagrangian for three non-interacting components of a fermion field, and the second introduces interactions between the gauge fields and the quarks. The quanta of the eight fields \mathcal{A}^A are called gluons, and are responsible for the observed strong interactions of quarks. To complete the process of establishing local gauge invariance, the transformation properties of the gluon fields must be chosen such that the covariant derivative $\sum_b (D_\mu)_{ab} q_b$ transforms in the same way as the quark field itself,

$$\sum_b (D'_\mu)_{ab} q'_b = \sum_{b,c} \Omega_{ab}(x) (D_\mu)_{bc} q_c \quad (1.7)$$

This is achieved with the relationship

$$\sum_A \mathcal{A}'^A_\mu \lambda^A = \Omega(x) \left[\sum_A \mathcal{A}^A_\mu \lambda^A \right] \Omega^{-1}(x) + \frac{2i}{g_S} (\partial_\mu \Omega(x)) \Omega^{-1}(x) \quad (1.8)$$

where the colour indices of the λ^A and $\Omega(x)$ matrices are suppressed.¹

One further contribution must be inserted in the Lagrangian, to specify the equations of motion for the gluon fields. In quantum electrodynamics, the Lagrangian for the photon field A is given by

$$\mathcal{L}_{\text{photon}} = -\frac{1}{4}F_{\mu\nu}F^{\mu\nu} \quad , \quad (1.9)$$

where F is simply a quantized form of Maxwell's electromagnetic field strength tensor

$$F_{\mu\nu} = \partial_\mu A_\nu - \partial_\nu A_\mu \quad (1.10)$$

Applying the Euler-Lagrange Equations to $\mathcal{L}_{\text{photon}}$ gives the familiar Maxwell Equations, governing the internal dynamics of the field. An analogous term appears in the Lagrangian of QCD,

$$\mathcal{L}_{\text{gluon}} = -\frac{1}{4} \sum_A F_{\mu\nu}^A F_A^{\mu\nu} \quad (1.11)$$

but here the eight field strength tensors for the gluons are

$$F_{\mu\nu}^A = \partial_\mu \mathcal{A}_\nu^A - \partial_\nu \mathcal{A}_\mu^A - g_S \sum_{B,C} f^{ABC} \mathcal{A}_\mu^B \mathcal{A}_\nu^C \quad (1.12)$$

where the structure constants f^{ABC} are defined by the commutation relations of the SU(3) generators, $[\lambda^A, \lambda^B] = 2if^{ABC}\lambda^C$. The last term of Equation (1.12), which is derived by imposing local SU(3) gauge symmetry on the octet of gluon fields, arises because the gauge transformations of QCD do not commute. The expansion of the product $F_{\mu\nu}^A F_A^{\mu\nu}$ in Equation (1.11) gives rise to an array of terms containing products of two, three and four gluon fields. The three- and four-gluon terms in the Lagrangian are due to the self-interaction of the gluon field, which has no analogue in QED.

The collection of all terms together lead to complete Lagrangian density of QCD ²:

$$\mathcal{L}_{\text{QCD}} = \sum_a \bar{q}_a (i\gamma^\mu \partial_\mu - m) q_a + \frac{ig}{2} \sum_{a,b} \sum_A \bar{q}_a (\gamma^\mu \mathcal{A}_\mu^A) \lambda_{ab}^A q_b - \frac{1}{4} \sum_A F_{\mu\nu}^A F_A^{\mu\nu} \quad (1.13)$$

The derivation of the Feynman rules associated with the QCD Lagrangian, and their formal interpretation can be found in Ref. [10]. The terms in the Lagrangian correspond to the permitted vertices as shown in Figure 1.1.

¹A simpler transformation law, of the form $\mathcal{A}'^A = \mathcal{A}^A + \delta\mathcal{A}^A$, exists when the gauge transformation $\Omega(x)$ differs only infinitesimally from the identity matrix.

²When performing practical calculations, some further terms need to be inserted to fix the gauge and to remove infinite over counting of equivalent gauge configurations. These are discussed in Ref. [10].

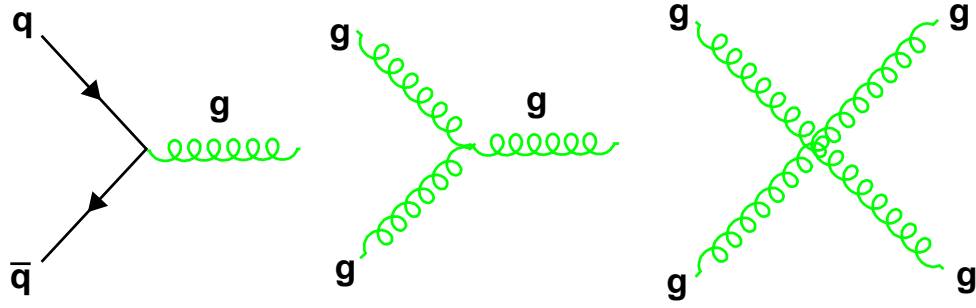


Figure 1.1: Basic vertices in QCD describing quark-gluon and gluon self couplings.

Up to this point, the coupling constant of QCD has been denoted g_S . However, the related quantity is also expressed as $\alpha_S = g_S^2/4\pi$.

1.2.2 Renormalization and Running of α_S

1.2.2.1 Renormalization

In quantum field theories like QED and QCD, dimensionless physical quantities \mathcal{R} can be expressed by a perturbation series in powers of coupling parameter α_S or α , respectively. When calculating \mathcal{R} as a perturbation series in α_S ultraviolet divergences occur. Because \mathcal{R} must retain physical values, these divergences are removed by a modification of the Lagrangian of the theory. This is called “renormalization” [10, 11] and it introduces an energy scale μ , which depends upon the renormalization scheme undertaken. For example, in the modified minimal subtraction (\overline{MS}) scheme, this represents the energy scale at which the ultraviolet divergences along with a constant term get subtracted. As a consequence of this procedure, \mathcal{R} and α_S become functions of the renormalization scale μ . It turns out that \mathcal{R} depends on the ratio Q^2/μ^2 and on the renormalized coupling constant $\alpha_s(\mu^2)$:

$$\mathcal{R} \equiv \mathcal{R}(Q^2/\mu^2, \alpha_S) ; \alpha_S \equiv \alpha_s(\mu^2).$$

Identifying the renormalization scale with the physical energy scale of the process, $\mu = Q$, eliminates the presence of a second and unspecified scale. In this case α_S transforms to the “running coupling constant” $\alpha_S(Q^2)$, and the energy dependence of \mathcal{R} enters only through the energy dependence of $\alpha_S(Q^2)$.

1.2.2.2 Energy Dependence of α_S

While QCD does not predict the actual size of α_S at a particular energy scale, its energy dependence is precisely determined. The running of the strong coupling constant is given by the Renormalization Group (RG) equations. However, the concept of RG asserts that the observables of the theory remain independent of the choice of this scale μ . The RG equations of QCD are:

$$\mu^2 \frac{\partial \alpha_S}{\partial \mu^2} = -\alpha_S^2 \sum_k \beta_k \alpha_S^k \quad (1.14)$$

where the first three β -functions [12], in the \overline{MS} scheme, in terms of n_f (the number of flavour degeneracy of quarks) are:

$$\begin{aligned} \beta_0 &= \frac{33 - 2n_f}{12\pi} \\ \beta_1 &= \frac{153 - 19n_f}{24\pi^2} \\ \beta_2 &= \frac{77139 - 15099n_f + 325n_f^2}{3456\pi^3} . \end{aligned}$$

1.2.2.3 Asymptotic Freedom and Confinement

The solution of Equations (1.14) at energy Q^2 is related to the solution at energy μ up to lowest order by:

$$\alpha_S(Q^2) = \frac{\alpha_S(\mu^2)}{1 + \beta_0 \alpha_S(\mu^2) \ln(\frac{Q^2}{\mu^2})} . \quad (1.15)$$

Since the most accurate measurements of α_S have been at $Q^2 = M_Z^2$, $\mu = M_Z$ is chosen to be the reference scale, and we write $\alpha_S \equiv \alpha_S(M_Z)$. The above relations show that α_S decreases with increasing Q^2 for $n_f \leq 16$ (demonstrating the property of asymptotic freedom). This is contrary to the analogous running of the electromagnetic or weak coupling constants which increase with increasing energy.

Likewise, Equation (1.15) indicates that $\alpha_S(Q^2)$ grows to large values and actually diverges to infinity at small Q^2 : for instance, with $\alpha_S(\mu^2 \equiv M_Z^2) = 0.12$ and for typical values of $n_f = 2 \dots 5$, $\alpha_S(Q^2)$ exceeds unity for $Q^2 \leq \mathcal{O}(100 \text{ MeV} \dots 1 \text{ GeV})$. Clearly this is the region where perturbative expansions in α_S are not meaningful anymore, and we may regard energy scales of μ^2 and Q^2 below the order of 1 GeV as the non-perturbative region where confinement sets in, and where Equations (1.14) and (1.15) cannot be applied.

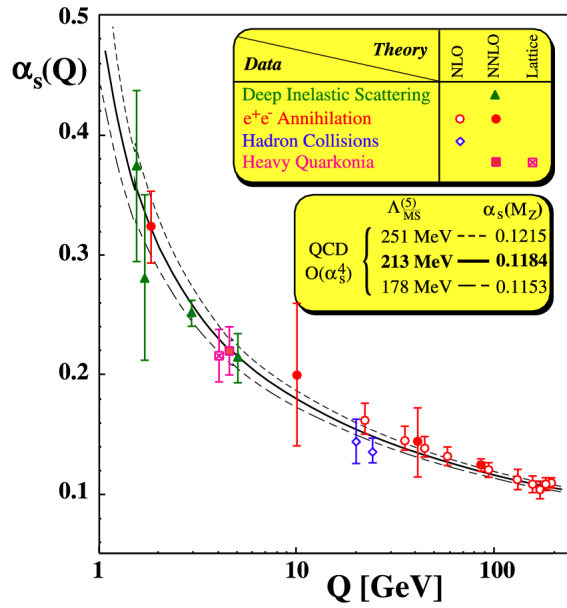


Figure 1.2: Running of the strong coupling constant.

1.2.2.4 The Λ Parameter

Alternatively, as another parametrization of $\alpha_s(Q^2)$, a dimensional parameter Λ can also be used as the free parameter of QCD, interchangeably with α_s . The parameter Λ , marking the boundary between the perturbative and non-perturbative energy domains of QCD, may be defined as:

$$\Lambda = \mu^2 \exp \left(\frac{1}{-2\beta_0 \alpha_s(\mu^2)} \right) .$$

Up to leading order, the energy (Q^2) dependence of the strong coupling constant is given by the following formula :

$$\alpha_s(Q^2) = \frac{1}{\beta_0 \ln(Q^2/\Lambda^2)} .$$

The parametrization of the running coupling $\alpha_s(Q^2)$ with Λ instead of $\alpha_s(\mu^2)$ has become a common standard.

QCD has been tested in a variety of experiments and all the measurements are consistent with the non-abelian nature of QCD which predicts asymptotic freedom[13]. Figure 1.2 shows the strong coupling constant measured at various energies [14] together with expectations from QCD.

1.3 Cross Section for Hadron Collisions

Since the discovery of the substructure of atoms by Rutherford in 1903, particle physics experiments have been based on the same method. Highly energetic probe particles are used to get information on the structure and the interactions of the target material. An important parameter of such investigations is the resolution ΔR which can be achieved with a probe particle. Here, ΔR is a measure for the minimal distance between two objects which still can be resolved. For particle beams, this resolution is of the order of magnitude of their de Broglie wavelength

$$\lambda = \frac{h}{p} \tag{1.16}$$

where h is Planck's constant and p is the momentum of the beam particle.

To get deeper and deeper insights of the substructure of particles requires therefore increasing beam energies. In addition, to create particles with high masses in experiments and to study their properties, the centre-of-mass energy \sqrt{s} of the particle collisions has to exceed the energy of the desired particle, related by Einsteins equivalence of mass and energy $E = mc^2$. For fixed target experiments, \sqrt{s} increases only with the square root of the energy. Therefore, collider experiments in which the particles of the two beams have equal energy E are favoured because of the linear increase of the centre-of-mass energy with E , following

$$\sqrt{s} = 2E \tag{1.17}$$

1.3.1 Cross Section

A measure for the probability for a certain process to take place in a collision of two particle beams is the cross section which connects the reaction rate per target particle W with the incoming flux ϕ by

$$\sigma = \frac{W}{\phi} \tag{1.18}$$

The unit of the cross section is the barn [b]³. According to this equation, σ can be determined experimentally by measuring the reaction rate. From a theory point of view, this rate depends on the Hamiltonian of the interaction H_{int} and can be derived from quantum mechanics. According to Fermi's Second Golden Rule, the reaction rate

³The unit of barn is defined by $1\text{b} = 10^{-28}\text{m}^2$

W reads as

$$W = \frac{2\pi}{\hbar} |M_{if}|^2 \rho_f \quad (1.19)$$

Here, ρ_f denotes the phase space which is available for the final states and M_{if} is the matrix element between the initial and final-state wave function which reads as

$$M_{if} = \langle \psi_f | H_{int} | \psi_i \rangle \quad (1.20)$$

1.3.2 Elastic Electron-Proton Scattering

To investigate the substructure of the proton, electrons are an ideal candidate for scattering experiments as they are to the current standard of knowledge point-like particles, which means that no substructure has to be taken into account. To resolve the substructure of the proton with an approximate diameter of about 1 fm, the de Broglie wavelength of the accelerated electrons must be at least in the same order of magnitude, which corresponds to an energy of 200MeV. Increasing this energy leads to the emerging of finer substructures. In the following, the basics of elastic scattering are briefly discussed.

For the description of an elastic scattering, the transferred four-momentum is one of the key variables and can be expressed as

$$Q^2 = -q^2 = -(k - k')^2 \sim 4EE' \sin^2\left(\frac{\theta}{2}\right) \quad (1.21)$$

In this equation, k and k' denote the four-vectors of the electron respectively before and after the interaction. As both, the electron and the proton are charged spin-1/2 particles, the interaction of the charge of the electron with the spin of the proton has to be considered as well as the interaction of both spins. The latter is already included in the Mott cross section. The final differential cross section for elastic electron-proton scattering is described by the Rosenbluth formula

$$\frac{d\sigma}{d\Omega} = \left(\frac{d\sigma}{d\Omega}\right)_{Mott} \cdot \frac{E'}{E} \left[\frac{G_E^2(Q^2) + \tau G_M^2(Q^2)}{1 + \tau} + 2\tau G_M^2(Q^2) \tan^2 \frac{\Theta}{2} \right] \quad (1.22)$$

This formula takes the finite size of the proton into account by introducing two form factors which depend on the transferred four-momentum. The electric form factor $G_E^2(Q^2)$ is the Fourier transformation of the charge distribution inside the proton whereas the magnetic form factor $G_M^2(Q^2)$ represents the distribution of the magnetic moment of the proton. The abbreviation τ is defined as

$$\tau = \frac{Q^2}{4M_P^2} \quad (1.23)$$

and M_P denotes the mass of the proton.

1.3.3 Deep-inelastic Scattering and PDFs

A further increase of the energy of the electron leads to inelastic scattering which can be observed for electron-proton collisions with a centre-of-mass energy larger than 5 GeV. In such interactions, the proton can be excited, which has to be taken into account for the energy conservation when deriving a formula for the differential cross section.

The invariant mass W of the excited proton state after the interaction is calculated from the four vector of the exchanged photon q and proton P before the interaction according to

$$W^2 = P'^2 = (P + q)^2 = M^2 + 2Pq + q^2 = M^2 + 2M\nu - Q^2 \quad (1.24)$$

with ν defined as

$$\nu = \frac{Pq}{M} \quad (1.25)$$

In the case of a fixed target experiment, the protons are at rest in the laboratory frame and the last equation simplifies to $\nu = E - E'$. As a result of the excitation of the proton, which implies that $W > M$, the following constraint can be deduced from Equation 1.24 for inelastic processes:

$$2M\nu - Q^2 > 0 \quad (1.26)$$

For elastic processes, $M = W$ and the last expression reads as $2M\nu - Q^2 = 0$. With the new constraint for the inelastic scattering, the cross section can be expressed to be

$$\frac{d^2\sigma}{d\Omega dE'} = \left(\frac{d\sigma}{d\Omega}\right)_{Mott} \cdot [W_2(Q^2, \nu) + 2W_1(Q^2, \nu) \tan^2 \frac{\Theta}{2}] \quad (1.27)$$

As a result of the additional degree of freedom due to the inelasticity of the process, the cross section is presented in double differential form. Again, the two functions $W_{1,2}(Q^2, \nu)$ describe the distribution of magnetic momentum and electric charge of the proton. In this context, a new variable is introduced, the **Bjorken- x** which is defined as

$$x = \frac{Q^2}{2M\nu} \quad (1.28)$$

and corresponds to the fraction of the proton momentum carried by the scattered parton in the infinite momentum frame in which the proton is regarded as a collinear stream of fast moving partons and masses are negligible. Instead of the form factors $W_{1,2}(Q^2, \nu)$,

the dimensionless form factors $F_{1,2}$ are commonly used which depend on the Bjorken- x and can be expressed as follows:

$$F_1(x, Q^2) = Mc^2 W_1(Q^2, \nu) \quad (1.29)$$

$$F_2(x, Q^2) = \nu W_2(Q^2, \nu) \quad (1.30)$$

Measurements of the electric form factor F_2 of the proton have shown that it does not depend on Q^2 which suggest scattering at a point-like charge. This was a strong hint for the proton and the neutron being composite of point-like objects. These constituents have been identified with the predicted quarks.

The Bjorken limit is defined as $Q^2, \nu \rightarrow \infty$ with x fixed. In this limit, the structure functions are observed to obey an *approximate scaling* law, i.e. they depend on the dimensionless variable x :

$$F_i(x, Q^2) \rightarrow F_i(x). \quad (1.31)$$

Bjorken scaling implies that the virtual photon scatters off pointlike constituents.

In addition, the Callan-Gross-Relation which connects the electric and magnetic form factor for spin-half particles to

$$2xF_1(x) = F_2(x) \quad (1.32)$$

has been proven experimentally. The combination of the results implies that quarks are charged, point-like particles with spin 1/2.

Parton Distribution Function

The QCD parton model and the structure functions $F_{1,2}$ can be expressed in terms of the Parton Distribution Functions (PDFs). The Parton Distribution Function $f_i(x)$ can be defined as the probability, $f_i(x)dx$, of finding a parton of type f (a quark/anti-quark flavour or a gluon) in the hadron that carries a fraction within $[x, x+dx]$ of the hadron momentum. All the constituent partons together have to carry the total hadron momentum, i.e.

$$\sum_i \int_0^1 x f_i(x) dx = 1 \quad (1.33)$$

Other constraints are put on the PDFs by the quantum number of the hadrons. For example, in the case of protons the total expected number of up-quarks (down-quarks) is

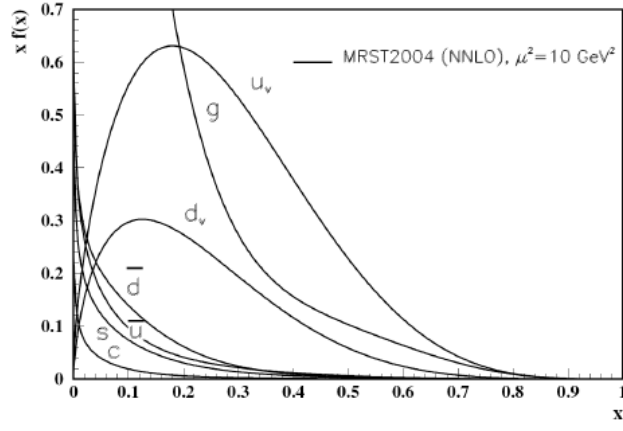


Figure 1.3: Distribution of $xf(x)$ (where $f(x)$ is the parton distribution function) as a function of the momentum fraction x at $\mu^2 = 10 \text{ GeV}^2$ for different partons.

two (one), i.e.

$$\int_0^1 dx (f_u(x) - f_{\bar{u}}(x)) = 2 \quad (1.34)$$

and

$$\int_0^1 dx (f_d(x) - f_{\bar{d}}(x)) = 1 \quad (1.35)$$

More so called sum rules exist for the electrical charge of the hadron and other observables. These rules can be used to constrain the distribution using the experimental deep inelastic scattering data.

The PDFs for quarks and gluons at a scale $\mu^2 = 10 \text{ GeV}^2$ scale as calculated by the MRST collaboration in 2004 are shown in Fig. 1.3. Closer examination of Fig. 1.3 shows that the structure function decreases with increasing Q^2 at large x and has the opposite behaviour at small x .

1.3.4 Hadroproduction

The application of the parton model to processes involving two hadrons in the initial state is discussed in this section. Parton distribution functions measured in the lepton-hadron scattering can be adapted in hadron-hadron scattering. The scattering process for QCD, eg. $q\bar{q} \rightarrow q\bar{q}$, $q\bar{q} \rightarrow gg$ etc can be studied in the production of large transverse momentum jets (described later) in hadron-hadron collisions. The high-energy interactions of hadrons are described by the QCD inspired parton model. In this model a hard scattering process between two hadrons is the result of an interaction between the quarks and gluons which are the constituents of the incoming hadrons. The incoming hadrons provide beams of partons which possess varying fractions of the momenta of their parent hadrons, as

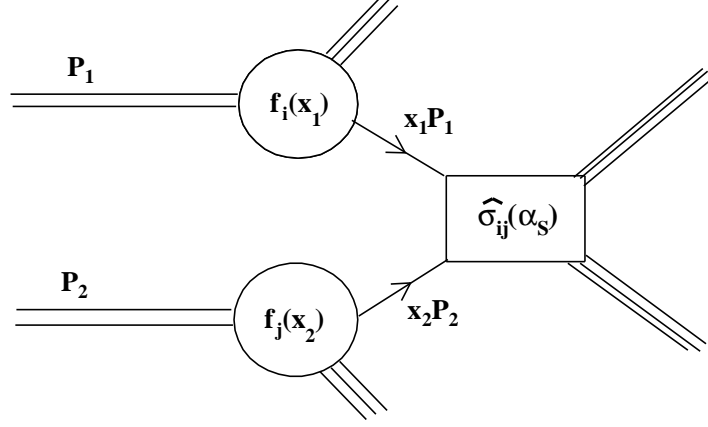


Figure 1.4: The parton model description of a hard scattering process in a hadron-hadron collision.

described in section 1.3.3.

The cross section for a hard scattering process initiated by two hadrons with four-momenta P_1 and P_2 can be written as

$$\sigma(P_1, P_2) = \sum_{i,j} \int dx_1 dx_2 f_i(x_1, \mu^2) f_j(x_2, \mu^2) \hat{\sigma}_{ij}(p_1, p_2, \alpha_S(\mu^2), Q^2/\mu^2) \quad (1.36)$$

corresponding to the structure illustrated in Fig.1.4. The momenta of the partons which participate in the hard interaction are $p_1 = x_1 P_1$ and $p_2 = x_2 P_2$. The characteristic scale of the hard scattering is denoted by Q . This could be, eg., transverse momentum of a jet. The functions $f_i(x, \mu^2)$ are the usual QCD quark or gluon distributions, defined at a factorisation scale μ . The short distance cross-section for the scattering of partons of types i and j is denoted by $\hat{\sigma}_{ij}$. Since the coupling is small at high energy, the short-distance cross section can be calculated as a perturbation series in the running coupling α_S .

The factorisation scale μ in Eq. 1.36 is an arbitrary parameter. It can be thought of as the scale which separates the long and short distance physics. Thus a parton emitted with a small transverse momentum, less than the scale μ , is considered part of the hadron structure and is absorbed into the parton distribution. A parton emitted at large transverse momentum is part of the short distance cross-section. The scale μ should be chosen to be of the order of the hard scattering scale Q which characterises the parton-parton interaction.

Luminosities

At a particle collider the rate N at which events of a given type occur is determined by the luminosity of the machine L , multiplied by the cross section for the relevant scattering process, σ :

$$N = L\sigma \quad (1.37)$$

The machine luminosity L is controlled by the parameters of the collider described in detail in chapter 2. The process cross section σ is, of course, independent of the machine parameters. Nevertheless, for hard scattering process at a hadron collider it is helpful to consider it as a product of the parton luminosity factor, for the relevant partons i and j inside the colliding hadrons, and a sub-process cross section $\hat{\sigma}_{ij}$ for the parton-parton collision. From Eq. 1.36 the parton luminosity is determined by the parton distribution functions, $f_i(x_1, \mu^2)$ and $f_j(x_2, \mu^2)$. Since the partons only carry a fraction of their parent hadron's momentum, the available center-of-mass energy-squared of the parton-parton collision, \hat{s} , is less than the overall hadron-hadron collision energy, s , by a factor of $x_1 x_2 \equiv \tau$. The cross section can be written as:

$$\sigma(s) = \sum_{ij} \int_{\tau_0}^1 \frac{d\tau}{\tau} \left[\frac{1}{s} \frac{dL_{ij}}{d\tau} \right] [\hat{s} \hat{\sigma}_{ij}] \quad (1.38)$$

where the sum runs over all relevant pairs of partons $\{ij\}$. The minimum centre of mass energy-squared at which the hard subprocess can occur, denoted by $\tau_0 s$, provides a lower cut-off on the x -range of the participating partons. The first object in square brackets in Eq. 1.38 has the dimensions of a cross section. The second object in square brackets is dimensionless and is approximately determined by couplings. Hence knowing the luminosities cross sections can be estimated.

Kinematic variables related to hadron collisions

The scattering of two hadrons provides two broadband beams of incoming partons. These incoming beams have a spectrum of longitudinal momenta determined by the parton distribution functions. The centre of mass of the parton-parton scattering is normally boosted with respect to that of the two incoming hadrons. It is therefore useful to classify the final state in terms of variables which transform simply under longitudinal boosts. For this purpose, the rapidity y , the transverse momentum p_T and the azimuthal angle ϕ are introduced. In terms of these variables, the four momentum of a particle of mass m

may be written as

$$\begin{aligned} p^\mu &= (E, p_x, p_y, p_z) \\ &= (m_T \cosh y, p_T \sin \phi, p_T \cos \phi, m_T \sinh y) \end{aligned} \quad (1.39)$$

where the transverse mass is defined as $m_T = \sqrt{p_T^2 + m^2}$. The rapidity y is defined by

$$y = \frac{1}{2} \ln \frac{E + p_z}{E - p_z} \quad (1.40)$$

and is additive under the restricted class of Lorentz transformations corresponding to a boost along the z direction. Rapidity differences are boost invariant.

In practice the rapidity is often replaced by the pseudorapidity variable η ,

$$\eta = -\ln \tan(\theta/2) \quad (1.41)$$

which coincides with the rapidity in the limit $m \rightarrow 0$. It is a more convenient variable experimentally, since the angle θ from the beam direction is measured directly in the detector. It is also standard to use the transverse energy

$$E_T = E \sin \theta \quad (1.42)$$

rather than the transverse momentum p_T , because it is the former quantity which is measured in a hadron calorimeter.

In a hard scattering process, the coloured partons form a spray of roughly collinear colourless hadrons which is called jets. A jet is defined as a concentration of transverse energy E_T in a cone of radius R , where

$$R = \sqrt{(\Delta\eta)^2 + (\Delta\phi)^2}. \quad (1.43)$$

By defining R in terms of $\Delta\eta$ (rather than $\Delta\theta$) we obtain a jet measure invariant under longitudinal boosts. In two dimensional η, ϕ plane, curves of constant R are circles around the axis of the jet. Details of jet algorithms are described in Chapter 4.

1.4 Outline of the Thesis

The thesis addresses QCD studies with high p_T jets. Tools have been developed to study of the multi-jet topologies and global event shape variables in hadronic events which test the validity of the perturbative QCD at the energies that will be probed by LHC pp collisions and allow for measurement of the strong coupling constant, α_s . The thesis also addresses the analysis of test beam data to have a thorough understanding of CMS

calorimeter system.

The thesis is organized as follows:

Chapter 2 gives a description of the LHC and the various components of the CMS detector in details. Special emphasis is given to the description of CMS calorimeter.

Chapter 3 describes the methods of Monte Carlo event generation and reconstruction. Special emphasis given on track and calorimeter Jet reconstruction.

Chapter 4 gives an overview of various jet algorithms used in CMS and also about the jet energy scale corrections which are applied to calorimetric jets to get back to the particle level jets. It also talks about the event selection which is used for the QCD multi-jet analysis as well as event shape.

Chapter 5 describes the experimental set-up used in the test beam experiments. An overview of beam line elements is given in this chapter. This chapter also includes a detailed description of the methods of particle identification.

The detailed analysis performed with the test beam data is described in chapter 6. This chapter includes comparison between energy response and resolution in the barrel and endcap of the calorimeter with single pion data.

Chapter 7 elaborates the studies with multi-jet topological variables. Contributions of detector effects and various systematic uncertainties are talked about. Comparisons are made among the expected distributions and different event generator models.

Global event shape variables are discussed in chapter 8.

Chapter 9 summarizes the findings from these analysis.

Chapter 2

LHC Machine and CMS Experiment

2.1 LHC Machine

The Large Hadron Collider (LHC) [17] will be operational by 2009-10 and it will push the energy frontier as well as the luminosity frontier to a totally new regime. The LHC will investigate processes with really tiny cross sections, down to the femtobarn. The main reason that drove the choice of a hadron collider was the need to build a machine capable of probing physics at the TeV scale. The LHC is housed in the same tunnel at CERN as the large electron-positron collider, LEP. Protons being much heavier than electrons will have lot less energy loss due to synchrotron radiation and can be accelerated to much higher energies within the same tunnel. Thus the maximum centre of mass energy is limited only by the maximum bending field attainable at this stage. Hadron colliders provide a complex environment compared to an electron-positron collider through the production of many associated low energy particles. But they provide access to a wider energy spectrum, which can be explored simultaneously.

A schematic description of the LHC accelerator complex and its services is shown in Figure 2.1. The LHC will have two counter circulating proton beams, accelerated to 7 TeV in a 27 km ring, resulting in a total centre of mass energy of 14 TeV. The two beams will collide in four interaction points and four experiments are built around these interaction points. Two general purpose experiments, ATLAS and CMS, will do general Standard Model measurements and will seek new physics; one experiment, LHCb, is dedicated to B meson physics and it will carry out precise measurements of CP violation; one experiment, ALICE, will investigate heavy ion physics (lead ions will be accelerated in a later phase of LHC operation). The LHC can be regarded as a discovery machine with an extremely wide energy range, being able to investigate mass scales from order of few GeV, as in the case of B-meson physics, up to a few TeV, for the discovery of new vector bosons or quark compositeness. In order to extend the LHC capability to explore new physics rare processes, an enormous effort has been made to raise the proton momentum as much as

CERN Accelerator Complex

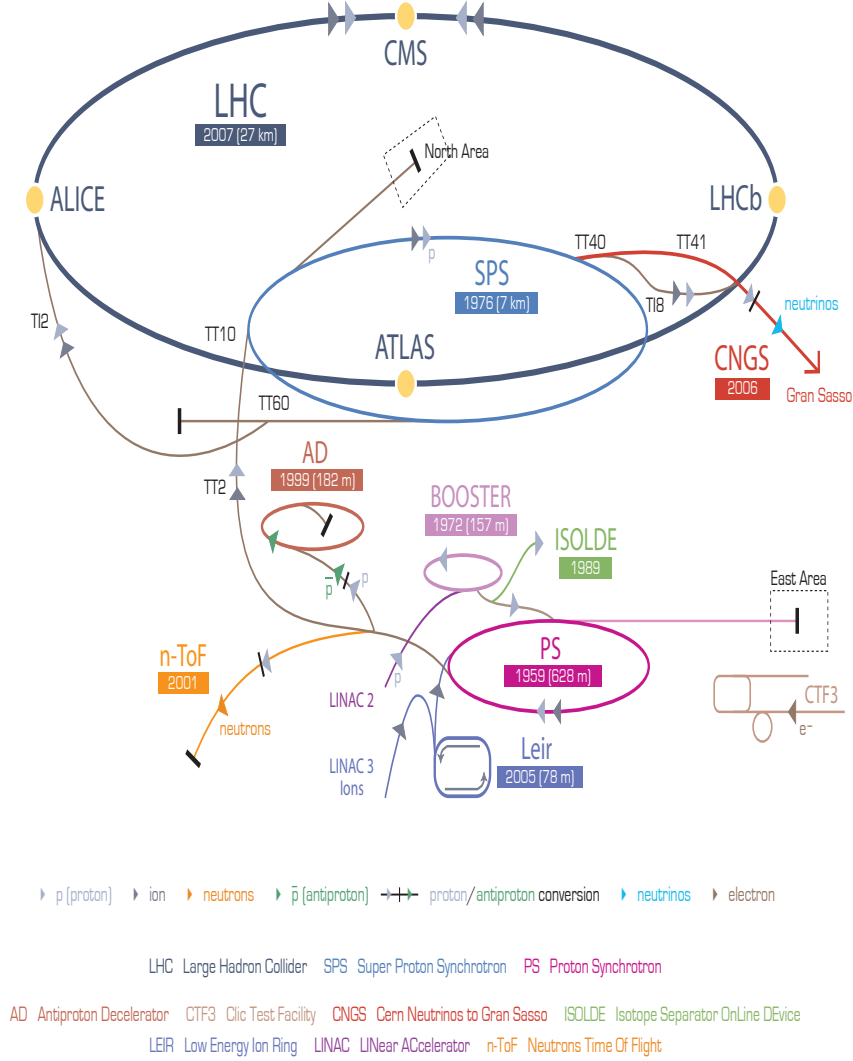


Figure 2.1: Overview of the CERN Accelerator Complex. The hadron beams are accelerated by several successive facilities to the LHC injection energy of 450 GeV before being accelerated in the LHC to higher energies.

possible. In particular, a very sophisticated magnet system is needed to keep such high momentum protons in the machine orbit. The formula that connects the bending radius with the particle's momentum and the magnetic field is:

$$B[T] = \frac{p[GeV/c]}{0.3\rho[m]} \quad (2.1)$$

where B is the magnetic field in Tesla, p the momentum in GeV/c, ρ the orbit radius in metres. For a circumference of about 27 km, the magnetic field needed for 7 TeV/c

protons is about 5.4 T. Actually, since the LHC is made of curved and rectilinear sections, the superconductor dipoles are required to produce an 8.3 T magnetic field. This value is close to the technological edge for superconducting magnets nowadays.

Since the beam energy is limited by the bending power of the magnetic system and by the circumference of the machine, another handle to raise the rate of interesting and rare events is the luminosity L . The event rate n for a process with cross section σ is

$$N = L\sigma \quad (2.2)$$

The luminosity is connected to the beam properties with the following relation:

$$L = f \frac{n_1 n_2}{4\pi\sigma_x\sigma_y} \quad (2.3)$$

where n_1 and n_2 are the number of particles in beam 1 and 2 respectively, f is the collision frequency, σ_x and σ_y are transverse dimensions of the beams. The proton bunches at LHC will collide at a frequency of about 40 MHz, corresponding to a spatial separation between bunches of about 7.5 m. The frequency cannot be raised further, because of the limiting requirement of avoiding further collisions on the side of each interaction region. The transverse dimensions of the beam can be squeezed down to 15 μm .

During the start up period (the first six months of operation approximately) the luminosity will be $2 \times 10^{32} \text{ cm}^{-2} \text{ s}^{-1}$. The luminosity will then be raised gradually to $1 \times 10^{34} \text{ cm}^{-2} \text{ s}^{-1}$.

The need for such a high luminosity has driven the choice to a proton-proton collider, instead of a proton-antiproton machine. Although a proton-antiproton machine has the advantage that both beams can be kept in the same beam pipe and in orbit by the same bending magnets, production of intense beams of antiprotons needed to reach the desired luminosity is an unfeasible task. Table 2.1 describes the main design characteristics of the LHC.

In hard proton proton collisions, the centre of mass energy $\sqrt{\hat{s}}$ is related to the total centre of mass energy \sqrt{s} as:

$$\sqrt{\hat{s}} = \sqrt{x_1 x_2 s} \quad (2.4)$$

where x_1 and x_2 are the energy fractions of the two partons participating in the hard scattering process. The centre of mass system of the two interacting partons is not motionless in the laboratory frame, but rather it is on average boosted along the direction defined by the colliding beams. For this reason Lorentz invariant observables are very important to characterize the event. One such observable is the transverse momentum p_T , defined as the projection of the momentum vector on a plane perpendicular to the

Data	pp collision
Proton energy (at collision)	7 TeV
Relativistic gamma	7461
Number of bunches	2808
Bunch spacing	25 ns
Number of particles per bunch	1.15×10^{11}
Longitudinal emittance (4σ)	2.5 eVs
Number of collisions/crossing	~ 20
Transverse normalized emittance	$3.75 \mu\text{m rad}$
Circulating beam current	0.582 A
Stored energy per beam	362 MJ
RMS bunch length (collision)	7.55 cm
Half crossing angle	$142.5 \mu\text{rad}$
Geometric luminosity reduction factor	0.836
Energy loss/turn	$\sim 7 \text{ keV}$

Table 2.1: Parameters for the Large Hadron Collider relevant for the peak luminosity operation.

beam axis.

At designed luminosity, there will be 2808 bunches in the LHC ring, each one being a ns long and separated by 25 ns and each having 1.15×10^{11} protons. At the time of nominal operation, the transverse emittance of the beam will be $3 \mu\text{m}$. The size of the beam will be ~ 16 microns in transverse direction at the collision point. The nominal bunch length will be 11.24 cm and it will be 7.5 cm at the collision point.

To obtain the design luminosity of the beam, the protons are made to travel through a sequence of accelerating and focusing setups. A schematic of CERN accelerator complex is shown in Figure 2.1. The protons are obtained from a duoplasmatron source and are delivered to Radio Frequency Quadrapole (RFQ) which accelerates them to 750 keV followed by a linear accelerator (Linac2) which accelerates protons to 50 MeV. The first circular machine is Proton Synchrotron Booster (PSB) which accelerates these protons to 1.4 GeV. The injection of bunches to PSB determines the transverse size of proton bunches. The next accelerator, CERN Proton Synchrotron (PS), prepares the bunches with a spacing of 25 ns and delivers the beam at 25 GeV followed by the Super Proton Synchrotron (SPS) which accelerates the protons to 450 GeV. The protons extracted from the SPS are accelerated to 7 TeV by the LHC.

2.2 CMS Detector

The Compact Muon Solenoid (CMS) [18] is one of the two general purpose detectors to be used at the LHC. The main physics goal of the CMS is to look for the Higgs boson

which is presumed to be responsible for Electroweak symmetry breaking and/or to look for the signatures of any new physics which may be unraveled at TeV energy scale. The design of the CMS is optimized to look for these signatures over a wide range of energy. The Higgs and new physics can manifest themselves as a variety of final state topologies of e^\pm , γ , μ^\pm , jets and the particles which do not leave any signature in detector and their presence is recorded as an imbalance in the measured transverse energy.

At the design luminosity of LHC, 20 inelastic collisions are expected on an average for every bunch crossing and there would be a bunch crossing every 25 ns. This implies 1000 charged tracks emerging from the interaction point every 25 ns. To be compatible with the LHC bunch crossing timing, the response time of the detector components and electronics should be less than 25 ns. The effects of pile up can be reduced by fine transverse granularity of the detector. The detector components and the on-detector electronics have to be radiation hard to withstand the high radiation environments of the LHC for a decade of operation. The physics program of the LHC requires the CMS to

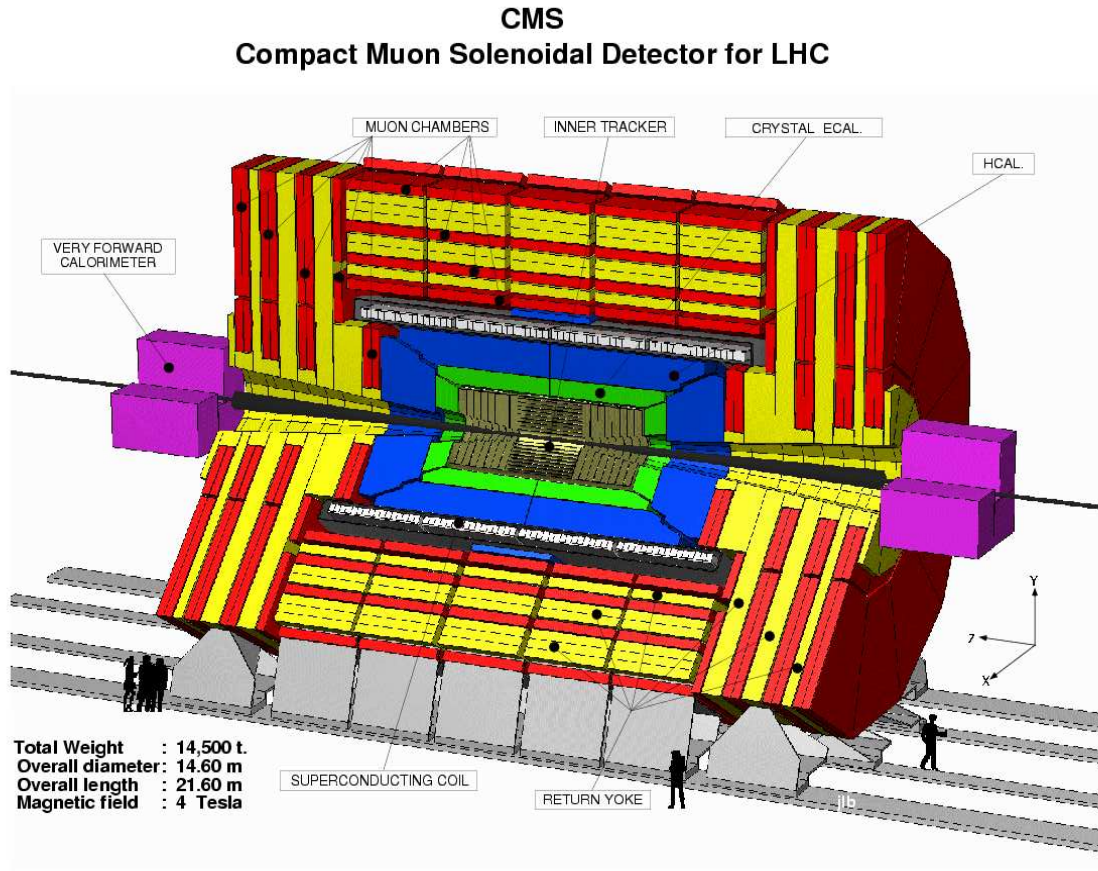


Figure 2.2: An overview of the CMS detector. Main detector components such as tracker, calorimeter, superconducting coil which produces the magnetic field and the muon chambers are illustrated.

provide:

- good momentum resolution for muons over a wide range of transverse momenta and angle and good di-muon mass resolution and unambiguous charge determination up to a momentum of 1 TeV/c;
- a robust tracker to measure the momentum of charged particle, to determine the primary interaction vertices accurately and to tag b-jets and τ -decays efficiently;
- the best possible electromagnetic calorimeter which provides a good di-photon mass resolution, efficient π^0 rejection, good isolation of leptons and photons at high luminosities and a good geometrical coverage;
- good di-jet mass resolution and missing transverse energy resolution which require a highly hermetic hadron calorimeter with a fine lateral segmentation.

As the name suggests, the design concept of the CMS is governed by the choice of configuration of the magnetic field which is needed to bend the muons to measure their momenta using muon detectors. The requirement of good momentum resolution over a wide range of muon transverse momentum leads to the choice of a high magnetic field. CMS has chosen a 4 Tesla solenoidal magnetic field enabling a compact design of the detector. The overall dimensions of the CMS detector are 21.6 m long, 14.6 m in diameter and a total weight of 12 500 tons.

The coordinate system adopted by the CMS has the origin centred at the nominal collision point inside the experiment. As shown in the Figure 2.2 the z -axis points along the beam direction from the Point 5 to the Point 4 and the x -axis pointing radially inward towards the centre of the LHC. The transverse direction is usually presented in terms of the azimuthal angle ϕ and pseudo-rapidity η which is defined as $-\ln \tan(\theta/2)$ where θ is the polar angle. Transverse missing energy is measured as the imbalance of energy measured in the transverse plane.

2.2.1 Tracker

The CMS tracker [19] is designed to measure the charged particles emerging from proton-proton interactions and to efficiently reconstruct the secondary vertices due to decays of long-lived particles like B meson. A high granularity and very fast detector is required which can also withstand the intense radiation environments of the LHC.

The CMS tracking system covers the pseudo-rapidity region up to $|\eta| < 2.5$. An overview of the tracker is given in Figure 2.3. In view of having maximum granularity with minimum material budget, the innermost compartment of the tracker is chosen to be a silicon pixel detector. The pixel detector consists of three 57 cm long concentric

layers at a radii of 4.4, 7.3 and 10.2 cm and two disks of pixel on each side of barrel at $z = \pm 34.5$ cm and $z = \pm 46.5$ cm. The pixel cell size is chosen to be $150 \times 100 \mu\text{m}^2$ and a spacial resolution of $10 \mu\text{m}$ is achieved in both the r - ϕ and z -directions. The pixel detector delivers two to three high precision space points on each charged particle trajectory.

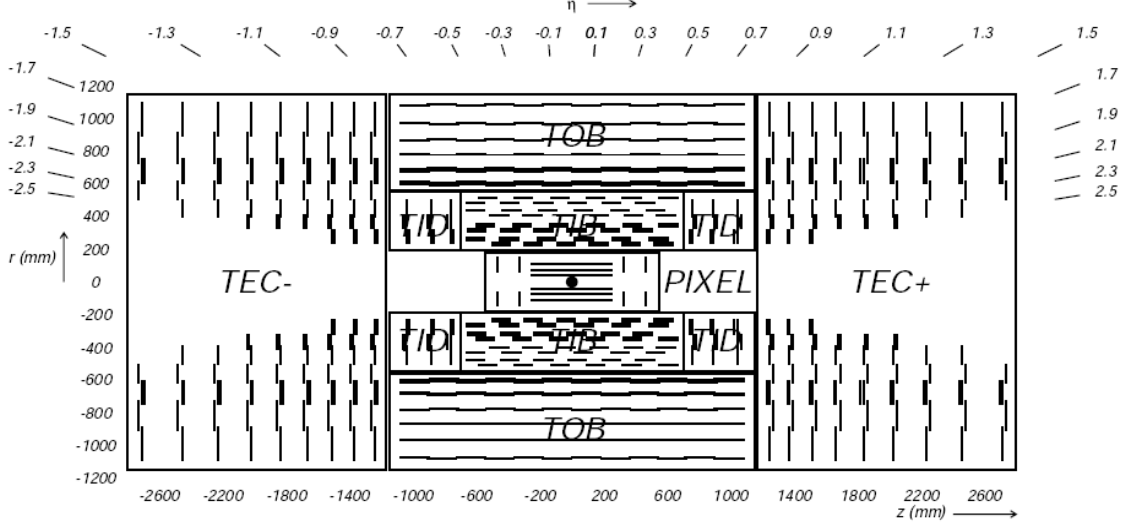


Figure 2.3: Layout of the CMS Tracker showing various components of the detector.

Silicon strip technology is used for $r > 10$ cm, as the track density in space reduces as $1/r^2$. The Tracker Inner Barrel (TIB) consists of four layers of silicon strip modules spanning 140 cm along the beam axis at radii of 25.5, 33.9, 41.9 and 49.8 cm. The Tracker Inner Disks (TID) are an assembly of three disks placed between $z = \pm 80$ cm and $z = \pm 90$ cm. Each disk consists of three rings in the radius from 20 cm and 50 cm. The strips are parallel to the beam axis in the barrel and radial on the disks. The strip pitch is 80 microns for inner two layers and 120 microns for the outer two layers of TIB and it varies between 100 microns and 141 microns for the silicon sensors of inner disks.

The Tracker Outer Barrel is an assembly of 6 concentric cylinders in radii between 55.5 cm and 116 cm and the cylinders are 2.18 m long. The micro-strip sensors are 500 microns thick and the pitch is 183 microns on the layers 1-4 and 122 microns on the layers 5-6. It provides 6 $r\phi$ measurements with a single point resolution of 53 microns and 35 microns respectively. The TOB is complemented with Tracker End Caps (TEC) at both the ends. The TEC consists of 9 disks placed in the region from $z = \pm 124$ cm to $z = \pm 282$ cm and it spans $22.5 \text{ cm} < |r| < 113.5 \text{ cm}$ in radial direction. TEC provides up to 9 ϕ measurements per trajectory.

The modules in the first two layers of TIB, the first two rings of TID, the two innermost layers of TOB and rings 1, 2, 5 of TEC carry a second layer of micro-strip detectors mounted back-to-back but making an stereo angle of 100 mrad and providing a measurement of z -coordinate in the barrel and r -coordinate on the disks. With this tracker layout,

a minimum of nine hits are ensured in the strip detectors up to $|\eta| < 2.5$ and at least four of these hits are two-dimensional measurements.

The position and the orientation of the tracker modules can deviate from their nominal values due to the deformation arising from tracker cooling, stress from access and magnetic field, out-gassing of components in dry nitrogen etc. This leads to the degradation of the resolution of the track parameters. A dedicated laser alignment system has been employed to monitor the position and orientation of selected tracker modules which is aimed to generate alignment information on a continuous basis. The vertex constraints from $Z \rightarrow \mu^+ \mu^-$, mass constraints etc. are used to obtain a unique alignment parameter set.

2.2.2 Calorimeter

The CMS calorimeter comprises two major components, an Electromagnetic Calorimeter (ECAL) [20] and a Hadron Calorimeter (HCAL) [21]. The design of ECAL is optimized to measure the di-photon mass peak of Higgs in intermediate mass range in the channel $H \rightarrow \gamma\gamma$. It is aimed to provide an excellent identification of electrons and photons and a good rejection of background to hadrons and jets. The HCAL is optimized to measure the energy of hadrons and jets. It is designed to provide a good hermetic coverage up to $|\eta|=5$ to reduce uncertainties in the measurement of the missing transverse energy (E_T). The missing E_T indicates the presence of weakly interacting particles in the final state which escape the detector and is a crucial quantity to look for new physics beyond the Standard Model. A large part of the CMS calorimeter is placed inside the 4 Tesla magnetic field. The physical locations of the various components of ECAL and HCAL are shown in the Figure 2.4.

2.2.2.1 Electromagnetic Calorimeter

The Electromagnetic Calorimeter of the CMS is a homogeneous calorimeter made of Lead Tungstate (PbWO_4) crystals and it covers up to $|\eta| < 3.0$ in pseudo-rapidity. Lead tungstate is a high density material (8.28 gm/cm^3) with radiation length (X_0) of 0.89 cm and Moliere radius of 2.2 cm. These properties of (PbWO_4) makes it possible to achieve a fine granularity to measure narrow showers with an excellent position resolution. It offers a fast timing response such that 80% of the signal is collected in 25 ns.

The central part of ECAL (ECAL Barrel or EB) is made of 23 cm ($25.8 X_0$) long PbWO_4 pyramidal crystals. It covers up to $|\eta| < 1.479$ and extends from a distance of 1.29 m from the beam axis. The transverse dimensions of the crystal are $22 \times 22 \text{ mm}^2$ at the front face and it corresponds to $\Delta\eta \times \Delta\phi = 0.0175 \times 0.0175$. The crystals are $26 \times 26 \text{ mm}^2$ at the rear surface. The EB is divided into two halves along z, each composed of 18

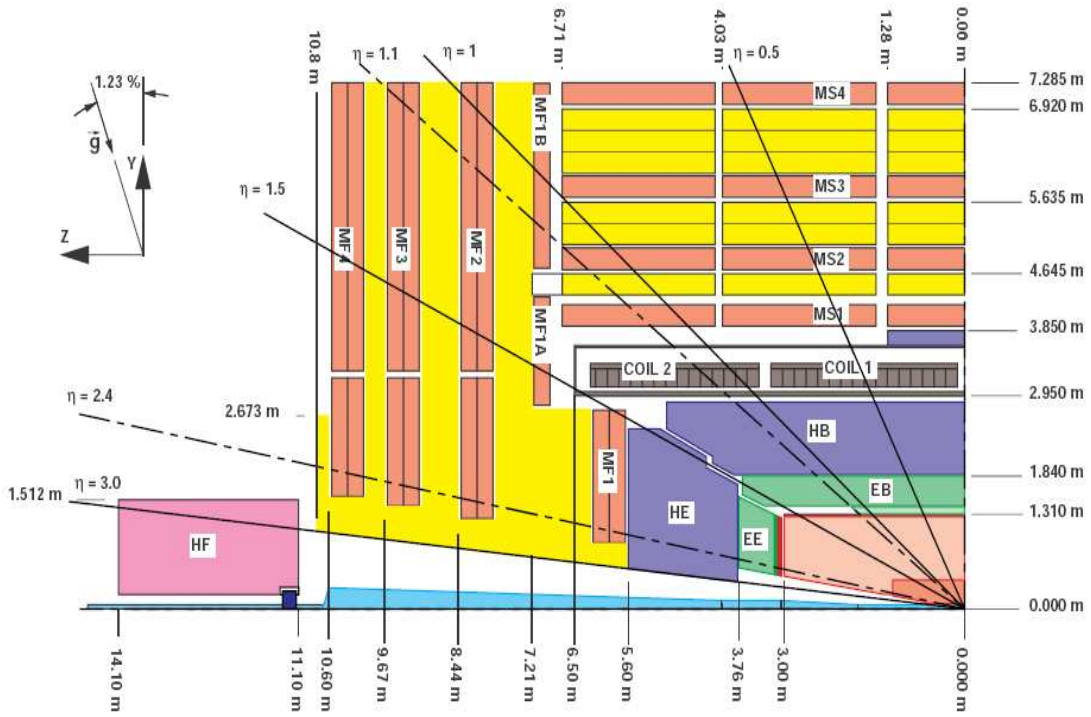


Figure 2.4: Cross sectional view of the CMS detector with approximate dimensions and positions.

identical super-modules covering 20° in ϕ . There are 360 crystals in ϕ and 85 crystals in η in each half-barrel. The crystals are contained in a thin-walled aluminium casing called a submodule. The submodules are arranged into modules of different types containing 20 crystals in ϕ and 20 or 25 crystals in η . Each such submodule has crystals which are left and right reflections of a single shape. In total, there are 17 different shapes for the crystals. Four modules make one super-module having 1700 crystals.

The crystals are mounted in a quasi-projective geometry tilted by an angle of 3° with the direction of a vector originating from nominal interaction vertex both in η and ϕ . This tilt is introduced to avoid cracks aligned with particle trajectories. The light produced by the passage of a particle is totally internally reflected in the crystal and is read by the photo-detectors located at the rear face. Every crystal is polished after machining to maximize the total internal reflection.

Every crystal of EB is read with two Avalanche Photodiodes (APDs) mounted at the rear face and each has a sensitive area of $5 \times 5 \text{ mm}^2$. The APDs are chosen for their fast timing response (rise time $< 2 \text{ ns}$), radiation hardness and insensitivity to the presence of a magnetic field of 4 Tesla. The APDs are operated at a gain of 50 which is achieved by applying a voltage in the range 340-430 volts.

The Endcap of ECAL or EE covers the pseudo-rapidity range of $1.479 < |\eta| < 3.0$. The longitudinal distance between the interaction vertex and the endcap envelope is 3.144 m. The EE is made of 220 mm long crystals ($24.7 X_0$) with rear face of $30 \times 30 \text{ mm}^2$ and

front face of $28.62 \times 28.62 \text{ mm}^2$. The crystals are grouped into mechanical units called super-crystals comprising 5×5 crystals. Mechanically each endcap is divided into two halves or ‘Dees’. The crystals are mounted in a uniform x - y grid. The exposure to the high radiation environment will cause the formation of the colour centres which will result in a wavelength dependent attenuation of scintillation light.

The EE crystals are read out using Vacuum Photo-Triodes (VPTs). A VPT is a single dynode photomultiplier. The anode is made of a very fine copper mesh ($10 \mu\text{m}$ pitch) and the cathode is made of bi-alkali material with a quantum efficiency of 22% at 430 nm. The mean gain of a VPT used for CMS EE crystals is 10.2 in the absence of any magnetic field and degrades by a maximum of 10% in a magnetic field of 4 T. The variation of response depends on the alignment of the VPT axis with the direction of the magnetic field in a very modest manner. The VPTs used for EE is 25 mm in diameter and has an active area of approximately 280 mm^2 . One VPT is glued to the back of every EE crystal.

The amount of scintillation light produced in the crystal depends upon the temperature of the crystal. The gain of the EB photo-detector is also sensitive to the variation in temperature. The overall response of the the crystal-APD system to electrons is observed to be varying as $-3.8\% \text{ C}^{-1}$ in test beam experiments. Therefore it is mandatory to maintain the temperature of the crystals at a constant temperature of $18^\circ \pm 0.05^\circ \text{ C}$ to achieve the nominal energy resolution. One APD capsule in every 10 EB crystals and one VPT capsule in every 25 EE crystals is equipped with a temperature sensor to monitor the crystal temperature. Cold water running through the thermal screen located in the from of every module and pipes embedded in aluminium grid is used to stabilize the temperature of the ECAL system.

Electronics and Data Acquisition

The analog signals obtained from the APDs and VPTs are preamplified and shaped and amplified by three amplifiers with nominal gains of 1, 6 and 12. The complete system is integrated on a chip called Multi Gain Pre-Amplifier (called MGPA). The three analog outputs of MGPA are digitized in parallel by a multichannel 40 MHz, 12-bit ADC. The 12-bit highest non-saturated signal along with the two bits coding the ADC number are sent to the pipeline. The energy is summed up in strips of five crystals along ϕ and data from five such strips are sent to the Trigger Concentrator Card (TCC). TCC generates the trigger primitives which is a sum of transverse energy in 5×5 crystals of a tower and a ‘fine-grain’ electromagnetic bit to identify electromagnetic shower candidates on the basis of lateral shower profile and send them to L1 calorimeter trigger processor. On receiving L1 acceptance, the corresponding data, ten samples per channel with 40 MHz frequency, are transmitted in $\sim 7.5 \mu\text{s}$ to the Data Concentrator Card (DCC) where data suppression is done according to some pre-defined algorithms. After checking the data integrity and

updating the error flags in the event header, the DCC event is sent to the central CMS Data Acquisition (DAQ) system.

ECAL Calibration

The calibration of ECAL includes the determination of absolute energy scale and the channel-to-channel relative calibration (inter-calibration of channels). The main source of channel-to-channel variation is the variation in the scintillation light yield of crystals which has an RMS of 7% within the crystals of a super-module and 15% among all the crystals of barrel. The inter-calibration of crystals is done by the cosmic muons which deposits 250 MeV energy on traversing the full length of the crystal. The final inter-calibration will be done using isolated photons or electrons originating in the processes $W \rightarrow e\nu$ and from mass reconstruction of $\pi^0 \rightarrow \gamma\gamma$ and $\eta^0 \rightarrow \gamma\gamma$.

The radiation induced degradation of the transparency of the crystals is monitored using laser pulses injected into the crystals via optical fibres and measured using silicon PIN diodes. The initial energy scales and calibrations are obtained using electron beams of momenta between 20 and 250 GeV/c in the CERN H4 test beams of year 2004.

2.2.2.2 Preshower Detector

The CMS Preshower Detector is installed in front of the ECAL endcaps and covers $1.653 < |\eta| < 2.6$. The main purpose of the detector is to distinguish direct photons from those coming from neutral pion decays by making use of its high granularity. The preshower is a sampling calorimeter made of 2 layers of lead radiators and silicon strip sensors. The total thickness of the preshower is 20 cm. The first lead layer is $2 X_0$ thick and the second layer is $1 X_0$ thick. Therefore, almost 95% of single incident photons start showering before reaching the second layer of silicon sensors. The orientation of the strips in the two planes is orthogonal. Each silicon sensor has 32 strips (1.9 mm pitch) on an active area of $61 \times 61 \text{ mm}^2$. The nominal thickness of silicon sensors is $320 \mu\text{m}$. The sensor is glued to a ceramic support which also houses the electronics for the preshower. Each such assembly is called a micro-module and 7, 8 or 10 micro-modules are assembled to form a ladder. The ladders are attached to the lead plates in x - y configuration.

2.2.2.3 Hadron Calorimeter

The design of the CMS Hadron Calorimeter (HCAL) is constrained by the fact that the whole calorimeter should reside inside the magnetic bore and the choice of the design of the electromagnetic calorimeter. This severely restricts the amount of absorber material that can be put in the space available between the rear end of ECAL and the magnetic coil. The HCAL is divided into a central barrel, an outer hadron calorimeter, an endcap

and a forward calorimeter to make best use of the space available and provide maximum hermiticity possible.

HCAL Barrel (HB)

The central part of HCAL or HB [22] is a sampling calorimeter made of brass absorber and scintillator and it extends in pseudo-rapidity up to $|\eta| \leq 1.3$ with full coverage in azimuth. It extends from 1.77 m to 2.95 m in radial direction. The absorber material for HB is chosen to be cartridge brass which is 70% copper and 30% zinc by composition and has a density of 8.53 g/cm³. It is a non-magnetic material with short interaction length of 16.42 cm and higher mechanical strength than pure copper, thus making a compact design of HB possible. The HCAL barrel is divided into two cylindrical halves known as HB+ and HB- and each half-barrel is made of 18 identical wedges in azimuth (ϕ). Each wedge consists of 17 sampling layers. The first absorber plate is made of 40 mm thick stainless steel plate followed by eight layers of 50.5 mm thick brass plates and six plates of 56.6 mm thick brass plates. The last absorber layer is made of 75 mm thick stainless steel. Stainless steel is used in the first and the last layers to provide sufficient mechanical strength to the wedge. The absorber plates are bolted together in a staggered geometry with slots to fit scintillator megatiles. The HCAL provides $\sim 5.8\lambda_I$ material at the normal incidence of a particle from interaction point of CMS ($\theta=90^\circ$). The effective thickness increases as $1/\sin(\theta)$ and it becomes $10.22 \lambda_I$ at $|\eta|=1.17$ ($\theta=34.5^\circ$). The ECAL in front of the HCAL contributes an additional $1.1 \lambda_I$ in terms of material budget.

The active layers interspersed between the brass absorber plates are made of 3.7 mm plastic scintillators of Kurray SCSN81 type. This scintillator is chosen for its reasonable radiation hardness and the long term stability. These scintillators have an attenuation length of ~ 80 cm and therefore the light output is uniform for the tiles of varying lengths. The first and the last layers of HB are 9 mm thick (and is made of Bicron type scintillator) and the remaining fifteen layers are 3.7 mm thick. With this configuration, $\sim 1\%$ of total energy of incident particle is deposited in the active layers. Each scintillator layer is divided into 4 lateral sectors in azimuth (ϕ) and 16 sectors in pseudo-rapidity (η) resulting in towers of $\Delta\eta \times \Delta\phi = 0.087 \times 0.087$ throughout the wedge. Each ϕ layer, called a megatile, is divided into 16 individual units and the neighbouring units are isolated from each other by filling in the grooves with epoxy glue. They are made light tight by packing them into plastic sheets.

Each HB tile is grooved to accommodate a WaveLength Shifting (WLS) fibre along the periphery. The attenuation length of WLS fibres is ~ 1.8 m. To minimize the loss of light during the transportation of the light to photo-sensors which are located a few meters away, the WLS fibre is sliced to a multi-clad Kuraray clear fibre which has a longer attenuation length (~ 8.0 m). The end tip of WLS fibres which lies inside the scintillator is

coated with a thin layer of aluminium which acts as a reflector. The average reflectivity is 83% with a spread of 6.5% [23]. The clear fibres transport the light from scintillator tiles to the Hybrid Photodiode. The optical signal from all the 17 layers in a given η - ϕ segment are summed up for the η towers 1-14. The tower 15 has a fewer layers of scintillators so as to accommodate readout boxes and has readout towers with a slightly different grouping for the two outer and the two inner ϕ -slices. The tower 16 has a partial overlap with HE and the layers are grouped into two independent readouts.

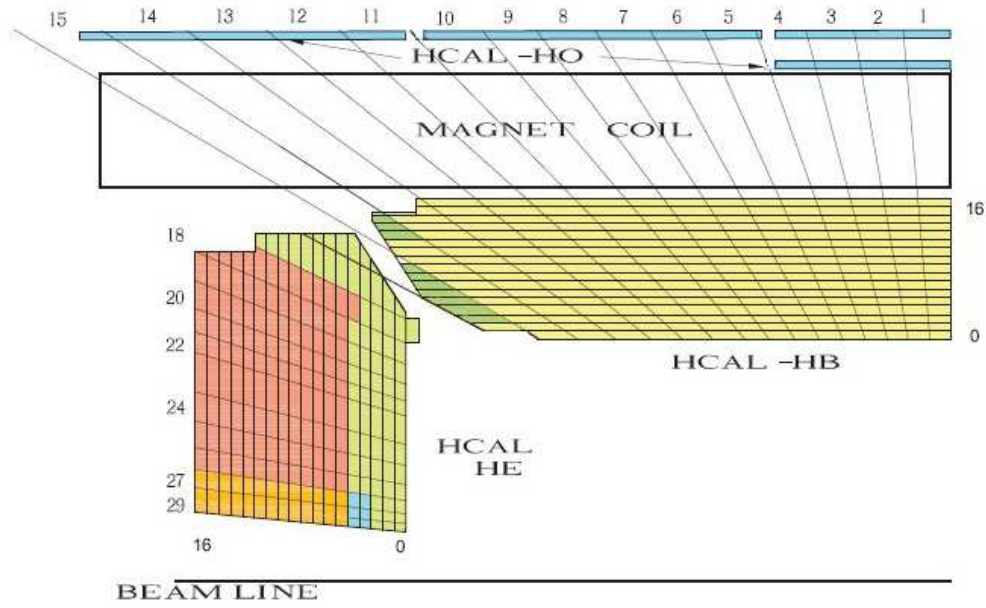


Figure 2.5: Grouping of layers of the barrel and the endcap hadron calorimeter in the (r, z) plane. Different groupings are shown in different colours.

Outer Hadron Calorimeter (HO)

At $\eta = 0$, the thickness of HB is only $5.8 \lambda_I$ and is not enough for a satisfactory containment of the hadronic shower generated by a particle of a few hundred GeV energy. To ensure adequate sampling, the HB is extended beyond the magnetic coil and is called Outer Hadron Calorimeter (HO) [24].

The main idea is to use the magnet coil which is $1.4 \lambda_I$ thick at $\eta = 0$ as an additional absorber material, to provide one more sampling layer up to $|\eta| < 1.3$ to identify the showers which started in the rear layers of HB and to measure the shower energy which is beyond the geometrical reach of HB. Geometrically, return yoke is in the form of five rings

identified by the numbers $-2, -1, 0, +1, +2$. HO is placed as a first sensitive layer in each of these rings. The thickness of HB is minimum at $\eta = 0$ and therefore, an additional layer of scintillators is placed just before a tail catcher iron block to provide an additional sampling in the region $|\eta| < 0.35$. Radially, inner layer of HO in ring 0 is at 3.82 m and the outer layer in ring 0 and the single layers in all other rings are at a distance of 4.07 m. The total depth of the calorimeter system is thus extended to a minimum of $11.8 \lambda_I$ in the barrel region.

The HO scintillator tiles are made from Bicron BC408 scintillator plates of 10 mm thickness. The HO geometry is divided into 12 identical sectors in ϕ to follow the design of rings of the return yoke in azimuthal direction. In transverse direction, the HO is segmented into the towers of $\Delta\eta \times \Delta\phi = 0.087 \times 0.087$ to map the HB towers as closely as possible. The tiles for a given ϕ are all assembled into one unit and packed in a white tyvek paper for complete reflectivity and light tightness and plastic sheets. Each tray corresponds to one ϕ slice of 5° .

The scintillator light produced in HO tiles by the passage of a charged particle is collected using 0.94 mm diameter Kurray Y11 multi-clad WLS fibres. There are four sigma “ σ ” shaped grooves in every HO tile to accommodate a WLS fibre. Outside the scintillator tile, the WLS fibre is optically spliced to a multi-clad Kurray clear fibre which transports the optical signal to the HPD.

HCAL Endcap (HE)

The Hadron calorimeter Endcaps (HE) [25] covers the pseudo-rapidity region of $1.3 < |\eta| < 3$ which accounts for 13.2% of the total solid angle and spans the regions which contain nearly 35% of total particles produced in the final state. The absorber used in the HE is also made of cartridge brass C26000 chosen for its non-magnetic properties, mechanical strength and small absorption length. Geometrically, the HE is made of 18 sections measuring 20° in ϕ and closes HB from both the ends. The whole absorber structure is made of 79 mm thick brass plates bolted together with radial gaps to accommodate 4 mm thick scintillator megatiles. There are 18 active layers in each HE wedge. The thickness of the endcap calorimetric system is about $10 \lambda_I$.

The tiles are trapezoidal shaped scintillator 4 mm thick SCSN81 (9 mm thick Bicron BC408 for layer 0) and are machined with a groove to accommodate WLS fibres. The transverse granularity of HE is $\Delta\eta \times \Delta\phi = 0.087 \times 0.087$ for $|\eta| < 1.6$ and $\Delta\eta \times \Delta\phi \approx 0.17 \times 0.17$ for $|\eta| > 1.6$ (Figure 2.5). Longitudinally, the towers 27, 28 and 29 have three division in depths and are read out separately. Except towers 16 and 17 which have an overlap with HB, other tower have two longitudinal readouts.

Photodetector for HCAL Barrel and Endcap

The photo detectors used in HCAL should be able to work in the presence of 4 Tesla magnetic field and at the same time should be able to give a good signal to noise ratio for a MIP signal crossing 3.7 mm tiles of HB. An optimal choice under these conditions is to use multi-channel silicon photo-diodes as optical transducers for both the barrel and the endcap HCAL detectors. The photo-detectors used for HCAL are called Hybrid Photo-diodes [26]. A HPD consists of a bi-alkali photo-cathode and it is held at a HV of -8kV at a distance of 3.3 mm from a pixelated silicon photo-diode.

Photons are collected by WLS fibres in the scintillator tiles and are transported to the Optical Decoder Units (ODU) where the fibres corresponding to a readout tower are bundled together and are aligned to the photo-cathode of a channel of a multi-pixel HPD.

Forward Calorimeter (HF)

The Forward Calorimeter (HF) [27] covers a pseudo-rapidity region of $3.0 < |\eta| < 5.0$. The huge particle fluxes in this high rapidity region and the corresponding heavy radiation doses govern the choice of absorber and active material of HF. It is made of steel absorber structure with 5 mm grooves which house quartz fibres as active material.

HF has a cylindrical structure and is located at ± 11.15 m from the interaction point. It is made of 18 modules on either side of the CMS detector. The fibres run parallel to the beam line and are bundled together to give a transverse granularity of $\Delta\eta \times \Delta\phi = 0.175 \times 0.175$.

The generation of signal is based on Cerenkov process. When the velocity of charged particles of shower exceed that of light in the medium, Cerenkov photons are produced. A fraction of these photons hit the core-cladding interface of fibre at an angle greater than critical angle and get transported to the end of fibre by internal reflection. Half of these fibres span the complete length of HF and the other half starts from a distance of 22 cm from front face. The two sets of fibres are read out separately. Electron/photons deposit most of the energy in the front of the detector. The hadronic showers are longer and equal amount of energy is expected in both the longer and the shorter fibres. The bundle of fibres terminate on one end of air-core light guides that penetrate through a 42.5 cm thick shielding to house photomultiplier tubes and the front end electronics housed in readout boxes. Each light-guide ends on a standard bi-alkali photo-cathode of a 8-stage photomultiplier tube with a borosilicate glass window.

Digitization and Data Acquisition

A schematic overview of HCAL front end readout electronics is shown in Figure 2.6. The analog output from HPDs for HB/HO/HE and PMTs for HF is digitized using a charge

integrating circuit called QIE - the Charge (Q) Integrator (I) and Encoder (E) [28] and [29]. The chip is designed to provide a constant relative precision over a wide dynamic range of 1 fC to 10,000 fC. The wide dynamic range is achieved by using a multiple scaled range technique. The input current is integrated over four different ranges and the range which is not at full scale is chosen for the digitization by a non-linear ADC. The output of ADC makes 5 bit mantissa and the range index is stored as the exponent of the floating point output (2 bits). There are four such sets of integrators referred to as CapID 0, 1, 2 and 3 and each one integrates for 25 ns. At any given time, one set is collecting the charge, one is settling, one is read out and one is being reset.

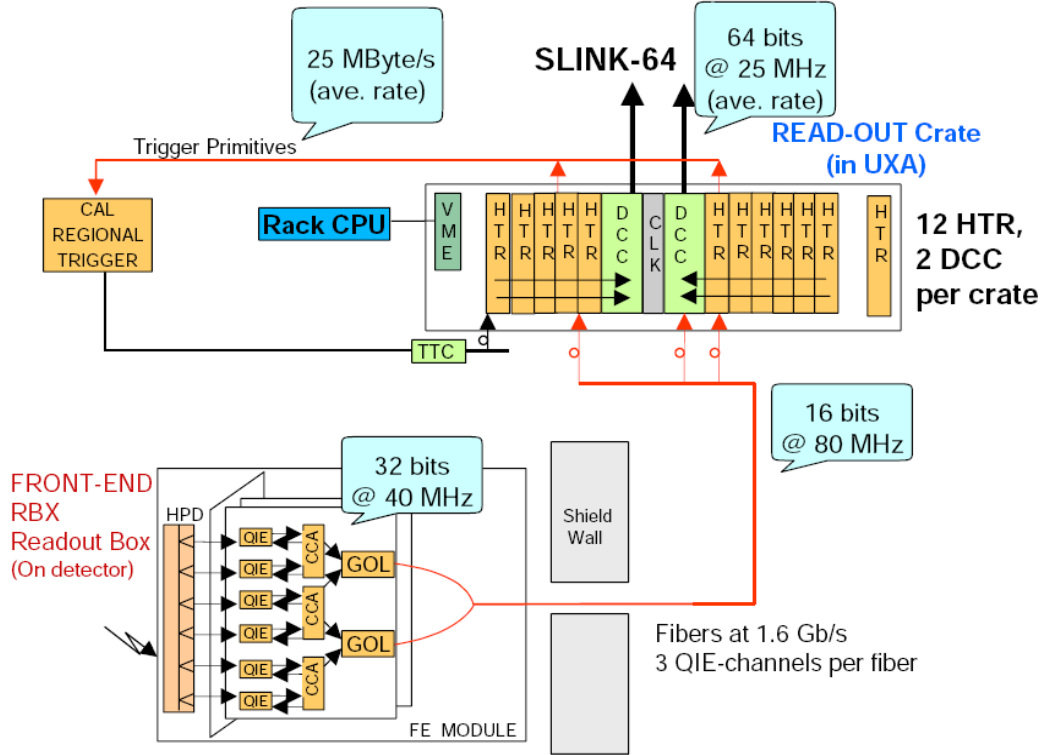


Figure 2.6: A schematic view of HCAL readout electronics.

Data from the front end electronics is sent to the HCAL Trigger/ReadOut or HTR board via Gigabit Optical Links (GOL). Each link carries data from three QIE channels. An HTR board can receive data from 48 channels (16 data fibres). It is equipped with optical receivers, timing and trigger circuits (TTC), serial low voltage digital signal (LVDS-Channel Link) outputs to the Data Concentrator Card (DCC) and FPGA.

The HTR contains two data pipelines, a Level-1 trigger pipeline and a DAQ pipeline. The trigger pipeline assigns the front-end data to a particular LHC bunch crossing and sends them to the CMS trigger. The input raw stream data are deserialized and synchronized to a local clock. The channel numbers carried by each fibre are demultiplexed. The data carried by each channel is converted to 16 bit linear energy values by a linearizing

Look Up Table (LUT). A Finite-Impulse Response (FIR) is used to subtract the pedestals and to assign all the energy to a single bunch crossing. Finally the energy is converted to E_T and compressed to a 8 bit word and is sent to Level-1 trigger along with a muon-id bit.

The data acquisition pipeline stacks the front-end data and sent to Data Concentrator Card (DCC) via LVDS links. Event building, protocol checking, event number checking and bit error corrections are performed for each channel by LVDS link receiver boards. The output of event builder is sent to CMS DAQ. The information sent to trigger is also sent to special trigger DAQ for monitoring the trigger performance. DCC contains dedicated logics for error detections and event synchronization.

Calibration Techniques for HCAL

The calibration system of HCAL is designed to understand the detector response and uniformity, and to monitor the stability of the detector over the time during collision data taking. It is aimed to keep track of changes in the signal strength due to aging of detector components and effects due to radiation damage.

There are various steps involved in the process of generating the electronic signal after a particle passes through the scintillator which can result in a tower-to-tower variation in the response.

The emission of photoelectrons at the photo-cathode and the amplification in HPD or PMT has an inherent statistical uncertainty associated with the process. The fluctuations in the number of particles present in a shower determines the intrinsic resolution of the calorimetric system and this contribution decreases with the increasing energy of the incident particle. The resolution of a realistic calorimeter can thus be described as $a/\sqrt{E} \oplus b$ where a is the coefficient of the stochastic term which decreases as the number of particles in a shower increases and the constant term b is determined by the leakage of shower in transverse and longitudinal directions and the precision with which the tower-to-tower calibration is determined. The uncertainty coming from the variation of tower-to-tower response can be minimized by properly inter-calibrating the towers with respect to each other.

The initial absolute energy scale is determined by studying the response of few wedges of HCAL using particles of known energies and identity in test beam experiments along with the relative calibrations obtained from radioactive sourcing. The final energy scales will be determined using in situ physics processes. But it would take some time to collect data and understand it to get reliable calibrations. Therefore it is very important to have reasonable initial energy scales determined from test beams to optimize trigger thresholds at the beginning of data taking.

- Charge injector calibration for the ADC

The ADC-to-Charge conversion factors for each range of QIE channel are obtained using a charge injector. These calibration constants are given by the ratio of measured response over input response. The average spread of these constants is $\sim 2 - 3\%$ for both HB and HE QIEs and the mean values are 0.91 ADC/fC and 0.36 ADC/fC respectively. The pedestal value of a QIE depends on which of the four internal integrator (CapID) is being used for the event under consideration. As a consequence, all the conversion factors are obtained for each set of the capacitors individually.

- Radioactive Source Calibration

Every HB/HE megatile and each tray of HO is equipped with a stainless steel tube of 1.3 mm outer diameter and 0.97 mm inner diameter through which a wire carrying a radioactive source in its tip can run along its length at a constant ϕ . The tube is located in a groove in the 2 mm thick black plastic covering the trays. Outside the tray, the tube is inserted into a low-friction 3 mm diameter acetyl plastic tube using a special brass cone coupler. A point like Cs-137 gamma source with a strength of nearly 3 mCi is mounted on the tip of a long flexible stainless steel wire and the motion of this wire is governed by an electric source driver which used two small motors. One motor controls the selection of source tube via a spiral indexer which can select up to 380 different channels. The other motor drives the storage reel to extend or retract the wire through acetyl tubing outside the calorimeter and through a stainless steel tube inside the calorimeter.

The data acquisition for the source testing uses the same high speed electronics employed for the HCAL. The signal from the source depends on the thickness of the scintillator tile. The HB readout chain with a gain of ~ 2000 for photo-detectors results in a small shift of the signal in the source on and off conditions. The observed signal is of the order of only a fraction of least count of ADC. This weak strength of the signal obtained from source is taken into consideration while designing the QIE chip for digitization such that the ADC bin width remains constant near the pedestal region. In the source calibration mode, the QIE is operated in high gain mode. The sensitivity of ADC is 1/3 fC per least significant bit while the nominal sensitivities in the four ranges are 1:5:25:125 fC per least significant bit. The data for the source testing are taken in histogramming mode. The source moves typically with a speed of 10 cm/sec. With the front end electronics clocked at the LHC frequency of 40 MHz, 800K events can be collected every 2 mm. Instead of storing such a huge amount of data in its raw format, the firm-wire in the readout electronics accumulates histograms at every 2 mm position. The mean and the RMS of these histograms are stored for final analysis to obtain the relative strength of the signal

in various towers.

The high radiation environment during LHC data taking would result in the activation of the HCAL absorber and change in response of the scintillator depending upon its η position. To keep track of the change in signal strength during data taking, layers 0 and 9 are permanently coupled via the acetyl tubing to the source drivers installed in the 8 cm gap at the back of a few wedges. Other megatile layers in the assembled calorimeter can be tested only when the detector is accessible during shutdown periods.

- Online calibration with physics processes

The HCAL barrel and endcaps can be calibrated using isolated tracks from $\tau \rightarrow \pi\nu$ in $W \rightarrow \tau\nu$ and $Z, \gamma^* \rightarrow \tau\tau$ processes and isolated track from minimum bias sample by making use of the measurements of tracker.

2.2.3 Magnet

The CMS collaboration has chosen a solenoidal magnetic field where the field lines are parallel to the proton beam and the bending of muons is in the transverse plane. In this plane the small transverse dimensions of the beam determines the transverse position of the vertex to an accuracy of better than 20 μm . The strong bending allows the trigger based on the tracks coming from the vertex. The momentum measurement in a solenoid starts at zero radial distance which makes a compact design possible for a given bending power of the magnet.

The final states containing more than one muon (*e.g.* $H_{\text{SUSY}} \rightarrow ZZ^{(*)} \rightarrow 4\mu$, $H_{\text{SM}} \rightarrow ZZ^{(*)} \rightarrow 4\mu$) are clean signatures of new physics. A precise knowledge of the momentum and unambiguous determination of the charge of particles is mandatory to efficiently trigger on interesting events containing high p_T electrons and muons. Both the momentum and information about the charge of a charged particle can be determined by measuring the curvature of the trajectory using a tracking system.

The superconducting magnet [30] is 6 m in diameter and 12.5 m in length and produces 4 Tesla magnetic field at full current and the resultant stored energy is 2.6 GJ. The distinctive feature of the solenoid is four-layer winding of stabilized reinforced NbTi conductor. The total weight of the solenoid is nearly 200t. The flux is mainly returned through an iron yoke, 1.56 m thick in the barrel and 1.45 m thick in the endcap. The total weight of the return yoke is 10000t. Four muon stations are integrated with the iron yoke for a full geometric coverage and robustness. The whole tracking system and the calorimeter are kept inside the magnet solenoid.

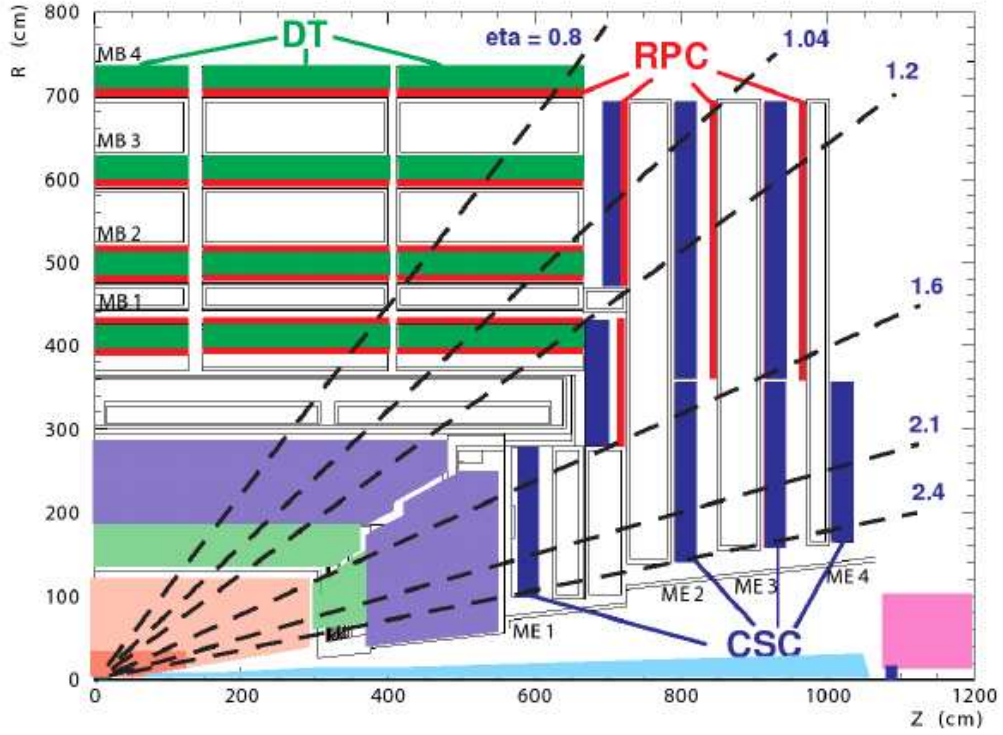


Figure 2.7: Quarter-view of the CMS detector. The muon system is labeled.

2.2.4 Muon Chambers

The Muon detection system [31] of CMS consists of four stations interspersed among the layers of the magnetic flux return plates. It is designed to measure the momentum of muons and unambiguously determine their charge over the entire kinematic reach of LHC. It is made of Drift Tubes (DT) in the barrel region and Cathode Strip Chambers (CSC) in the end caps. The DT and CSC systems are complemented by a dedicated triggering system consisting of Resistive Plate Chambers (RPCs) (as shown in figure 2.7).

The Drift Tube (DT) chambers cover the pseudo-rapidity region up to $|\eta| < 1.2$. The DTs are arranged in 4 layers of rectangular drift cells staggered by half-a-cell and is called a super-layer (SL). First three DT chambers contain 3 super-layers. Two SLs in every chamber have wires along the beam axis and provide measurement $r\phi$ plane. The third SL has wire perpendicular to the beam axis and measure z-position of the track. The z-measurement is not present in the outermost (fourth) muon station. Each drift cell has a cross section of $13 \times 42 \text{ mm}^2$ and the design includes a 50 micron diameter gold plated stainless wire, 2 cathode strips and 2 field shaping strips. The cells are filled with a gas mixture of 15% Ar+85% CO_2 and are operated at the atmospheric pressure. With this configuration, single wire resolution better than 250 microns is achieved. The staggered cell geometry allows an efficient standalone bunch crossing identification.

In the endcap regions of CMS endcaps, the muon rates and backgrounds are higher

and magnetic field is non-uniform. The cathode strip chambers (CSC) are chosen for the pseudo-rapidity region $0.9 < |\eta| < 2.4$ for their fast response, fine segmentation and high radiation resistance. There are four stations in each endcap. The CSCs are multi-wire proportional chambers comprised of 6 anode wire planes interleaved among seven cathode panels. By interpolating charges induced on cathode strips by avalanche positive ions near a wire, precise localization of an avalanche along the wire direction can be determined. The cathode strips run perpendicular to beam line radially outward in direction at constant $\Delta\phi$ width and provide measurement in $r\phi$ plane. The anode wires are perpendicular to strips and provide measurement in η . The nominal gas mixture used is 40% Ar + 50% CO₂ + 10% CF₄.

Resistive Plate Chambers (RPC) are gaseous parallel plate detectors which are capable of tagging the time of an ionising event in a much shorter time than the time difference of 25 ns between two consecutive LHC Bunch Crossings (BX). Therefore, a fast dedicated muon trigger device based on RPCs can identify unambiguously the relevant BX to which a muon track is associated even with high background rate as expected at the LHC. CMS has employed six layers of double-gap RPCs in the barrel and four layers in the endcap.

For optimal performance of the muon spectrometer over the entire momentum range up to 1 TeV/c, the different muon chambers must be aligned with respect to each other and to the central tracking system to within a few hundred μm in $r\phi$. The muon system is equipped with an optical alignment system of LED and laser beams which monitor the position of 250 DT chambers in the barrel and 486 CSCs in the endcap. The alignment of the chambers can also be achieved using muon tracks from the cosmic data or processes like $Z \rightarrow \mu^+ \mu^-$. The optical alignment system is independent of the sources of uncertainties like the knowledge of magnetic field, material description and drift velocity which are all present in track based algorithm.

2.2.5 Trigger and Data Acquisition System

LHC will produce interactions at 40 MHz frequency, but only a small fraction of these events can be written on disk due to limitation in disk i/o capability. On the other hand the vast majority of events produced is not interesting, because it involves low transferred momentum interactions (minimum bias events). Thus, a trigger system is needed to save interesting events at the highest possible rate. The expected rate of events written to disk is foreseen to be 100 Hz.

CMS has chosen a two-level trigger system, consisting of a Level-1 Trigger (L1) and a High Level Trigger (HLT) [32]. Level-1 trigger runs on dedicated processors, and accesses information with coarse level granularity from calorimeters and muon system. A Level-1 trigger decision has to be taken for each bunch crossing within 3.2 μs . Level-1 trigger task is to reduce the data flow from 40 MHz to 100 kHz (figure 2.8).

The High Level Trigger is responsible for reducing the L1 output rate down to the target of 100 Hz. The HLT code runs on a farm of commercial processors and can access the full granularity information of all the sub-detectors.

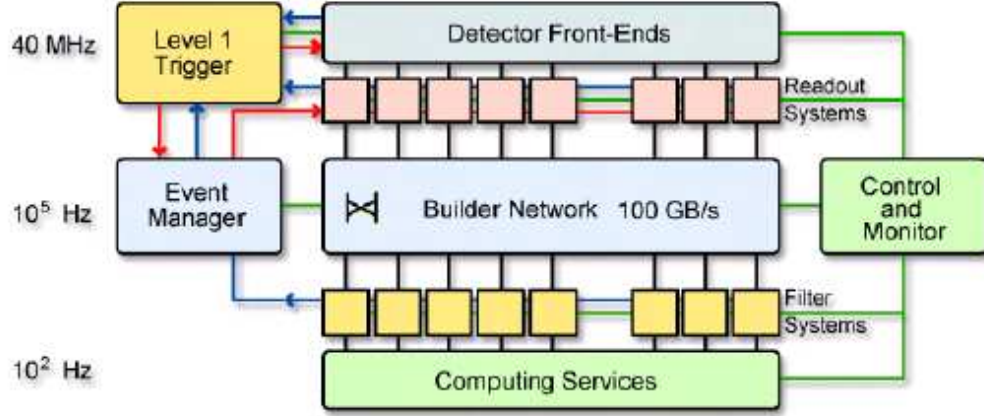


Figure 2.8: General architecture of CMS DAQ system.

2.2.5.1 Level-1 Trigger

The Level-1 trigger is responsible for the identification of electrons, muons, photons, jets and missing transverse energy. It has to have a high and carefully understood efficiency. Its output rate and speed are limited by the readout electronics and by the performances of the Data Acquisition (DAQ) system. It consists of three main subsystems:

- L1 Calorimeter Trigger
- L1 Muon Trigger
- L1 Global Trigger

The L1 Global Trigger is responsible for combining the output of L1 calorimeter trigger and L1 muon trigger and for making the decision. L1 Muon Trigger is actually a composite system itself: information from RPC, CSC and DT specific triggers are combined in the so called L1 Global Muon Trigger. The organization of CMS Level-1 Trigger is schematically summarized in Figure 2.9.

L1 Calorimeter Trigger

The input for L1 Calorimeter Trigger is calorimeter towers which are clusters of signals collected both from ECAL and HCAL. Energy deposits in the towers are calculated by high level calorimeter readout circuits, called Trigger Primitive Generators (TPG). The

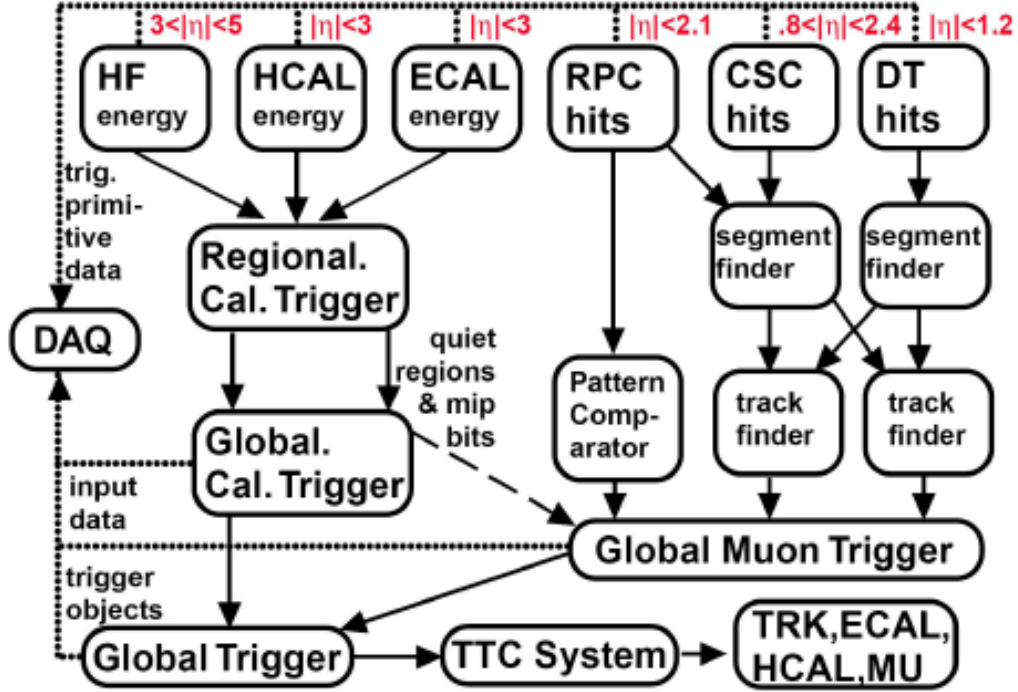


Figure 2.9: Level-1 trigger components.

Regional Calorimeter Trigger (RCT) finds out electron, photon, and jet candidates along with their transverse energy and sends them to the Global Calorimeter Trigger.

The Global Calorimeter Trigger sorts the candidates according to their transverse energy and sends the four highest candidates to the L1 Global Trigger.

L1 Muon Trigger

The RPC trigger electronics builds track segments, gives an estimate of the p_T and sends these segments to the Global Muon Trigger. It also provides the CSC logic unit with information to solve hit position ambiguities in case two or more muon tracks cross the same CSC chamber.

The CSC trigger builds Local Charged Tracks (LCT), that are track segments made out of the cathode strips only. A p_T value and a quality flag are assigned to the LCTs. The best three LCTs in each sector of nine CSC chambers are passed to the CSC track finder, which uses the full CSC information to build tracks, assign them a p_T and a quality flag and sends them to the Global Muon Trigger.

DTs are equipped with track identifier electronics, which is able to find groups of aligned hits in the four chambers of a super-layer. Those track segments are sent to the

DT track correlator which tries to combine segments from two super-layers, measuring the coordinate. The best two segments are sent to the DT track finder which in turn builds tracks and sends them to the Global Muon Trigger.

The Global Muon Trigger sorts the RPC, CSC and DT muon tracks and tries to combine them. The final set of muons is sorted according to the quality, and the best four tracks are passed on to the L1 Global Trigger.

L1 Global Trigger

The L1 Global Trigger is responsible for collecting objects created from the calorimeter and muon triggers and for making a decision whether to retain the event or not. If the event is accepted, the decision is sent to the Timing Trigger and Control (TTC) system, which commands the readout of the remaining subsystems.

In order to take the decision, the L1 Global Trigger sorts the ranked objects produced by the calorimeter and the muon system and checks if at least one of the thresholds in the Level-1 trigger table is passed.

Since there are large uncertainties in the cross section of many processes, the Level-1 trigger thresholds for the initial low luminosity data taking have been designed for an output rate of 16 kHz, instead of the planned 50 kHz, that is the design limit for low luminosity.

2.2.5.2 High Level Trigger

The High Level Trigger (HLT) is designed to reduce the Level-1 output rate to the goal of 100 events/s which are written to the mass storage system. HLT code runs on commercial processors and performs reconstruction using the information from all sub-detectors. Data read from sub-detectors are assembled by a builder unit and then assigned to a switching network that dispatches events to the processor farm. The CMS switching network has a bandwidth of 1 Tbit/s.

This simple design ensures maximum flexibility to the system, the only limitation being the total bandwidth and the number of processors. The system can be easily upgraded adding new processors or replacing the existing ones with faster ones as they become available. Since the algorithms are implemented using high-level software, improvements in the algorithms can be easily implemented and they do not require any hardware intervention.

The HLT code is run on a single processor for a given event and the time available to make a decision is restricted to a maximum of 300 ms. The restriction on the time for the selection process imposes several constraints on the resources an algorithm can use. The reliability of HLT algorithms is of capital importance, because events not selected by HLT are lost for further analysis.

In order to efficiently process events the HLT code has to reject uninteresting events as soon as possible and computationally expensive algorithms must be run only on good candidates for interesting events. In order to meet this requirement the HLT code is organized in a virtually layered structure:

- Level 2: uses only muon and calorimeter information;
- Level 2.5: uses also the pixel information;
- Level 3: makes use of the full information from all tracking detectors.

Each step reduces the number of events to be processed in the next step. The most computationally expensive tasks are executed in the Level 3; time consuming algorithms such as track reconstruction are only executed in the region of interest. Besides, since the ultimate precision is not required at HLT, track reconstruction is performed on a limited set of hits, and is stopped once the required resolution is achieved.

Chapter 3

Simulation and Reconstruction

Event simulation and reconstruction are two software corner stones of any high energy physics experiment. The signals from the detector are translated into energy flow of the particles produced in the high energy interactions through these sets of programs. All software related to simulation and reconstruction for CMS is embedded inside the software framework CMSSW [33].

Event generation is the very first component in the process of simulation. Within CMSSW this can be done with many event generator programs. These programs can be run from within the framework, using dedicated interface libraries. The configuration of the event generators is performed by feeding cmsRun with the appropriate configuration file containing the flags to be set in the event generator. The event generator is responsible for filling the HepMC [34] record with all information about the currently generated event. The HepMC record is then captured by the CMSSW framework and stored in the Event.

After the event has been generated, simulation of detector effects is carried out. The first step in the simulation of instrumental effects is the smearing of the vertex position. The event primary vertex, that is placed by the event generator at the origin of CMS coordinate system, is smeared according to the distribution of expected position of pp impaction point per bunch crossings. The next step is the simulation of the interaction of particles with the detector. The description of these interactions is achieved using GEANT4 [35]. Once energy deposits and multiple scattering effects in the CMS sub-detectors are simulated, the simulation of signals produced by the sub-detectors follows. This step is known as digitization.

The chain described so far is often referred to as full simulation chain. The most time consuming step of the full simulation is actually the simulation of detector effects using GEANT4. The time needed to fully simulate an event with GEANT4 can amount to several minutes.

For this reason a fast simulation of the detector effects has been set up. In the fast simulation, the GEANT4 step and the digitization step are skipped and detector

level quantities, such as the hit positions in the tracker and the energy deposits in the calorimeters, are described using parametrized functions that aim at reproducing the full simulation results.

Starting from the simulated signals in each sub-detector (or from the low level reconstructed quantities produced by the fast simulation), the reconstruction of the event follows. With this approach exactly the same algorithms that will be used on real data are run on simulated samples.

3.1 Event Generation

The structure of events produced at high energy colliders is extremely complex, and Monte Carlo integration is necessary to effectively simulate realistic events. Event generators are complex computer programs that subdivide the problem of producing events into a sequence of tasks that can be handled separately with the help of both analytic and numeric computation.

Different event generators implement computations with different levels of precision using different techniques. More precise calculations take into account several orders in perturbation theory. However, they are available only for a limited number of processes, thus making it hard to derive predictions on inclusive quantities. On the other hand these quantities can often be described with reasonable precision with programs which implement lower order calculations.

Multi-particle final states are described as a product of a term describing the dynamics of the process and one describing the kinematics or phase space which takes care of the standard conservation laws. Integration of the multi-dimensional phase space is done using random numbers which essentially sample the probability distribution. Protons being composite objects, the basic interaction is often between the constituents of the protons. Because of the complexity, the event generators subdivide the process into several components shown in Figure 3.1. The basic steps in the event generation are:

Parton Distributions: For collisions of composed particles like protons, it is important to know the momentum fraction of the partons for the simulation. The parton distribution function is described in chapter 1.

Hard Subprocess: The hard process characterizes fundamentally the event and is well described by perturbation theory. It has to be considered, that it is possible to produce heavy particles with a subsequent decay to partons, in a time shorter than the beginning of the parton shower. These short-lived resonances are closely connected to the hard process itself.

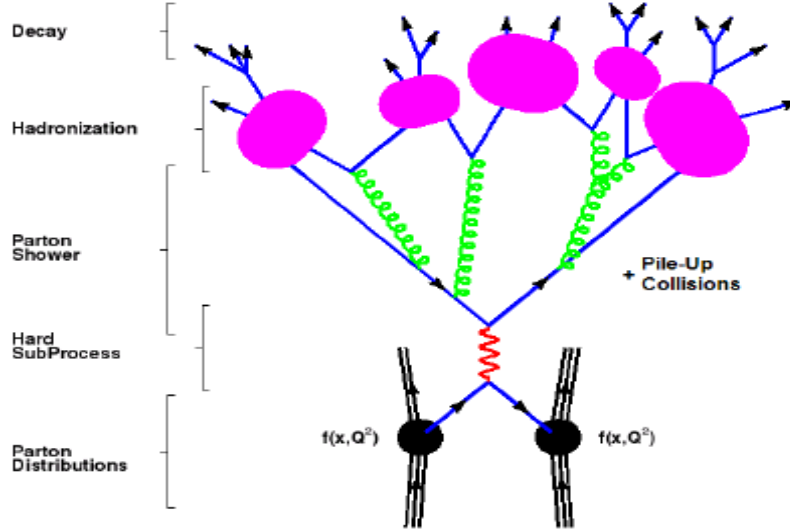


Figure 3.1: Schematic overview of the basic structure components in generating events through the process of hard scattering, parton shower, hadronization and decays.

Parton Shower: The parton shower is linked to higher order QCD effects. Partons can radiate, for example to gluons, before or after the hard process took place, the initial or final state radiation, respectively. Additionally, all partons branch, what is described by an event generator with a splitting function. The branching or showering continues until a certain cut-off point is reached. Due to the showering, jets of quarks and gluons are produced in the direction of the primary parton.

Hadronization: Coloured particles do not exist. So the quarks and gluons, produced in the shower cannot be understood as free particles. The confinement of the strong interaction leads to new quark-antiquark pairs through vacuum polarization, if two coloured particles separate. So the partons in the jets have to be grouped to colourless objects or hadrons which can be seen by the detector. Hadronization proceeds at a scale of low momentum transfer where the strong coupling constant becomes large resulting in a break down in perturbation theory. The generators use different hadronization models to simulate this process.

Decay: The formed hadrons often have rather short lifetimes and they decay into long lived lighter hadrons.

Underlying Event and Pile-Up: The initial partons for the hard process stem from the primary hadrons, which are left over as coloured hadron remnants. But these partons of the remnant can also interact with other partons, leading to multiple

parton interactions, which is called the underlying event. Furthermore, it is possible, that other proton-proton collisions appear during the same bunch crossing. This pile-up as well as the underlying event has to be added to the event simulation, too.

Many generators exist nowadays that can make calculations up to several partons in the final state. Among the general purpose ones there are many tree level generators: PYTHIA [36], HERWIG [37]. ALPGEN [38], MADGRAPH/MADEVENT [39, 40] are able to make matrix element calculations for a number of processes, and to match the matrix element outcome with parton showers. A few generators which can perform the full Next-to-Leading Order (NLO)[41] calculation with all virtual corrections included are also available for a limited number of processes; an example is the program called MC@NLO.

PYTHIA

PYTHIA [36] is an event generator using parton shower and with hadronization and decay codes. It can be used for general purpose to obtain a full event simulation of high energy collisions of electrons, positrons, protons or antiprotons. It is also capable to handle events produced with another matrix element generator to carry out the showering and hadronization. The hadronization model is based on the LUND string model, where a linear confinement between two quarks is assumed. When they move apart, a colour flux tube is stretched until the stored energy in this tube or string is high enough to produce a new quark-antiquark pair.

HERWIG

The Herwig Monte Carlo program [37] is based on parton shower simulation using a coherent branching algorithm. While the energy fractions are distributed according to the Leading Log Approximation (LLA), phase space is restricted to an angular-ordered region. The choice of evolution variable is $\approx E^2(1 - \cos \theta)$, where E is the energy of the branching parton and θ is the angle between the two resulting partons. This facilitates the inclusion of interference phenomena [42, 43, 44] in the treatment of parton shower development. The description of hard gluon emission is improved by matching the parton shower calculation to an $\mathcal{O}(\alpha_S)$ matrix element calculation. Fragmentation is performed by a cluster model, which incorporates the preconfinement property of perturbative QCD[45, 46, 47, 48].

ALPGEN

ALPGEN [38] is a parton level generator for multi-parton hard processes at hadron colliders. The matrix elements are evaluated in leading order in QCD and electroweak interactions for many Standard Model parton processes. Spin correlations are taken into

account as well as the full information on the colour and flavour structure is given for the parton level events. The generator is designed especially with the focus on multi-jet final states.

MADGRAPH

MADEVENT[39] is a multi-purpose, tree level event generator which is powered by the matrix element generator MADGRAPH. A process dependent, self-consistent code for a specific Standard Model process is generated upon the user's requests. Given the process, MADGRAPH automatically generates the amplitudes for all the relevant subprocesses and produces the mappings for the integration over the phase space. This process dependent information is packaged into MADEVENT, and a stand-alone code is produced that can be downloaded from the web site and allows the user to calculate cross sections and to obtain unweighted events automatically. Events can be also generated directly from the web, by filling a form and letting the code run over the MADGRAPH dedicated clusters.

Once the events have been generated - event information, (*e.g.* particle identifiers, momenta, spin, colour connections) is stored in the Les Houches format, which may be passed directly to a shower Monte Carlo program. To interface MADGRAPH to CMSSW and pass the events to PYTHIA, the MADGRAPH Interface package has been written. MadGraphInterface is a CMSSW package in the GeneratorInterface subsystem that allows to read in events in the Les Houches format, perform parton shower and hadronization using PYTHIA and write CMSSW objects (`edm::HepMCProduct`) in the event (`edm::Event`).

3.1.1 Modelling Perturbative QCD

Perturbative QCD describes the radiation of gluons off the primary quarks and the subsequent parton cascade due to gluons splitting into quarks or gluons, and radiation of gluons off secondary quarks. As the centre of mass energy increases, hard gluon emission becomes increasingly important, relative to fragmentation, in determining the event structure. There are two complementary approaches towards describing the perturbative QCD: (a) Matrix Element approach and (b) Parton Shower approach.

Matrix Element approach: In the Matrix Element (ME) [49] approach, Feynman diagrams are calculated, order by order. But the calculations become increasingly difficult for the higher order diagrams, in particular for the loop diagrams. Matrix element calculations, therefore, exist only up to second order in α_S [50]. The final state consists of at most four partons. This approach takes into account exact kinematics, and the full interference and helicity structure. The strong coupling constant, α_S , has a well defined meaning in this approach. The matrix element

approach is required to determine α_S and to study QCD in 3-jet and 4-jet events. Emission of multiple soft gluons, limits the applicability of the matrix elements.

Parton Showers: The parton shower approach [51] is derived within the framework of leading logarithm approximation (LLA). Only the leading terms in the perturbative expansion are kept and resummed. Sub-leading corrections, which are down in order by factors of $\ln Q^2$, or by powers of $1/Q^2$, are thus neglected. Nevertheless, different schemes have been devised to take into account some sub-leading corrections like next-to-leading terms (NLLA).

An arbitrary number of branching of one parton into two or more may be put together, to yield a description of multi-jet events, with no explicit upper limit on the number of partons involved. Development of the parton shower is based on an iterative use of the basic branching $q\bar{q} \rightarrow q\bar{q}g$, $g \rightarrow q\bar{q}$, $g \rightarrow gg$. A probabilistic approach is used to describe these branching.

Angular Ordering: Colour coherence phenomenon in the final state has been well established in e^+e^- annihilation [52]. Particle production in the region between quark and anti-quark jets in $e^+e^- \rightarrow q\bar{q}g$ events is measured to be suppressed with respect to the region between (anti)quark and gluon jets. This asymmetry, arises from the amplitudes of the q , \bar{q} and g . In the language of pQCD, is called as coherence effect. The study of coherence effects in hadron-hadron collisions is considerably more subtle than that in e^+e^- annihilation due to the presence of coloured constituents in both the initial and final states. During hard interaction, colour is transferred from one parton to another. Gluon radiation associated with the incoming or outgoing partons leads to the formation of jets of hadrons around the direction of these coloured emitters. It is the interference of such emissions that produces the colour coherence effects in the perturbative QCD calculations.

An important consequence of colour coherence is the Angular Ordering (AO) approximation of the sequential parton decays. To leading order in N , the number of colours, AO leads to a suppression of soft gluon radiation in certain regions of phase space. In the case of outgoing partons, AO results in a uniform decrease of successive emission angles of soft gluons as the partonic cascade evolves away from the interaction. However, for the incoming partons, the emission angles increase as the process develops from the initial hadrons to the hard process. Monte Carlo simulation including coherence via AO is available for both initial and final state evolutions. While AO provides an approximate description of colour coherence effects, QCD calculations taken to sufficiently high order should model the effects properly. Use of the latter approach, however, is limited, due to the current lack of higher-order calculations.

For example, in a branching $q \rightarrow qg$ the final state q and g share the newly created pair of opposite colour-anticolour charges, and therefore q and g can not emit subsequent gluons incoherently. If one considers only emission that should be associated with the q or the g , to a good approximation (in the soft region), there is a complete destructive interference in the regions of non-decreasing opening angles, while partons radiate independently of each other inside the regions of decreasing opening angles ($\theta_{q\bar{q}} < \theta_{qg}$, once azimuthal angles are averaged over. The details of the colour interference pattern are reflected in non-uniform azimuthal emission probabilities. Colour coherence is approximated by the angular ordering parameter (AO) in the PYTHIA event generator.

3.1.2 Non-Perturbative Aspects of QCD

3.1.2.1 Fragmentation Process

Colour confinement is understood only qualitatively to arise out of the requirement that the colour field between the quarks and gluons are confined to distances of the order of a fermi, since the strength of the strong coupling (α_S) increases with distance. Fragmentation of partons into observable hadrons is governed by soft non-perturbative processes that cannot be described from the first principle, starting from the QCD Lagrangian. An attempt to understand the dynamic behaviour of quarks in colour fields with growing distance scales has led to the development of many phenomenological models for hadronization, the widely used being:

Independent Fragmentation: The independent fragmentation model [53] assumes that the fragmentation of any system of partons can be described as an incoherent sum of independent fragmentation procedures for each parton separately. Each parton gives rise to its own jet of hadrons. The process is to be carried out in the overall centre-of-mass frame of the jet system, with each jet fragmentation axis given by the direction of motion of the corresponding parton in that frame. The fragmentation process can be viewed as an iterative procedure, where an initial quark picks up an antiquark from a vacuum fluctuation to form a meson leaving behind the other quark. The sharing of momentum between the meson and the remaining quark is described by a fragmentation function $f(z)$, which is the probability density for the meson to carry a fraction z of the initial quark momentum. The remaining quark carries the momentum $1 - z$. Transverse momentum components are introduced according to a Gaussian distribution with zero mean and a standard deviation of typically 300 MeV/c. The procedure is repeated with the remaining quarks, until the energy falls below a cutoff. Gluons can be treated by splitting them into a quark-antiquark pair first and then following the same mechanism as described

above for hadron production.

String Fragmentation: The string fragmentation model [54] is based on the idea that, as the partons ($q\bar{q}$ pair) produced in interactions move apart, a colour flux tube (string) is stretched between the q and the \bar{q} . The transverse dimension of the tube is of the typical hadronic size, roughly 1 fm which provides a natural scale for the creation of transverse momenta. For a $q\bar{q}g$ system, where all the partons are moving from a common origin, a string is stretched from the q end via the g to the \bar{q} end. In other words, the gluon can be seen as a kink on the string, as shown in Figure 3.2, which carries energy and momentum. As a consequence, a gluon has two string segments attached to it.

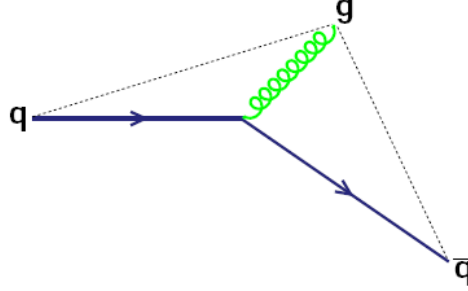


Figure 3.2: String representation of a $q\bar{q}g$ system. For such a system where all the partons move apart from the common origin a string is stretched from the q end via the g to the \bar{q} end.

If several gluons are present in the system, they will still appear as kinks between the q and \bar{q} ends, although the configuration will be much more complicated. When two partons connected with a string segment have a small invariant mass, two such nearby partons together drag out a string very much like what would have been dragged out by one single parton with the summed momentum. A soft gluon does not affect the string evolution significantly. These properties of the string motion are the reasons why the string fragmentation scheme is safe with respect to soft or collinear gluon emission.

When the partons move apart, the potential energy stored in the string increases, and the string may break producing a new quark-antiquark pair at a point when the energy density reaches about 1 GeV/fm. Thus the system splits into two colour singlet quark-antiquark pairs. If the invariant mass of either of these string segments is large enough, string pieces may break further. The quarks and antiquarks from adjacent branches can then form mesons. Baryon formation is also possible via

di-quark production ($1 : 10^9$). Finally only the on-shell hadrons remain in the spectrum, each hadron corresponding to a small piece of string.

Cluster Fragmentation: Cluster fragmentation [55] is used only for developed parton configuration. The clusters are considered to be the basic units from which the hadrons are produced. A cluster does not have an internal structure and is characterized by its total mass and total flavour content. No explicit assumptions about fragmentation functions and the generation of transverse momenta are required. The decay of the cluster is assumed to be isotropic in the rest frame of the cluster. There are different cluster fragmentation schemes which differ to the extent to which string fragmentation ideas are incorporated:

- A parton shower picture is used to produce a partonic configuration. At the end of the shower evolution, all the remaining gluons are split into $q\bar{q}$ pairs. The quark from one splitting may combine with an antiquark which is close in phase space to form a colourless cluster as shown in Figure 3.3. These clusters subsequently decay isotropically into observable hadrons according to flavour content and phase space. There is basically only one free parameter, the maximum cluster mass. Clusters with higher mass first decay into smaller clusters, which subsequently decay into hadrons.
- Parton showers or matrix elements are used to generate a partonic configuration, with string stretched in between the partons. These strings subsequently fragment into clusters, which again decay into the final hadrons.

3.2 Detector Simulation with Geant4

3.2.1 Treatment of Particles in Simulation

Simulation of detector effects relies heavily on a very accurate description of particle interactions with matter. GEANT4 simulation toolkit [35] is developed to provide an infrastructure for the same. In a realistic detector used in high energy physics experiments, a particle passes through numerous detector elements made of different materials, shapes and sizes and it interacts with the detector material or decays. A physics process can be defined by an initial and a final state with well defined cross section or mean life. A model is an implementation of a physics process in the simulation machinery. GEANT4 provides a framework to simulate a wide range of physics processes with more than one model in most of the cases.

GEANT4 also provides the facility to create a hierarchical tree structure of volumes to model complicated detectors using the concept of logical volumes and physical volumes.

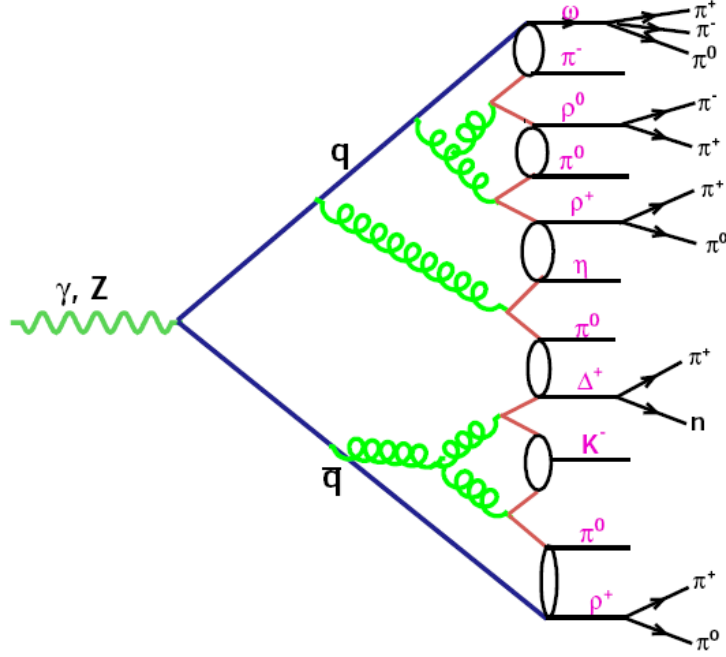


Figure 3.3: One cluster fragmentation scenario. Shower evolution is followed by forced $g \rightarrow q\bar{q}$ branchings and formation of clusters which decay into hadrons.

A logical volume represents a detector component of a certain shape made of a given material and has attributes which are independent of its physical position in the detector. A physical volume represents the spatial positioning or placement of the logical volume with respect to the mother volume (the enclosing volume). Using this concept, a complex detector like CMS can be described with a high degree of accuracy. However, the number of these logical and physical volumes can be very large in a complex detector. CMS, for example, is described by over a million of geometry volumes.

A particle is defined by some basic properties like the mass, charge etc. and it can be accompanied by a list of physics processes to which it is sensitive. The materials which comprises the detector can be made of a single element or a mixture of elements (isotopes). Some of the physical properties of a material like density can be described or can be calculated from the element composition. The interaction length and the radiation length and all other material dependent characteristics like excitation energy losses, coefficients of Bethe-Bloch formula etc. are calculated from the material composition.

In the treatment of the particles by GEANT4, a particle is treated in step by step manner through various detector elements. At every step, the distance to the point of decay or interaction with the current material is calculated for all the processes which the particle can undergo.

The quantities related to a physical interaction are recorded in a format which enables

making a direct comparison with the measurements done in an experiment. When a particle traverses the sensitive volume of a detector, the attributes of the interaction with the material like the energy deposited in each step, the time of interaction etc. is stored as a ‘hit’. These hits or a collection of hits can be digitized to get the simulated detector output.

3.2.2 Electromagnetic Processes

The electromagnetic physics process inside GEANT4 provides several models describing the electromagnetic interactions of electrons, positrons, muons, photons, charged hadrons and ions. These models are valid for the projectiles with kinetic energy above 1 keV.

The mean energy lost by any charged particle traversing a material through the ionization is simulated as a continuous process according to the Bethe-Bloch formula. The energy loss is treated as continuous as long as the energy of the electron ejected from the atom is below a threshold ¹. GEANT4 takes into account the fluctuations in continuous energy distributions for both the thin and the thick targets.

The Standard Electromagnetic Physics List (G4EmStandard) is used for a detailed description of electromagnetic interactions and is a major part of the reference configurations like LHEP, QGSP, QGSC etc.

The particles are tracked to the end of their range as long as the range is greater than a user defined range cut. The range is calculated numerically by integrating the energy losses for various particles. When the range becomes less than the range cut, all the energy of the particle is added to the energy deposited in the last step taken.

3.2.3 Hadronic Processes

The showers initiated by hadrons in a calorimeter are very complicated in terms of the variety of processes involved and the enormous number of final states which are possible for every hadronic interaction. Although the underlying theory involved in the development of a hadronic shower is QCD, yet it is difficult to give a single self-sufficient model to describe the hadronic showers in simulation. There are three energy regimes where different effects become prominent: Chiral Perturbation theory (< 100 MeV), the Resonance and Cascade region (100 MeV to 20 GeV) and the QCD Strings (> 20 GeV). There are a number of physics models to describe the physics processes in these energy regimes.

Three classes of models exists for modelling the final states:

Data driven models: These models are based on the libraries derived from real data whenever the data is available over a wide range of energy. Data driven modelling

¹The threshold is always expressed in terms of range in the medium in GEANT4 physics models.

is mainly used in neutron transport, photon evaporation, absorption at rest, calculation of inclusive cross sections and isotope production. These models are mostly used to describe low energy neutron transportation (< 20 MeV), radioactive decays and coherent elastic scattering (pp, np and nn).

Parametrized models: The parametrized models are derived both from the data and the theory. The data are parametrized and extrapolated to get the cross sections, multiplicities and the angular distributions. The final states are then determined keeping in mind the conservation laws.

Theory driven models: The theory driven models give a good description of high energy final states ($E_{\text{CMS}} > 5$ GeV). The models are based on diffractive string excitation and dual parton model or on the quark-gluon string model. Below 5 GeV centre of mass energy, cascade models are provided. Data are used for normalization and validation.

3.2.4 Physics Lists

A combination of these models (known as a physics list) can be used to obtain a faithful representation of showers over a wide range of energies from a few GeV to a few TeV accessible at the present day hadron colliders. The combination of various models is known as physics list. Some of the physics lists used for CMS are: LHEP, QGSP and QGSP_BERT.

LHEP

The LHEP physics list is based on a parametrized modelling for all hadronic interactions for all particles. This list combines the high energy parametrized (HEP) and low energy parametrized (LEP) models describing inelastic interactions for all hadrons. LEP is valid for the projectiles in the energy range between 1 GeV and 25 GeV while the HEP is valid for projectiles between 25 GeV and 10 TeV. The incident particle collides with a nucleon inside the nucleus and an intra-nuclear cascade is initiated. The final state consists of a recoil nucleon, the scattered incident particle, and possibly many hadronic secondaries.

QGSP

QGSP is the basic physics list applying the quark gluon string model [56, 57] for high energy interactions of protons, neutrons, pions, kaons and nuclei. The high energy interaction creates an excited nucleus, which is passed to the Precompound model of nuclear de-excitation. The string excitation takes place by the exchange of a parton which results

in both the rearrangement of partons and the momentum exchange. The hadrons are produced by string fragmentation following an iterative scheme $\text{string} \Rightarrow \text{hadron} + \text{new string}$. One of the most commonly used fragmentation function is the LUND model [59]. The hadrons are randomly formed on one end of the string. The quark content of the hadrons determines its species and charge. Interactions at the lower energies (below 25) GeV are modelled by the low energy parametrized (LEP) model.

QGSP_BERT

QGSP_BERT is the same as the QGSP physics list but uses the Bertini cascade mode [60, 61] for primary protons, neutrons, pions and kaons below 10 GeV. The Bertini model produces more secondary neutrons and protons than the LEP model, yielding a better agreement to experimental data.

3.3 Event Reconstruction

Reconstruction means the creation of physics quantities or objects from the output of the detector. This step does not distinguish between data recorded by the data acquisition systems of the real detector or the simulated detector response. The algorithms for the different reconstruction steps are available as modules in the framework. In the following, reconstruction of tracks and jets is presented in detail.

3.3.1 Track Reconstruction

The core of the CMS software for reconstruction of charged particles is modularized in four stages. The first stage provides seeds for further reconstruction, based on pairs or triplets of hits which are selected to be compatible with the interaction region and a lower p_T limit. Due to the low occupancy and the unambiguous 2-dimensional position information, the pixel layers provide generally the best seeding. In the region of high $|\eta|$, pixel and strip measurements are combined together to extend the geometrical acceptance of the pixel sub-detector and this provides an efficient seeding up to $|\eta| < 2.5$.

The second reconstruction stage uses a first estimate of the track parameters, calculated from the seed, to collect the full set of measurements associated to the same charged particle. It is based on a combinatorial Kalman filter approach: starting from the current parameters, the trajectory is extrapolated to the next layer of the tracker and compatible hits are selected based on the χ^2 between the predicted and the measured positions. The Kalman update of the predicted parameters with each of the compatible hits provides a new set of trajectory candidates. Many candidates are built in parallel until the hits

on the last layer of the tracker are added. Eventually, ambiguities are resolved between tracks sharing a substantial number of hits.

The third stage consists of a least-square fit in the form of a Kalman filter for the final estimation of the track parameters. A “forward” fit proceeding outwards from the interaction region removes the approximations used in the track finding stage and provides an optimal estimate of the track parameters at the outside of the tracker. A “backward” fit in the opposite direction yields the estimate of the track parameters in the interaction region and - combination with the forward fit - at each of the intermediate layers.

In the final stage a quality selection is applied to the set of reconstructed trajectories in order to reject candidates that are likely to be ghost tracks: *i.e.* measurements due to noise, or uncorrelated particles, that are accidentally aligned along a short helical trajectory and therefore fake a genuine track. In addition to requirements on the number of hits, the χ^2 of the fit and the energy, tracks are selected also according to their compatibility with the reconstructed vertices. While basically no vertex compatibility is requested for long trajectories with many hits and a good χ^2 , the selection cuts are very stringent for short tracks with bad χ^2 and low p_T .

According to simulation studies, the efficiency for reconstructing muons is close to 100% in the full η range of the geometrical acceptance of the tracking detector. Conversely, the tracking efficiency for pions varies between 85% and 95%. In order to identify and reconstruct the maximum number of charged hadrons, very short tracks with as few as three hits are considered by the reconstruction software. Nevertheless many particles interact in-elastically with the tracker material even before they cross three sensitive layers: because three is the minimum number of measurements necessary to provide a standalone measure of a trajectory’s curvature, these particles cannot be reconstructed. The plot of the tracking efficiency versus η for pions is clearly correlated to the distribution of the Tracker’s material. The larger the material budget, the lower is the efficiency.

3.3.2 Jet Reconstruction

As a consequence of the confinement in QCD, coloured partons of the hard process hadronizes and only a collimated stream of colour-neutral objects can be observed with detectors. In order to create a link between these observables and the energetic partons created in the hard process, the concept of jets is introduced.

A jet is defined as the cluster of all particles which are supposed to originate from the same initiator. This allows to link the properties like momentum and energy of the jet to the parton. For the clustering of the particles, different jet clustering algorithms have been developed. However, it is impossible to unambiguously map each hadron to a dedicated parton.

In CMS, two different types of objects are used as input collection for the jet algo-

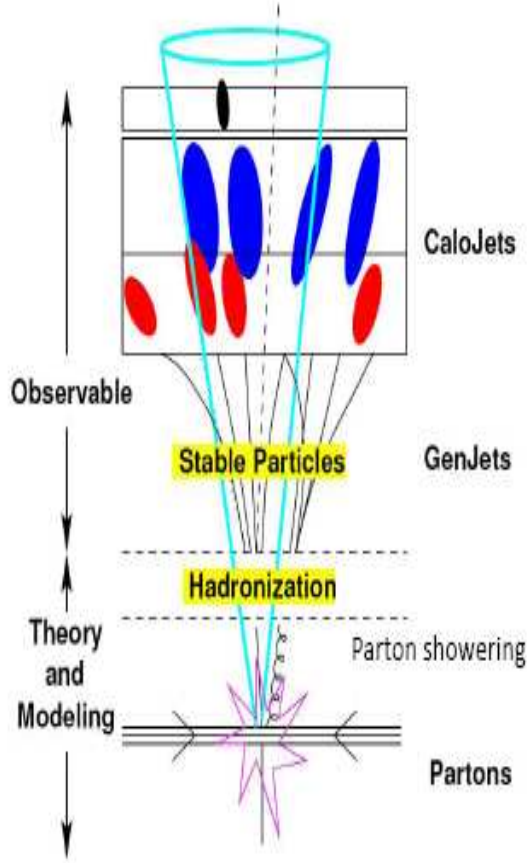


Figure 3.4: Visualization of the final state definition in CMS. Jets clustered from the hadronic final state based on Monte Carlo truth information are called particle jets or GenJets in CMS. Taking calorimeter information as input objects leads to calorimeter jets or CaloJets.

rithms. The first type comprises all hadronic final state particles which are listed in the Monte Carlo truth information. This includes also neutrinos and muons from resonance decays. Clustering these objects leads to particle jets and are called GenJets in CMS.

Whereas the basis idea of the clustering algorithms remains the same, the actual implementation differs. To be able to run an algorithms on objects coming from different levels of theory calculation, generation or reconstruction, the properties of the objects used as input to the algorithm should be comparable. A suitable choice is for example a four vector like quantity, which provides a three dimensional direction and the energy as both information can be derived either from calculated particle properties or measured energy deposit in a calorimeter cell. For clustering of the input objects, each jet algorithm has to provide the following basic functionality:

- a distance measure, which defines the separation of two objects.

- a procedure to decide whether objects are combined or not,
- and a recombination scheme, which defines how objects are combined.

There are two different techniques used for the clustering. Cone type algorithms cluster objects together being in a cone while clustering algorithms combine objects having the smallest distance of all possible pair wise combinations.

To compare jet results between different experiments and theory prediction, a precise non-ambiguous definition of the jet algorithms and the input variables is required. Such a possible definition as well as the actual implementation of the different algorithms, which have been used for this study including their basic properties are presented in the next chapter.

3.3.2.1 Calorimeter Jet Reconstruction

Calorimeter jets are reconstructed using energy deposits in the electromagnetic and hadronic calorimeter cells, combined into calorimeter towers as inputs. A calorimeter tower consists of one or more HCAL cells and the corresponding ECAL crystals (covering the same η/ϕ region). In the barrel region of the calorimeters ($|\eta| < 1.4$), the unweighted sum of one single HCAL cell and 5×5 ECAL crystals form a projective calorimeter tower. The association between HCAL cells and ECAL crystals is slightly more complex in the endcap regions of the electromagnetic calorimeter ($1.4 < |\eta| < 3.0$). Beyond the coverage of the ECAL, each calorimeter tower corresponds to one hadronic calorimeter cell. To reject electronic noise, the deposit in a given cell is only added to the tower energy if it passes the **Scheme B** energy thresholds [58], which are listed in Table 3.1 for the various detector regions. Towers are only considered for further clustering into jets if they furthermore fulfill $E_T > 0.5$ GeV to reduce the impact of additional Pile-Up (PU) interactions in the event. Both requirements will be revisited and optimized once the hardware settings of the CMS calorimeters for first collision data are finalized.

Scheme	HB[GeV]	HO[GeV]	HE[GeV]	Σ EB[GeV]	Σ EE[GeV]
B	0.90	1.10	1.40	0.20	0.45

Table 3.1: Energy thresholds (in GeV) for calorimeter noise suppression “Scheme B”. Σ EB and Σ EE refer to the sum of ECAL energy deposits associated with the same tower in the barrel and in the endcap respectively.

3.4 CMS Simulation and Reconstruction Software

The CMS simulation and reconstruction software, CMSSW[33], is a C++ framework that can be configured via Python [62] scripts.

CMS Event Data Model (EDM) is based on the concept of an Event. An Event is a C++ class that contains the information about a physics event, raw level data as well as reconstructed quantities. Reconstruction algorithms can access information from the Event and put reconstructed quantities in the event. Events can be read from and written to ROOT [63] tuples.

CMSSW can be run feeding the desired Python configuration script using the executable cmsRun. The configuration file contains the modules, *i.e.* the algorithms, that the user wants to run and it specifies the order in which they need to be run. The executable reads in the configuration file and, using a plugin manager, finds out the libraries in which the modules to be run are defined and loads them.

Six types of modules can be implemented in CMSSW and dynamically loaded via the plugin mechanism:

Source: These modules are used either to load events from a ROOT file or to produce events running an event generator.

EDProducer: These modules read in the events provided by a Source, apply an algorithm to the data contained in the event and produce other data to be put in the Event. All the reconstruction algorithms are implemented inside EDProducers.

EDFilter: They work exactly as an EDProducer, but they return a boolean value after the event has been processed. This boolean value can be used to decide whether to continue further processing or to skip the event.

EDAnalyzer: These modules are used to analyze and characterize events. They cannot put additional data in the Event, but can access the information stored in the Event and, *i.e.* produce analysis histograms.

EDLooper: They are used for particular tasks, such as track based alignment, in which there is a need to loop on a set of events more than once.

OutputModule: These modules are used to write events to a file after all the other modules were executed.

Often modules need auxiliary information that is not stored in the event. This asynchronous information is stored in the EventSetup object.

Chapter 4

Jets and Event Selection

4.1 Jets in Hadron Colliders

Jet production is the dominant process in high transverse energy hadron-hadron collisions. This process is well described by perturbative QCD where the scattering cross section is convoluted with a pair of parton distribution functions that express the momentum distribution of partons within the proton. The hard scattering cross section can be written as an expansion in the strong coupling constant $\alpha_S(Q^2)$. The leading term in this expansion corresponds to the emission of two partons. The next term includes diagrams where an additional parton is observed in the final state due to gluon radiation (*e.g.* $gg \rightarrow ggg$).

The collider experiments, such as Tevatron, have made very high precision measurements of inclusive jet rates, as well as the rate of n -jet events, $n \geq 2$. At present, in CMS, perturbative calculations exist to next-to-leading order ($\alpha_S(Q^2)$) only for the inclusive and di-jet rates. The next-to-leading order (NLO) calculation for three-jet rate is close to completion. These allow quite precise studies of QCD, albeit for very inclusive quantities.

At NLO, the cross sections begin to depend on the exact definition of the jets, since the jets begin to develop internal structure. The experiments have used measures of this internal structure as a cross-check on the reliability of the calculations, as well as a study of QCD in its own right. In fact these more exclusive event properties contain considerably more information about QCD dynamics, and make an ideal place to study QCD.

4.2 Jet Definition

Coloured partons from the hard scatter evolve via soft quark and gluon radiation and hadronisation process to form a spray of roughly collinear colorless hadrons which is called jets. Jets are the experimental signatures of quarks and gluons.

Nomenclature

A jet algorithm specifies a procedure by which an arbitrary set of (physical) four-vectors is mapped into a set of jets. To compare experimental results with theoretical predictions, the following elements have to be specified when dealing with jets according to the Standard Model Handles and Candles Working Group of the Les Houches Workshop 2007 [64].

The specification includes the name of the algorithm, all its parameters and the recombination scheme, which defines how the constituents of a jet are combined to calculate the energy and direction of the jet.

All the corrections done to the jet kinematics need to be specified for a consistent comparison among different experimental results or between data and Monte Carlo simulations. For example, it has to be specified whether measured input objects have been corrected for some aspect or if muons or neutrinos from Monte Carlo simulations are considered.

A more detailed discussion including recommendations for the jet definition and the specification of the final state truth level can be found in [64].

4.2.1 Jet Algorithms

A jet algorithm is a set of mathematical rules that reconstruct unambiguously the properties of a jet.

The first jet algorithms for hadron physics were simple cones. Over the last few decades, clustering techniques have greatly improved in sophistication. There are several jet reconstruction algorithms which have been coded and studied for CMS: the iterative cone, the mid-point cone, the inclusive k_T jet algorithm and seedless infrared safe cone algorithm. The midpoint-cone and k_T algorithms are widely used in offline analysis in current hadron collider experiments, while the iterative cone algorithm is simpler and faster and commonly used for jet reconstruction in trigger systems.

Most of algorithms under discussion define the momentum of a jet in terms of the momenta of its constituent particles in the same way, inspired by the Snowmass accord [65]. The transverse energy, $E_{T\text{jet}}$, pseudorapidity, η_{jet} , and azimuth, ϕ_{jet} , of the jet are given by:

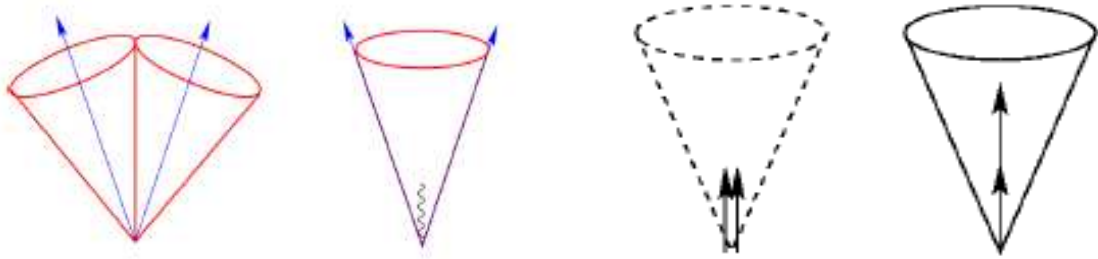
$$\begin{aligned} E_{T\text{jet}} &= \sum_{i \in \text{jet}} E_{Ti}, \\ \eta_{\text{jet}} &= \sum_{i \in \text{jet}} E_{Ti} \eta_i / E_{T\text{jet}}, \\ \phi_{\text{jet}} &= \sum_{i \in \text{jet}} E_{Ti} \phi_i / E_{T\text{jet}}. \end{aligned} \tag{4.1}$$

where E_{Ti} , η_i , ϕ_i are the transverse energy, pseudo rapidity and azimuthal angle of the

constituent particle i . Boost-invariant variables are only used here, so whenever the variable ‘angle’ is mentioned, this will refer to the Lorentz-invariant opening angles $R_{ij} = \sqrt{(\eta_i - \eta_j)^2 + (\phi_i - \phi_j)^2}$. Also the term ‘energy’ will refer to the mean transverse energy, $E_T = E \sin \theta$, where θ is the polar angle.

Infra-Red and Collinear Safety

One of the desired features of jet algorithms is to have collinear and infrared safe behaviour. Requiring that addition of an infinitely soft parton does not affect the output of a jet clustering algorithm is called infrared safety. Such soft partons may be a result of soft gluon radiation during the parton shower or the hadronization. Algorithm which start with the jet clustering around towers with high energy deposit, the seed tower or simply denoted as seed, can be sensitive to soft radiation as schematically illustrated in Figure 4.1(a). As shown on the left hand side part of the figure, addition of a soft parton to a configuration with two separated jets could lead to merging of these two jets into a single jet. Such soft radiation may come from pile-up and the underlying event.



(a) Infrared safety.

(b) Collinear safety.

Figure 4.1: Illustration of infrared and collinear safety in jet algorithms.

Collinear safety denotes in this context that addition or replacement of any massless parton by an exactly collinear pair of massless partons should not affect the output of the jet algorithm. This means that for example collinear gluon radiation emitted during the jet evolution does not lead to a different interpretation. An example for collinear unsafe behaviour are seed based algorithms as drawn in Figure 4.1(b). Starting with one jet produced in the hard process, two scenarios are possible. If the resulting energy concentration is sufficient to produce a seed for the jet clustering, the algorithm clusters it into one jet. The situation changes if the energy deposit is split into two equal parts. The energy concentration may no longer be sufficient to act as a seed for the clustering and no jet is found. This may happen through collinear radiation effects or due to the granularity of the calorimeter. A cluster of particles which hits exactly the middle of two calorimeter towers would not be clustered into a jet whereas the same energy deposit in

one tower results in a jet.

Iterative Cone Algorithm

In the iterative-cone concept with cone radius R , particles are clustered into jets according to the following steps:

1. the particles are passed through a calorimeter with cell size $\delta\eta \times \delta\phi$ (in LHC, for barrel part of the hadron calorimeter, $\delta\eta \times \delta\phi = 0.087$). In the parton-level algorithm, this is simulated by clustering together all partons lying within a cone of size $\delta\eta \times \delta\phi$ of each other.
2. every calorimeter cell (cluster) with energy above E_0 , is considered as a ‘seed cell’ for the following step (in LHC, $E_0 = 1$ GeV).
3. a jet is defined by summing all cells within an angle R of the seed cell according to Equation 4.1.
4. if the jet direction does not coincide with the seed cell, step 3 is reiterated, replacing the seed cell by the current jet direction, until a stable jet direction is achieved.
5. a long list of jets is thus obtained, one for each seed cell. Many entries in this list are duplicates: these are removed¹.
6. some jets could be overlapping. Any jet that has more than 50% of its energy in common with a higher-energy jet is merged with that jet: all the cells in the lower-energy jet are considered part of the higher-energy jet, whose direction is again recalculated according to Equation 4.1.
7. any jet that has less than 50% of its energy in common with a higher-energy jet is split from that jet: each cell is considered part only of the jet to which it is the nearest.

It is to be noted that despite the use of a fixed cone of radius R , jets can contain energy at angles greater than R from their direction, because of step 6. This is not a particular problem. This algorithm is not collinear or infrared safe algorithm.

k_T Algorithm

The fully inclusive k_T algorithm including an R parameter [66] is discussed here. It clusters particles (partons or calorimeter cells) according to the following iterative steps:

¹In $D\phi$, any candidate jet with energy below 8 GeV are also thrown away. For jets above 16 GeV, this makes only a small numerical difference, which is not important and so these jets are kept.

1. for every pair of particles, a closeness variable is defined

$$d_{ij} = \min(E_{Ti}, E_{Tj}) R_{ij}^2 (\approx \min(E_{Ti}, E_{Tj}) \theta_{ij}^2 \approx k_T^2)$$

2. for every particle, a closeness variable to the beam particles is defined

$$d_{ib} = E_{Ti}^2 R^2$$

3. if $\min(d_{ij}) < \min(d_{ib})$, particles i and j are merged according to 4.1 (other merging schemes are also possible [67]).
4. if $\min(d_{ij}) < \min(d_{ib})$, jet i is declared complete.

These steps are iterated until all jets are complete. In this case, all opening angles within each jet are $< R$ and all opening angles between jets are $> R$.

Midpoint Cone Algorithm

The midpoint cone algorithm is designed to address some disadvantages of the iterative cone algorithm. First, all objects above a certain threshold are taken as seeds and the objects inside this cone are clustered into proto-jets. In contrast to the previously discussed iterative cone algorithm, the objects are not removed from the input list and can therefore belong to different proto-jets. For all proto-jets which are closer than the diameter of the cone, the midpoint is calculated as the direction of the combined momentum. Then, a second iteration is done based on the midpoints and the proto-jets as seeds leading to an increased number of proto-jets after this second step. As no objects are removed from the input list, objects may belong to several jets and the proto-jets overlap. This is then resolved by some splitting and merging procedure.

This procedure starts with the proto-jet with the highest transverse energy. If the jet does not share objects with other proto-jets, it is defined as stable and removed from the list. If there is an overlap with other proto-jets, the further processing depends on the fraction of transverse energy shared between the two jets. If this is smaller than the splitting parameter E_{slpt} , the objects are assigned to the proto-jet which is nearest in the η - ϕ plane. Otherwise, the two jets are merged into one according to the selected recombination scheme. The stable cones after these steps are the final jets.

Adding midpoints as seeds for the second iteration improves infrared and collinear safety compared to the iterative cone algorithm. But this procedure cannot solve the problem completely.

SISCone Algorithm

The Seedless Infrared-Safe Cone (SISCone) algorithm [68, 69] is a cone clustering algorithm, which is designed to be infrared safe. Whereas infrared and collinear unsafety have been introduced into the iterative cone and midpoint cone algorithms by using a dedicated number of seeds for the jet clustering, the SISCone algorithm avoids this by searching for all stable cones. Using a brute force technique for this would be to test all subsets of N input objects for stability. However, such an approach is not suitable as the number of such distinct subsets grows with N^2 , which has implications for the needed computing time.

Therefore, the SISCone algorithm follows a more advanced approach by exploiting the fact that a circle enclosing a set of two input objects can be moved around such that two of the remaining objects lie on its circumference. Reversing this allows the determination of all stable cones with a radius R by testing the circles defined by a pair of objects and radius R . With this procedure, all stable proto-jets can be found which may overlap. Splitting and merging is done by the same procedure as described above for the midpoint cone algorithm except that the scalar sum of transverse momentum is used as the ordering parameter. A detailed description of these procedures can be found in [68] and a cartooned description is shown in Figure 4.2. It has been demonstrated, that the hard jets are affected by the addition of soft objects in a fraction less than 10^{-9} of the investigated events. For comparison, about 15 percent of the events are affected with the midpoint cone algorithm.

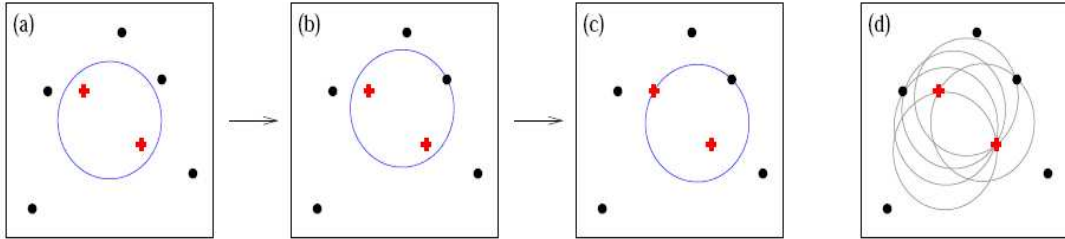


Figure 4.2: Steps followed in SISCone algorithm: (a) Some initial circular enclosure; (b) moving the circle in a random direction until some enclosed or external point touches the edge of the circle; (c) pivoting the circle around the edge point until a second point touches the edge; (d) all circles defined by pairs of edge points leading to the same circular enclosure.

4.3 Jet Energy Scale

The measurements made using the CMS detector need to be corrected for detector effects. For studies using jets, it is important to correct the energy and direction of jets reconstructed from the energies deposited in the calorimeter towers. The most important issue in this connection is the energy scale.

Jets are supposed to measure the energy of the partons which are created through hard scattering process in the proton-proton interactions. The partons manifest themselves as a set of stable particles through the process of hadronization and decay (of unstable particles). These particles interact with the detector material and deposit their energies. The calorimeter system measures part of these energies and this is used to reconstruct back the energy of the stable particles. These stable particles in turn are reconstructed back to jets using jet algorithm and their kinematic properties are computed. Calorimetric measurements assume that the final reconstructed energy is proportional to the response seen in the detector and often a linearity relation is assumed. However, test beam measurements show that the linearity relation is not true, in particular for low energy particles. The composition of particles in a jet has large fluctuation and translation of calorimeter energy to final jet energy is highly non-trivial.

Monte Carlo studies produce outputs at the level of stable particles using event generators based on QCD models. These generator level objects are combined into generator level jets (GenJets). These stable particles go through detector simulation and eventually produced energy deposits in the calorimeter towers (CaloTowers). Jets reconstructed from these calorimeter towers (CaloJets) will not have the same kinematic quantities as the corresponding generator level jet. Correction at various levels is required to go from the raw CaloJet measurements to go back to measurements unfolded from all detector effects.

The prior method of correcting the kinematic quantities of CaloJets back to GenJets on average at CMS has been a monolithic MCJet correction which is described elsewhere [70]. A more manageable approach would utilize factorized corrections which are intended to replace the MCJet approach. Early implementations of the factorized corrections are now available in the CMS software.

4.4 Corrections to Calorimetry Jets

Correction to the kinematic quantities of calorimeter jets is decomposed into (semi) independent factors applied in a sequential order. The levels envisaged so far are listed below and pictured in Figure 4.3 [71].

1. Offset: to take care of corrections for pile-up, electronic noise, and jet energy lost

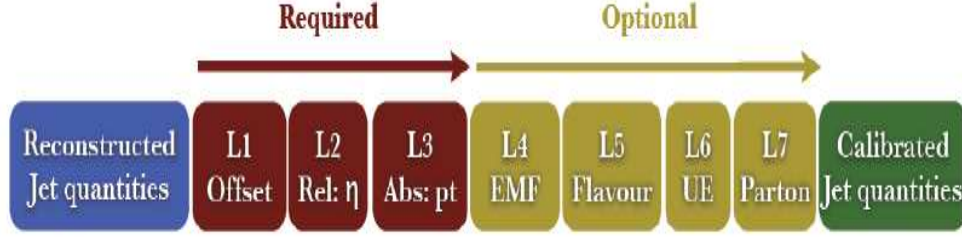


Figure 4.3: Schematic overview of the factorised multi-level jet correction in CMS. Starting with an uncalibrated calorimeter jet, several corrections are applied in a sequential order. In this scheme, required correction levels are indicated in brown boxes.

by thresholds;

2. Relative: correction for variations in jet response with pseudo-rapidity relative to a control region;
3. Absolute (p_T): correction to particle level versus jet p_T in the control region;
4. EMF: correction for variations in jet response with electromagnetic energy fraction;
5. Flavor: correction to particle level for different types of jet (light quark, c, b, gluon);
6. Underlying Event: correction for luminosity independent underlying event energy;
7. Parton: correction to the parton level.

Here the corrections are factorized to better understand the jet energy scale and to reduce the systematic uncertainty. In this approach each level is individually determined and understood. Systematic uncertainties can then be determined (semi) independently for each level, providing a better overall understanding of the origins of systematic uncertainty in the jet energy scale.

The Tevatron experiments found that factorization into multiple levels is needed in order to measure the jet energy scale using in-situ collider data [72, 73]. It allows to determine, refine and understand the corrections of the different levels almost independently. Additionally, systematic uncertainties can be investigated for each level, which yields a better understanding of the origins of systematic uncertainties on the jet energy scale.

In this context the first three levels are required whereas the remaining are optional corrections, offering calibrated jets according to the requirements of the final physics analyses. In addition, such a modular approach enables the jet energy calibration to evolve with time and the variable amount of data. With the beginning of data taking,

mainly MC driven methods will be applied, but with increasing statistics and an improved understanding of the detector, data-driven calibrations will become available.

4.4.1 Offset Correction

The primary goal of the level 1 offset correction is to subtract energy due to pile-up events and electronic noise from the jet energy. Here pile-up refers to additional proton-proton collisions, occurring close enough in time to the hard scattering such that the calorimeter response includes their effects in integrating the signal. Here electronic noise refers to any noise in the readout chain above the calorimeter tower thresholds which may be included in the jet energy computation. Both pile-up and electronic noise produce an energy offset which need to be subtracted from the energy measurement. The initial plan to estimate the level 1 offset energy is to measure it in the collision with zero-bias triggers (random trigger with two non-empty beam buckets).

The estimation of this offset energy is complicated by the cell thresholds in the presence of real energy. It will be easier for a CaloTower to pass the read out threshold in presence of pile-up and electronic noise. The zero suppression correction is designed to account for this effect and achieve greater precision in the estimation of the offset correction. The plan for measuring this correction with data, requires special runs without zero suppression (without thresholds) and measures the difference in jet energies with and without energy thresholds. This zero suppression correction will likely come later in the run, after the calorimeter pedestal subtraction, noise levels and channel to channel calibrations are stabilized.

4.4.2 Relative Corrections

The level 2 (η dependence) correction [70] aims at removing jet response variations in the CMS detector as a function of pseudo-rapidity. The goal is to make the jet response uniform at all η values. Figure 4.4(a) shows the results of a simulation of the CaloJet response before corrections, in which there are large variations as a function of jet η outside the barrel region. Figure 4.4(a) also shows that after level 2 corrections the jet response as a function of η becomes at the value expected in the barrel. This flattening of jet response is done using di-jet balancing method.

Estimates of the level 2 correction from Monte Carlo truth are already available [74]. This method will be eventually replaced with a data-driven method and will go through a closure test using MC information.

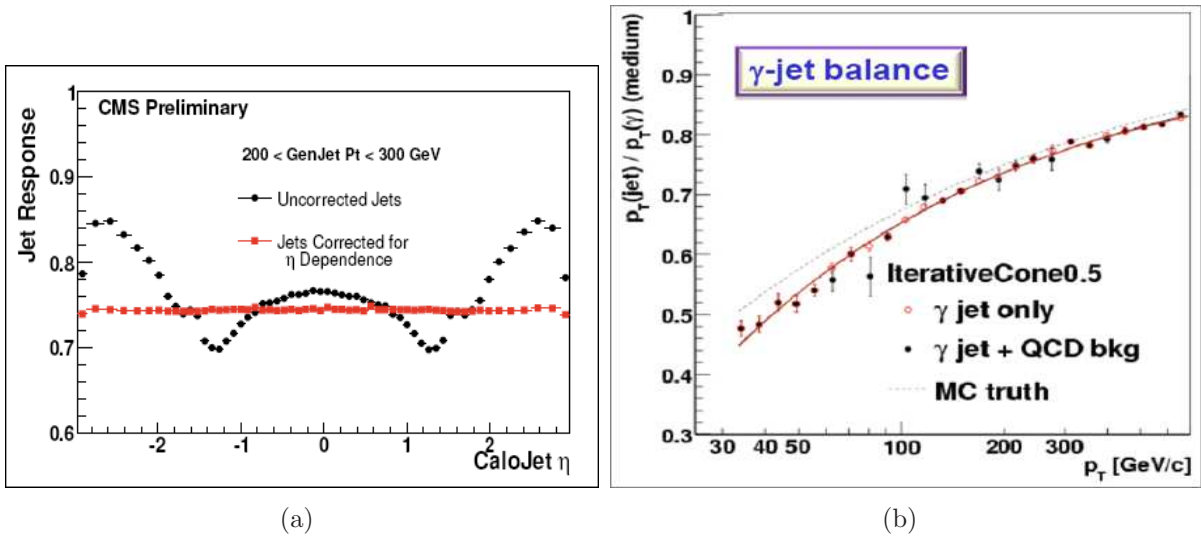


Figure 4.4: Relative and absolute corrections on calorimeter jets. (a) Calorimeter jet response as a function of pseudorapidity without (filled circles) and with corrections (filled squares). (b) Simulated calorimeter response to jets as a function of particle jet p_T .

4.4.3 Absolute Correction

The level 3 p_T dependent correction is to remove jet response variations in the CMS detector as a function of jet energy which primarily results from a non-linear response of the calorimeter. This correction is done by a data-driven method using $\gamma + \text{jet}$ and $Z + \text{jet}$ data sample [74] (Figure 4.4(b)). Here the jet p_T will be balanced with that of a high p_T γ or Z whose energy are well measured with the electromagnetic calorimeter or the muon detector.

4.4.4 Optional Corrections

In addition to the three levels of calibration discussed above, four optional corrections are envisaged in CMS and they are briefly mentioned below. A more detailed description can be found in [71].

4.4.4.1 Electromagnetic Energy Fraction

The response of the detector can be divided into the response for various types of particles and therewith in a separate response for the electromagnetic and the hadronic component of the shower. To improve the jet resolution, additional correction factors based on the fraction of the jet energy measured by the electromagnetic calorimeter (EMF) are envisaged to be applied after the calibration of the absolute jet energy scale. Up to now, MC calibration factors are available, and it has been demonstrated that improvements of the jet resolution between 5 percent and 10 percent are feasible.

4.4.4.2 Jet Flavour

The calorimeter response is different for jets originating from gluons, light or heavy quarks. Compared to the light quark jets, the calorimeter energy response for c and b jets is smaller due to difference in the jet fragmentation and presence of semileptonic decays of the heavy quarks. Gluon jets are broader as a result of the higher colour charge of the gluon. Especially analyses which are able to identify the flavour of a jet in the final state will benefit from such flavour specific correction factors on top of the required calibrations. These corrections are referred to as level 5 in the final approach and are currently estimated from Monte Carlo truth information.

4.4.4.3 Underlying Event

The optional level 6 calibration is designed to remove the energy offset of the jet coming from the underlying events. Conceptually, the underlying event is the component of the pp interaction that does not originate from the hard parton scattering and is assumed to be luminosity independent and uniformly distributed in an event. Although the underlying event depends on the details of the hard interaction, it is planned to provide a generic underlying event connection which can be used for all analyses. In the early data, this correction will be determined from the energy per jet area from minimum bias events at low energy after having subtracting the level 1 offset correction.

4.4.4.4 Parton Level

Several of the previously discussed calibrations correct jets back to particle jets. The parton level correction (level 7) attempts to correct these jets back to the properties of the original parton. This step will also be useful for the combination of available correction factors within one calibration to emphasize that this calibration level is model and process dependent and relies strongly on the MC generator.

4.5 Event Selection

Global event shape and multi-jets are studied by simulating a large sample of events using event generators based on QCD models and processing them through the entire simulation and reconstruction chain of the CMS detector.

4.5.1 Monte Carlo Sample

The MC sample used for this analysis consists of simulated QCD di-jet events at $\sqrt{s} = 10$ TeV pp collisions. They are produced in the context of the Summer08 official CMS

production with the PYTHIA 6.416 event generator using the DWT tune [75] in 21 \hat{p}_T bins. The PYTHIA event generator is based on leading order (LO) matrix elements of $2 \rightarrow 2$ processes matched with a parton shower to describe multi-jet emission due to initial and final state radiation. In the analysis the QCD multi-jet events consisting of the Standard Model processes $qq \rightarrow qq$, $gq \rightarrow gq$, $qq \rightarrow gg$, $gg \rightarrow qq$ and $gg \rightarrow gg$ are used (where q stands for a quark and g for a gluon). The events are generated within the range $0 < \hat{p}_T < 5000$ GeV/c, where \hat{p}_T is defined as the momentum of the exchanged parton in the LO matrix element. The events have been passed through a full GEANT4 [76] based simulation of the CMS detector. The generation is done in the CMS software version 2.1.7 and the reconstruction using 2.1.8 assuming the ideal detector conditions². The phase space range of each sample as well as the corresponding cross section and the number of events used, are summarized in Table 4.1.

Sample	\hat{p}_T (GeV)	σ (pb)	Events processed
QCDDijetPt0To15	0-15	5.156e10	101054
QCDDijetPt15To20	15-20	9.494e8	142560
QCDDijetPt20To30	20-30	4.010e8	87300
QCDpt30	30-50	9.47e7	2572317
QCDpt30	50-80	1.22e7	336481
QCDpt80	80-120	1.617e6	2770915
QCDpt80	120-170	2.56e5	439426
QCDpt170	170-230	4.83e4	2387128
QCDpt170	230-300	1.06e4	523027
QCDpt300	300-380	2.63e3	2224789
QCDpt300	380-470	7.22e2	707011
QCDpt470	470-600	2.409e2	2141797
QCDDijetPt600To800	600-800	62.492	28620
QCDDijetPt800To1000	800-1000	9.421	20880
QCDDijetPt1000To1400	1000-1400	2.343	24640
QCDDijetPt1400To1800	1400-1800	1.568e-1	27744
QCDDijetPt1800To2200	1800-2200	1.38e-2	22848
QCDDijetPt2200To2600	2200-2600	1.296e-3	22560
QCDDijetPt2600To3000	2600-3000	1.14e-4	22800
QCDDijetPt3000To3500	3000-3500	8.43e-6	20880
QCDDijetPt3500Toinf	> 3500	1.81e-8	34320

Table 4.1: Details of the MC samples used in the present analysis.

The distributions are obtained by summing the distribution from each bin with appropriate weight ($= \frac{\sigma}{N}$ where σ and N are cross section and number of generated events for the \hat{p}_T bin). The combined distribution is then scaled to give an integrated luminosity

²The exact string defining the samples in the CMS database book keeping system (DBS) is /QCDDiJetPt*to*/Summer08.IDEAL.V9.v*/GEN-SIM-RECO (exclusive \hat{p}_T bins) and /QCDpt*/Summer08.IDEAL.V9.v*/GEN-SIM-RECO (inclusive \hat{p}_T bins).

of 10 pb^{-1} with appropriate prescale factor.

4.5.2 Event Selection for Calorimeter Jets

The selection of hadronic events is based on the energy measured in the electromagnetic and hadron calorimeters. A particle can deposit its energy in more than one region. Energies deposited in the different regions are combined to determine energy of the particle.

Calorimeter jets are reconstructed using energy deposits in calorimeter towers (CaloTowers) as inputs. CaloTowers measure energies of both the charged and the neutral particles resulting from the hadronization of the partons. However, due to the strong magnetic field of the CMS detector, some of the low momentum charged particles will fail to reach the calorimeter. Also the charged particles will reach the calorimeter with a finite shift in the azimuthal direction which decreases with increasing p_T and this results a distorted measurement of the jet direction.

4.5.2.1 Event Clean-up

In data, in addition to jets from the hard scattering of beam protons, large calorimetric signals originating from noise, beam halo energy deposits or cosmic ray showers will also be observed. All such sources of noise and non-collision deposits or cosmic ray showers will also be observed. All such sources of noise and non-collision data can produce large amounts of transverse energy E_T that is not balanced by any partner in a physical scattering process and that appears as so-called missing E_T (MET). Since imperfect detector calibrations may lead as well to missing E_T in otherwise well-balanced collision events, MET is usually compared to the scalar sum of all transverse energies (ΣE_T). So in order to remove the strongly affected and therefore unbalanced events we plan to impose an upper limit on the relative missing E_T : ($MET/\Sigma E_T$). Figure 4.5 shows the distribution of this quantity in QCD simulated events and in CRAFT [77] data. Typically, real collision events give rise to low $MET/\Sigma E_T$ values (due to finite jet resolution) while noise events are maximally unbalanced in the transverse plane and lead to high $MET/\Sigma E_T$ values. The optimal value for $MET/\Sigma E_T$ has already been studied for QCD samples [78]. It has been shown that for events with jets with high transverse momenta (for example, events with leading jet $p_T > 100 \text{ GeV}/c$) the cut $MET/\Sigma E_T < 0.3$ becomes more than 99% efficient.

4.5.2.2 Trigger Selection

The jet clustering algorithm used at the trigger level is the Iterative Cone algorithm (with radius $R = 0.5$). Table 4.2 summarizes the transverse energy thresholds and the expected

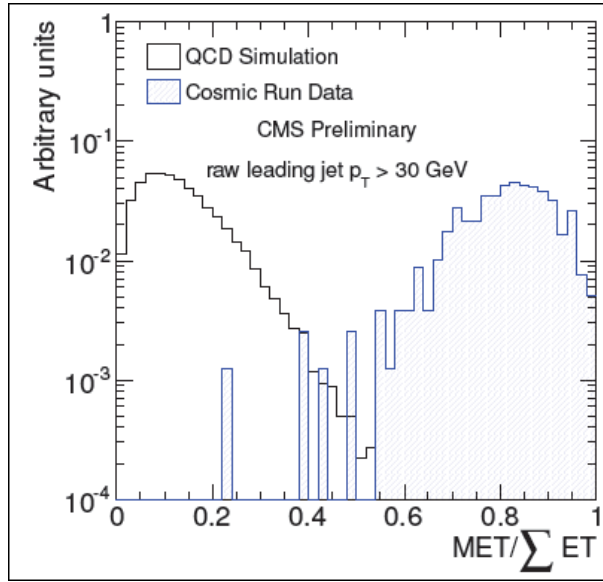


Figure 4.5: Distribution of the $\text{MET}/\Sigma E_T$ for simulated QCD events and the Cosmic data.

Sample	HLT15	HLT30	HLT50	HLT80	HLT110	HLT180
MC prescale	500×20	500×5	50×1	5×2	1×1	1×1

Table 4.2: Trigger table proposed for $L = 10^{31} \text{ cm}^{-2} \text{ s}^{-1}$.

prescale factors for the various triggers. The expected prescale factors are given for the luminosity condition: $L = 1 \cdot 10^{31} \text{ cm}^{-2} \text{ s}^{-1}$.

	Prescale	No. of events passing selection	After prescale
HLT50	50	6675995	133519
HLT80	10	6670639	667064

Table 4.3: Number of events passing the prescale for two HLT trigger paths.

The analysis with multi-jets depends strongly on the choice of triggers. This analysis is chosen to be performed with a single jet trigger as it will provide enough data for these measurements. The events are chosen based on HLT80 as a single jet trigger as it has a small prescale value (10) and with an instant luminosity of $L = 10^{31} \text{ cm}^{-2} \text{ s}^{-1}$. it will take a few weeks to accumulate 10 pb^{-1} data. Table 4.3 shows that the HLT80 trigger path allows more number of events in this trigger menu than HLT50, given the prescales. The inefficiency of that single jet trigger is quantified in Figure 4.6 where the turn on curve for HLT80/HLT50 indicates an offline threshold of 110 GeV to be put on the leading jet p_T for the trigger to become more than 99% efficient.

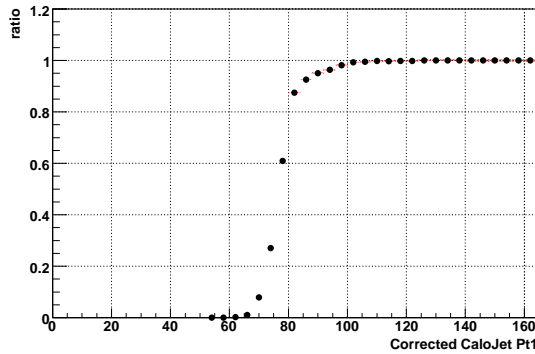


Figure 4.6: Turn on curve in the efficiency plot as a function of p_T of the most energetic jet in the HLT trigger menu HLT80.

4.5.2.3 Offline Selection

After the beam clean-up and trigger selection, all the jets are required to have their $p_T > 50$ GeV/c and lie within a pseudo-rapidity range of $|\eta| < 3$ which includes the barrel and the endcap calorimeters.

4.5.3 Event Selection for TrackJets

CMS has an excellent tracking detector which is capable of measuring trajectories of charged particles in a rather dense environment. At the same time the tracks could be associated to the corresponding primary vertices. Thus they are not as badly influenced at higher luminosities with a larger pile-up condition. So it may be worthwhile to look for jets constructed using the tracks only. This will also provide an independent method of jet reconstruction. Calorimeter and track jets not only carry independent information, they also have independent systematic uncertainties. In view of this, measurements using TrackJets are looked into.

4.5.3.1 Track Selection

Figure 4.7 shows p_T distribution of all reconstructed tracks and also the number of valid hits in the reconstructed tracks. The tracks for jet reconstruction are selected according to the following quality criteria:

- number of crossed tracker layers $n_i > 7$
- normalized fit $\chi^2 < 100$
- transverse momentum $p_T > 0.9$ GeV/c
- angular acceptance to match with tracker coverage ($|\eta| < 1.3$).

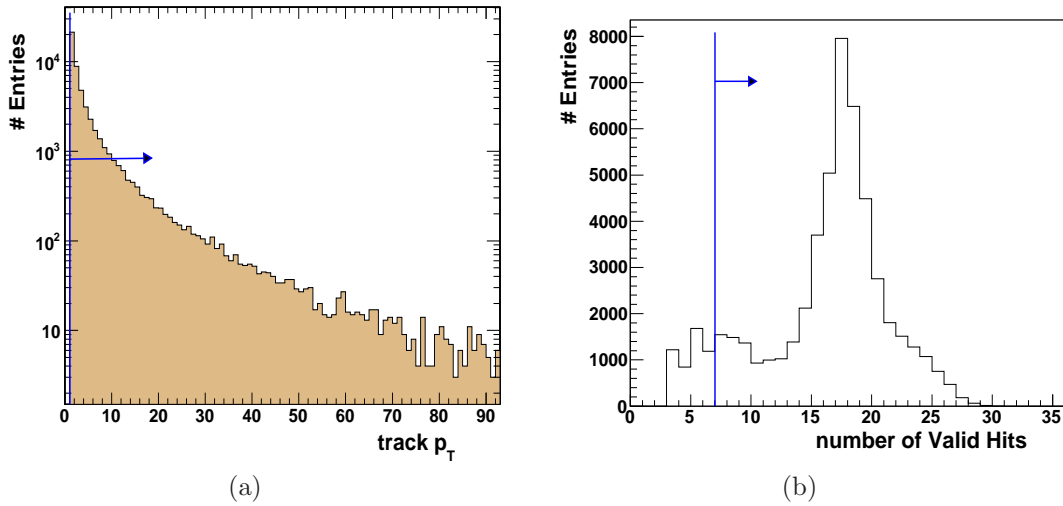


Figure 4.7: Distribution of (a) p_T and (b) number of valid hits of charged tracks. The accepted regions are shown with arrows.

4.5.3.2 Jet reconstruction from charged tracks

The jets are reconstructed using the iterative cone algorithm where the cone size parameter is set to $R = 0.5$. The same Jet clustering algorithm is applied on the following inputs:

- Selected tracks (TrackJets)
- Calorimeter Towers (CaloJets)
- Generated stable particles (Genjets): jets of all stable particles
- Generated stable charged particles (ChargeGenjets): jets of all charged stable particles.

Charged particles represent the jet component that is measured best both in terms of energy resolution and of angular direction which is well determined at the interaction point. The nominal CMS tracking momentum resolution is

$$\frac{\Delta p_T}{p_T} = 0.2 \cdot 10^{-3} \frac{p_T}{GeV/c} \pm 0.01$$

that should be compared to the hadronic calorimeter energy resolution which is

$$\frac{\Delta E}{E} = \frac{1.2}{\sqrt{E(GeV)}} \pm 0.07$$

From these formulae it can be inferred that the tracking momentum measurements are better than the calorimeter measurements for particles with energies up to several hundreds of GeV. Moreover the direction of charged particles at the interaction point is extremely well determined by the track reconstruction with resolutions $\Delta\phi \sim \Delta \cot\theta \sim 10^{-3}$.

For these reasons one can expect the charged tracks picture of a multi-jet event to be cleaner than the CaloTower picture with more collimated true jets, with less overlap and interference, and less background (*e.g.* pile-up events).

Also jet finding with charged tracks only is completely independent from jet finding with CaloTowers and is an excellent alternative way to find/count jets, and determine their directions.

4.5.3.3 Trigger selection

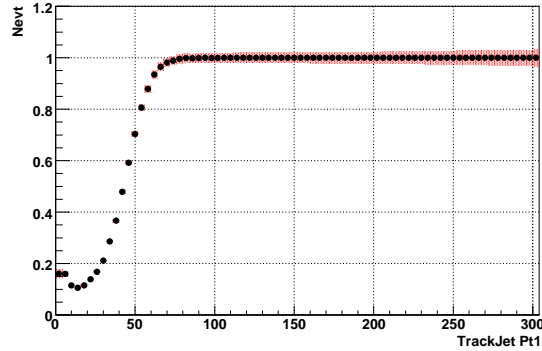


Figure 4.8: Turn on curve in the efficiency plot as a function of p_T of the most energetic TrackJet in the HLT trigger menu HLT80.

The leading jet threshold for the jets from charged tracks are determined in similar fashion as it is measured for calorimeter jets. The inefficiency of a single jet trigger (HLT80) is quantified in Figure 4.8 where the turn on curve for HLT80/HLT50 indicates an offline threshold of 80 GeV/c on leading jet p_T will make the trigger more than 99% efficient.

4.5.3.4 Offline selection

After the beam clean-up and trigger selection, all the jets from charged tracks are required to have their $p_T > 25$ GeV/c and lie within a pseudo-rapidity range of $|\eta| < 1.3$ which is up to the barrel.

Chapter 5

Test Beam Experimental Setup

5.1 Introduction

A slice of the CMS calorimeter, including prototypes of the Hadron Calorimeter (HCAL) and the Electromagnetic Calorimeter (ECAL) is exposed to the test beams at CERN in the North H2 [79] experimental area. The response of the calorimeter is measured over a wide range of momentum of the hadrons, mainly pions from 2 GeV/c to 300 GeV/c.

A detailed description of the experimental setup, the methods used for particle identification using the beam line elements and the procedure to calibrate the detector are discussed in this chapter.

5.2 Experimental Setup

5.2.1 TB2006 Calorimeter Setup

The setup of the calorimeter modules in the 2006 test beam (TB2006) experiment is shown in Figure 5.1. This experimental setup consists of the barrel hadron calorimeter (HB), the barrel electromagnetic calorimeter (EB) and the outer hadron calorimeter (HO). Measurements are performed with production module of EB, final design modules of HB and HO, and front-end electronics as in the final CMS detector configuration. A special beam line is constructed to measure calorimeter response down to 2 GeV/c.

Figure 5.1 shows a photograph of the moving platform that held two HB wedges plus a production EB super module which is placed in front of the HB, and the HO behind the HB. The HE module seen on the platform is not used in this test. The placement of the components is in the same geometric relationship as in the CMS experiment. The two-dimensional movement of the platform in the η and ϕ directions allows the beam to be directed onto any tower of the calorimeter mimicking a particle trajectory from the interaction point of the CMS experiment. Four scintillation counters are located three

meters upstream of the calorimeters and a coincidence among a subset of the counters is used as the trigger.

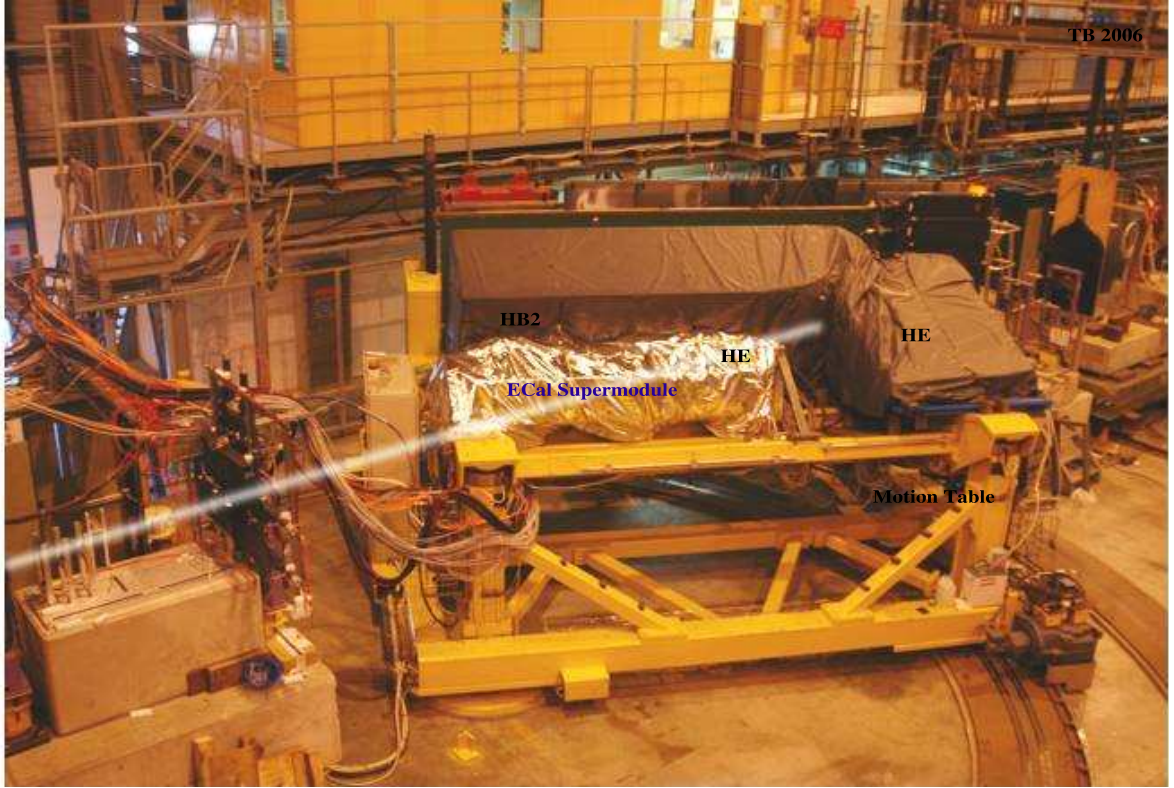


Figure 5.1: Calorimeter setup in the 2006 test beam.

The two HB wedges used during the 2006 test beam experiment are configured somewhat differently:

- HB1 : The configuration of the HB1 module is the same as the one used in the 2004 test beam setup, *i.e.* summing up the the light output of all the 17 scintillator layers optically while keeping the lateral segmentation in η and ϕ in tact.
- HB2 : The readout of the second wedge is configured to study the longitudinal development of the shower. one of the ϕ slices ($i\phi = 5$) is read out with a configuration similar to HB1. For the remaining ϕ slices, each of the 17 layers is read out individually by summing up the light output from five η towers between $i\eta = 5$ to $i\eta = 9$.

The first active layer of HB is made of a scintillator which is 1.5 times brighter than the rest of the scintillators and is 10 mm thick. Since this layer is read out together with all other layers to make a readout tower, external light attenuators are used to bring the light output from this layer down to the level of that from other layers.

One sector of the outer hadron calorimeter (HO) is installed in three rings of the calorimeter setup. Every sector has 6 trays in ϕ . Only selected towers of HO are read out

electronically. There are blocks of aluminium and iron between HB and HO to mimic the CMS magnet.

5.2.2 TB2007 Calorimeter Setup

The setup of the calorimeter modules in the 2007 test beam (TB2007) experiment is shown in Figure 5.2. The 2007 test beam setup includes 3 calorimeters - HE (hadronic), EE (electromagnetic) and ES (preshower). For the preshower detector, it is the first time that a complete read out chain is made which has on-detector, off-detector integrated into the main CMS DAQ system (for the combined beam test), DQM (Data Quality Monitoring) and DCS (Detector Control System).



Figure 5.2: Calorimeter setup in the 2007 test beam.

HE Configuration

One prototype wedge of the HCAL endcap is installed and tested in the TB2007 experiment. The configuration of the HE prototype module used is slightly different from the nominal one used in the CMS experiment. The layer 0 of a standard module of HE is absent in the prototype, shown in Figure 5.3. The nose structure at $i\eta$ tower 18 is also absent in the prototype module. Only the towers from $i\eta = 16$ to $i\eta = 25$ are present in the prototype module while HE extends up to $i\eta = 29$ in the final HE module. The active layers of HCAL endcap are grouped into two or three longitudinal segments. The difference in the read out configuration between the prototype and a nominal endcap module in the CMS detector is shown in Figure 5.3. There is also a small difference in ϕ grouping

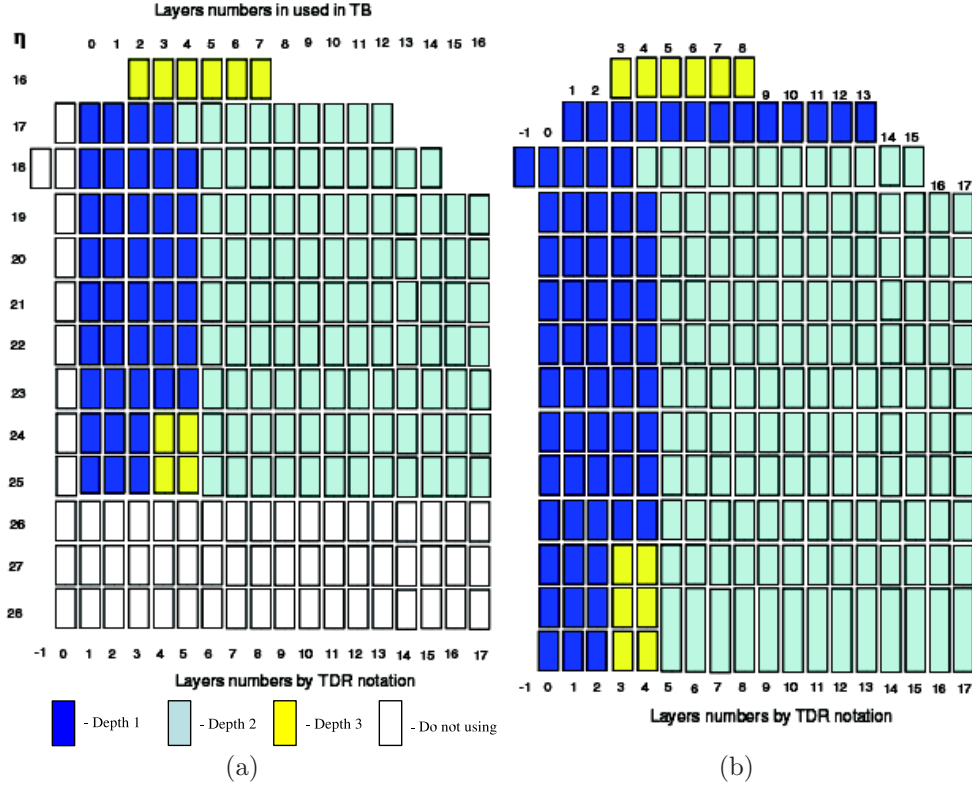


Figure 5.3: The grouping scheme of layers to depths of the HE modules used in the (a) test beam setup and (b) in the CMS setup.

between the prototype and the nominal module for the tower $i\eta = 21$. The nominal one has a width of 10° while the prototype uses a width of 5° for this tower.

ECAL Configuration

EE

In the 2007 experimental setup, four super-crystals of ECAL are installed in front of the HE wedge. Each super-crystal contains 25 crystals (5×5). Each crystal of the super-crystal is read out using a pair of VPTs mounted on its rear face (Figure 5.4).

ES

The preshower detector used in the test beam has two orthogonal layers of silicon strip sensors positioned behind two planes of lead absorbers (Figure 5.5). Each Silicon sensor measures $63 \times 63 \text{ mm}^2$, with an active area $61 \times 61 \text{ mm}^2$ divided into 32 strips (1.9 mm pitch). The nominal thickness of the silicon is $320 \mu\text{m}$. The thickness of the two absorbers are nominally $\sim 2 X_0$ and $\sim 1 X_0$. The preshower prototype has 1024 channels of real electronics.

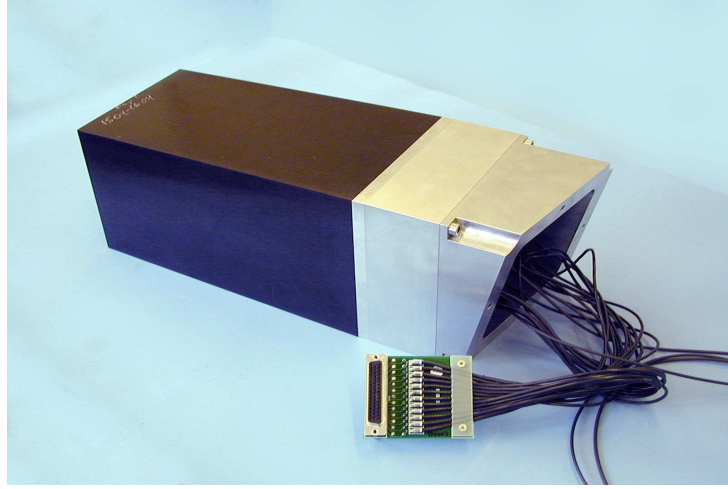


Figure 5.4: EE super-crystal as used in the 2007 test beam.

Motion Table

The whole calorimeter setup is mounted on a table which can move along the horizontal (along η) as well as the vertical direction (along ϕ). The table is designed in such a way that its pivot mimics the interaction point of the real CMS detector. The beam coming through the pivot appears as if it is coming from the actual interaction point. The two dimensional motion of the table makes it possible to centre the beam at various $\eta - \phi$ locations of the detector with respect to the pivot point (the CMS interaction point).

5.2.3 Electronics and Data Acquisition

The photo electrons produced at the photo-cathode of the HCAL read out device are accelerated by an electric field set at 8 kV. The gain of the Hybrid Photo Diode (HPD) is ~ 1600 at this setting of high voltage. Each HPD registers signal from η towers of ϕ slice. The analog signal from a HPD is digitized using a non-linear multi-range analog-to-digital converter in the charge integrating electronics (QIE) circuit. The HPD along with the QIE chip is housed in a Readout Module (RM). Four RMs are enclosed in a Readout Box (RBX). One such readout box is mounted at the end of η tower of each wedge. The digital electronics modules used for TB2007 experiments are production versions running at a clock speed of 40.079 MHz. The optical decoding units (ODUs) in the readout boxes of HB2 are replaced with special units to read each scintillator layer individually.

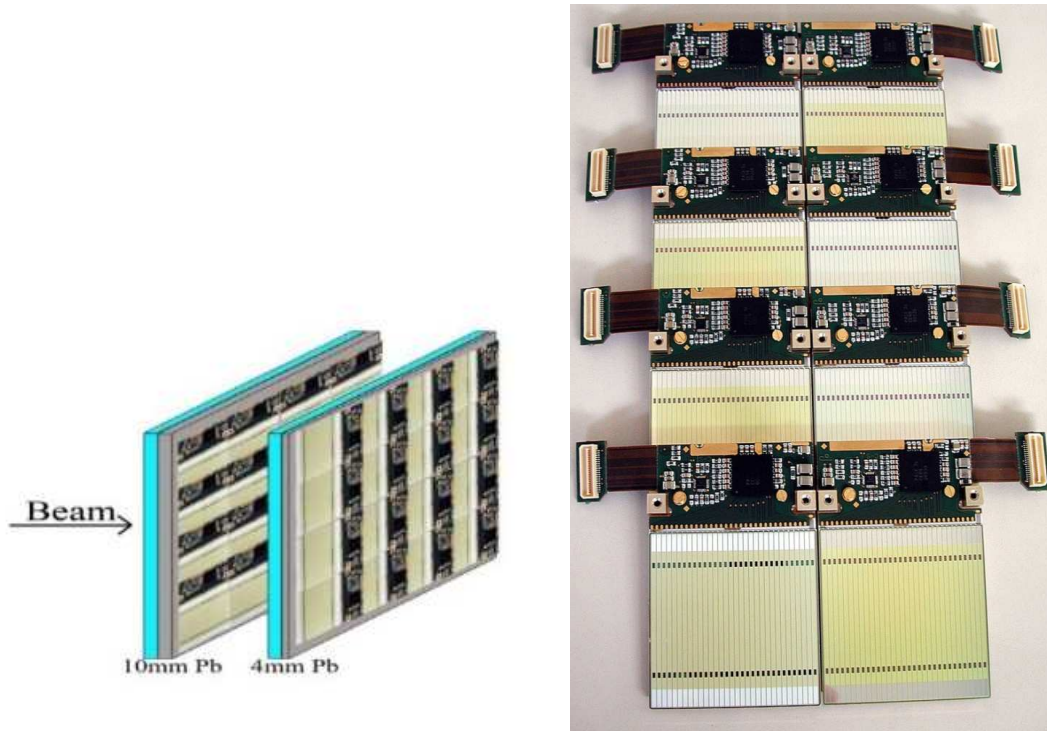


Figure 5.5: The two planes of the preshower detector and an ES ladder as used in the 2007 test beam.

5.3 H2 Beam Line

Figure 5.6 schematically depicts the CERN H2 beam line. The beam line is designed to operate in two distinct modes. In the high energy mode, various particles are produced when 450 GeV/c protons from the Super Proton Synchrotron (SPS) [80] strike a production target (T2) 590.9 m upstream of the calorimeters, and particles with momenta between 15 GeV/c and 350 GeV/c are transported to the calorimeter setup. In the very low energy (VLE) mode, an additional target (T22) located 97.0 m upstream of the calorimeter is used for particle production and the momenta of particles are limited to 9 GeV/c. As shown in Figure 5.6, a dog-leg configuration is utilized for the momentum selection of these low momentum particles. In the high energy mode, the T22 target and the VLE beam dump are removed from the beam line.

The particles with different momenta bend differently while traversing a dipole magnetic field. Therefore a beam of particles with given momenta can be selected by allowing only these particles through a slit and stopping the rest using thick absorbers. The setup used to derive the secondary beams H2 and H4 [79], is known as the T2 Wobbling Station. The direction of the incidence of the primary proton beam on the target is governed by bending magnets. The maximum usable beam momentum is 100 GeV/c for electrons and 350 GeV/c for hadrons.

In the VLE mode, two Cerenkov counters (CK2 and CK3), two time-of-flight counters (TOF1 and TOF2) and muon counters [Muon Veto Wall (VMW) of $100 \times 240 \text{ cm}^2$, Muon Veto Front (VMF) of $80 \times 80 \text{ cm}^2$ and Muon Veto Back (VMB) of $80 \times 80 \text{ cm}^2$] are used to tag electrons, pions, kaons, protons, anti-protons and muons.

The original H2 beam line is most efficient for the transportation of medium to high energy particles. The low energy pions, however, decay in flight before reaching the calorimeter modules. For example, 67% of 9 GeV/c pions would decay in flight before reaching the calorimeter modules installed $\sim 583 \text{ m}$ downstream the T2 target. In the year 2004, the beam line is modified to run with an additional target, T22, which is installed 493 m downstream to target T2 ($\sim 90 \text{ m}$ upstream the calorimeter system). Additional bending magnets and focusing elements are installed to derive well defined tertiary beams of momentum 2-9 GeV/c from the particles produced at T22 using 80 GeV/c pions produced at the target T2. A schematic of the VLE beam path is shown in Figure 5.7.

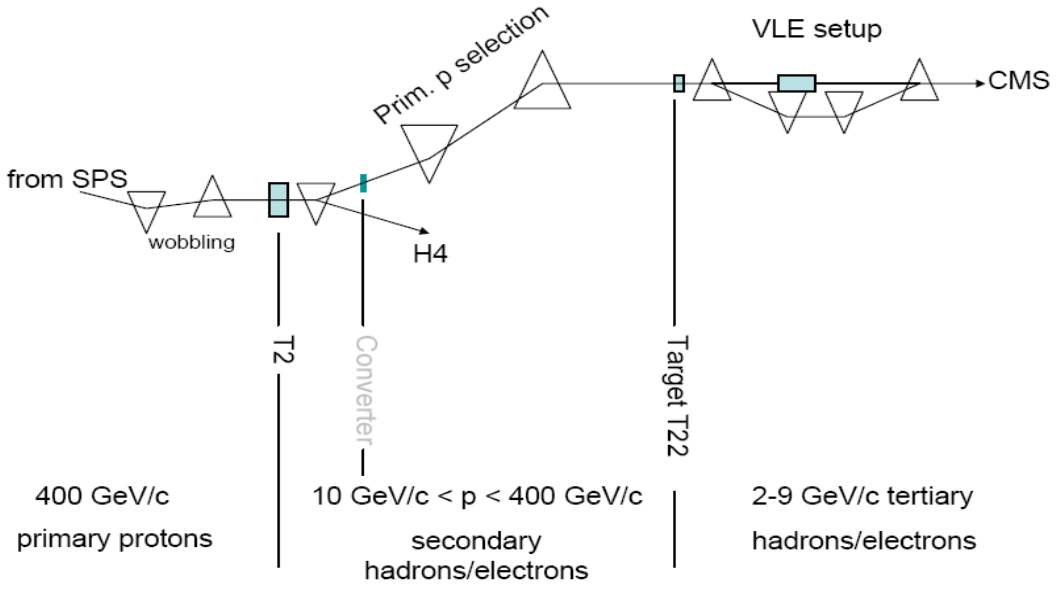


Figure 5.6: A Schematic diagram to show the location of secondary target T22 and the VLE beam line.

5.4 Beam Line Counters and Particle Identification

5.4.1 Beam Line Counters

Several detectors are employed in the beam line to monitor and adjust the steering and focusing of the beam.

- Differential Cerenkov counters with Achromatic Ring focus are employed in H2 main beam line to obtain particle identification. It is a 3.88 m Cerenkov counter filled with helium at a maximum pressure of 15 bar. The working principle is based on the fact that the direction of Cerenkov light produced by a particle depends upon the velocity of the particle ($\beta = \text{velocity}/c$) for a given refractive index (n) of the medium.

$$\cos \theta = 1/n\beta$$

The differential counter is equipped with an optical system to focus this light to give a ring image. The diameter of the ring depends on the mass of the particle traversing the medium. The light so produced is detected using photo multiplier tubes (PMT).

- Scintillator filaments are used to study beam profiles. These are mobile scintillator filaments of 200 microns width and 4 mm thickness (along beam). The light produced by the particles traversing these scintillators is collected by two photo-multipliers in coincidence.
- Scintillator counters of 10 cm diameter and 4 mm thickness are employed for flux measurement and beam tuning.
- Multiwire proportional chambers are installed at various positions in the beam line to measure beam profiles integrated over a full burst. These counters have a wire spacing of 1 mm and a sensitive area of $10 \times 10 \text{ cm}^2$. However, based on the cabling, only every second or third wire can be read out, thus limiting the effective wire spacing to 2 or 3 mm.
- Delay line wire chambers are used to measure the beam profile. These chambers provide a measurement of the impact point in horizontal as well as vertical directions. Three wire chambers (A, B and C) are installed in front of the calorimeter prototype and two chambers (D and E) are installed further downstream.

5.4.2 Beam Cleaning

In the high energy mode of the beam line, data are taken mainly with negative beams. In this mode, there is hardly any anti-proton contamination. If the beam line is configured for positive particles, at very high momenta, *e.g.* 300 GeV/c, the beam consists almost purely of protons.

The particle content depends on the momentum. At the higher end, pions dominate. At lower momenta, the beam consists mostly of electrons. The hadron part of the beam, though dominated by pions have presence of kaons and protons as well. The information

from some of these beam line detectors like the wire chambers, scintillators and Cerenkov counters are used for cleaning up the beam. There is an additional set of detectors which is installed for an efficient particle identification, especially at low energies where beam contamination is not negligible. The position of the various detectors used for the particle identification and the beam cleaning is shown in Figure 5.7.

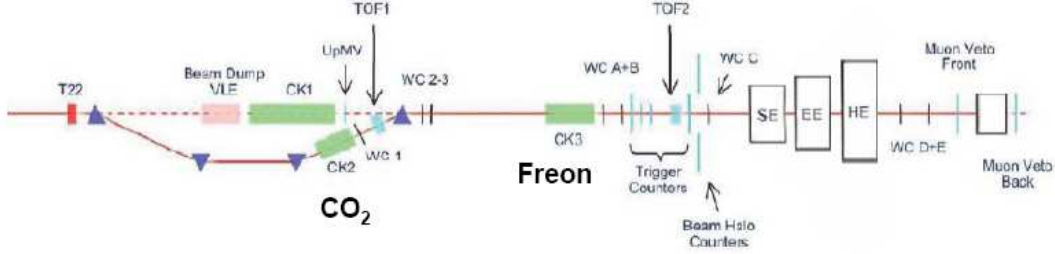


Figure 5.7: A schematic view of beam line elements showing the location of detectors used for beam cleaning and particle identification.

Trigger Scintillators

The beam trigger is established by the coincidence of the trigger scintillator counters. There are four scintillators S1 ($14 \times 14 \text{ cm}^2$), S2 ($4 \times 4 \text{ cm}^2$), S3 ($2 \times 2 \text{ cm}^2$) and S4 ($14 \times 14 \text{ cm}^2$) which can be combined to get beam profiles of $14 \times 14 \text{ cm}^2$, $4 \times 4 \text{ cm}^2$ or $2 \times 2 \text{ cm}^2$. Figure 5.8 shows pulse height distributions for all the four scintillators. The shaded parts of the distributions show the pedestals. A combination of $S1 \cdot S2 \cdot S4$ or $S1 \cdot S3 \cdot S4$ is used to select the window of incident particles (4×4 or 2×2 respectively).

A typical pulse height distribution of signals in S4 is shown in Figure 5.9. The peaks corresponding to multiple particles traversing the scintillator are clearly resolved. Such events are indication of interactions in the beam line and are rejected in the offline analysis on the basis of signal in S4 which is the nearest one to the calorimeter (2.78 m from the pivot point).

Beam Halo Counters

Beam Halo (BH) counter is an arrangement of four scintillators, each of $30 \times 100 \text{ cm}^2$ making a hole of $7 \times 7 \text{ cm}^2$ around the beam line. This arrangement is installed at a distance of 2.62 m from the pivot point and is used to veto beam halo and the wide-angle secondaries produced in the beam line interactions. Figure 5.10 shows QADC distributions for the four beam halo counters. The shaded histograms correspond to the pedestal distributions. In order to veto out muons or other beam halo particles a threshold is chosen at the boundary of the pedestal distribution.

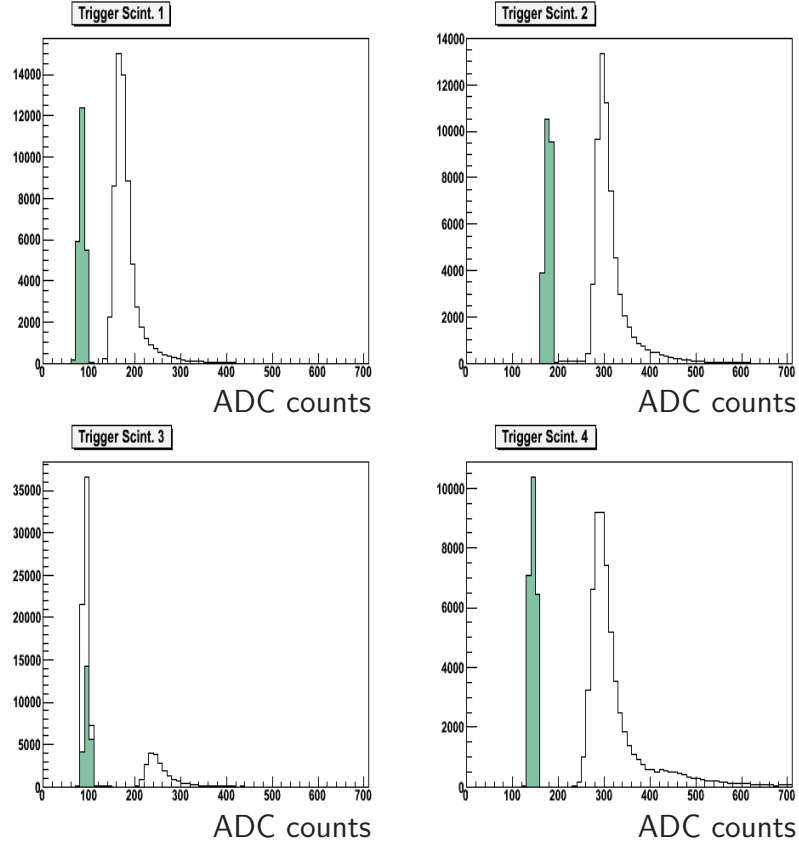


Figure 5.8: Pulse height distributions in the four trigger scintillators, S1-S4. Shaded histograms show the pedestal events.

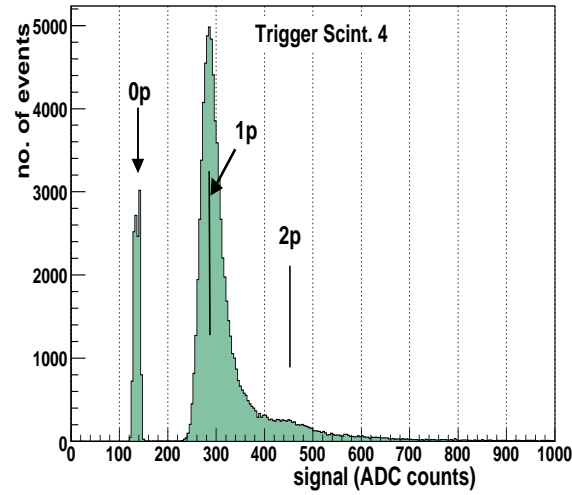


Figure 5.9: Signal distribution for the trigger scintillators, S4, which is closest to the calorimeter. The peaks showing multi-particle events.

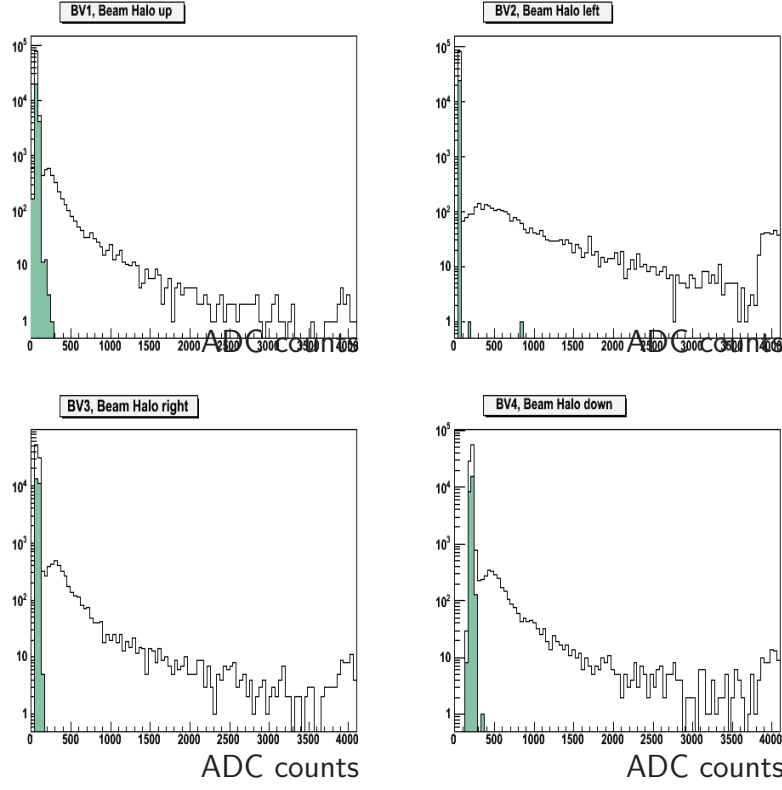


Figure 5.10: Pulse height distributions in the beam halo counters. Shaded histograms show the pedestal events.

Wire Chambers

Three wire chambers (WC) installed at a distance of 2.0 m (WC-C), 4.04 m (WC-B) and 5.14 m (WC-A) from the pivot point are used to determine the position of the particles in horizontal and vertical planes transverse to the beam direction. These chambers use a delay line and the anode wires to produce a two-dimensional measurement of position of a particle traversing each of the two chamber planes with a resolution of $\sim 350 \mu\text{m}$ in any of the directions. One end of each anode wire in a plane is electrically coupled to a location to produce a direct anode signal (A). When the ionization avalanche of a traversing particle produce signal on an anode wire, the coupled pulse is split and travels to the two ends of the delay line (R & L). By recording the time of the signals, position along the delay line is given as

$$d = (R-A) - (L-A) = R - L \text{ (in units of time)}$$

This time difference is converted to the distance using a slope and offset determined by the chamber calibration. Beam profiles (reconstructed hit position y vs x) for a 100 GeV/c and 5 GeV/c momentum tunes are shown in Figure 5.11 for WC-C. Clearly at higher energies, the beam is more focused. The red points represent the combination $S1 \cdot S2 \cdot S4$ (4×4) and black points represent $S1 \cdot S3 \cdot S4$ (2×2). At higher beam energies sufficient particle/spill can be obtained even using 2×2 window but for low momenta a broader

window 4×4 is chosen to ensure sufficient particles/spill.

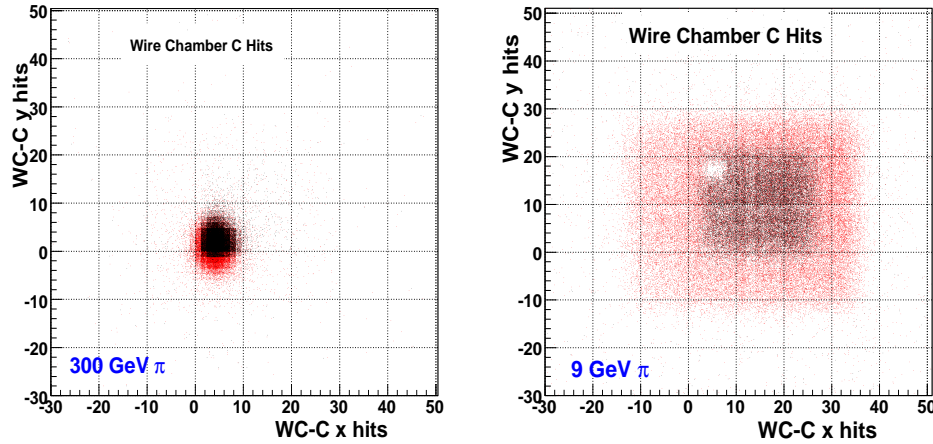


Figure 5.11: Beam profiles measured by wire chamber C for 300 GeV/c and 30 GeV/c negative beam during 2007. Black points show the trigger selection of S1·S3·S4 and red points show a trigger selection of S1·S2·S4.

5.4.3 Particle Identification

Identification of particles in a beam is performed using Muon Veto counters (VM), Cerenkov counters (CK2 and CK3) and Time-of-Flight (TOF) system.

Muon Veto Counters

The muon veto counters, the VMFront and the VMBack, are 80×80 cm² scintillators located behind the calorimeter. The VMBack is shielded by a 80 cm thick block of iron. Only the shielded VMBack is used to tag muons in high energy beam tunes to ensure that the late starting showers are not tagged. Figure 5.12 shows the distribution of signal and pedestal (shaded) for a pion beam of momentum 150 GeV/c. For high momenta particles only VMB is used for vetoing muons out but for lower momenta VMF is also used along with VMB. When tested with a pure muon beam at 225 GeV/c the efficiency of muon rejection was found out to be better than 99%.

Cerenkov Counters

CK2 and CK3 are threshold Cerenkov counters installed in the beam line to identify the particles in various momentum ranges by varying the gas pressure. The refractive index (n) of a gas depends on the pressure and velocity of light in medium is c/n . So the pressure of the gas can be adjusted such that velocity of particles of a given mass is greater than speed of light in the medium and thus allowing them to produce Cerenkov light while

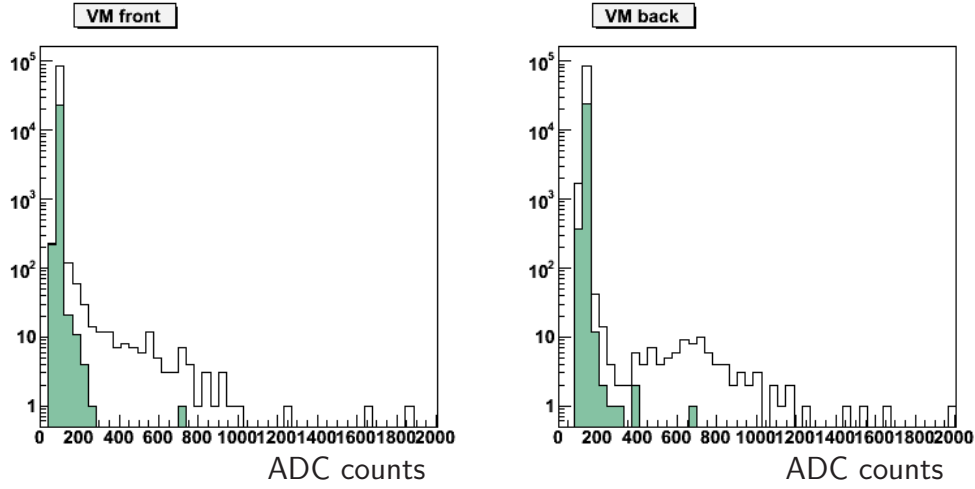


Figure 5.12: Pulse height distributions in the front and back muon veto counters used to tag muons coming from primary beam line.

traversing the gas. The Cerenkov counter CK2 is a 1.85 m long counter filled with CO₂ at 0.35 bar. This is used to identify electrons in the VLE mode. No other particle gives a signal at this pressure and the efficiency of the counter is measured to be better than 99% in identifying electrons.

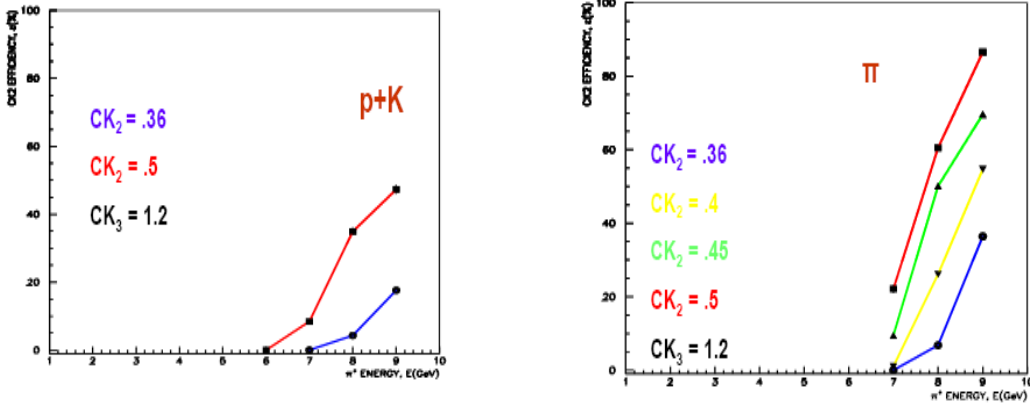


Figure 5.13: Efficiencies of the Cerenkov counters at different pressures for hadrons (proton, kaon and pion) at different energies.

The Cerenkov counter CK3 is also 1.85 m long and it is filled with Freon134a. The pressure is maintained at 0.88 bar when used in the beams with momentum below 3 GeV/c to double-tag the electrons. At higher beam momenta (> 4 GeV/c), the pressure in CK3 is set to 1.2 bar in order to separate pions from kaons and protons. Figure 5.14 shows the signals in CK2 and CK3 with 5 GeV/c beam particles. The CK2 is triggered when an electron passes through and the CK3 triggers when a pion or an electron passes through. The remaining particles are anti-protons and kaons which are distinguished by time-of-flight system described in the next section.

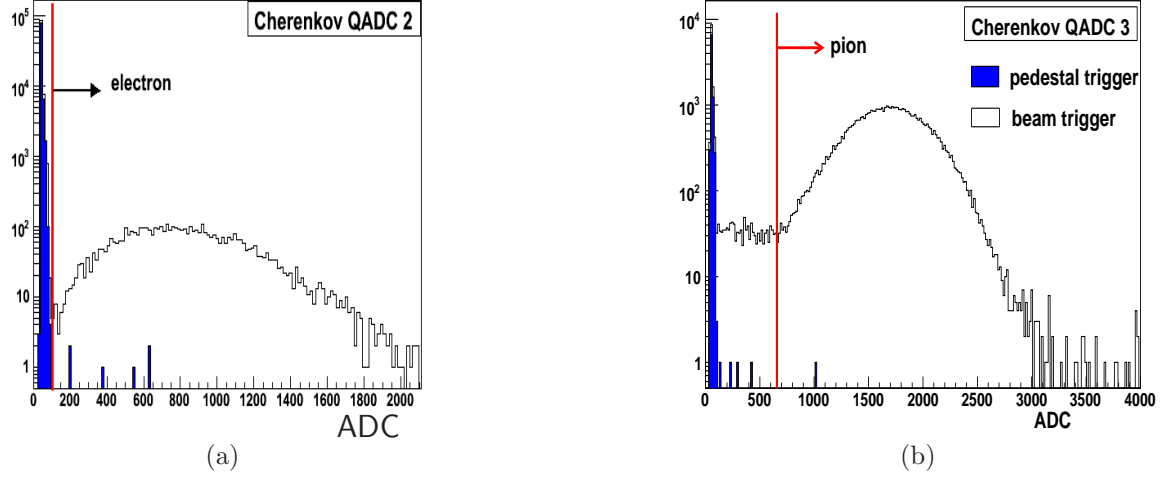


Figure 5.14: Signals in (a) CK2 (used to identify electrons) and (b) CK3 used to distinguish pions from kaons and protons above 5 GeV/c particles.

Time of Flight Detector

The Time-of-Flight detector system consists of two scintillators TOF1 and TOF2, each being $10 \times 10 \text{ cm}^2$ in area and 2 cm in thickness. The scintillation light produced is guided using trapezoidal shaped air-core light guides to the fast photomultiplier tubes mounted on the either side of the scintillators. The analog pulses are discriminated by constant fraction discriminators.

Calibration of Time of Flight Detector

Figure 5.15 shows the time of flight spectra at four different beam momenta. A comparison of the spectra for positive and negative beam runs shows that the peak positions vary by 3 TDC counts approximately. This indicates the possibility of an offset. For the runs where there is a clear separation between protons and pions, the difference between the two peaks is found to remain similar for positive and negative beam runs.

Converting TDC Information to Time

For those runs with clearly separated peaks the time difference (TDC counts) ($d\tau$) for proton and pion is noted. The differences in inverse of velocities for proton / pion is also calculated. The mathematical relation to calculate time difference given the velocities of proton and pion is given below:

$$\begin{aligned}
 d\tau &= \frac{L}{v_\pi} - \frac{L}{v_p} \\
 &= L \left(\frac{1}{v_\pi} - \frac{1}{v_p} \right).
 \end{aligned} \tag{5.1}$$

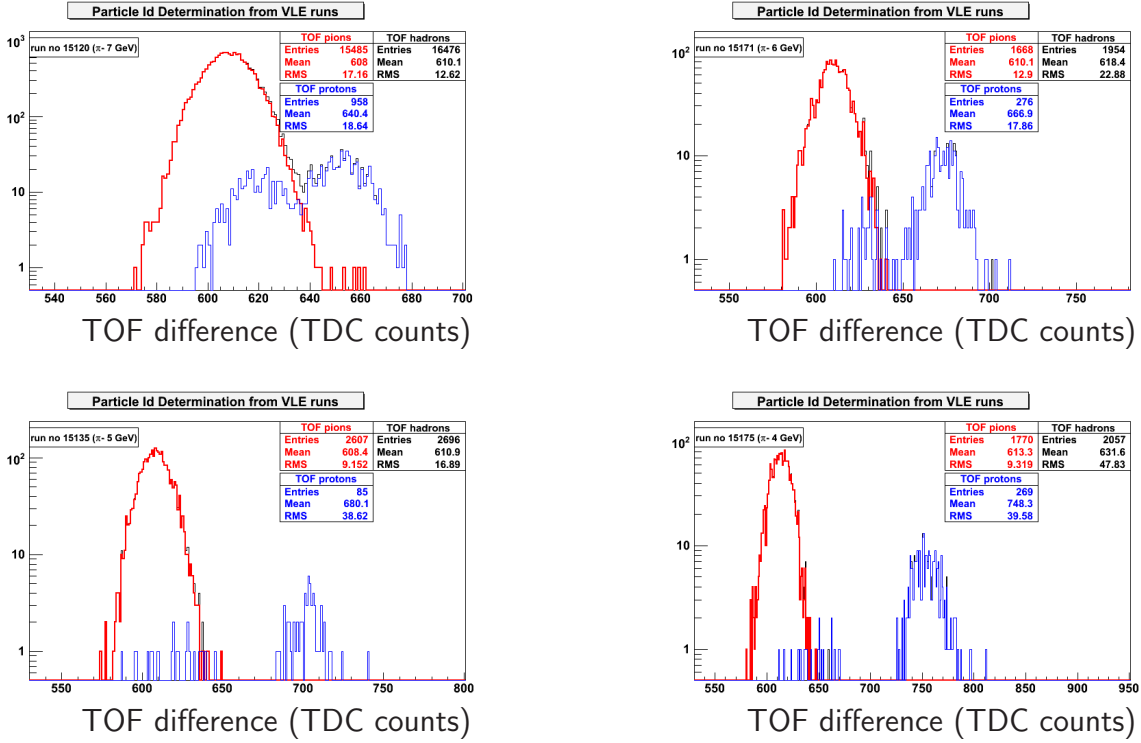


Figure 5.15: Time of flight measurement for four sets of data: 6 GeV/c π^- , 6 GeV/c π^+ , 4 GeV/c π^- and 4 GeV/c π^+ . Red lines represent possible pion candidate and blue lines correspond to a possible mixture of kaon and proton.

The difference in time flight ($d\tau$) in units of TDC counts is plotted in Figure 5.16(b)) as a function of the difference of the inverse velocities of the two particles (proton and pion) using beams at different momenta. Figure 5.16(a) shows a similar plot using the relation in Equation 5.1. The ratio of two slopes is found out to be 33.8 which provides the conversion factor for TDC to pico second (1 TDC count = 33.8 ps).

The fit parameters are used to find the expected peak positions of proton and kaon using the pion peak position as a reference (for each run), *e.g.*

$$\tau_{proton} = \tau_{\pi} + p_0 + p_1 \times \left(\frac{1}{v_{\pi}} - \frac{1}{v_p} \right).$$

A table is prepared using pion peak position as a reference and the fit parameters from Figure 5.16(a) to estimate the other peak positions (expected).

The plots in Figure 5.17 with distributions of the TOF difference is revisited. The data are fitted with peaks for p (\bar{p}) and K^+ (K^-) with a double Gaussian and the peak positions of the double Gaussian peak are measured. These values match the expected values from Table 5.2 pretty well. From the double Gaussian fit the probability of each of the peaks in the total distribution is obtained. This gives an estimation of the individual content of kaon and proton (anti-proton). The fractions of pions, kaons and (anti-)protons

	Pion peak positions in TDC counts (data)	
Beam momentum (GeV/c)	From π^- runs	From π^+ runs
2	621.4	629.4
3	612.8	-
4	610.9	614.0
5	608.8	-
6	608.8	610.2
7	608.0	611.0
8	606.7	-
9	606.4	610.9

Table 5.1: Peak positions of pion from negative and positive beams.

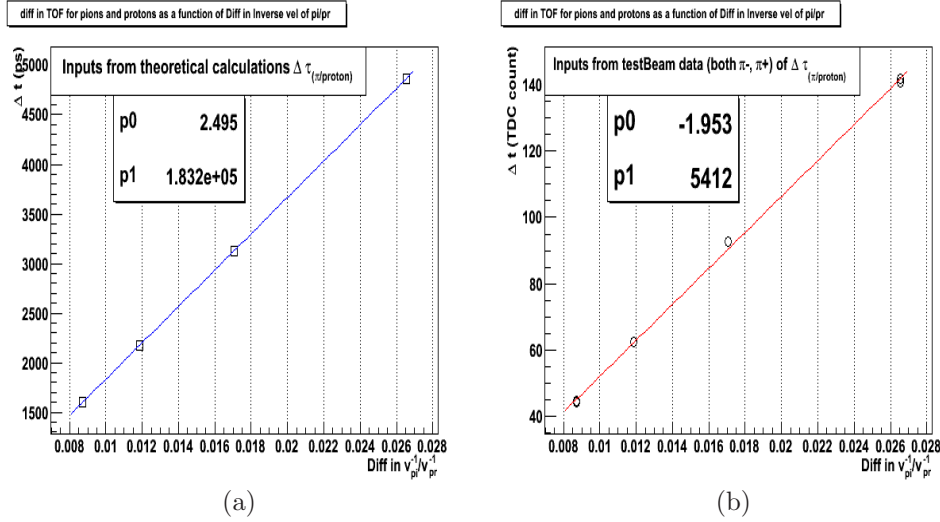


Figure 5.16: Calibration of Time of Flight Detector (a) from theoretical calculation and (b) from test beam data.

in the beam tabulated in Table 5.3 and Table 5.4 for different beam momenta.

The over all particle identification strategy is summarized in Table 5.5.

5.5 Detector Calibration

The inter-calibration of each HE scintillator tile of each layer is measured using radioactive source scan. The signal from a tower is then calculated by taking the average of all measurements from each of the scintillator layers and weighting these averages by the shower profile.

Calibrations of the HE towers are carried out using beams of 50 GeV/c pions. These calibration runs are taken before the EE module is mounted in front of the HE. The beam is directed at the centre of each tower. The gain is found out to be 0.213 GeV/fC.

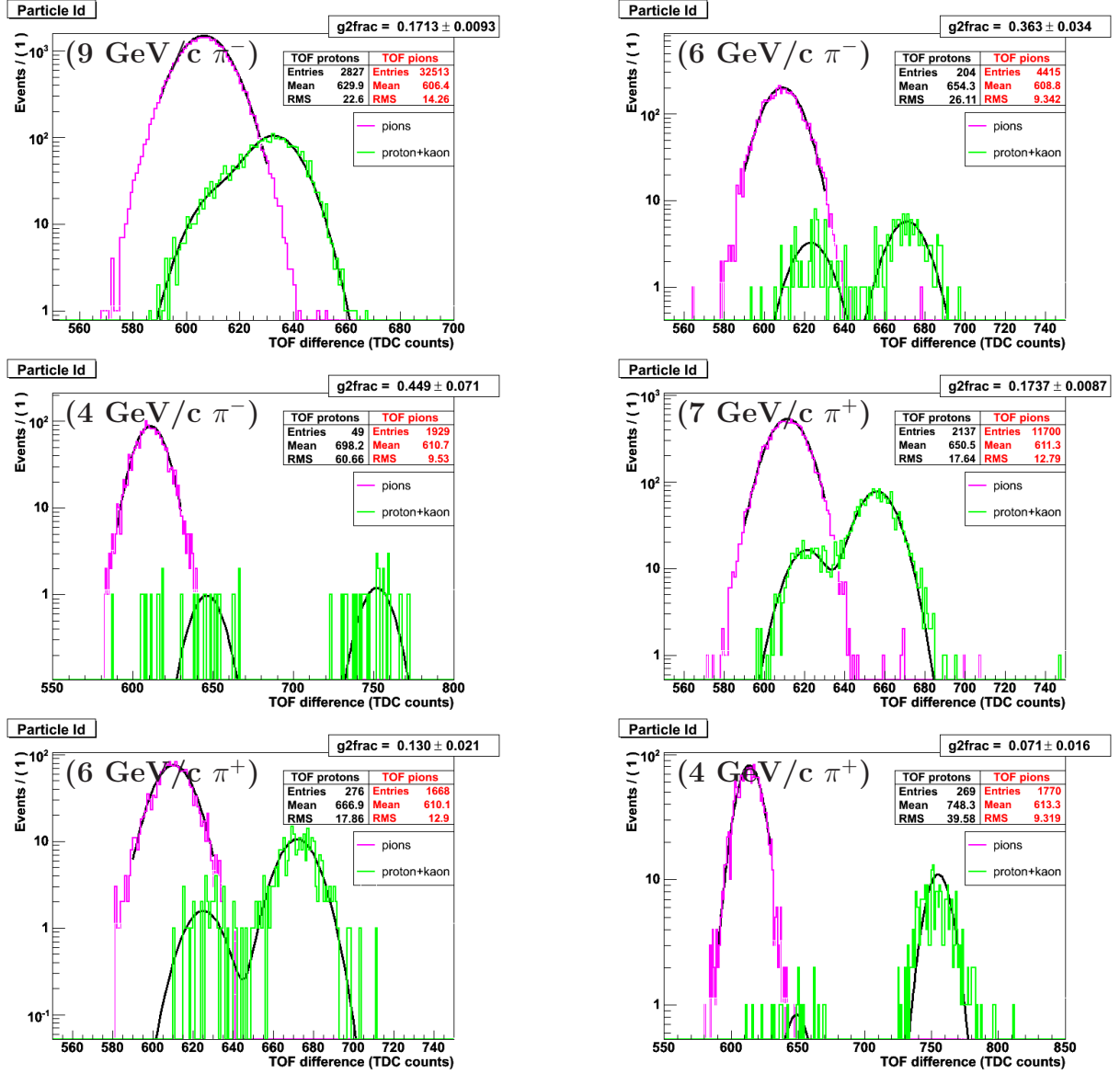


Figure 5.17: Time of flight measurement for six sets of data: 9 GeV/c π^- , 6 GeV/c π^- , 4 GeV/c π^- , 7 GeV/c π^+ , 6 GeV/c π^+ and 4 GeV/c π^+ .

Beam momentum (GeV/c)	Pion peaks	Kaon peaks	Proton peaks
2	621.4	768.4 ± 1.4	1172.0 ± 1.4
3	612.8	677.6 ± 0.2	863.4 ± 0.2
4	610.9	646.6 ± 0.2	752.5 ± 0.2
5	608.8	631.0 ± 0.2	699.1 ± 0.2
6	608.8	623.3 ± 0.1	671.1 ± 0.1
7	608.0	618.4 ± 0.1	653.4 ± 0.1
8	606.7	614.2 ± 0.1	641.0 ± 0.1
9	606.4	611.9 ± 0.1	633.1 ± 0.1

Table 5.2: Peak positions of pion from negative and positive beams.

$P_{\text{beam}}(\text{GeV}/c)$	π^-	\bar{p}	K^-
9	89	9.13	1.87
8	92	4.8	3.2
7	93	4.48	2.52
6	95	3.2	1.8
5	96	3.92	1.08
4	97	1.65	1.35
3	95	1.6	3.4
2	-	-	-

Table 5.3: Beam composition in the hadron beam of the negatively charged low energy beams.

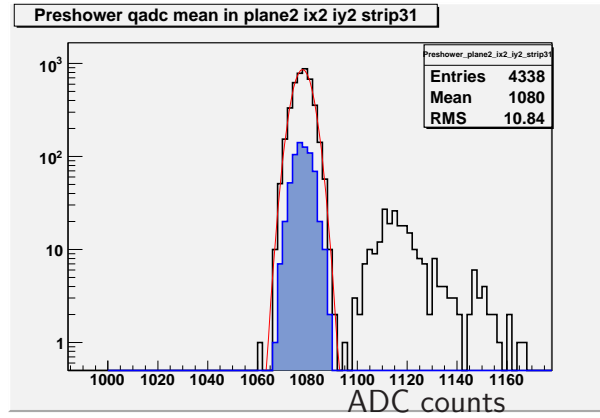


Figure 5.18: Calibration of the preshower was done using muon data in high gain mode. Shown here is the noise and MIP signal in one of silicon strips in the plane two.

Similarly, the EE calibration data are collected by pointing the beam to a selected set of crystals which form a tight grid pattern. The final set of crystal-to-crystal inter-calibration constants is obtained using the matrix inversion algorithm (S9) [81] with 100

$P_{\text{beam}}(\text{GeV}/c)$	π^+	p	K^+
9	67	29.37	3.63
7	84	13.28	2.72
6	85	13.05	1.95
4	86	13.02	0.98

Table 5.4: Beam composition in the hadron beam of the positively charged low energy beams.

Particle	The detectors
Muon	VM1-8 or VMF or VMB
Electron	CK2 (1-9 GeV/c), CK3 1-3 GeV/c
Proton	No CK3 and TOF
Kaons	No CK3 and TOF
Pions	The remaining

Table 5.5: The combination of detectors used in identifying particle types in the test beam setup.

GeV/c electron beam. The response of individual crystals to these electrons is equalized to achieve relative uniformity of the crystals. The observed response in every crystal is corrected for the dependence of the shower containment on the impact point of the electrons on the front face of the crystal.

For preshower the calibration constants are obtained in two gain modes. In the high gain mode the sensor strips are calibrated with muon and electron data. In the low gain mode the calibration is done using pion data[82].

The MIP is the energy unit in the ES and is defined as the mean deposited energy when a high energy pion/muon goes perpendicularly through the sensor (Figure 5.18). The preshower absolute calibration can only be performed with MIPs. The standard operation of the preshower is in the “low gain” (LG) mode. It has then a dynamic range (0-400 MIPs). The preshower is also designed to operate in the “high gain” (HG) mode with limited dynamic range (0-50 MIPs) in order to calibrate precisely the MIPs with good signal to noise ratio.

Chapter 6

Test Beam Analysis

In this chapter the analysis of test beam data recorded in the summers of 2006 and 2007 at the CERN H2 test beam area is presented. For 2006 test beam, an analysis is carried out with incident electrons. The focus is on calibration of the barrel hadron calorimeter (HB) with electrons and comparison of the calibration coefficients with those obtained from the muon beam. The longitudinal shower profiles are studied with electron and pion beams as well and a comparison is being made. Analysis with the 2007 test beam data includes noise study in different parts of the calorimeter as used in the test beam, reconstruction of the data with the final set of calibration constants and a study of response and resolution of single pions in a stand alone as well as in the combined calorimeter setup.

6.1 TB2006

A production super-module of the CMS ECAL barrel is used in the 2006 test beam runs along with prototype modules of HCAL. The HCAL in the test beam includes the barrel (HB), endcap (HE) and the outer hadron (HO) calorimeter. During 2006 test beam incident particles with momenta varying from 1 GeV/c to 300 GeV/c are used. Very low energy (VLE) beam line provides π^- , π^+ , e^- and e^+ in the momentum range of 1 to 9 GeV/c with good rate amounting to a few hundred per spill using a tertiary target (T22). At lower end of the energy range, particles are mostly electrons. There is a significant muon contamination as well. Identification of particle type is accomplished using the information from time of flight counters (TOF), Cerenkov detectors (CK) and muon veto counters.

The high energy beam line covers a momentum range from 10 to 300 GeV/c for hadrons through secondary particle production. For electrons/positrons, the range is between 10 and 150 GeV/c. The new CMS software framework (CMSSW) is used for validating the data for the first time in this test beam experiment.

6.1.1 Longitudinal Shower Profiles

A particle loses all its energy in the calorimeter through successive interactions thereby generating a shower of particles. This property is studied by examining the longitudinal shower profiles with electron beams at different energies in the barrel hadron calorimeter without keeping the ECAL module in front of it. Electron beams at low energy have large contamination from pions and muons. These contamination are significantly reduced by using the muon veto counters and the Cerenkov detectors.

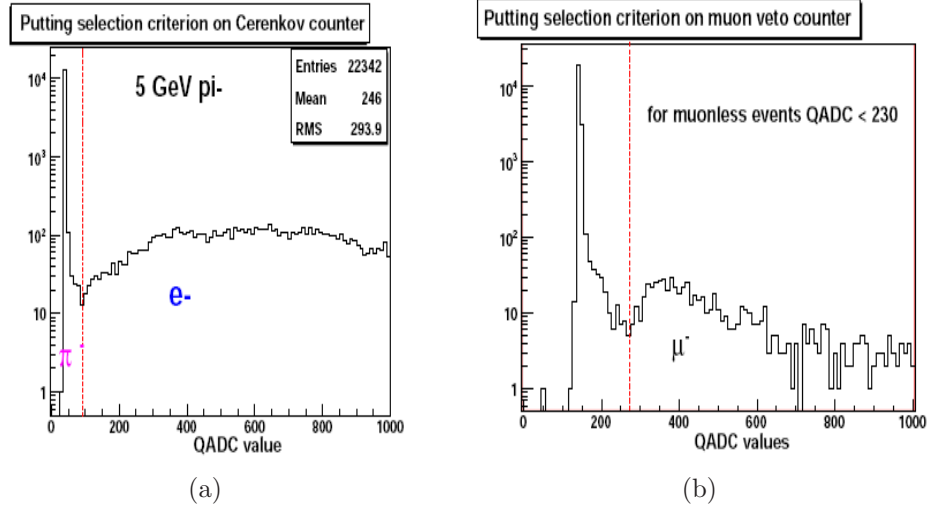


Figure 6.1: Selecting out (a) electrons and (b) muons from the negative pion beam using Cerenkov counter and muon veto counter respectively.

Figure 6.2(a) shows the ADC distribution for electron beam in the Cerenkov counter. There is a clear separation of hadrons (giving no signal) and electrons (with large QADC values) at a QADC value of 100. Figure 6.2(b) shows the ADC spectrum in the muon veto counters and muons can be rejected offline using a threshold of 230 counts in the QADC value.

At very low energies the pion beams have very large contamination from electrons and muons. At 2 GeV/c, the total contamination is as large as 70%. Electrons and pions are selected from their respective runs using the particle identification criteria as described above.

The longitudinal shower profiles with electron beam with momenta ranging from 2 GeV/c (VLE) to 300 GeV/c (HE) are studied using the HB2 alone configuration. The energy deposited in each layer is plotted as a function of layer number: 1-17. Figures 6.2(a) and 6.2(b) show the fraction of shower energy measured in each layer. From the beam purity consideration, the measurements from the high energy runs are more reliable.

Figures 6.2(c) and 6.2(d) show energy fraction measured in different layers for pion beams of momenta 2 GeV/c and 50 GeV/c. The shower profiles for pions as well as electrons have a sharply rising distribution followed by a falling part. Electrons start

showering very early in the calorimeter and deposit most of the energy in the very first few layers. In contrast the pions continue to deposit energies in the further layers and the shower development continues deeper in the calorimeter.

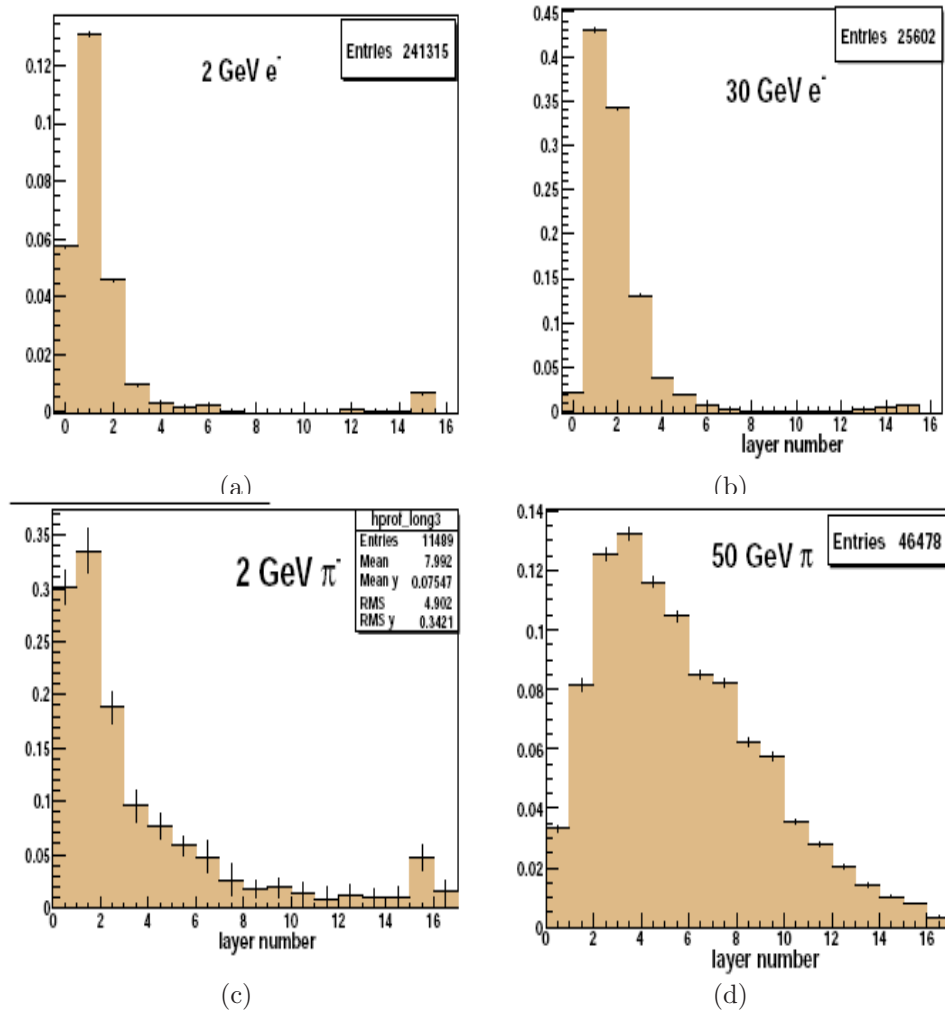


Figure 6.2: Longitudinal shower profiles of electrons and pions at various energies: (a) 2 GeV e^- , (b) 30 GeV e^- , (c) 2 GeV π^- and (d) 50 GeV π^- .

At higher beam energies, the shower continues to larger layer numbers for both electrons and pions. Figure 6.3 shows the mean shower depth as a function of beam energy for electrons and pions. It is worth noticing that the average shower depth increases logarithmically with energy for both these particles with slopes of 0.217 and 0.437 respectively, for electrons and pions, when fitted with a functional form of $p_0 \times \log E + p_1$. Thus showers for pions are much deeper than those for electrons and the difference in the shower size between pions and electrons increase with increasing energy.

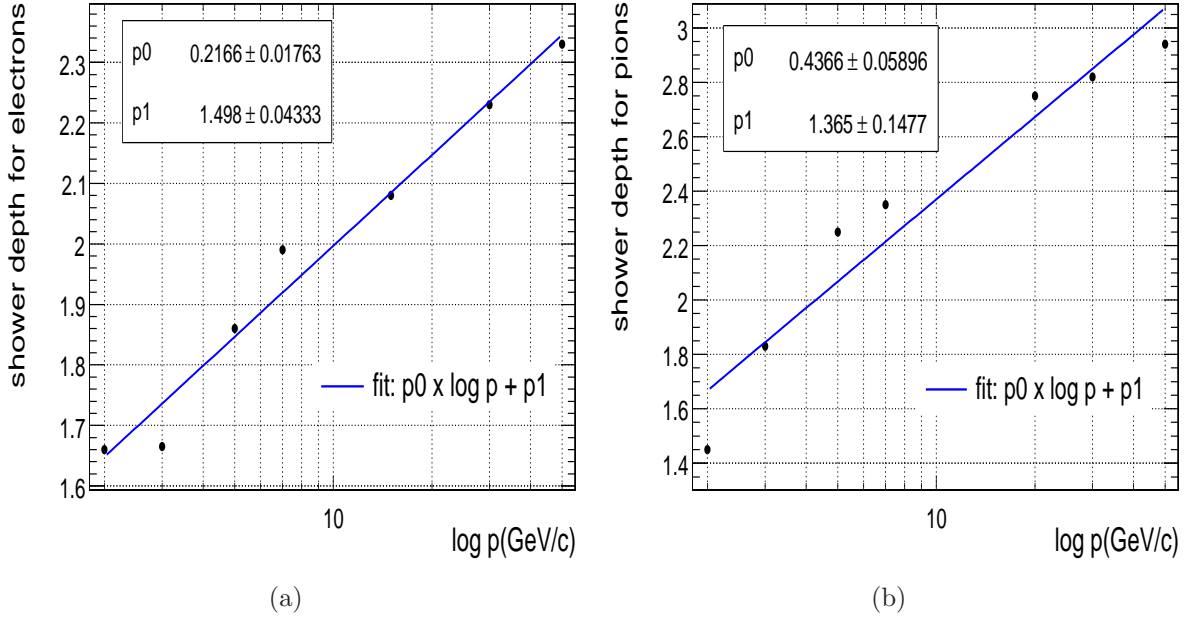


Figure 6.3: Shower depth as a function of incident beam energy for (a) electrons and (b) pions.

6.1.2 Calibration with Electron Beam

Electron beam of 50 GeV/c is used to calibrate the barrel hadron calorimeter, in particular the towers of the HB1 wedge which is read out with the standard lateral segmentation. Random trigger events are used to determine the position of the pedestal in each tower. Figure 6.4 (top part) shows the ADC spectrum of a given tower ($i\eta = 7$, $i\phi = 12$) for random trigger events. The spectrum is fitted to a Gaussian distribution and the mean value from the fit is used as the pedestal value. Bottom part of Figure 6.4 shows distribution of beam trigger events for the same HB1 tower after pedestal subtraction. This distribution is also fitted to a Gaussian distribution and the inverse of the mean from the fit gives a measure of the calibration constant.

Figure 6.5 shows the correlation between the calibration constants obtained from electron data with that obtained from muon scan data. There is a very clear correlation of the two set of measurements.

6.2 TB2007

The preshower detector is put to the test beam for the first time during 2007. The main focus of the 2007 test beam study is to understand the particle response in the endcap calorimeter. A comparison of the single particle response and resolution is made between the barrel and the endcap from the two test beam experiments in 2006 and 2007.

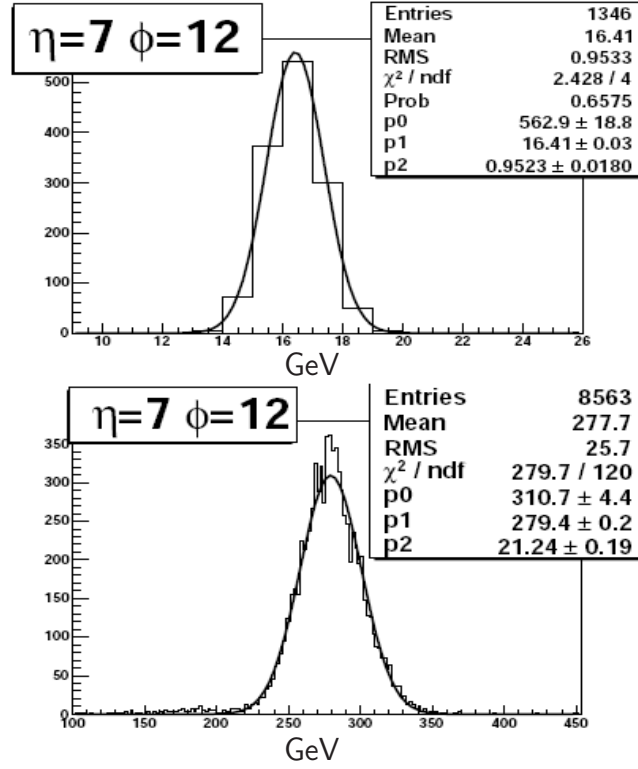


Figure 6.4: Calibration procedure for hadron barrel: Calibration constants as obtained from plots of the pedestal and the signal with electron data.

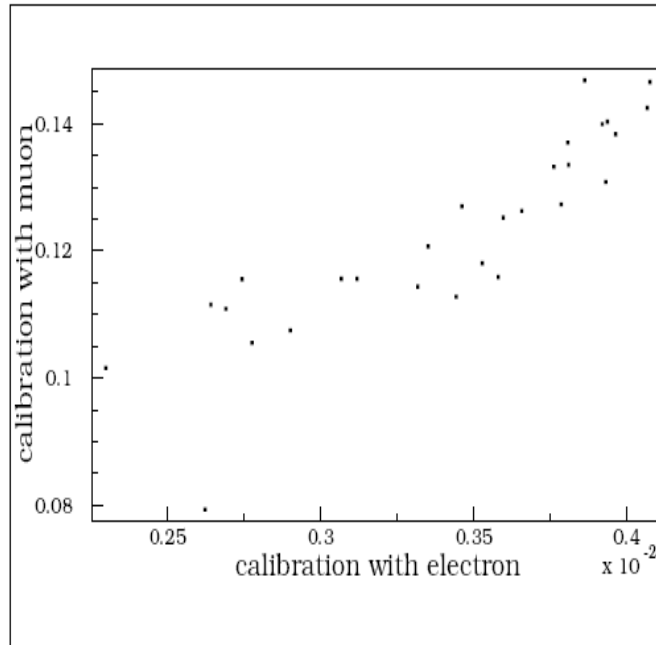


Figure 6.5: Correlation between the calibration constants from electron data and those from muons.

6.2.1 Reconstruction

The analog signal obtained from a HCAL readout channel is digitized in bins of 25 ns (time-sample). The signal is stored in 10 time slices (each of 25 ns) for offline analysis. The pedestals are established using random triggers and are subtracted from signal at the time of reconstruction. The pedestals are calculated for individual capIDs of a given channel. The charges in 6 time slices are summed up to get the total signal in a HCAL readout channel. The data acquisition and unpacking of the data for the offline analysis are done using a prototype software (HTBDAQ library). The maximum charge is usually contained in the sixth or the seventh time slice (Figure 6.6). The inter-calibrations for HE channels and the absolute energy scales are applied offline in the analysis. The charge collected from each ECAL crystal is amplified and shaped to a predefined form by the front-end electronics and is then digitized at the rate of 40 MHz. The absolute energy scale for ECAL is obtained using 50 GeV/c electrons.

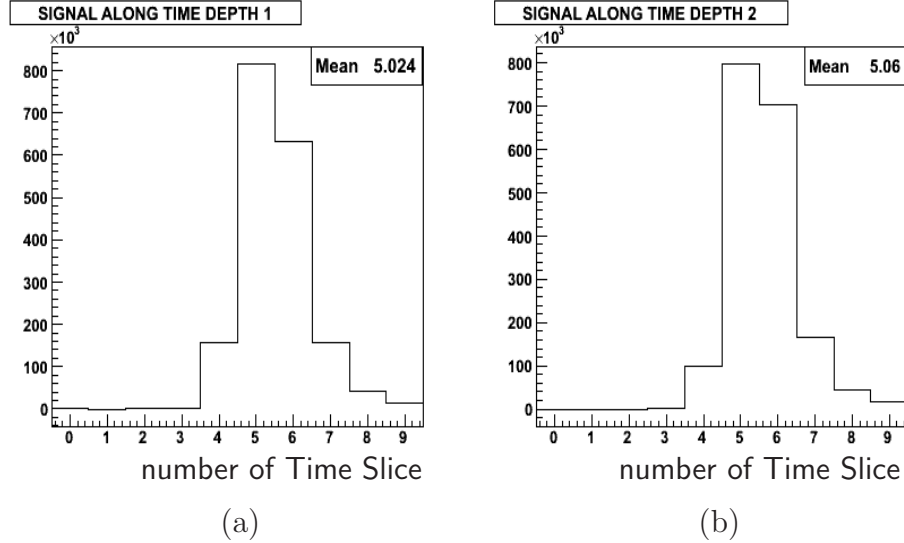


Figure 6.6: Energy distribution in 10 time slices in the (a) front and (b) back layers of the hadron endcap calorimeter.

6.2.2 Noise Levels in EE and HE

6.2.2.1 Noise in EE

The noise levels in various channels are studied using the randomly generated trigger within the spill and out of the spill. These events give the fluctuations in the full readout chain in absence of any beam particle. The energy distribution of these events is expected to peak at 0 for individual channels and the respective width measures the mean noise level

of the respective channel. The main contribution of the noise comes from the electronics noise.

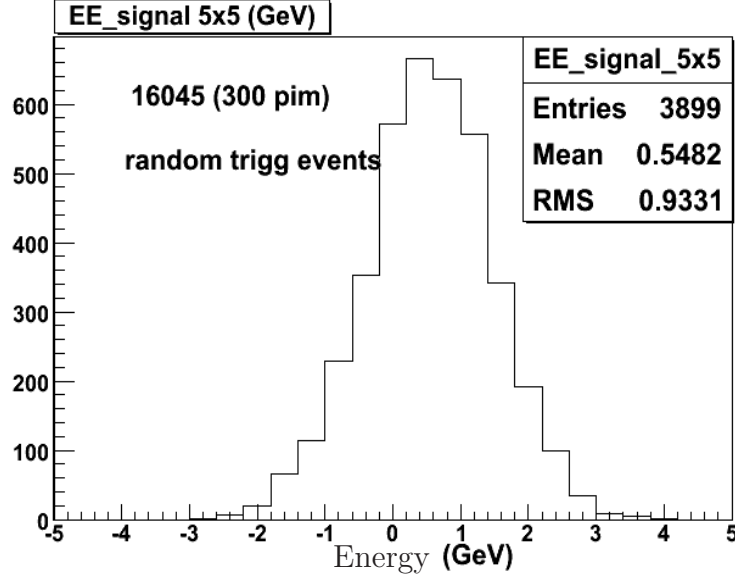


Figure 6.7: Energy spectrum of a crystal matrix comprising 5×5 crystals of EE from random trigger events. The width of the distribution measures the noise in the crystal matrix.

The endcap electromagnetic calorimeter has a noise level which is 4 times larger than that in the barrel. In the barrel part of ECAL (EB) average pedestal RMS is 1.2 ADC counts whereas in EE it is 2 ADC counts. Moreover in the EB, 1 ADC count corresponds to 37 MeV whereas the corresponding factor in the EE is 90 MeV/ADC count. This results in a noise/crystal to be 40 MeV in the EB and 180 MeV in the EE. This can be cross checked by looking at the reconstructed energy in a crystal matrix of 5×5 (25) crystals from random trigger events. As shown in Figure 6.7 the RMS of this distribution is 933 MeV. Hence the average noise per crystal can be calculated to be $933/\sqrt{25} = 186$ MeV which matches with the value mentioned above.

The high noise in EE demands that signals, to be used in a sum of $N \times N$ crystal matrix, should be above a certain threshold. First an estimate of the offset coming from random trigger events is made and it is then subtracted from the signal. The subtracted quantities are required to be greater than some $N \times \sigma$ where σ is the RMS value of the pedestal distribution. This threshold is varied and the effect is studied for different cluster sizes - namely 3×3 , 5×5 and 7×7 . It is worthwhile to mention here that due to high level of noise in EE crystals 7×7 (49) crystals are not summed up as in the study of the barrel module. Instead 5×5 (25) crystals are summed around the beam spot for measuring the signal. Figure 6.8 shows that around 2σ the signals for various clusters come close. So

signals only above twice the pedestal RMS are considered in the measurement of signals in the EE.

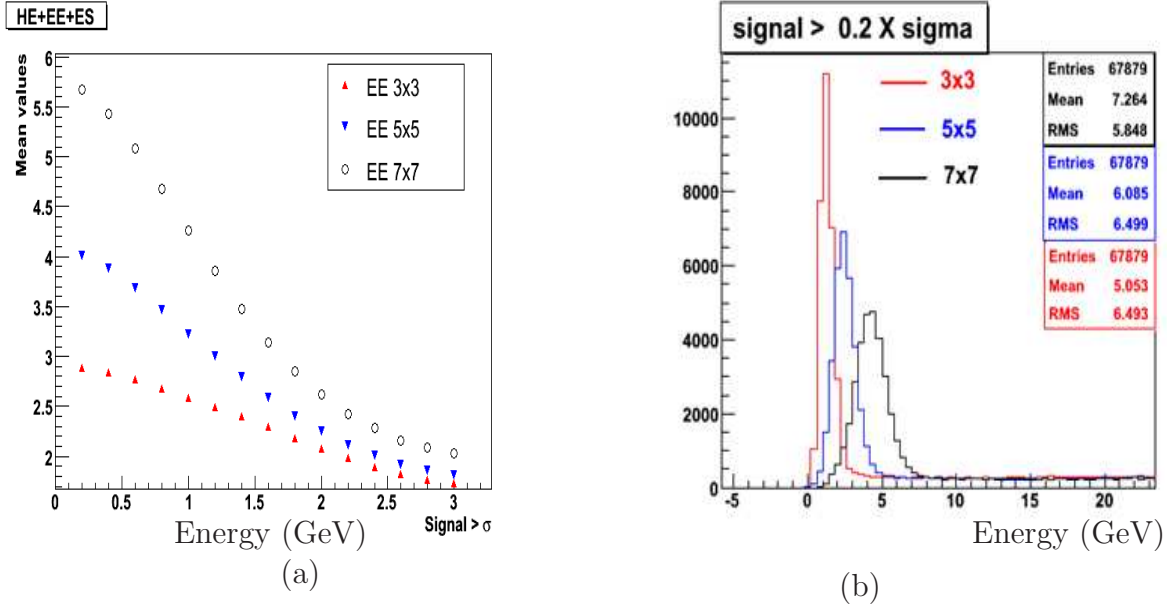


Figure 6.8: Energies contained in a matrix of $N \times N$ crystals surrounding the central crystal in the super crystals of EE are shown. Signal energy (GeV) greater than various RMS of pedestals (denoted by σ) for various cluster sizes is plotted in (a). For three different cluster sizes, energies which are greater than 0.2σ are plotted in (b).

6.2.2.2 Noise in HE

The noise level in HE towers is calculated from the energy sum of $4 \times 4 \times 2 = 32$ towers of HE (keeping in mind two depths of HE) in events with random triggers. Figure 6.12 shows such distribution. RMS of this distribution gives noise per tower to be $1683\text{MeV}/\sqrt{32} = 297\text{ MeV}$. For a HB tower the noise distribution is typically 200 MeV wide.

6.2.2.3 Noise in ES

Pedestals

In order to extract the total signal per sensor in ES, the first step is the pedestal subtraction for each channel for each time sample. The evaluation of the pedestals is done by using data from dedicated runs. These data are collected by triggering the system with an external pulse generator, without the presence of the beam. For every channel the raw values are fitted to a Gaussian distribution and the central value with its sigma are evaluated. Figure 6.10(a) shows typical pedestal distributions for one strip in X and one strip in Y.

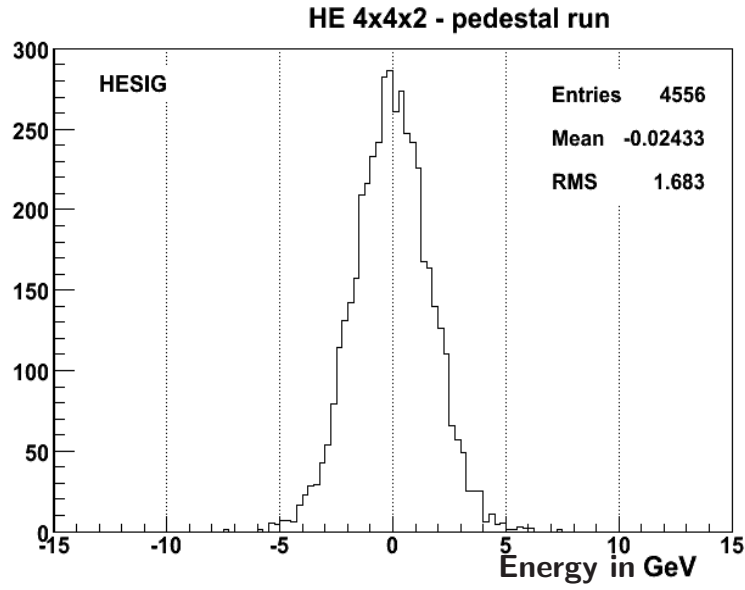
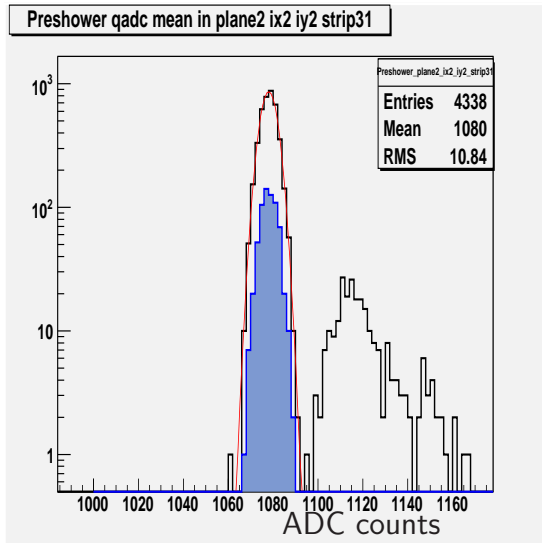
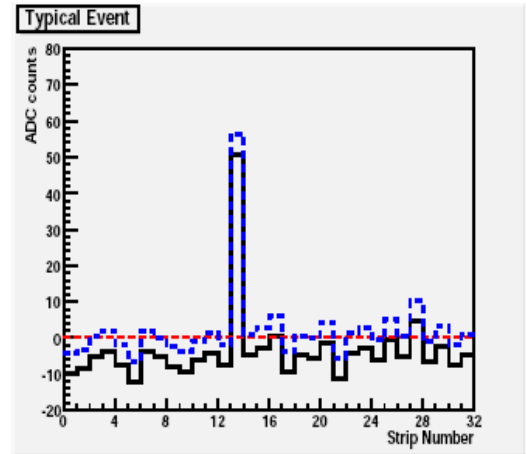


Figure 6.9: Noise in sum of 4×4 towers combining the two depths of the endcap hadron calorimeter.



(a)



(b)

Figure 6.10: Noise in the preshower detector (a) Pedestal (blue shaded) (b) Common Mode noise.

Common Mode Noise

After pedestal subtraction, the signal in a channel should correspond to the total charge deposited in the given strip. In fact this is not true because a small displacement of the baseline is observed, differing on an event by event basis. This is due to external sources of noise that affect a number of strips in parallel. This type of noise is called common mode (CM) and requires a correction on an event by event basis. The method of CM rejection is based on histogramming the measured amplitude in all channels of a single detector. Since the occupancy of the preshower sensors is low, a peak corresponding to the common mode is be seen, together with some hits. The CM value is obtained by fitting this peak to a Gaussian distribution. Figure 6.10(b) shows a single event (solid line), a common mode corrected event (dashed line) by shifting the baseline according to the estimated common mode value.

6.2.3 MIP Studies in ECAL

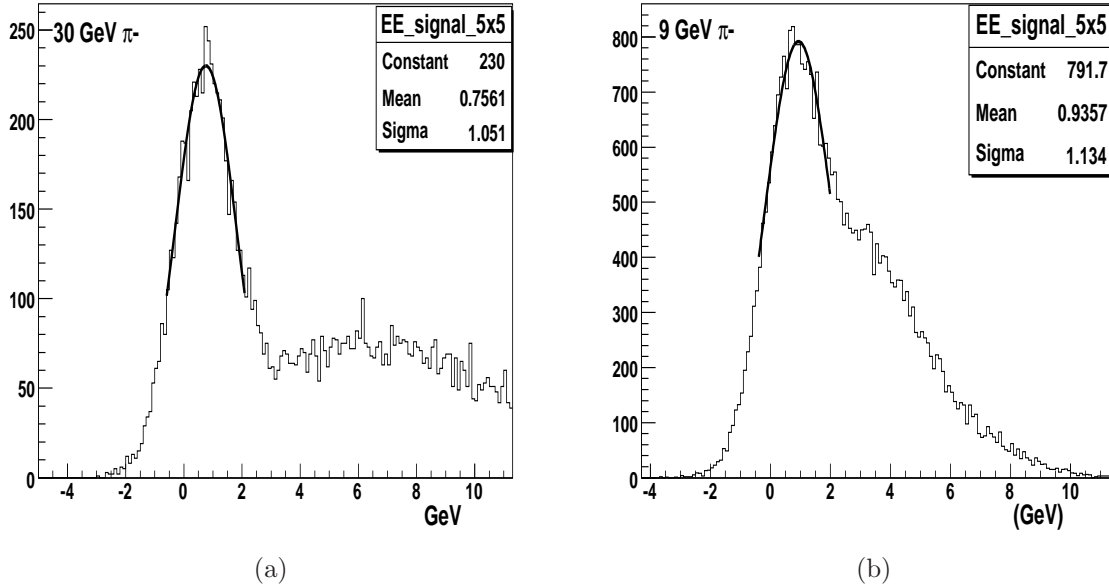


Figure 6.11: Signal in the ECAL for π^- beam at (a) 30 GeV/c, (b) 9 GeV/c showing the MIP peak.

The ECAL crystals are 23 cm long and correspond to $1.1 \lambda_I$ which means nearly 67% of hadrons would undergo a nuclear interaction in ECAL and start a hadron shower. However, 33% of hadrons are expected to deposit a small energy corresponding to a minimum ionizing particle (MIP) through ionization. The energy deposited in the ECAL within a matrix of 5×5 crystals is shown in Figure 6.11(a) for a 30 GeV/c pion beam and an attempt is made to fit the MIP peak with a Gaussian distribution. A mean value of 756 MeV is measured with a width of 1051 MeV. The energy measured in the

ECAL for a 9 GeV/c π^- beam-tune is shown in Figure 6.11(b) and the MIP peak in the ECAL is measured to be 935 MeV with a width of 1134 MeV. At the energies below 7 GeV it becomes difficult to separate the MIPs from the particles which interact and start showering in the ECAL. The events which deposit less than 1800 MeV (approximately 1σ from the mean position using Gaussian fit to the MIP peak) in the ECAL are taken as MIP in ECAL and are used to study the response of a stand-alone HCAL.

6.2.4 Energy Measurements

6.2.4.1 HCAL Alone Setup

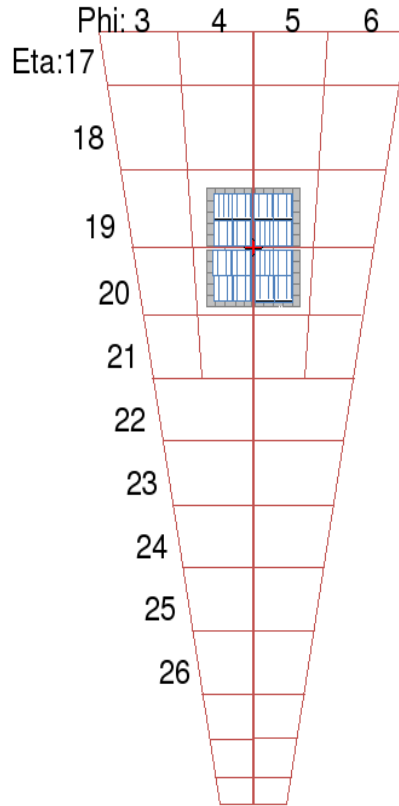


Figure 6.12: Illustration of the beam spot position in the HE towers geometry. The ECAL super-module is also shown in front.

Data exist for two types of detector configuration, with and without the ECAL in front of the HCAL endcap. They are analyzed separately but for both the analyses the same set of calibration constants is used, namely the one obtained from radio active source scan. As the shower develops, it spreads laterally in the neighbouring towers of the central tower where beam is shot. In the test beam 2007 most of the times the beam is shot at the junction of $i\eta = (19, 20)$ and $i\phi = (14, 15)$. Therefore, most of the times the towers with $i\eta = 18, 19, 20, 21$ and $i\phi = 13, 14, 15, 16$ are summed over as 4×4 . As HE has two

depths the relative share of energy deposits in the two depths are often used for ensuring no contamination of electron in the hadron beam for low energies.

Data are collected with negative pion beams over a momentum range of 4-300 GeV/c and with electron beam over a range of 50-100 GeV/c. For HCAL alone set up no high statistics data is available for the VLE set up. To obtain the energy scale for HCAL, the average signal produced by 50 GeV/c electron beam in the sum of 4x4 towers around the beam centre is used such that the measured energy in HCAL equals 50 GeV (Figure 6.13). The distribution is fitted with a Gaussian only around the peak position. The mean of the fit is compared with the nominal energy to get the scale. The ratio gives a factor $50/54.48 = 0.92$. The HCAL can also be calibrated using pions such that the signal produced by 50 GeV/c pion beam corresponds to 50 GeV energy measured in the HCAL. The ratio of two signals essentially gives the π/e for HCAL at 50 GeV/c incident momentum and it characterizes the performance of a calorimeter in terms of linearity of the response and the resolution for hadrons. The π/e is measured to be 0.836 for the CMS hadron calorimeter endcap at 50 GeV/c in the test beam experiments. This is the scaling factor used for energy deposited in HCAL wherever the results are presented using electron calibration for HCAL. The ECAL is calibrated using electron beams at 100 GeV/c using the signal measured in 5×5 crystals.

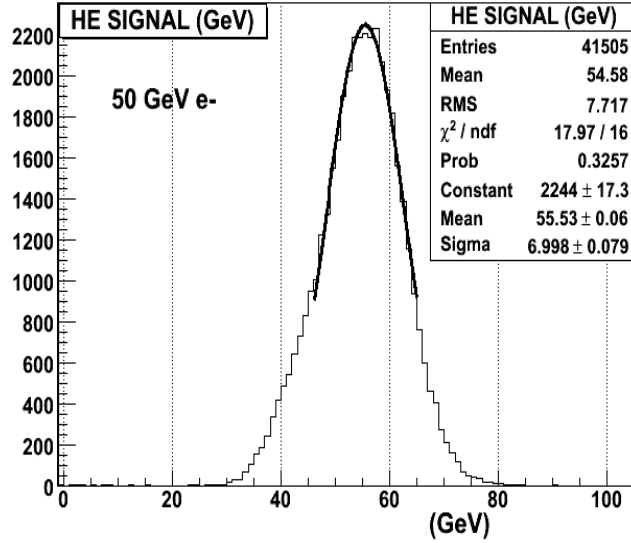


Figure 6.13: Calibrating HE energy summed over 4x4 towers using 50 GeV/c e^- . The distribution is fitted partially with a Gaussian. The mean of the fit is compared with the nominal energy to get the scale

Having calibrated the HE with 50 GeV/c electron it is worthwhile to look at the energy sharing between the two depths of HE. Figure 6.14 shows the energy distribution in the front (depth 1) and back (depth 2). Clearly one sees that for lower energies there

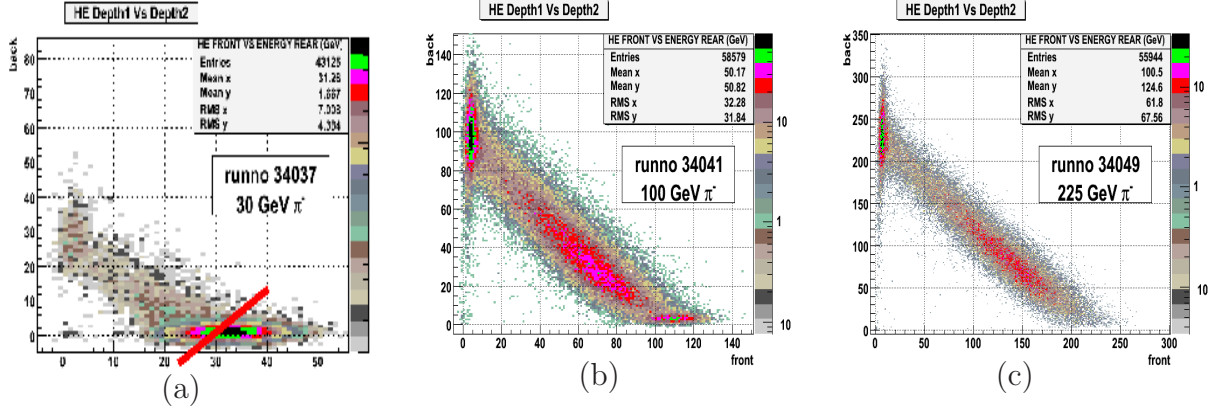


Figure 6.14: Total energy measured (in GeV) in the front part of the HE, versus that in the back part, for negative beams at (a) 30 GeV, (b) 100 GeV and (c) 225 GeV. HE is calibrated using 50 GeV/c e^- . The different cuts to remove electrons are shown in these plots by solid lines.

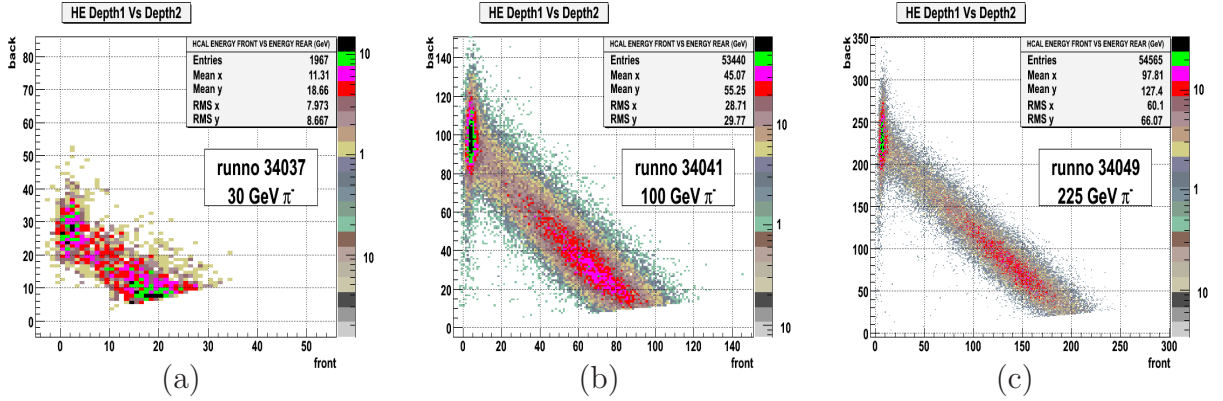


Figure 6.15: Total energy measured (in GeV) in the two depths of the HE, denoted as front and back for depth 1 and depth 2 respectively, for negative beams at (a) 30 GeV, (b) 100 GeV and (c) 225 GeV. HE is calibrated using 50 GeV/c e^- . Effect of those cuts are clearly seen.

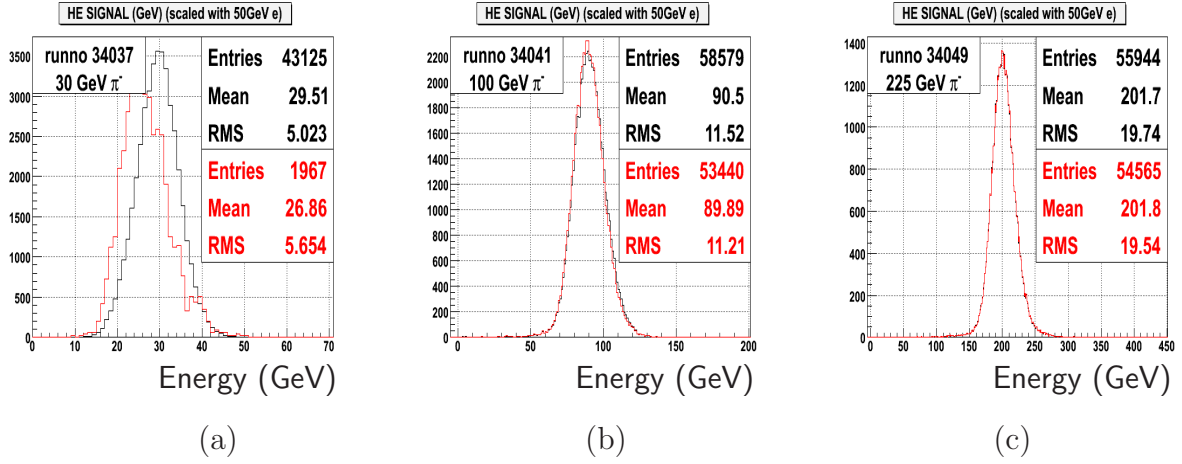


Figure 6.16: Total energy measured (in GeV) by combining the two depths of HE. Three energies of pion runs are shown (a) 30 GeV, (b) 100 GeV and (c) 225 GeV. Red and black lines represent the reconstructed energy before and after the cuts respectively.

is electron contamination in the beam as most of the energy is deposited in the front. For higher energies majority of energy fraction is in the back plane as hadron starts showering later. To eliminate the electron contamination for the beam, a cut is made in the two dimensional distribution (back vs front energy) as shown in Figure 6.14. The effect of such cuts is illustrated in Figure 6.15. The total energy measured in HE with such cuts is presented in Figure 6.16. These cuts remove electrons from the hadron beam and thus results in a correct estimation of reconstructed energy for hadrons. The response of the calorimeter for a given beam momenta is defined as the ratio of the reconstructed energy to the nominal beam energy. The resolution of the calorimeter for pions is defined as the ratio of RMS to the mean of the distribution. As it is seen from Figure 6.16 (a) the Mean of the reconstructed energy distributions is higher after the cuts and this results in a correct higher response. Similarly the RMS becomes smaller for the distributions after the cuts which improves the resolution of the detector.

Momentum (GeV/c)	Ratio of measured to nominal energy π^-
300	0.9013 ± 0.0038
225	0.8969 ± 0.0038
150	0.9074 ± 0.0038
100	0.8989 ± 0.0039
50	0.8884 ± 0.0039
30	0.8950 ± 0.0155

Table 6.1: Response for HCAL alone system with HCAL calibrated using 50 GeV/c electron.

Tables 6.1 and 6.2 show the response and resolution obtained from the mean and RMS of these distributions. The corresponding plots are shown as Figure 6.17

Momentum (GeV/c)	Resolution π^-
300	0.0880 ± 0.0004
200	0.0968 ± 0.0004
150	0.1061 ± 0.0005
100	0.1247 ± 0.0005
50	0.1667 ± 0.0007
30	0.2098 ± 0.0036

Table 6.2: Resolution for the HCAL alone system with HCAL calibrated using 50 GeV/c electrons.

The resolution of HE alone set up is fitted with a function

$$\frac{\sigma}{E} = \frac{a}{\sqrt{E}} \oplus b$$

and the fit to the resolution plot gives $a = 92.0\%$ and $b = 3.4\%$. The resolution is approximately 9% at the 300 GeV/c and 17% at 50 GeV/c.

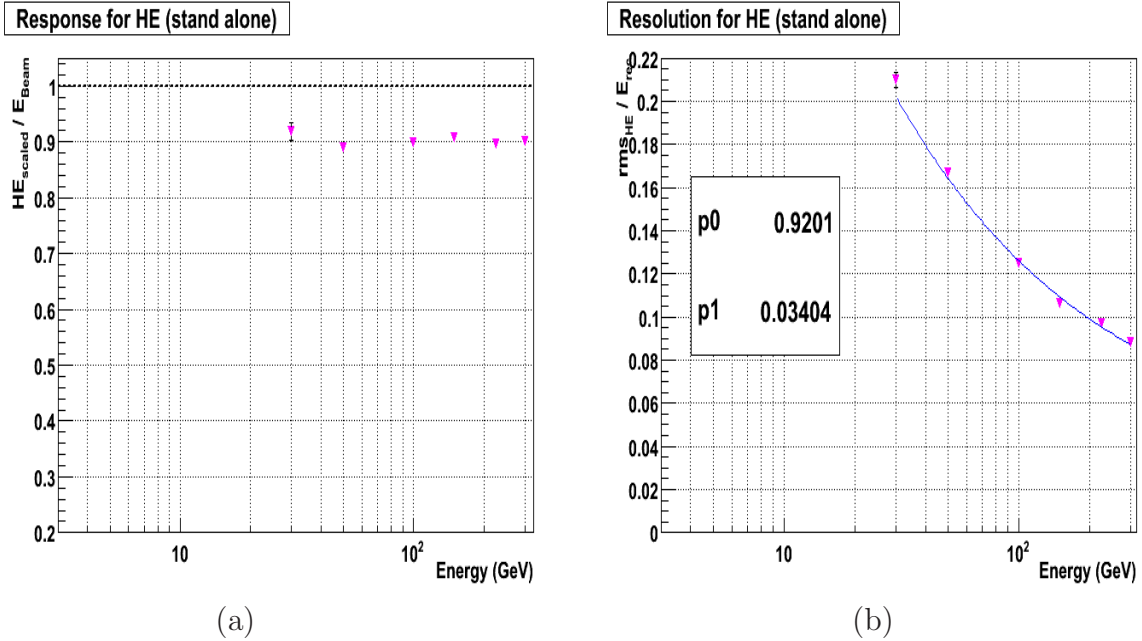


Figure 6.17: (a) Response and (b) Resolution of HCAL alone system for HCAL calibrated with 50 GeV/c e^- . Total energy measured in the two depths of HE

6.2.5 Energy Measurements in Combined Calorimeter System HE+EE

In the 2007 test beam experiment for the combined calorimeter system of ECAL and HCAL, data are collected with both negative and positive hadron beams over a momentum range of 2 to 300 GeV/c. Data sets with π^- (2-300 GeV/c) and p (2-350 GeV/c) taken with ECAL (with the preshower in front) and HCAL combined system are used for the analysis presented here. There are some very low energy runs taken with the combined calorimeter system without the preshower in front. Effect of the presence the preshower detector can be measured by looking at the energy response for the combined calorimeter system with and without the preshower in front (MIP is ES). To get the total energy of the calorimeter (without ES) the reconstructed energy of the HE (calibrated with 50 GeV/c electron) is added to the reconstructed energy within the EE.

$$E_{total} = E_{ECAL} + E_{HCAL}$$

Nearly 70% of the particles starts showering in the ECAL and depending upon the nature and depth of the first hadronic interaction in ECAL, the sharing of energy between ECAL and HCAL differs. The energy deposited in 4×4 towers is used to get the total energy deposited in HCAL. The energy shared between the HCAL and ECAL on an event-by-event basis is shown in Figure 6.18 for various π^- beam-tunes. The cluster of events with very small energy measured in the ECAL is due to the pions which do not undergo hadronic interaction in the ECAL and deposit energy only through ionization. On the other hand, there are events where almost all the energy is deposited in the ECAL and these events correspond to the interactions like charge exchange ($\pi^-p \rightarrow \pi^0n$). In such a reaction, almost all the energy is transferred to the π^0 which immediately decays to an $\gamma\gamma$ pair and develops a purely electromagnetic shower.

If the responses of ECAL and HCAL for electrons and hadrons are the same, a simple sum of energy deposited in the two compartments would add up to the incident energy and the data points would lie along a straight line given by

$$E_{ECAL} + E_{HCAL} = E_{Incident}$$

in the ECAL versus HCAL plane. The total energy measured in the calorimeter for 50 GeV/c and 9 GeV/c π^- is shown in Figure 6.19 for HCAL calibrated with 50 GeV/c electrons. The difference in the response of ECAL and HCAL to hadrons results in the non-Gaussian nature of the total energy distribution and a net degradation in the resolution. The HCAL can also be calibrated using 50 GeV/c π^- .

The response of the ECAL and HCAL to π^- , π^+ and protons, as measured in the test beam over a momentum range of 2 GeV/c to 300 GeV/c, is shown in Figures 6.20(a)

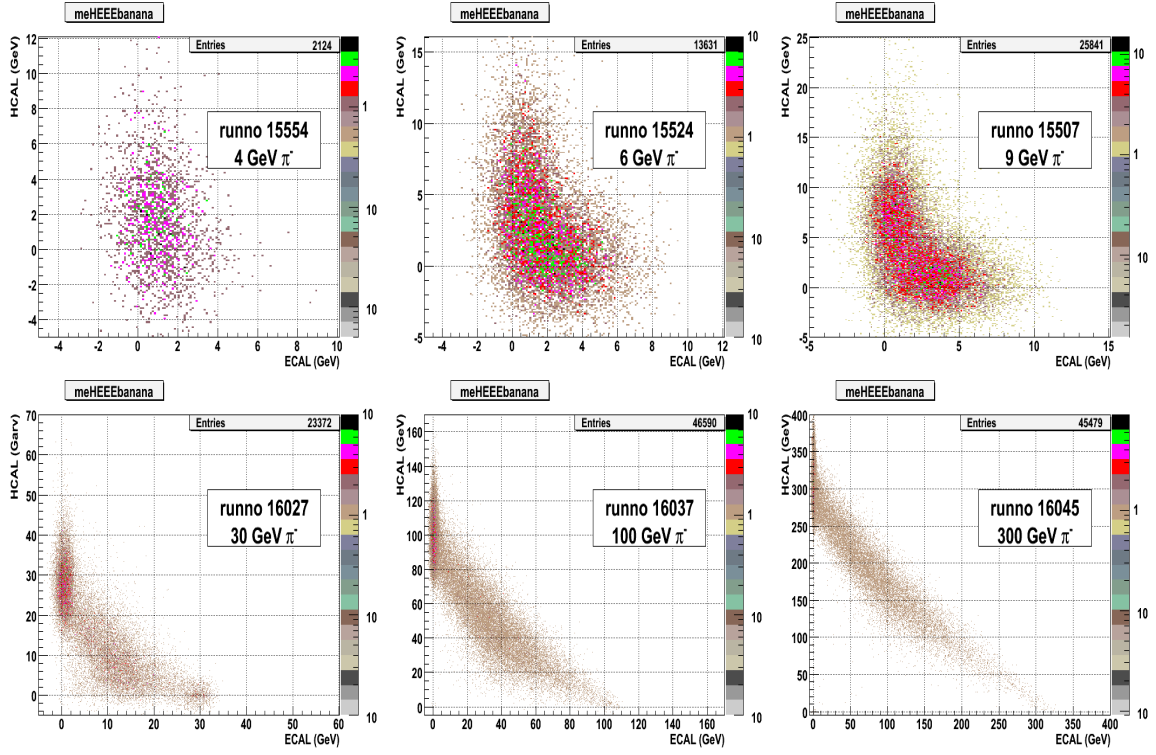


Figure 6.18: Energy measured in the HE towers as a function of energy measured in the central 5×5 EE crystals. The plot refers to π^- beams at various energies.

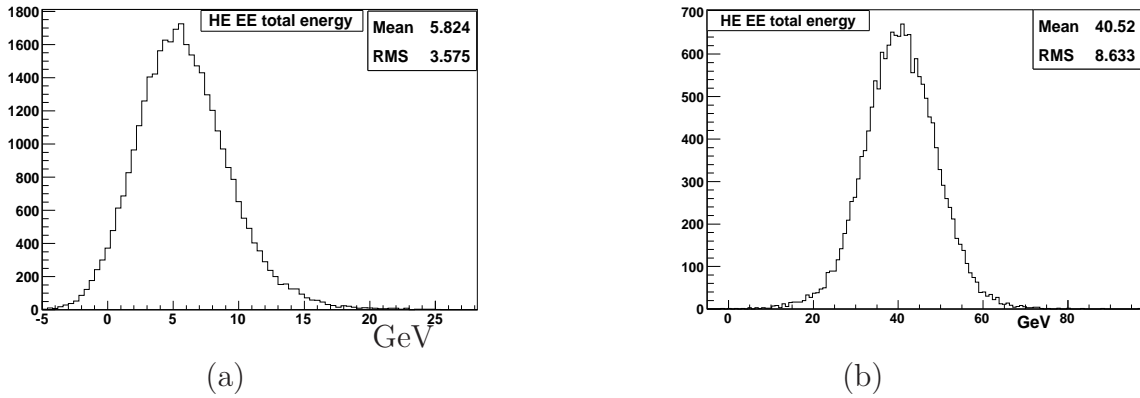


Figure 6.19: Total energy measured in the combined HCAL+ECAL system for (a) 9 GeV π^- and (b) 50 GeV π^- (with the HCAL calibrated using 50 GeV/c electron).

with HE being calibrated using 50 GeV/c electrons. The combined system is observed to be non-linear by 40% for pions over the energy region 2-300 GeV/c when HCAL is calibrated using 50 GeV/c pions and by 32% when HCAL is calibrated using electrons. The electromagnetic component in a hadronic shower is a function of energy and decreases logarithmically with the projectile energy. When combined with the fact that ECAL and HCAL have very different e/h values, one gets a highly non-linear calorimeter system. By calibrating HCAL to electrons, the energy scale of pions is effectively reduced resulting in an overall correction and observed improvement in linearity. The same plot also shows the 2006 test beam results (HB+EB) [83] as a comparison. It is interesting to find that for higher beam momenta the response from the endcap system is higher than that from the barrel. For low momenta the response from barrel and endcap are comparable. Suppression of noise in the EE crystals using the 2σ cut has very little effect on the mean energy response over a large energy region.

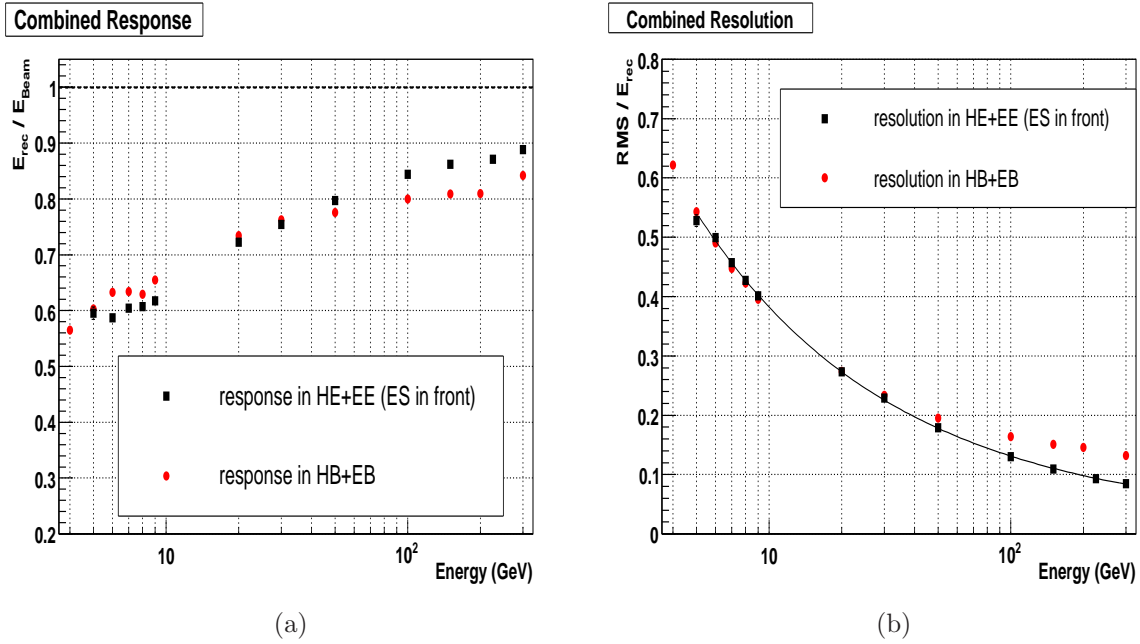


Figure 6.20: (a) Response and (b) resolution of the combined ECAL + HCAL system (with the preshower in front) measured as a function of beam momentum for π^- .

The resolution of the combined HE+EE set up is fitted with a resolution function

$$\frac{\sigma}{E} = \frac{a}{\sqrt{E}} \oplus b$$

and the fit to the resolution plot (Figure 6.20(b)) gives $a = 116.9\%$ and $b = 1.4\%$. For the HB+EB combined setup the respective terms are $a = 111.5\%$ and $b = 8.6\%$ [83].

The resolution for the combined calorimeter is worse than that of the HE alone system which is obvious due to the non-matching e/π between EE and HE. In Figure 6.20(b) it

is worthwhile to notice the effect of noise suppression. The black points in this plot shows the resolution without noise suppression in EE and they are much worse than resolution from the barrel calorimeter (shown in blue points). But after suppressing the noise, the resolution (shown as red points) improves and matches well with that in the barrel.

Momentum (GeV/c)	Response π^-
300	0.8882 ± 0.0041
225	0.8709 ± 0.0041
150	0.8620 ± 0.0039
100	0.8442 ± 0.0039
50	0.7972 ± 0.0037
30	0.7545 ± 0.0049
20	0.7224 ± 0.0035
9	0.6174 ± 0.0038
8	0.6071 ± 0.0032
7	0.6043 ± 0.0051
6	0.5870 ± 0.0085
5	0.5951 ± 0.0110
4	0.6708 ± 0.0145
3	0.8907 ± 0.0219

Table 6.3: Response for HCAL+ECAL (ES in front) with HCAL calibrated using 50 GeV/c electron.

For events which produce a MIP signal in the EE, the response and resolution are plotted in Figure 6.21 by the same procedure and are tabulated in Tables 6.5 and 6.6.

6.2.5.1 Beam Profile and MIP Fraction

Figure 6.11 shows the energy spectrum in ECAL for pions of 30 GeV/c and 9 GeV/c. The peak at ~ 800 MeV corresponds to MIP signal in ECAL. MIP's are selected using a cut on energy in the ECAL less than 1800 MeV, Fraction of such MIP like events in ECAL is shown as a function of available energy in Figure 6.22. Energy available to contribute to the visible signal is given as $\sqrt{p^2 + m^2} - m$ where p is momentum and m is the mass of the particle. For a 2 GeV/c proton only 1.27 GeV is available to create a measurable signal. The figure shows a rise in the MIP fraction for energies above 50 GeV which is rather strange as from the previous experience in the test beam 2006 (with the barrel detectors) a decrease in fraction of MIP events is expected for pion momentum above 100 GeV/c. This is due to the fact that the pions start losing energy through bremsstrahlung.

A gap within the ECAL super crystals could also cause MIP like signal in the ECAL. So the possibility of gap in the material of the combined calorimeter is investigated. In order to verify this the wire chamber hit position and energy weighted occupancy in the

Momentum (GeV/c)	Ratio of measured RMS to nominal energy π^-
300	0.0845 ± 0.0003
200	0.0932 ± 0.0004
150	0.1094 ± 0.0005
100	0.1303 ± 0.0006
50	0.1791 ± 0.0008
30	0.2288 ± 0.0014
20	0.273 ± 0.0013
9	0.4012 ± 0.0024
8	0.4272 ± 0.0022
7	0.4575 ± 0.0039
6	0.4994 ± 0.0072
5	0.5281 ± 0.0097
4	0.8054 ± 0.0174
3	1.4290 ± 0.0351

Table 6.4: Resolution for HCAL + ECAL (ES in front) with HCAL calibrated using 50 GeV/c e^- .

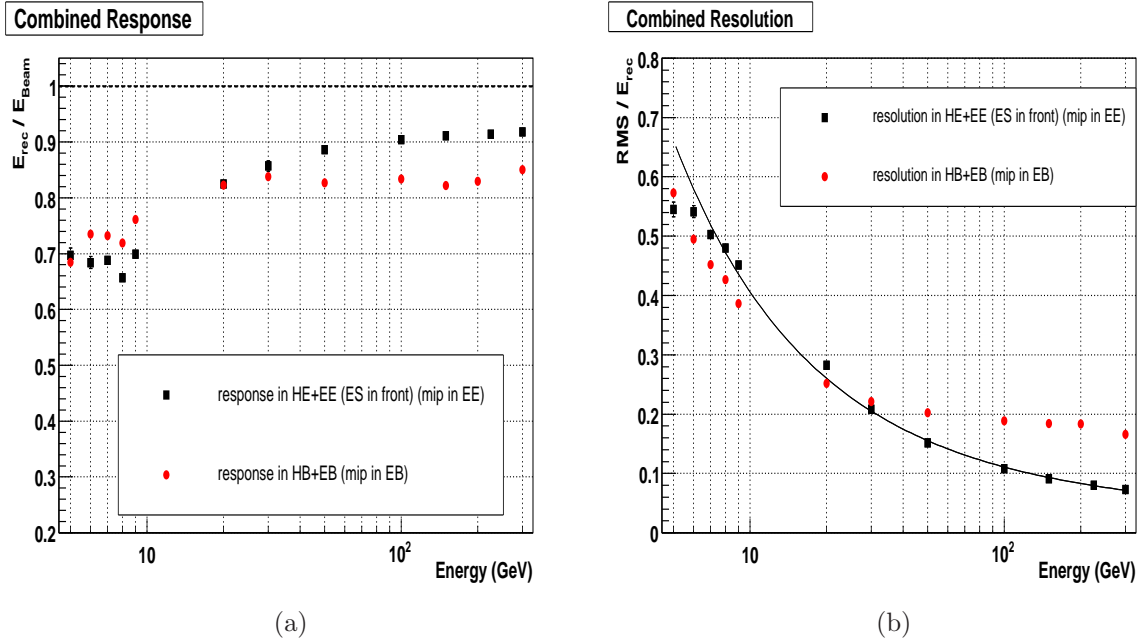


Figure 6.21: (a) Response and (b) resolution of the combined ECAL + HCAL system (with the preshower in front) with MIP in EE measured as a function beam momentum for π^- .

Momentum (GeV/c)	Response π^-
300	0.9178 ± 0.0059
225	0.9140 ± 0.0067
150	0.9109 ± 0.0063
100	0.9041 ± 0.0065
50	0.8862 ± 0.0068
30	0.8570 ± 0.0094
20	0.8248 ± 0.0068
9	0.6753 ± 0.0060
8	0.6507 ± 0.0048
7	0.6212 ± 0.0071
6	0.5844 ± 0.0108
5	0.5708 ± 0.0128
4	0.6352 ± 0.0158
3	0.7652 ± 0.0206

Table 6.5: Response for HCAL+ECAL (ES in front) with MIP in EE and with HCAL calibrated using 50 GeV/c electron.

Momentum (GeV/c)	Ratio of measured RMS to nominal energy π^-
300	0.0730 ± 0.0004
225	0.0798 ± 0.0005
150	0.0910 ± 0.0006
100	0.1080 ± 0.0007
50	0.1517 ± 0.0011
30	0.2082 ± 0.0022
20	0.2825 ± 0.0023
9	0.4512 ± 0.0040
8	0.4802 ± 0.0035
7	0.5026 ± 0.0057
6	0.5414 ± 0.0100
5	0.5452 ± 0.0122
4	0.8220 ± 0.0204
3	1.0642 ± 0.0287

Table 6.6: Response for HCAL+ECAL (ES in front) with MIP in EE with HCAL calibrated using 50 GeV/c electron.

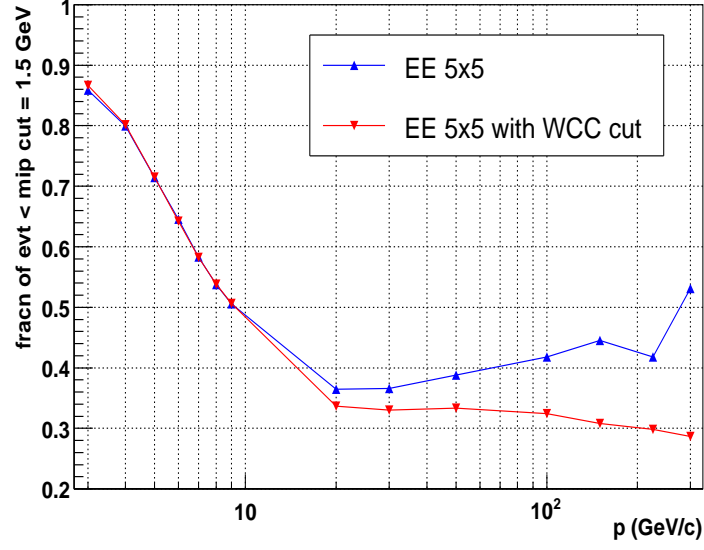


Figure 6.22: Fraction of events which deposit less than 1.8 GeV in the electromagnetic calorimeter as a function of beam momenta.

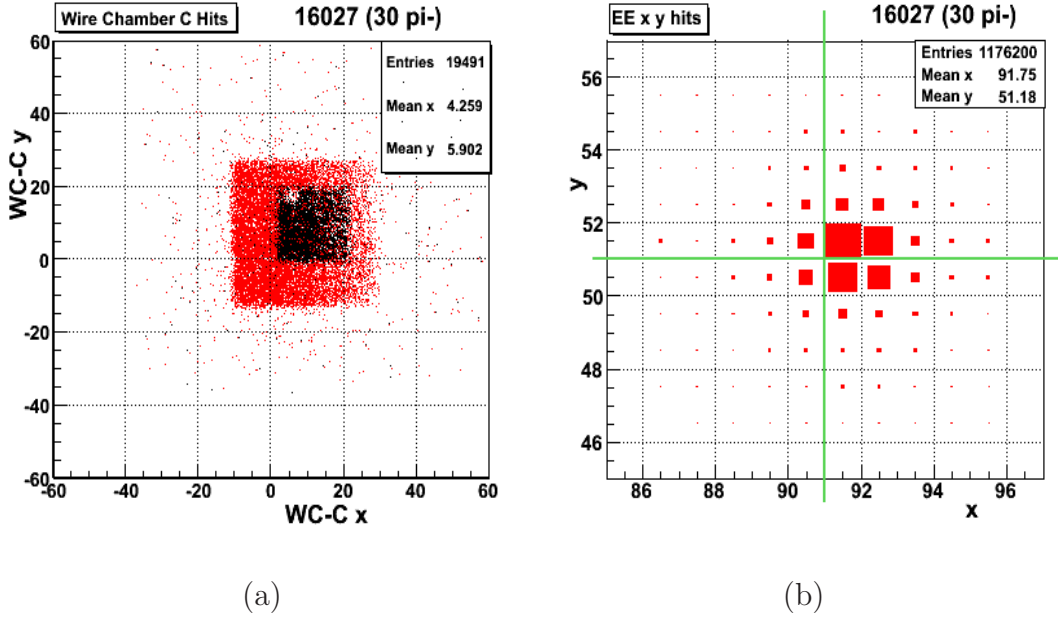


Figure 6.23: (a) Wire Chamber hits for two different trigger windows: $4\text{ cm} \times 4\text{ cm}$ (shown in red) and $2\text{ cm} \times 2\text{ cm}$ (shown in black). (b) Energy weighted occupancy in the EE crystals, x and y representing the crystal numbers in x and y direction respectively.

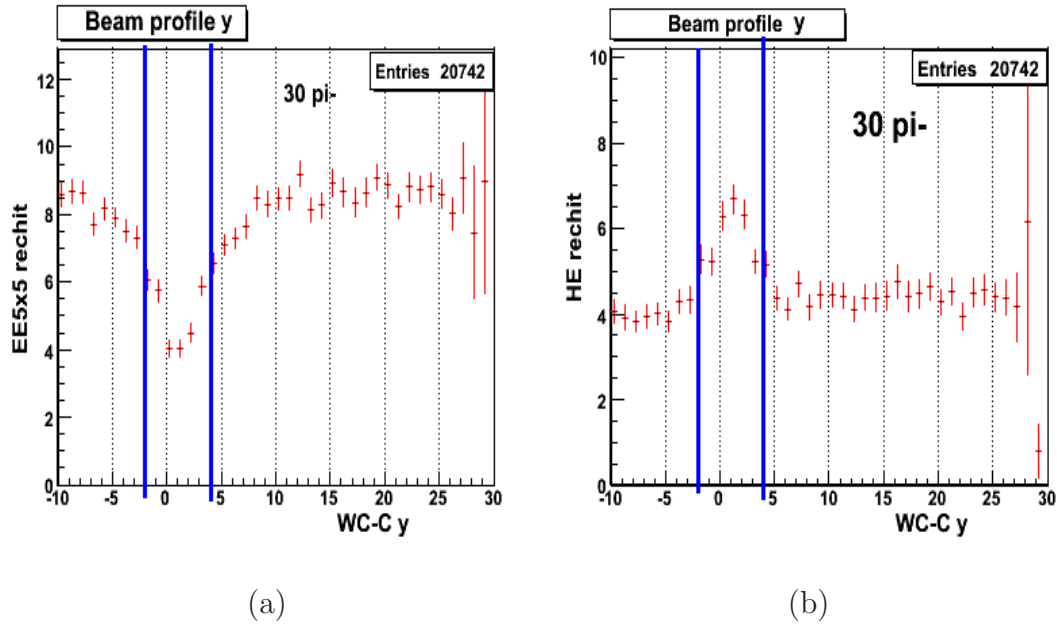


Figure 6.24: Beam profile for (a) EE and (b) HE as a function of the y coordinate measured in the wire chamber C.

ECAL crystals are studied in Figure 6.23. The Wire chamber C is the one upstream from the EE and closest to the calorimeter. Two triggers controlled by the scintillators S1-S4 are used in the test beam experiment. When a coincidence of S1, S2 and S4 is operational, the beam window has the size of $4\text{cm} \times 4\text{cm}$. On the other hand the beam window shrinks to $2\text{cm} \times 2\text{cm}$ when coincidence is demanded for all 4 scintillators. The EE occupancy plot in Figure 6.23 refers to effective beam size of $4\text{cm} \times 4\text{cm}$. It suggests that the beam is not shot exactly at the centre of the four super crystals, but it is shifted in the x direction. But in the y direction the beam was at the junction of the super crystals.

The wire chamber is then used to select a small window (40 mm in x and 1 mm in y direction) to the EE and the small window is slid over the EE crystals to scan any possible gap. Figure 6.24 shows a dip in the EE beam profile for the wire chamber window of 6 mm (from -2 mm to +4 mm) indicating a possible gap between the EE super crystals. A peak in HE beam profile for the same window of wire chamber y position reinforces the previous inference. Therefore, events are rejected if they correspond to the wire chamber y position for that region (Figure 6.25). The effect of that cut is evident in the MIP fraction plot in Figure 6.22. With this cut the corrected MIP fraction in the ECAL is found to decrease with energy for pion momentum above 100 GeV/c. The MIP fraction is constant for pions down to some ~ 8 GeV/c and then it starts increasing at lower energies. At these energies the peaks due to MIPs are no longer well separated from the energy deposited by pions in hadronic interactions and this may be the reason for this increase.

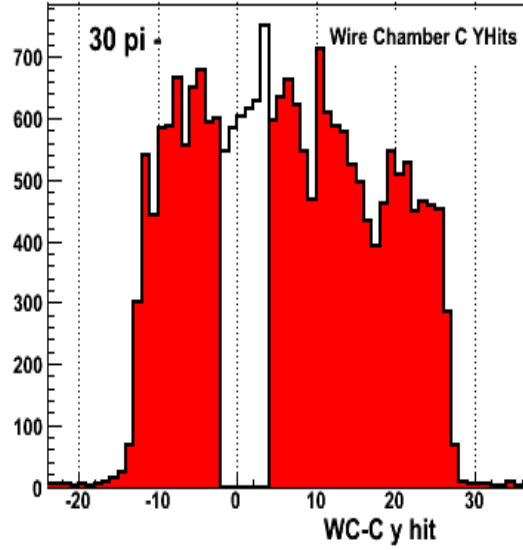


Figure 6.25: Cut on the wire chamber y position to mask the gap between EE super-modules.

6.2.6 Energy Measurements in the Preshower Detector

High energy focused beam is used to obtain the pulse shape for the preshower detector. In the test beam setup, the preshower detector has two planes. The plane in front gives information for x direction and the second plane gives information of the y coordinate. Figure 6.26 shows the occupancy in the two planes of the preshower detector. The occupancy plot in plane 1 clearly shows the missing two blocks in the top two corners. This is because of the way the ladders are placed for making the ES module.

Figure 6.27 shows the reconstructed energy in the two planes. It shows a MIP peak and a long tail indicating the start of a shower.

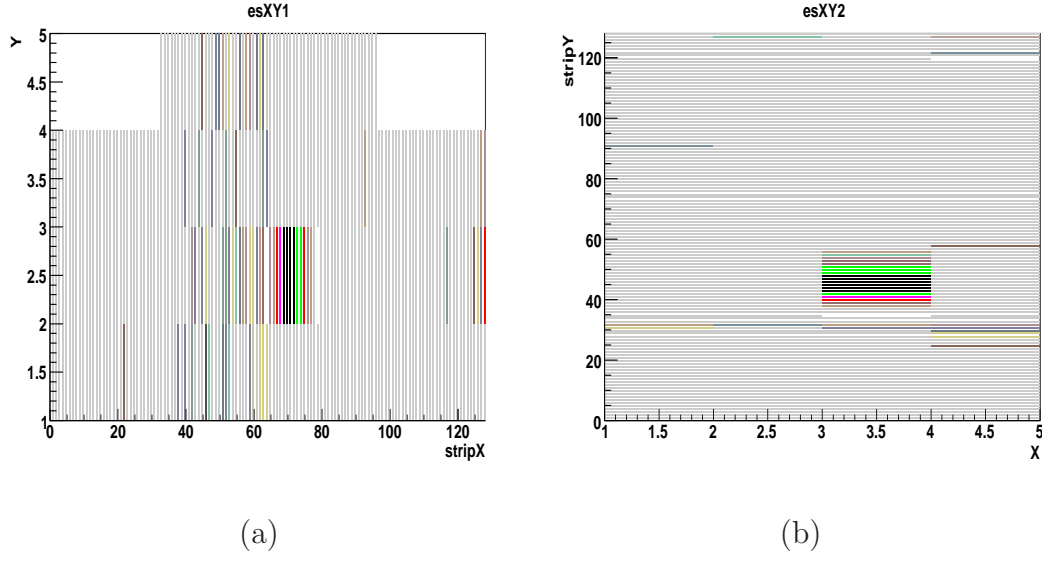


Figure 6.26: BeamSpot in the two planes - (a) plane 1 and (b) plane 2, of preshower for a 100 GeV focused e^- beam.

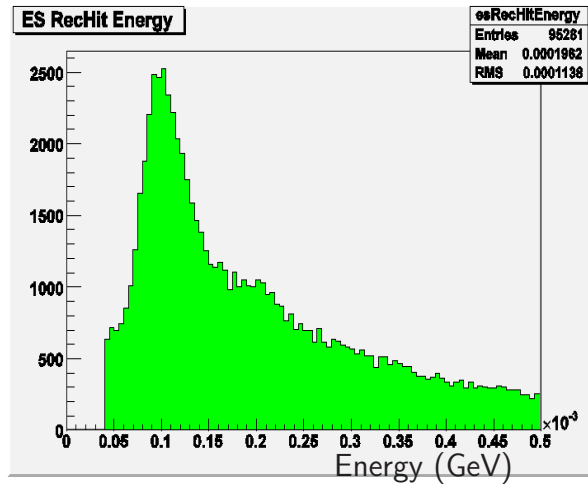


Figure 6.27: Combined energy in the two planes of the preshower detector for a 100 GeV electron beam.

Chapter 7

Multi-jet Studies

7.1 Multi-jet Topological Variables

Jet production is the dominant process in high p_T hadron-hadron collisions. This process is well described by perturbative QCD in terms of scattering cross section of two constituent partons convoluted with a pair of parton distribution functions that express the momentum distributions of partons within the proton. The hard scattering cross section itself can be written as an expansion in the strong coupling constant $\alpha_S(Q^2)$. The leading term in this expansion corresponds to the emission of two partons in the final state. The next term includes diagrams where an additional parton is observed in the final state due to hard gluon radiation (e.g. $gg \rightarrow ggg$). Such diagrams, examples of which are seen in Figure 7.1, diverge when any of the three partons become soft or when two of the partons become collinear.

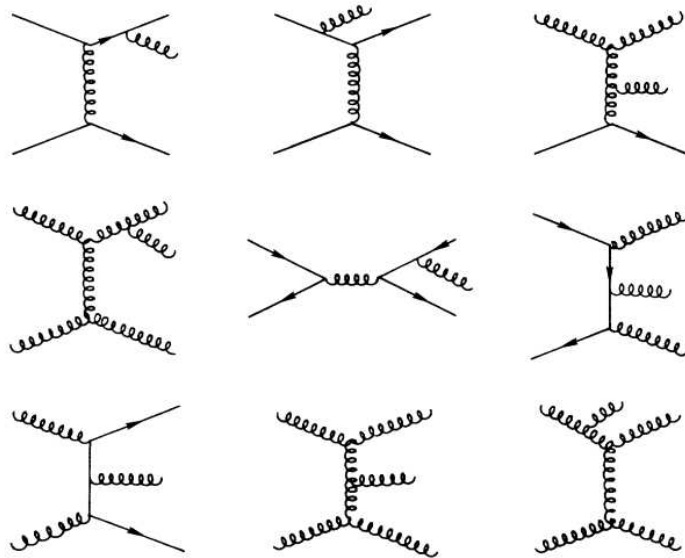


Figure 7.1: Feynman diagrams for 3 parton final state.

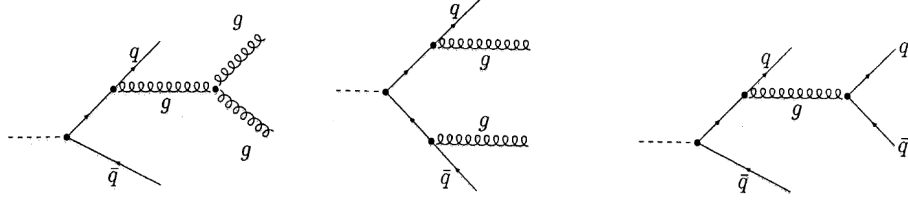


Figure 7.2: Feynman diagrams for 4-parton final state.

Perturbative QCD predicts two classes of 4-jet events which correspond to the processes: $q\bar{q}/gg \rightarrow q\bar{q}gg$ and $q\bar{q}/gg \rightarrow q\bar{q}q\bar{q}$. The first diagram in the Figure 7.2 contains a *three gluon vertex*, a consequence of the non-Abelian nature of QCD.

In order to study the three and four parton final state a class of observables are defined for QCD studies. They have been studied widely in the earlier LEP (e^+e^-) [84, 85] and the Tevatron ($p\bar{p}$) [86, 87] experiments. Here several multi-jet observables are studied using simulation samples of hadronic events with the CMS detector. The kinematic and angular properties of these variables are computed from the four-vectors of jets.

7.1.1 3-parton Variables

The topological variables are defined in the parton or jet centre-of-mass system (CM). The topological properties of the three-parton final state in the centre-of-mass system can be described in terms of five independent variables [86]. Three of the variables reflect partition of the CM energy among the three final-state partons. The other two variables define the spatial orientation of the planes containing the three partons.

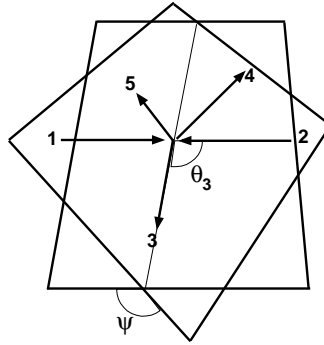


Figure 7.3: An Illustration of the three-jet angular variables - ψ and θ_3 . The angle ψ is the angle between the plane containing the beam line and the highest energy jet in the CM frame of the 3-jet system, and the next two highest energy jets. As $\psi \rightarrow 0^\circ$ or 180° , the contribution of initial state radiation from incoming partons increase the rate.

It is convenient to introduce the notation $1+2 \rightarrow 3+4+5$ for the three parton process. Here, numbers 1 and 2 refer to incoming partons while the numbers 3, 4 and 5 label the

outgoing partons, ordered in descending energies in the parton CM frame, i.e., $E_3 > E_4 > E_5$. The final state parton energy is an obvious choice for the topological variables for the three parton final state. For simplicity, E_i ($i = 3, 4, 5$) is often replaced by the scaled variable x_i ($i = 3, 4, 5$), which is defined by $x_i = 2E_i/\sqrt{\hat{s}}$, where \hat{s} is the centre of mass energy of the hard scattering process. By definition, $x_3 + x_4 + x_5 = 2$. The internal structure of the three parton final state is determined by any two scaled parton energies. The third one is calculated using the above relation. With this choice it is important to consider $\sqrt{\hat{s}}$ as the third independent variable.

The angles that fix the event orientation can be chosen to be (1) the cosine of the polar angle of parton 3 with respect to the beam ($\cos\theta_3$), (2) the azimuthal angle of parton 3 (ϕ_3), and (3) the angle between the plane containing partons 1 and 3 and the plane containing partons 4 and 5 (ψ) defined by

$$\cos\psi = \frac{(\vec{p}_1 \times \vec{p}_3) \cdot (\vec{p}_4 \times \vec{p}_5)}{|\vec{p}_1 \times \vec{p}_3||\vec{p}_4 \times \vec{p}_5|} \quad (7.1)$$

where \vec{p}_i is the parton momentum. Figure 7.3 illustrates the definition of the topological variables for the three parton final state. The five independent kinematic variables are chosen to be $\sqrt{\hat{s}}$, x_3 , x_5 , $\cos\theta_3$, and ψ . Because of the differences in the spins and couplings of quarks to gluons and gluons to gluons, the QCD predictions for these subprocesses can differ depending on whether one selects subprocesses initiated by gg , gq , or $q\bar{q}$. Another set of interesting variables is the scaled invariant masses of jet pairs: $\mu_{ij} = \frac{m_{ij}}{\sqrt{\hat{s}}}$ where m_{ij} is the invariant mass of partons i and j . The scaled invariant mass (μ_{ij}) is sensitive to the scaled energies of the two partons, the angle between the two partons, and the correlation between these variables. Using dimensionless variables and making comparisons of normalized distributions minimizes the systematic uncertainties due to detector resolution and jet energy scale and therefore facilitates comparison between data and theoretical calculation.

7.1.2 4-parton Variables

To define a four-parton final state in its centre of mass system, eight independent parameters are needed. Two of these define the overall event orientation while the other six fix the internal structure of the four-parton system. In contrast to the three-parton final state, there is no simple relationship between the scaled parton energies and the opening angles between partons. Consequently, the choice of topological variables is less obvious in this case. Variables are defined here in a way similar to those investigated for the three-parton final state. The four partons are ordered in descending energy in the parton CM frame and labeled from 3 to 6. The variables include the scaled energies (x_i , with $i = 3, \dots, 6$), the cosines of polar angles ($\cos\theta_i$, with $i = 3, \dots, 6$) of the four jets,

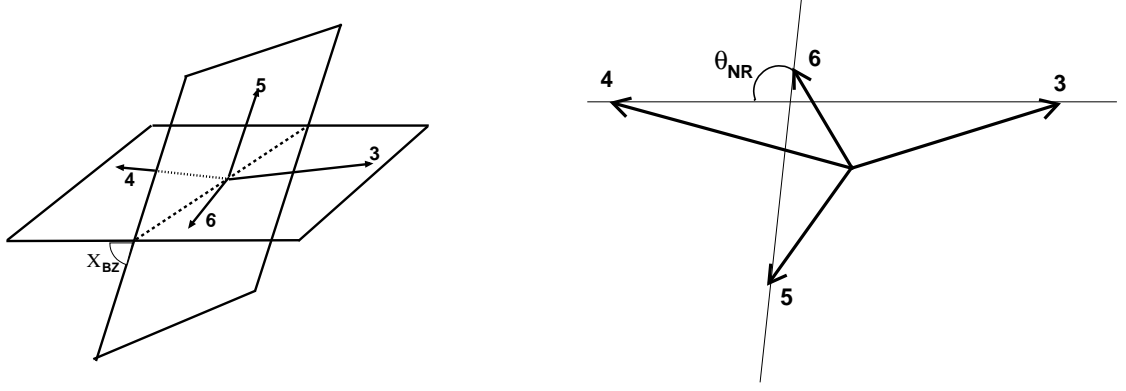


Figure 7.4: Illustration of the Bengtsson-Zerwas angle (χ_{BZ}) and the Nachtmann-Reiter angle (θ_{NR}) definitions for the four jet events. The left figure shows the Bengtsson-Zerwas angle which is the angle between the plane containing the two leading jets and the plane containing the two non-leading jets. The right figure shows the Nachtmann-Reiter angle which is the angle between the momentum vector differences of the two leading jets and the two non-leading jets.

the cosines of the opening angles between partons ($\cos \omega_{ij}$, with $i, j = 3, \dots, 6$ and $i \neq j$), and the scaled masses ($\mu_{ij} = m_{ij}/\sqrt{\hat{s}}$, with $i, j = 3, \dots, 6$ and $i \neq j$) of parton pairs. In addition, two variables characterizing the orientation of event planes are investigated. One of the variables is the Bengtsson-Zerwas angle (χ_{BZ}) [88] defined (Figure 7.4) as the angle between the plane containing the two leading jets and the plane containing the two non-leading jets:

$$\cos \chi_{BZ} = \frac{(\vec{p}_3 \times \vec{p}_4) \cdot (\vec{p}_5 \times \vec{p}_6)}{|\vec{p}_3 \times \vec{p}_4| |\vec{p}_5 \times \vec{p}_6|} \quad (7.2)$$

The second variable is the cosine of the Nachtmann-Reiter angle [89] ($\cos \theta_{NR}$) defined as the angle between the momentum vector differences of the two leading jets and the two non-leading jets:

$$\cos \theta_{NR} = \frac{(\vec{p}_3 - \vec{p}_4) \cdot (\vec{p}_5 - \vec{p}_6)}{|\vec{p}_3 - \vec{p}_4| |\vec{p}_5 - \vec{p}_6|} \quad (7.3)$$

Figure 7.4 illustrates the definitions of χ_{BZ} and θ_{NR} variables. Historically, χ_{BZ} , θ_{NR} were proposed [88][89] for e^+e^- collisions to study gluon self coupling. Their interpretation in pp collisions is rather complicated, but the variables can be used as a tool for studying the internal structure of the four-jet events.

The original idea for proposing these angular variables was to quantify the differences between the Abelian and non-Abelian theories. The basic idea is to measure the relative orientation of the planes containing the primary $q\bar{q}$ jets and the secondary gg or $q\bar{q}$ jets.

In practice one cannot distinguish primary and secondary jets on an event by event basis, but on average the secondary jets are less energetic, in the same way that the gluon in $q\bar{q}g$ production is the least energetic jet on average.

7.2 Invariant mass of 3- and 4-jet system

Event selection for this study has been elaborately discussed in chapter 4. Events are preselected by requiring at least two calorimeter jets with raw (uncorrected) transverse momentum $p_T > 30$ GeV/c within a region of $|\eta| < 3.0$ (within the end cap region of the CMS calorimeter) which is considered specially suitable for early data analysis. Events are selected based on conditions described in chapter 4.

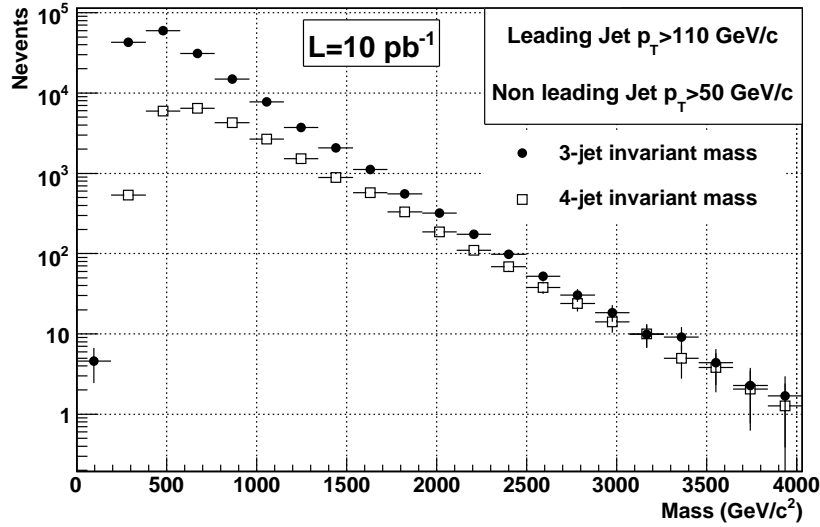


Figure 7.5: Distribution of invariant mass of the 3- and 4-jet events as expected from integrated luminosity of 10 pb^{-1} .

For the 3-jet case, the momenta of the three most leading jets are boosted to the CM frame of the three leading jets. All other jets in the event are ignored. The jets are reordered in descending energy in their CM system. The topological variables (x_3 , x_4 , $\cos \theta_3$ and ψ) are calculated.

Four jet events are selected in a similar manner. Events are required to have at least four jets satisfying the threshold. The four leading jets are boosted to their centre of mass frame and are ordered in decreasing energy.

The invariant mass distribution of the three(four) highest p_T jets in case of 3(4)-jet events is shown in Figure 7.5.

7.3 Multi-jet Topological Distributions

The effect of hadronisation is different for different multijet variables. Therefore, several variables need to be examined for a better understanding of the underlying nature of the fundamental processes. The topologies of the multijet variables are discussed below.

7.3.1 Topologies of Three-Jet Events

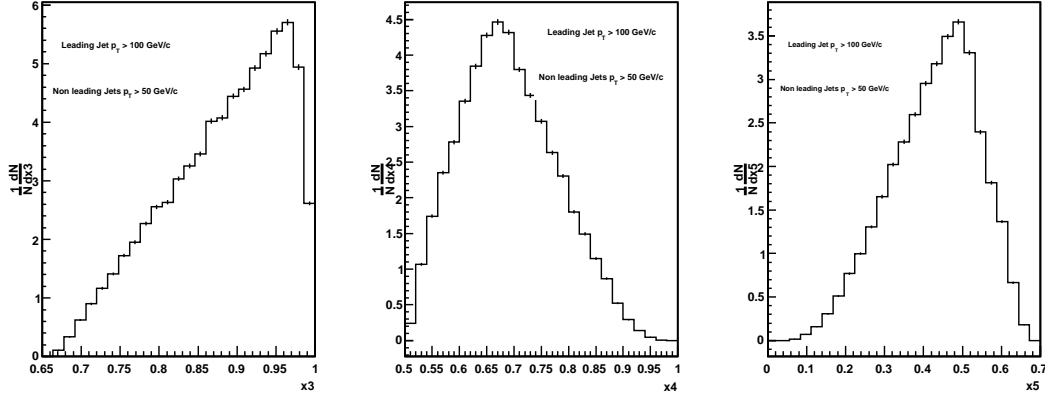


Figure 7.6: Particle level distributions of scaled energies of the three jets at $\sqrt{s} = 10$ TeV. The events are selected requiring the leading jet p_T to be above 110 GeV/c.

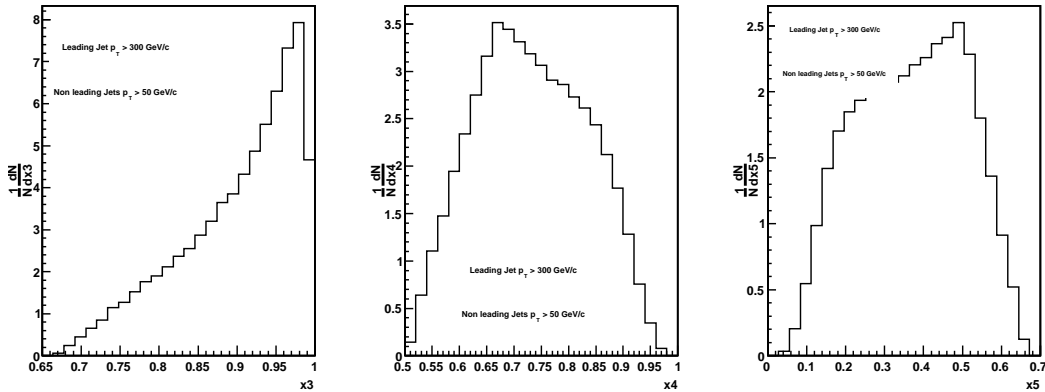


Figure 7.7: Particle level distributions of energy fractions of the three jets at $\sqrt{s} = 10$ TeV. The events are selected requiring the leading jet p_T to be above 300 GeV/c.

Figures 7.6, 7.7, 7.8 and 7.9 show the three jet topological distributions. In Figure 7.6 the scaled jet energies (x_3, x_4, x_5) are shown. The three jets are labeled in order of decreasing energy in the CM frame. The energy fraction for the leading jet peaks near 1 and the next leading jets distribute themselves to restore the relation $\sum_i^3 x_i = 2$. Figure

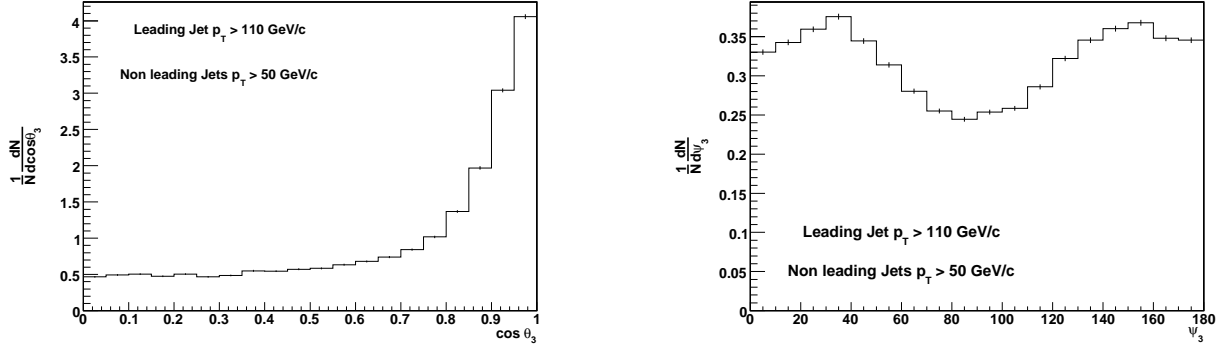


Figure 7.8: Particle level distributions of the angular variables for three jet case where the leading jet p_T is above 110 GeV/c. The left plot represents the cosine of the polar angle of the hardest jet with respect to the beam ($\cos \theta_3$). The right plot is for the angle between the plane containing partons 1 and 3 and the plane containing partons 4 and 5 (ψ).

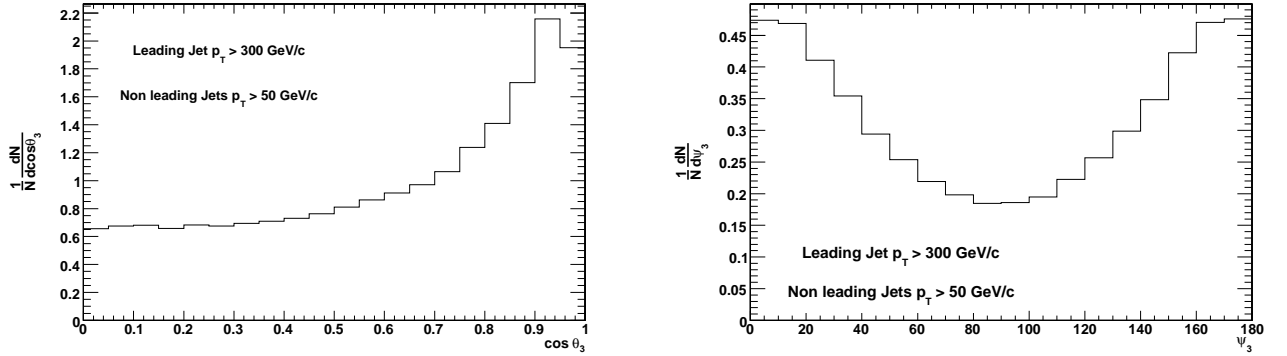


Figure 7.9: Particle level distributions of the angular variables for three jet case where the leading jet p_T is above 300 GeV/c. The left plot represents the cosine of the polar angle of the hardest jet with respect to the beam ($\cos \theta_3$). The right plot is for the angle between the plane containing partons 1 and 3 and the plane containing partons 4 and 5 (ψ).

7.7 shows that in the high p_T regime the scaled energy of the leading jet peaks sharply at 1 and for second leading jet shifts towards 1 as well leaving the scaled energy for the third leading jet to shift towards 0.

The $\cos \theta_3$ distribution is shown as the left plot of Figure 7.8. As in the angular distributions of two-jet events, an angular dependence characteristic of Rutherford t-channel scattering is noticed. The large angular coverage of CMS calorimeter allows to cover the entire $\cos \theta_3$ range. The measured ψ distribution is shown as the right hand side plot of Figure 7.8. The Ψ angle ranges from 0 to π with an almost symmetric distribution peaking at 30° away from both the limits. For higher p_T regime, as shown in Figure 7.9, Ψ angle peaks much closer to the two limits, 0 and π . Also the $\cos \theta_3$ distribution gets flattened out in the high p_T regime.

7.3.2 Topologies of Four-Jet Events

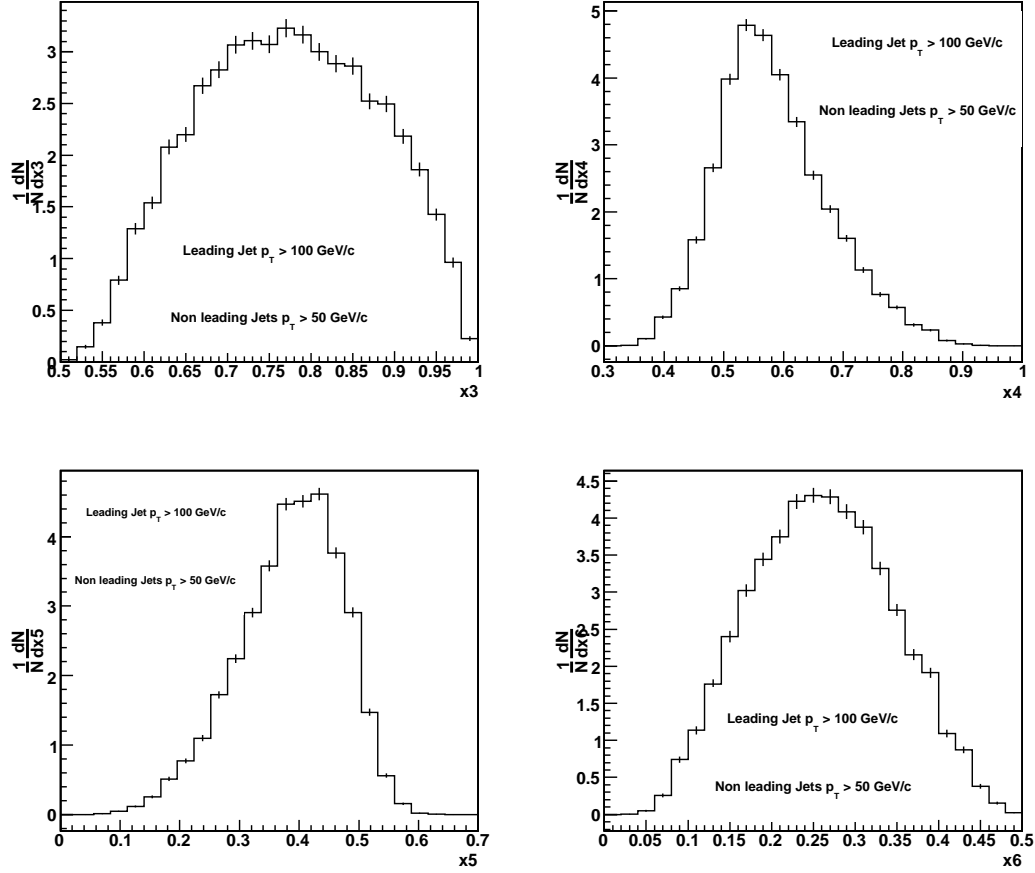


Figure 7.10: Particle level distribution of scaled energies of the four leading jets at $\sqrt{s} = 10$ TeV. The events are selected by requiring the leading jet p_T to be above 110 GeV/c.

The four scaled energies of four jet events are shown in Figure 7.10 and 7.11 for different p_T regimes. The four jets are ordered in decreasing energy in their centre of mass system. Out of the four scaled energy variables shown, only three distributions are independent. The other is fixed by the condition $\sum_i x_i = 2$. The scaled energy distributions look similar in both the p_T regimes.

Figure 7.12 shows the measured Bengtsson-Zerwas and Nachtmann-Reiter angles for inclusive 4-jet events where the leading jet p_T is above 110 GeV/c. The Nachtmann-Reiter angle is plotted as a function of cosine of the angle whereas the Bengtsson-Zerwas angle is plotted in unit of degrees. The Bengtsson-Zerwas angle shows a rather flat distribution. Had it been a $2 \rightarrow 2$ process the distribution would have been more populated near 0. But the presence of at least 4 jets (with the selection of inclusive 4-jet events) the distribution deviates away from 0 for the angular distribution. For the Nachtmann-Reiter angle, events tend to peak near 1. For high p_T regime (Figure 7.13), the distribution of

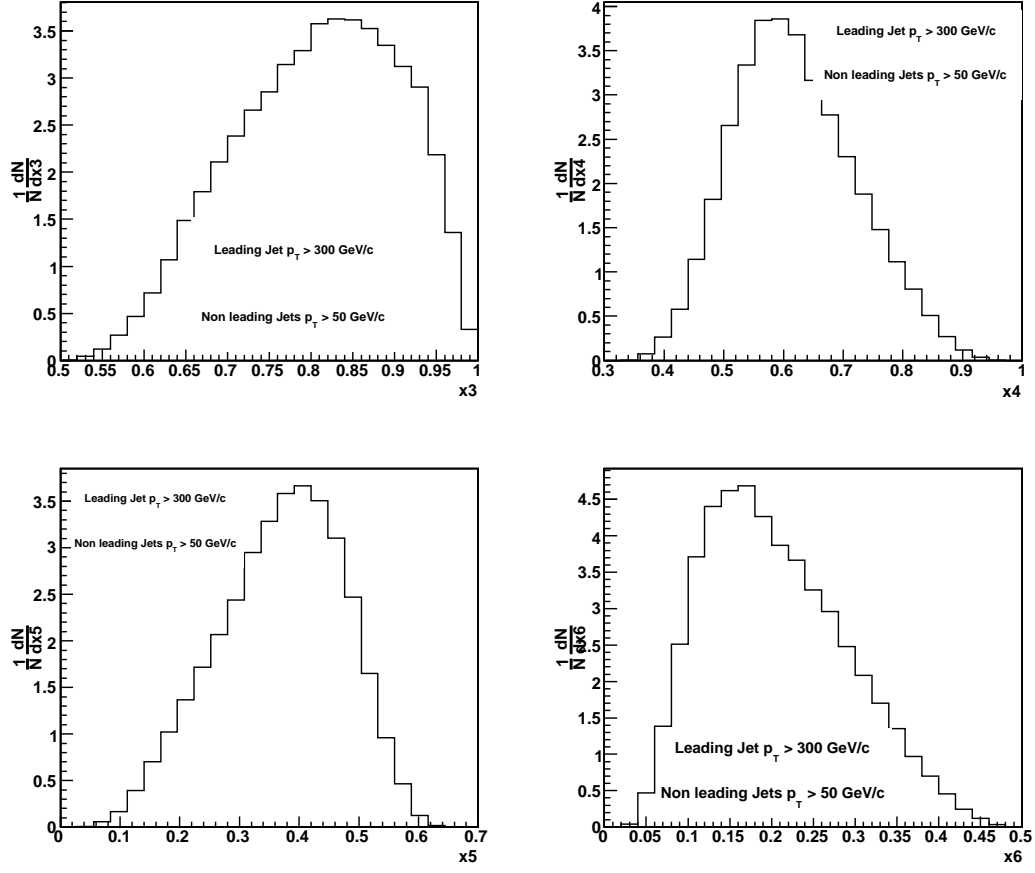


Figure 7.11: Particle level distribution of scaled energies of the four leading jets at $\sqrt{s} = 10$ TeV. The events are selected by requiring the leading jet p_T to be above 300 GeV/c.

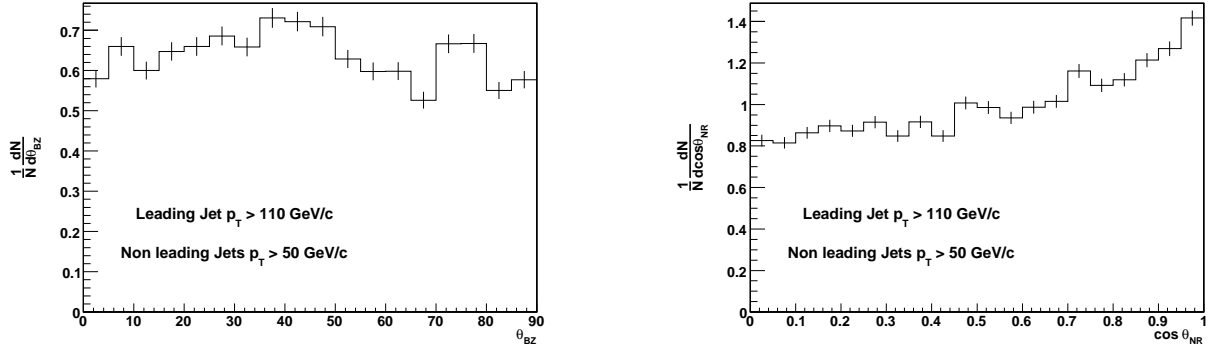


Figure 7.12: The plot on the left side shows the distribution of the angle between the plane containing the two leading jets and the plane containing the two non-leading jets (the Bengtsson-Zerwas angle, θ_{BZ}). The plot on the right side shows the distribution of the angle between the momentum vector differences of the two leading jets and the two non-leading jets (the Nachtmann-Reiter angle, $\cos\theta_{NR}$). The events are selected by requiring the leading jet p_T to be above 110 GeV/c.

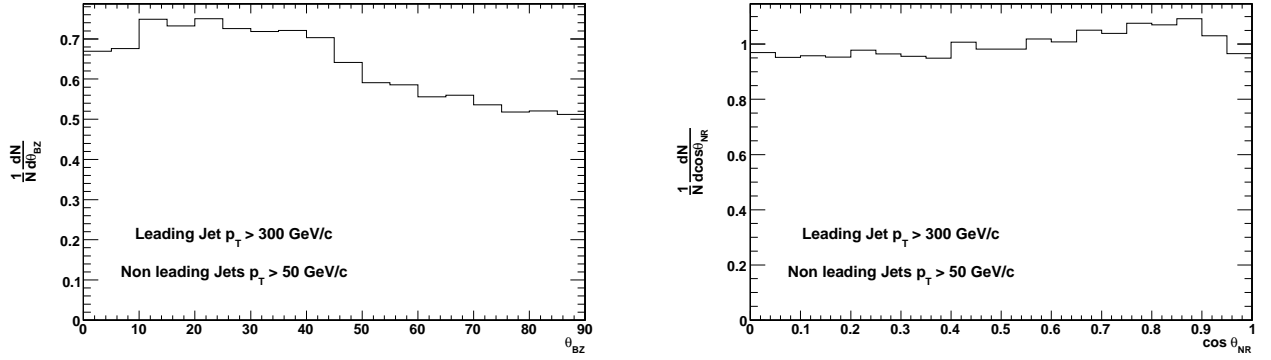


Figure 7.13: The plot on the left side shows the distribution of the angle between the plane containing the two leading jets and the plane containing the two non-leading jets (the Bengtsson-Zerwas angle, θ_{BZ}). The plot on the right side shows the distribution of the angle between the momentum vector differences of the two leading jets and the two non-leading jets (the Nachtmann-Reiter angle, $\cos \theta_{NR}$). The events are selected by requiring the leading jet p_T to be above 300 GeV/c.

Bengtsson-Zerwas angle seems to peak more towards zero and that for Nachtmann-Reiter angle becomes more uniform.

Variable	Stat uncertainty
3 Jet Variables	
x_3	1.65
x_4	1.84
x_5	1.67
Ψ	1.05
$\cos \theta$	1.84
4 Jet Variables	
x_3	3.87
x_4	3.72
x_5	3.73
x_6	3.91
θ_{BZ}	3.36
$\cos \theta_{NR}$	2.94

Table 7.1: Average statistical uncertainties for 3-jet and 4-jet variables.

Table 7.1 shows the average statistical uncertainty for the different variables as they are expected to be measured based on an integrated luminosity of 10 pb^{-1} . The average uncertainty due to statistical fluctuations is around 1–2% for 3-jet variables and is around 4% for the 4-jet variables. This is because of the fact that statistics is smaller for the inclusive 4-jet events as compared to inclusive 3-jet events.

7.4 Detector Effects

The particle level jets are smeared using a Gaussian distribution representing the detector resolution function and are compared to detector level jets (Calojets) with correction. The jets need to be smeared to take care of (1) energy resolution, (2) position resolution. Position resolution will affect the measurements in the jet directions and will give rise to resolutions in η as well as ϕ .

7.4.1 Energy Resolution

The effect of the jet energy resolution is studied by applying a jet energy resolution smearing function on generator level jets and comparing these to the jets which are not smeared. After the smearing, the jets are reordered in p_T . The following resolution smearing functions [91] (obtained for Monte Carlo samples produced during the summer of 2008) in the barrel region ($|\eta| < 1.4$) as demonstrated in Eq.7.4, has been used:

$$\frac{\sigma(p_T)}{p_T} = \sqrt{\left(\frac{4.35}{p_T[GeV/c]}\right)^2 + \left(\frac{1.34}{\sqrt{p_T[GeV/c]}}\right)^2 + (0.03)^2} \quad (7.4)$$

For the end cap region ($1.4 < |\eta| < 2.6$) the following parameters are used:

$$\frac{\sigma(p_T)}{p_T} = \sqrt{\left(\frac{5.03}{p_T[GeV/c]}\right)^2 + \left(\frac{0.96}{\sqrt{p_T[GeV/c]}}\right)^2 + (0.04)^2} \quad (7.5)$$

7.4.2 Position Resolution

The effect of position resolution is studied by smearing of the angular variables: pseudo-rapidity (η) and azimuthal angle (ϕ).

7.4.2.1 Resolution in Eta

The effect of the η resolution is studied by applying a resolution smearing function on generator level jets and comparing these to the unsmeared jets. The smearing function for η in the barrel region ($|\eta| < 1.4$) is

$$\sigma\eta = \sqrt{\left(\frac{1.43}{p_T[GeV/c]}\right)^2 + \left(\frac{0.27}{\sqrt{p_T[GeV/c]}}\right)^2 + (0.014)^2}, \quad (7.6)$$

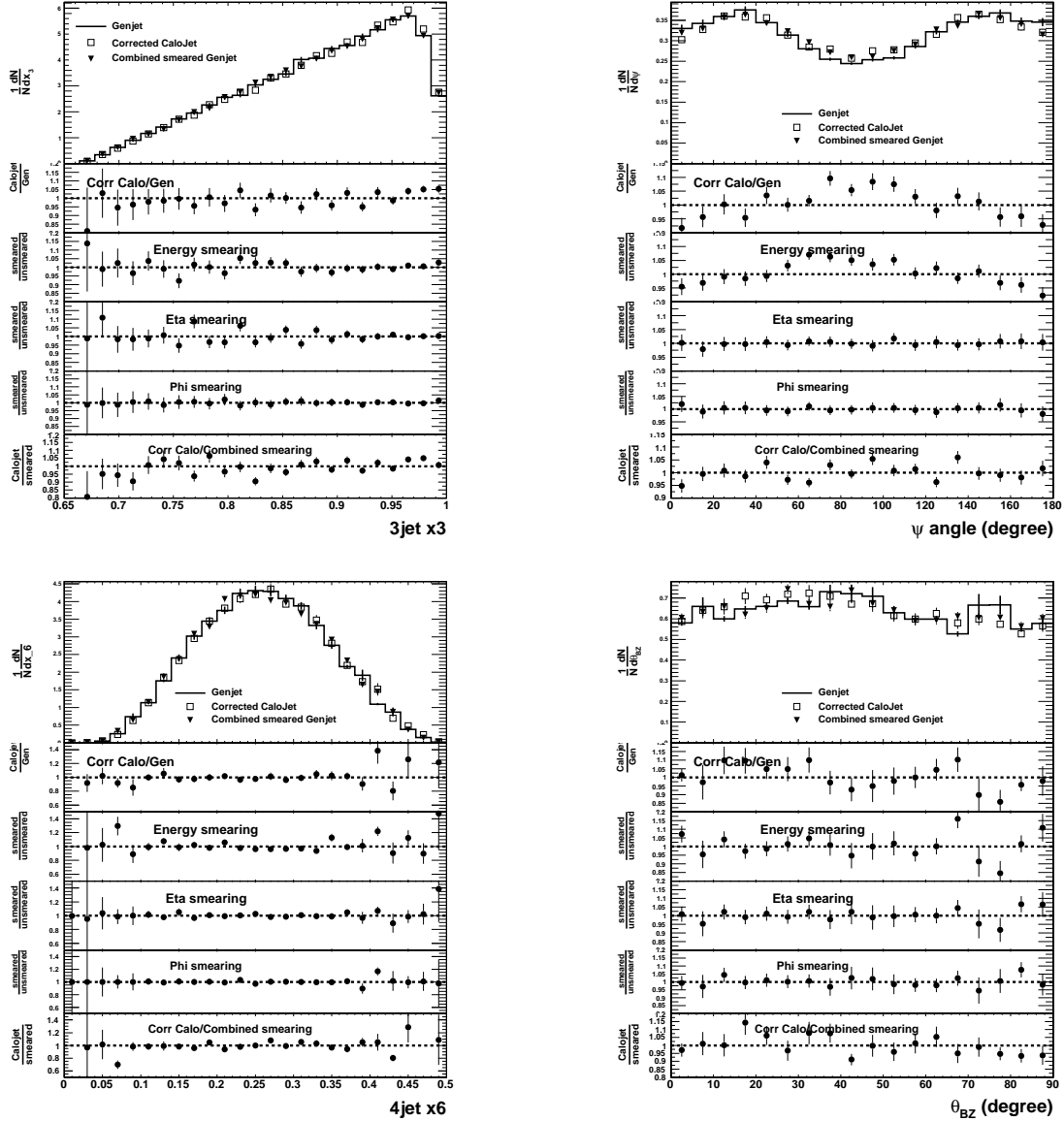


Figure 7.14: The effect of smearing of Genjets on the multi-jet distributions. The top left shows the energy fraction of the hardest jet in the 3-jet case. The top right plot shows the ψ angle for inclusive 3-jet events. Bottom left plot shows the energy fraction of the 4th leading jet in the 4-jet case. The Bengtsson-Zerwas angle is shown in the bottom right plot. In each of the figures the histograms from top to bottom are as follows: distributions with Genjets, corrected jets and combined smeared Genjets; ratio of corrected Calojets to Genjets; ratio of smeared and unsmeared Genjets with only energy smearing; ratio of smeared and unsmeared Genjets with only η smearing; ratio of smeared and unsmeared Genjets with only ϕ smearing; ratio of corrected Calojets to the smeared Genjets with energy+ η + ϕ smearing.

and for the endcap ($1.4 < |\eta| < 3.0$) region the function is

$$\sigma\eta = \sqrt{\left(\frac{1.47}{p_T[\text{GeV}/c]}\right)^2 + \left(\frac{0.22}{\sqrt{p_T[\text{GeV}/c]}}\right)^2 + (0.015)^2} . \quad (7.7)$$

7.4.2.2 Resolution in Phi

The effect of the ϕ resolution is studied by applying a resolution smearing function on generator level jets and comparing these to the unsmeared jets. The smearing function for ϕ in the barrel region ($|\eta| < 1.4$) is

$$\sigma\phi = \sqrt{\left(\frac{2.57}{p_T[\text{GeV}/c]}\right)^2 + \left(\frac{0.29}{\sqrt{p_T[\text{GeV}/c]}}\right)^2 + (0.010)^2}, \quad (7.8)$$

and for the endcap ($1.4 < |\eta| < 3.0$) region the function is

$$\sigma\phi = \sqrt{\left(\frac{2.06}{p_T[\text{GeV}/c]}\right)^2 + \left(\frac{0.28}{\sqrt{p_T[\text{GeV}/c]}}\right)^2 + (0.013)^2}. \quad (7.9)$$

7.4.3 Combined Effect of Energy and Position Resolution

After the studies of the individual effects of energy, η and ϕ resolutions, the combined smearing effect is studied. It is worthwhile to see whether a simple Gaussian smearing of energy, η , ϕ of the jets can reproduce the detector effects as observed in the calorimeter jets after corrections. In Figure 7.14 the top left plot shows the energy fraction of the most energetic jet in the 3-jet case. The top right plot shows the ψ angle in the 3-jet case. The bottom left plot shows the energy fraction of the 4th leading jet in the 4-jet case. The Bengtsson-Zerwas angle is shown as the bottom right plot.

In each of the figures the effect of the following quantities are examined:

- Ratio of Detector level jets to the Particle level jets,
- Effect of only energy smearing,
- Effect of only η smearing,
- Effect of only ϕ smearing,
- Effect of combined smearing.

The average of the ratios between smeared and generator level distributions are given in Table 7.2. As can be seen from the table, the dominating contribution due to detector correction comes from the energy resolution of the jets which is well within $\pm 5\%$ for all the variables. The effect of position resolution which is reflected in the smearing of η and ϕ is found to be small for most of the variables. The small residual difference between the detector level distributions and the generator level ones are assigned as systematic uncertainty in the unfolding of the detector corrections as discussed in Section 7.8.

Variable	RMS (in %) of the ratio between smeared and unsmeared distributions					
	Corr/Gen	E smear	η smear	ϕ smear	Comb smear	Corr/Combined
3 Jet Variables						
x_3	1.83	1.76	2.14	0.55	2.14	2.50
x_4	3.74	3.01	1.15	0.47	3.04	5.36
x_5	4.20	3.16	0.84	0.30	3.89	4.50
Ψ	2.80	2.18	0.49	0.52	2.21	1.78
$\cos \theta$	1.94	2.80	1.86	0.90	2.72	2.70
4 Jet Variables						
x_3	1.58	3.56	1.48	1.09	4.41	5.16
x_4	3.31	3.72	4.07	0.38	4.37	5.88
x_5	2.55	3.69	1.95	0.36	2.70	5.00
x_6	2.57	5.37	1.81	4.30	7.20	7.30
θ_{BZ}	3.86	4.74	2.41	1.89	4.05	3.51
$\cos \theta_{NR}$	4.00	3.66	4.34	2.50	2.14	2.76

Table 7.2: RMS (in %) of the ratio of the smeared and generator level distributions for different multi-jet variables.

7.5 Systematic Uncertainty

The leading source of systematic errors in QCD data analysis is the limited knowledge of the jet energy scale (JES). The JES uncertainty at start up is expected to be $\pm 10\%$ based on the best educated guess [92] from earlier experiments. Changing the JES correction within its uncertainty changes the jet shapes as jets migrate between p_T bins. However, jet spectra vary slowly with jet p_T . So the net effect on the distributions is expected to be small. To determine the impact on the jet spectra, the p_T of the jets are changed by $\pm 10\%$ and the whole analysis is repeated. The ratio of the distributions before and after the changes is examined. Figure 8.3 shows the resulting distributions due to the changes as well as the ratios for four multi-jet variables: energy fraction x_3 and angle Ψ in the 3-jet sample and energy fraction x_6 and the Bengtsson-Zerwas angle in the 4-jet sample. As can be seen from these plots, the distributions are not very sensitive to jet energy scale corrections. The error bars in the energy fraction x_3 is large for lower values which is mainly due to correlated errors. Table 8.1 summarizes average effect for several multi-jet variables in the 3-jet and the 4-jet samples. All these deviations are below 4%.

Table 8.1 summarizes average effect of uncertainty in the jet energy scale for several multi-jet variables in inclusive 3-jet and 4-jet samples. All these deviations are between 1% and 4%.

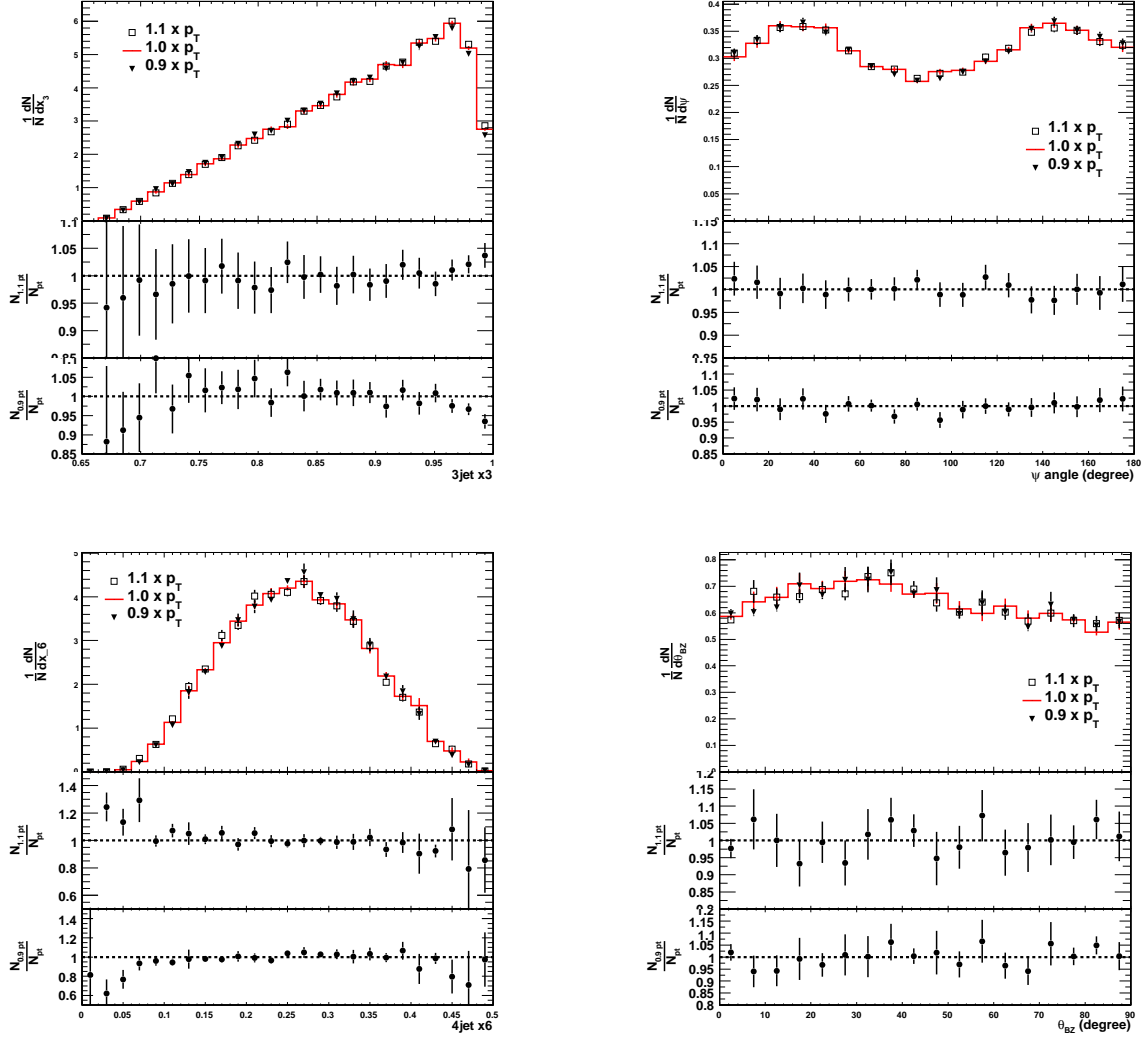


Figure 7.15: The effect of uncertainty in the jet energy scale on the multi-jet distributions. The top left shows the energy fraction of the hardest jet in the 3-jet case. The top right plot shows the ψ angle in 3-jet case. Bottom left plot shows the energy fraction of the 4th leading jet in the 4-jet case. The Bengtsson-Zerwas angle is shown in bottom right plot.

7.6 Sensitivity to Jet Algorithm

The influence of different jet clustering algorithm on the shape of the multi-jet distributions are studied by using different algorithms and with different jet resolution parameters. From these studies the algorithm (and resolution parameter) which gives rise to the smallest correction factors from calorimeter level jets to particle level jets is preferred.

The following algorithms are examined with the respective jet resolution parameters:

- the seedless infrared safe cone algorithm with radius $R = 0.5$ (SisCone5) or $R = 0.7$ (SisCone7) and an energy-sharing fraction of $f = 0.75$.

Variable	Jet p_T increased by 10%	Jet p_T decreased by - 10%	Average systematics
3 Jet Variables			
x_3	1.36	2.59	2.19
x_4	1.17	3.58	2.78
x_5	1.81	3.78	3.10
Ψ	0.86	1.14	1.02
$\cos \theta$	1.67	1.11	1.45
4 Jet Variables			
x_3	3.56	3.79	3.69
x_4	1.95	1.54	1.80
x_5	4.25	1.69	3.30
x_6	3.03	4.64	3.93
θ_{BZ}	2.50	2.34	2.42
$\cos \theta_{NR}$	2.09	1.99	2.07

Table 7.3: RMS (in %) of the ratio of distributions when jet p_T 's are increased or decreased by 10% with respect to the default distribution.

- the fast k_T algorithm [93] with a resolution parameter $D = 0.4$ (KT4) and $D = 0.6$ (KT6).

The normalized multi-jet distributions are quite sensitive to the specific choice of these jet algorithms, as can be seen in Figure 7.16. The plots show distributions of two typical variables, energy fraction x_3 of the most energetic jet in the 3-jet sample and the Bengtsson-Zerwas angle in the four jet sample. Detector as well as generator level distributions are shown in the figure. Table 7.4 summarizes the average level of correction for the multi-jet variables in the four different jet algorithms. The level of detector corrections are roughly similar. For 3-jet variables, SisCone5 seem to perform better than the others. This to certain extent justifies the use of SisCone5 as the default algorithm in this study.

7.7 Sensitivity to Different Event Generators

7.7.1 Parton Shower versus Matrix Element

In order to demonstrate the sensitivity of hadronic multi-jet distributions to different models of multi-jet production, the distributions are compared, as they are expected to be measured based on an integrated luminosity of 10 pb^{-1} , to the generator level predictions as obtained from two event generators that contain different models of QCD multi-jet production, PYTHIA 6.409 [36] and MADGRAPH. PYTHIA is based on a leading-order matrix elements of $2 \rightarrow 2$ processes complemented by a parton shower while MADGRAPH uses matrix element calculation.

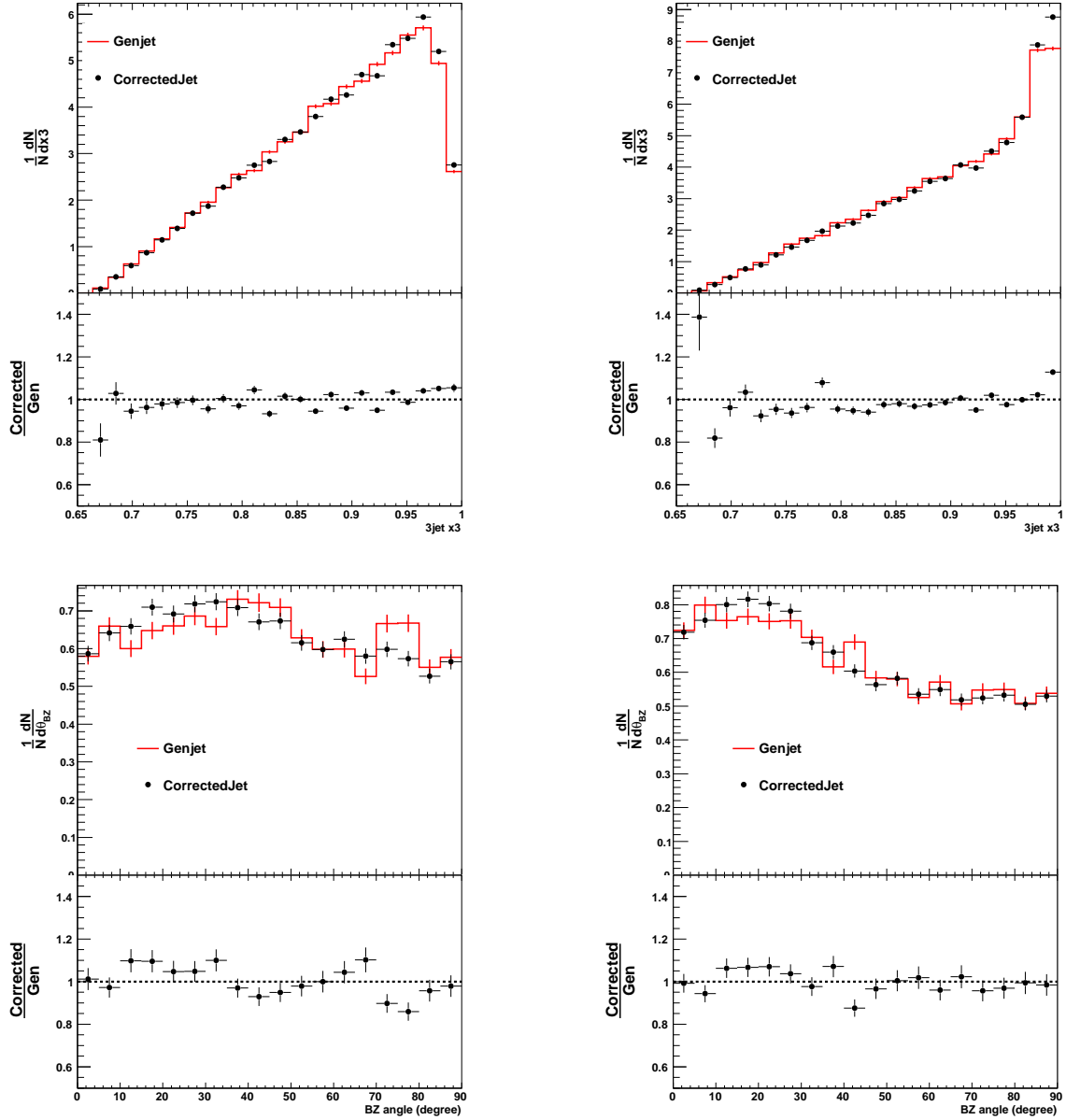


Figure 7.16: Distribution of multi-jet distributions for SC5 and KT4 jet algorithms. The lower histogram in each figure is the ratio of distributions obtained from corrected calorimeter level jets to the generator level jets. The top left shows the energy fraction of the hardest jet in the 3-jet case for SC5. The top right plot shows the same plot in the 3-jet case for KT4. Bottom left and right plots show the Bengtsson-Zerwas angle for SC5 and KT4.

7.7.1.1 MADGRAPH Production

In MADGRAPH, QCD multi-jet events are produced by calculating the multi-leg matrix elements at the tree level which are then passed to PYTHIA for the parton shower and hadronization. The MADGRAPH samples used in this study contain QCD processes from 2 up to 4 jets with a minimum jet $p_T > 20$ GeV/c. All other parameters are left to their default values.

Variable	RMS of detector level correction in			
	SisCone ($R = 0.5$)	SisCone ($R = 0.7$)	k_T ($D = 0.4$)	k_T ($D = 0.6$)
3 Jet Variables				
x_3	5.2	5.0	9.9	5.7
x_4	5.1	6.5	5.8	5.1
x_5	5.5	4.9	5.6	4.8
Ψ	5.2	4.8	6.3	4.3
$\cos \theta$	3.5	5.2	4.0	4.1
4 Jet Variables				
x_3	7.0	10.0	8.6	7.9
x_4	10.5	11.4	10.1	8.4
x_5	6.6	10.9	5.2	4.9
x_6	12.0	8.5	10.5	10.8
θ_{BZ}	7.0	5.8	5.0	5.3
$\cos \theta_{NR}$	6.4	6.8	4.4	7.0

Table 7.4: RMS (in %) of the ratio of distributions for Corrected and Generated jets for the four jet algorithms - Sisccone5, Sisccone7, KT4 and KT6.

The samples used are the MADGRAPH Fall08 samples [94]¹. These samples are binned in four HT bins (where HT is the sum of the transverse energy). The samples with their cross sections are tabulated in Table 7.5.

Sample	HT (GeV)	σ (pb)	Events processed
QCD100to250-madgraph	100-250	1.5E7	14229602
QCD250to500-madgraph	250-500	4E5	5376090
QCD500to1000-madgraph	500-1000	14E3	4922271
QCD1000toinf-madgraph	1000-inf	370	654114

Table 7.5: Details of the MADGRAPH Fall08 MC samples used in the present analysis.

Using these parameter choices, some distinct differences between the PYTHIA and MADGRAPH samples can be noted. In MADGRAPH the jet multiplicity is found to be larger than that in PYTHIA, because of more precise multi-leg matrix element treatment. Transverse momentum spectra of the four hardest jets are in good agreement between both the generators.

7.7.1.2 Comparison between PYTHIA and MADGRAPH

Figure 7.17 shows detector level distributions of several 3-jet and 4-jet variables (scaled energy distribution x_3 in the 3-jet sample, x_6 , Bengtsson-Zerwas and Nachtmann-Reiter angles in the 4-jet sample) from PYTHIA and MADGRAPH samples. There is significant difference among the distributions for PYTHIA and MADGRAPH which is expected as

¹Samples used: QCD*to*-madgraph/Fall08-IDEAL.v9.v1

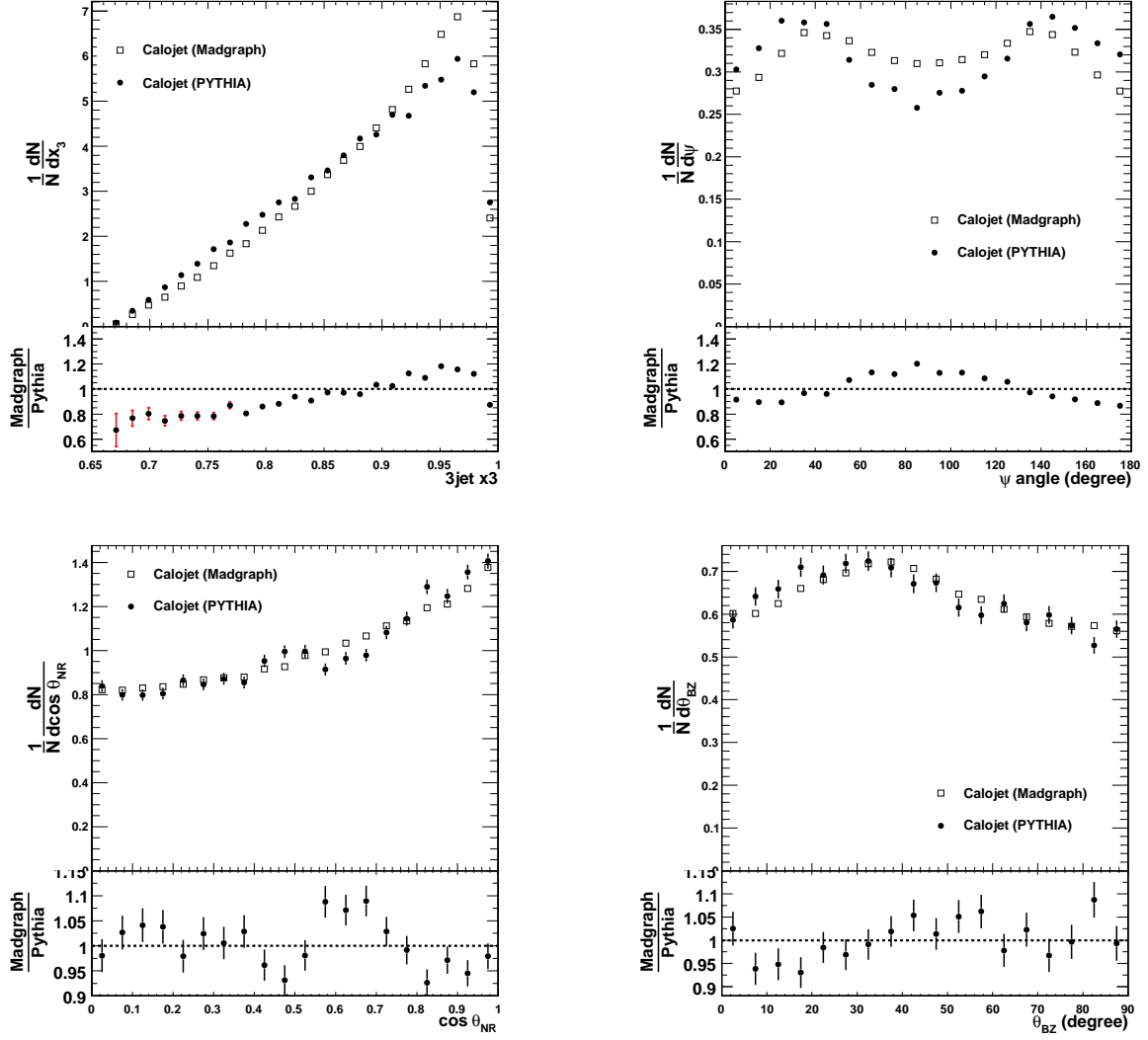


Figure 7.17: Multi jet distributions from generator level jets obtained using PYTHIA and MADGRAPH event generators. The top left shows the energy fraction of the most energetic jet in the 3-jet case. The top right plot shows the energy fraction of the 4th leading jet in the 4-jet case. Bottom left plot shows the Nachtmann-Reiter angle. The Bengtsson-Zerwas angle is shown in bottom right plot.

MADGRAPH does Matrix Element calculations and takes care of higher multiplicity jets (> 2 jets) whereas PYTHIA generates a $2 \rightarrow 2$ process. For the scaled energy for the leading jet MADGRAPH matches to PYTHIA within 20% whereas for fourth leading jet they match within 10%. For 3-jet and 4-jet angular variables the two generators match within 10% and 5% respectively which are comparable to the statistical uncertainties.

Table 7.6 summarizes the deviation between the two model predictions in the multi-jet variables. The results show that the multi-jet variables can be powerful handles in comparing and tuning different models of jet production.

3 jet Variables	Difference between MADGRAPH and PYTHIA	4 jet Variables	Difference between MADGRAPH and PYTHIA
x_3	17.5	x_3	9.0
x_4	9.6	x_4	11.6
x_5	16.8	x_5	13.6
Ψ	9.5	x_6	9.2
$\cos \theta$	25.1	θ_{BZ}	3.5
		$\cos \theta_{NR}$	4.0

Table 7.6: RMS (in %) of the ratio of distributions for corrected jets obtained from the two Monte Carlo samples using MADGRAPH and PYTHIA event generators.

7.7.2 Sensitivity to Colour Coherence

Color Coherence and Angular Ordering have described in detail in section 3.1.1. The structure of multi-jet events in hard processes is influenced by the underlying colour configurations at short distances. Colour coherence is approximated by the angular ordering parameter (AO) in the PYTHIA event generator. It is interesting to look at the dependence of angular ordering in multi-jet distributions.

Table 7.7 summarizes the deviation of the distributions of different multi-jet variables without and with the effect of angular ordering for generator level jets. The mean deviations are at the level of 5% which is comparable to the level of statistical error expected from 10 pb^{-1} data. So it may not be possible to see this effect from the early data.

3 jet Variables	Difference between Angular ordering off and on	4 jet Variables	Difference between Angular ordering off and on
x_3	3.9	x_3	4.4
x_4	4.4	x_4	2.7
x_5	3.9	x_5	2.7
Ψ	4.1	x_6	3.0
$\cos \theta$	5.6	θ_{BZ}	6.4
		$\cos \theta_{NR}$	4.5

Table 7.7: RMS (in %) of the ratio of distributions for generator level distributions for different multi-jet variables without and with angular ordering effects in the PYTHIA Monte Carlo.

7.7.3 Comparison between PYTHIA and HERWIG

Modelling of jet fragmentation will modify energy spectra of the constituent particles in the jet. Since calorimeter response has a strong dependence on the energy spectrum of the final state particles particularly for energies below 10 GeV, there may be significant differences in the multi-jet distributions due to differences in the fragmentation models.

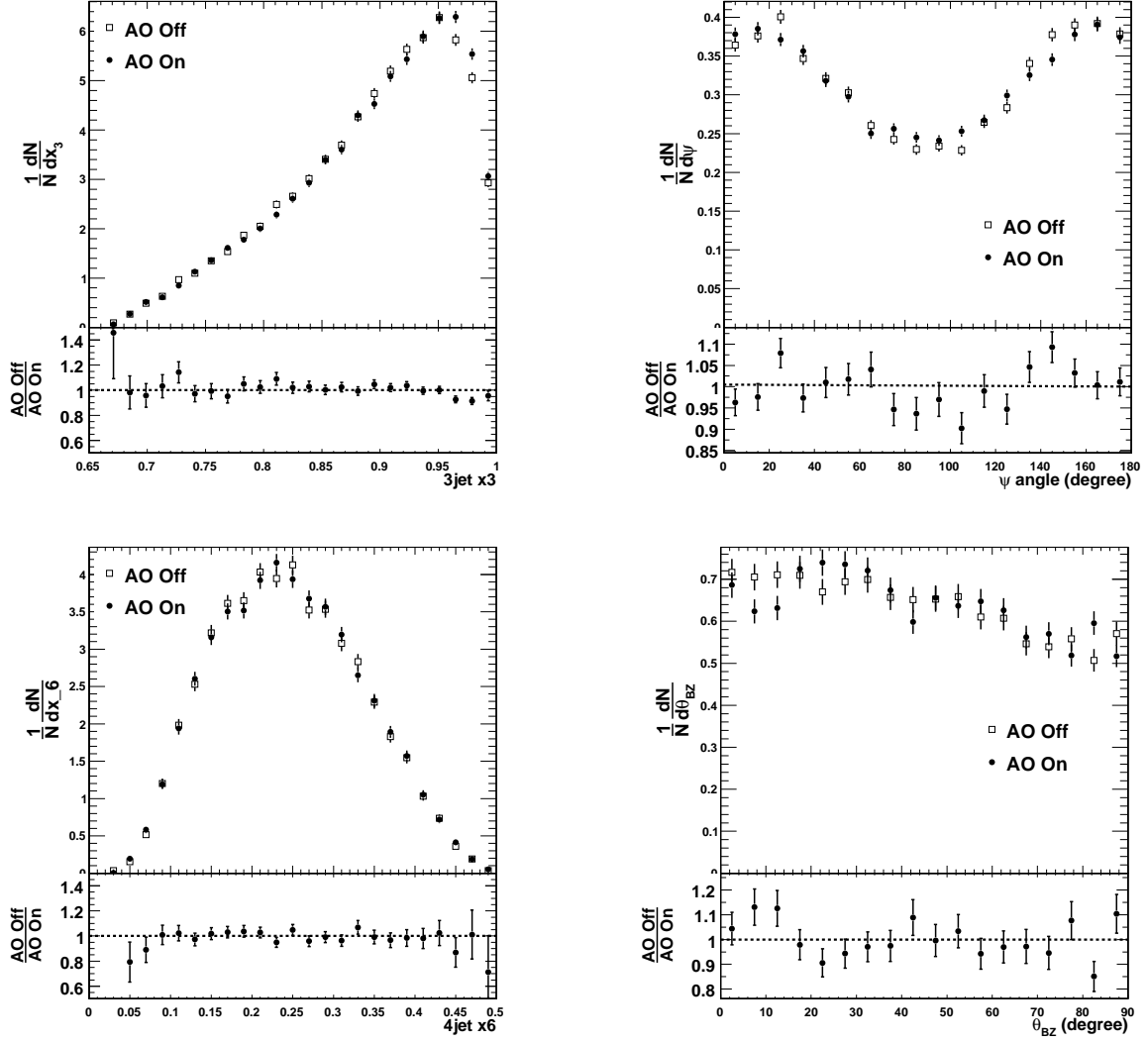


Figure 7.18: Multi jet distributions for PYTHIA with angular ordering parameter on and off. The top left plot shows the energy fraction of the most energetic jet in the 3-jet case. The top right plot shows the ψ angle in 3-jet case. The bottom left plot shows the energy fraction of the 4th leading jet in the 4-jet case. The Bengtsson-Zerwas angle is shown in bottom right plot.

Uncertainties due to the fragmentation model can be estimated by comparing results obtained using PYTHIA and HERWIG++. However HERWIG++ also uses a different model for underlying event. So this comparison will reveal the net effect of different fragmentation model as well as model for underlying event. Particle level distributions of multi-jet variables with these two different generators are shown in Figure 7.19. Significant differences ($\sim 20\%$) are observed in the scaled energies of jets between these two models. For the angular variables for 4-jets the difference is within 8%.

Table 7.8 summarizes the difference between the two event generators for scaled energy and angular variables.

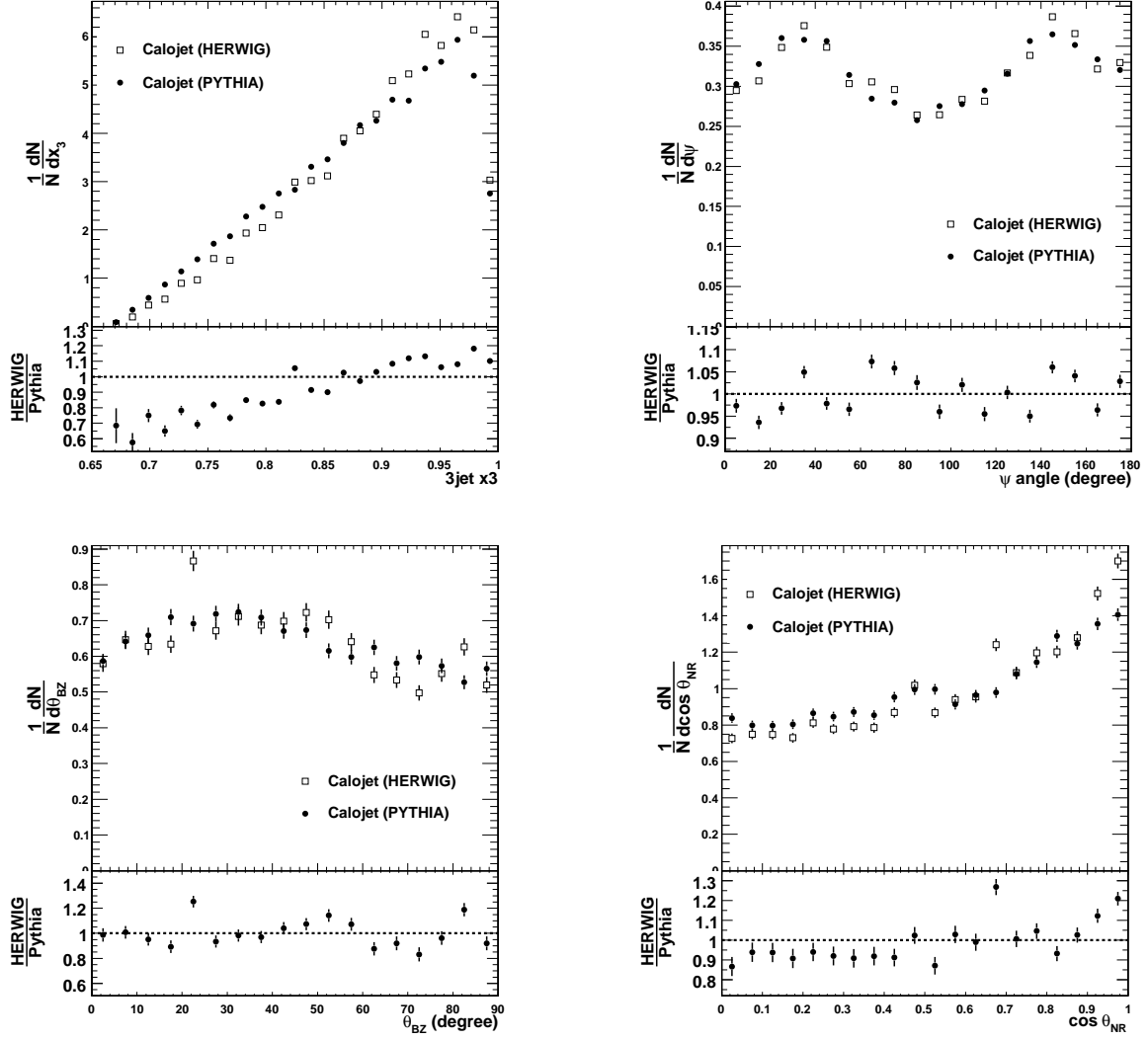


Figure 7.19: Multi jet distributions for PYTHIA and HERWIG event generators. The top plot left shows the energy fraction of the most energetic jet in the 3-jet case. The top right plot shows the energy fraction of the 4th leading jet in the 4-jet case. The Bengtsson-Zerwas angle is shown in bottom left plot. the bottom right plot shows the Nachtmann-Reiter angle for the 4jet case.

7.8 Results

In order to demonstrate the sensitivity of hadronic multi-jet distributions to different models of multi-jet production, the distributions obtained from the corrected calorimeter level measurements are unfolded to the particle level using a bin-by-bin correction factor from the generator and detector level information. These distributions are then compared with the generator level predictions as obtained from different event generators that contain different models of QCD multi-jet production, PYTHIA, MADGRAPH and HERWIG [95].

Figure 7.20 shows four such comparisons. The black error bars show the statistical

3 jet Variables	RMS of diff between HERWIG and PYTHIA	4 jet Variables	RMS of diff between HERWIG and PYTHIA
x_3	15.5	x_3	19.8
x_4	13.4	x_4	14.0
x_5	18.8	x_5	18.2
Ψ	3.9	x_6	20.4
$\cos \theta$	17.8	θ_{BZ}	8.6
		$\cos \theta_{NR}$	8.4

Table 7.8: RMS (in %) of the ratio of distributions for generator level jets obtained using HERWIG and PYTHIA event generators.

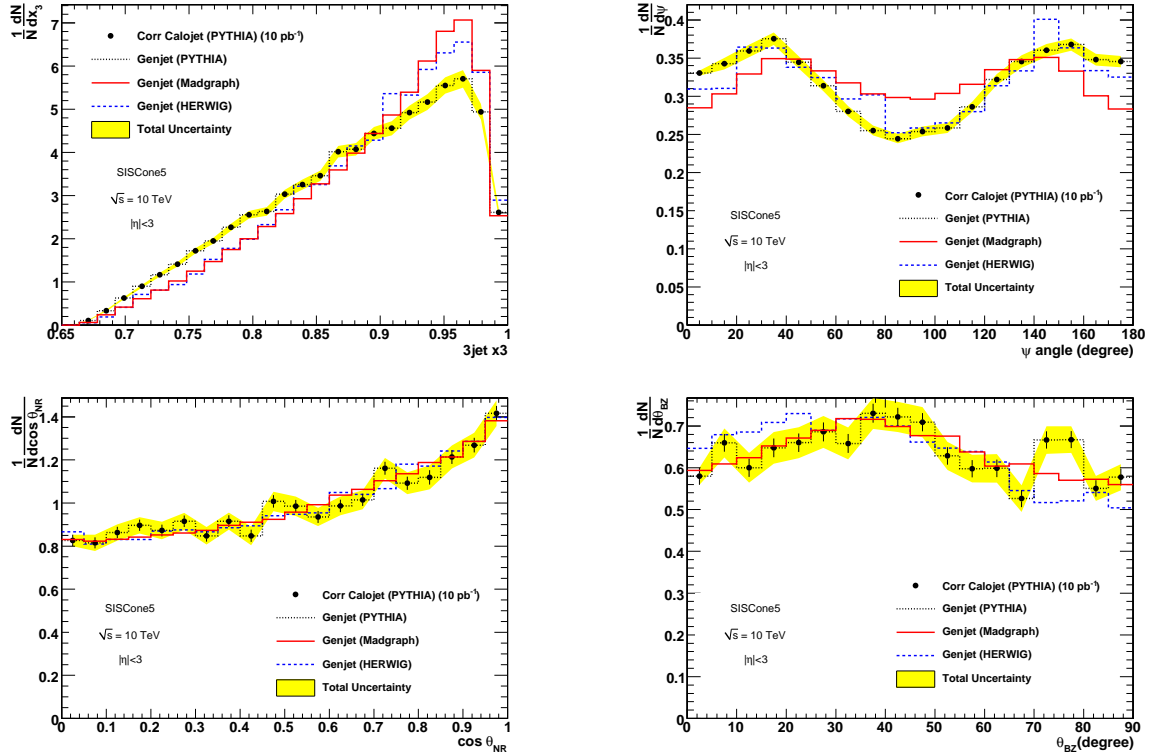


Figure 7.20: Multi jet distributions as they are expected to be measured based on an integrated luminosity of 10 pb^{-1} and unfolded to particle level, compared to different event generator models. The top left shows the energy fraction of the most energetic jet in the 3-jet case. The top right plot shows the Ψ angle in the 3-jet case. The bottom left plot shows the Nachtmann-Reiter angle. The Bengtsson-Zerwas angle is shown in bottom right plot. The error bars reflect the statistical uncertainty and the yellow band shows the total uncertainty which is a sum of statistical uncertainty and systematic uncertainty (from jet energy scale and from unfolding correction) added in quadrature.

fluctuation as expected from a measurement based on an integrated luminosity of 10 pb^{-1} . The yellow band shows the total uncertainty which is a sum of statistical uncertainty and systematic uncertainty added in quadrature. The systematic uncertainty comes from the jet energy scale and unfolding of detector level jets to the particle level. For the

scaled energy of the most energetic jet in 3-jet sample, the expected distribution with total uncertainty, as shown on the top left plot in Figure 7.20, can distinguish different event generators. The top right plot shows the ψ angle for which expected data can also distinguish between generators. For the two plots in the bottom, the Nachtmann-Reiter angle and the Bengtsson-Zerwas angle have less sensitivity in distinguishing among the event generators.

The unfolding of the observed signal in the LHC environment will be totally data driven whereas in this study the expected distributions are obtained using PYTHIA. The study here illustrates that these distributions are sensitive to model predictions and will enable to distinguish among the models.

Chapter 8

Study of Global Event Shape Variables

8.1 Global Event Shape Variables

Observables which describe the topology of hadronic events are known as event shape variables. They are functions of the 3-momenta p_i of all particles i detected in the final state and do not require identification of particle types. It is therefore straightforward to make comparisons between data and theory. They are sensitive to the amount of hard gluon radiation and offer one of the most direct ways to measure α_S in e^-e^+ annihilation. Some of the global event shape variables, for which improved analytical QCD calculations [96, 97, 98, 99, 100, 101] are available, are thrust, jet broadening, scaled heavy jet mass etc.

In order to be finite order-by-order in the perturbation theory, after renormalization for ultraviolet divergences, an observable should be both infrared and collinear safe. This implies that the observable should be insensitive to the emission of soft particles and to the splitting of one particle into two collinear ones. In other words, the observable should depend linearly on final state momenta. Apart from the theoretical arguments, infrared and collinear safe variables are also preferred for experimental reasons. They allow calorimetric measurements, and adding a soft particle or splitting a particle into two with half the energy, changes the measurement in a continuous way. Event shape variables, being linear in momenta, are infra-red safe and collinear safe quantities and hence are popular candidates for studying hadronic event structure.

Different event shape variables have different sensitivity to fragmentation and higher order perturbative effects. Therefore, an important estimate of theoretical uncertainties can be made by comparing the values of a physical parameter, α_S , for instance, derived from different variables.

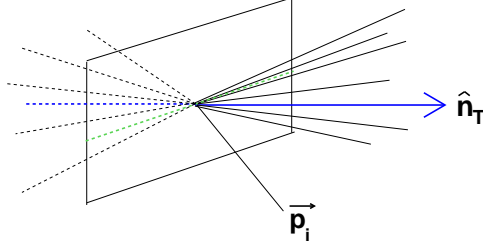


Figure 8.1: Orientation of the two hemispheres with respect to the thrust axis.

Thrust

One of the earliest variables defined in this category is the maximum directed momentum or *thrust* [102, 103] defined as

$$T = \frac{\sum |\vec{p}_i \cdot \vec{n}_T|}{\sum |\vec{p}_i|}$$

where \vec{p}_i is the momentum vector of particle i . The thrust axis \vec{n}_T is the unit vector which maximizes the above expression.

For a perfectly pencil-like *two jet* event, the thrust axis lies parallel to the jets, yielding $T = 1$, while for events with three and four jets in the final state thrust lies in the range $\frac{2}{3} \leq T \leq 1$, and $\frac{1}{\sqrt{3}} \leq T \leq 1$ respectively. All events satisfy $\frac{1}{2} \leq T \leq 1$. The thrust distribution is thus discontinuous with the multiplicity in the final state.

The concept of thrust was already in use before the advent of QCD. In 1964 [102], a “principal axis” equivalent to \vec{n}_T was proposed for the analysis of jets observed in hadron collisions, though the origin of the jets was hitherto unexplained. Later, in 1977 [103], it was recognized that this “maximum directed momentum” represented a calculable quantity in perturbative QCD.

It is evident from the definition that thrust is an infrared and collinear safe quantity. Thus the cross section

$$\sigma_T = \int_{1-T}^1 \frac{d\sigma}{dT} dT$$

is finite order by order in QCD perturbation theory and the experimental data of this quantity after correction for detector and hadronization effects should be directly comparable with perturbative calculations at the parton level.

The **thrust major** (T_m) is defined in the same way as thrust, except that the axis \vec{n} is constrained to be orthogonal to the thrust axis ($\vec{n} \perp \vec{n}_T$):

$$T_m = \max \left(\frac{\sum_i |\vec{p}_i \cdot \vec{n}|}{\sum_i |\vec{p}_i|} \right) \quad (8.1)$$

The axis which maximises the quantity in parentheses is $\vec{n}_{T_{maj}}$.

Heavy Jet Mass

The invariant masses (M_{\pm}) are calculated in the two hemispheres (S_{\pm}) by dividing the event by a plane normal to the thrust axis (\vec{n}_T):

$$M_{\pm}^2 = \left[\sum_{i \in S_{\pm}} p_i \right]^2$$

where p_i is the four momentum of particle i .

The *heavy jet mass* (M_H) is defined [104] to be

$$M_H = \max[M_+(\vec{n}_T), M_-(\vec{n}_T)] ,$$

and the differential cross section in term of this variable is calculated to be finite in the perturbation theory. The scaled heavy jet mass (ρ_H) is defined [105] as

$$\rho_H = \frac{M_H^2}{s} .$$

where s is the centre of mass energy.

The ρ_H variable vanishes for narrow *two jet* configuration, and it can span over a range $[0, \frac{1}{3}]$ for a large number of particles in the final state. For two particle in the final state, it becomes 0.

Jet Broadening

Both thrust and scaled heavy jet mass are sensitive to the longitudinal structure of jets and the resummed expressions are similar. It would be very desirable to have resummed predictions for event shape variables which are less correlated and hence complementary to thrust and scaled heavy jet mass. Event shape variables which are sensitive to the transverse development of jet are in particular interesting. The *jet broadening* [96, 97] variables are defined by dividing the event into two hemispheres S_{\pm} by a plane perpendicular to the thrust axis, and computing in each hemisphere the quantity

$$B_{\pm} = \frac{\sum_{i \in S_{\pm}} |\vec{p}_i \times \vec{n}_T|}{2 \sum_i |\vec{p}_i|} .$$

The sum in the denominator runs over all final state particles, while that in the numerator runs over particles in one hemisphere. The observables, total, B_T , and wide, B_W , jet

broadening, are then defined respectively as

$$B_T = B_+ + B_- \text{ and } B_W = \max(B_+, B_-) .$$

Both B_T and B_W become zero in the *two jet* region.

8.2 Event Shape Variables in Hadronic Collisions

The jet properties of hadronic events in pp collision have manifestly direct correspondence with the global event shape variables. However, in pp collision, the hard scattering process creates jets with high transverse momenta while there is always an underlying event. This underlying event is due to the hadronization of the remaining partons which do not take part in the hard scattering process. The underlying events contribute very little energy in the transverse plane while they have large contribution in the longitudinal (along beam) direction.

For this reason, global event shape variables in hadronic collision are defined in the transverse plane [106], i.e., shape variables like thrust, jet broadening parameters are defined in terms of momenta in the transverse plane rather than in terms of the 3-momenta of the particles.

The central hadronic event shapes are defined, which are computed from a subset of particles in the central region $|\eta| < \eta_C$ only, but remain sensitive to the emissions in the region $|\eta| > \eta_C$. Hence in the transverse plane, the central transverse thrust is defined as:

$$T_{\perp,C} = \max_{\vec{n}_T} \frac{\sum_i |\vec{p}_{\perp,i} \cdot \vec{n}_T|}{\sum_i p_{\perp,i}} \quad (8.2)$$

where $p_{\perp,i}$ are the transverse momenta with respect to the beam axis. The variable which is typically used for perturbative calculations is not $T_{\perp,C}$ itself, but

$$\tau_{\perp,C} \equiv 1 - T_{\perp,C} \quad (8.3)$$

Therefore, $\tau_{\perp,C}$ tends towards its smallest value for a $2 \rightarrow 2$ process. Similarly the other Central transverse event shape variables, such as central transverse major, central transverse total and wide jet broadening parameters are defined as $T_{m,C}$, $B_{T,C}$ and $B_{W,C}$, respectively. In the current study, these transverse event shape variables are constructed using jets with p_T above a certain threshold.

During early data taking period, jets measured from the energy deposits in the calorimeter towers (CaloTowers) will be best understood. So the primary measurements will come from corrected calorimeter jets (CaloJets) using default jet algorithm of CMS. Seedless cone algorithm (SisCone) with a cone size of 0.5 is used in this study. All jets

with p_T above 50 GeV in a given event are used in constructing these variables. Event selection makes use of events passing the high level trigger of HLT80 and has at least one jet with corrected energy above 110 GeV.

The studies are based on comparisons of the primary distributions to those obtained using jets clustered with the same algorithms from stable particles at the event generator level, which are referred to as generator jets (GenJets). An alternate event sample can be constructed using only the charged particles which will be detected in the tracking detector. Besides the fluctuations in the charged component, these measurements will be totally independent, the tracks being measured with totally different resolution both in terms of energy and angle. Also in an environment of event pile up, the tracks can be associated to the interaction vertex and will be free from additional bias. For these reasons, the measurements using track-jets will give a useful alternative with a different set of systematic uncertainties.

Figure 8.2 shows distributions of four central transverse event shape variables - thrust, major, total and wide jet broadenings. In the plots the distributions from corrected calorimeter jets as expected to be measured with 10 pb^{-1} of integrated luminosity are compared to those from the particle level jets. Also measurements using only charged particles at the detector level and at the generator level are compared. Good agreement among all the four measurements is seen for all these variables.

8.3 Systematic Uncertainty

The leading source of systematic uncertainties in QCD data analysis will be due to the limited knowledge of the jet energy scale (JES). The JES uncertainty at start up is expected to be $\pm 10\%$ as explained in Chapter 7. Changing the JES correction within its uncertainty changes the jet shapes as jets migrate between p_T bins. However, jet spectra vary slowly with jet p_T . So the net effect on the distributions is expected to be small. To determine the impact on the jet spectra, the p_T of the jets are changed by $\pm 10\%$ and the whole analysis is repeated. The ratio of the distributions before and after the changes is examined. Figure 8.3 shows the resulting distributions due to the changes as well as the ratios for the four event shape variables. As can be seen from these plots, the distributions are not very sensitive to the jet energy scale corrections.

Table 8.1 summarizes average effect for several event shape variables. All these deviations are between 4.0% and 6.5%.

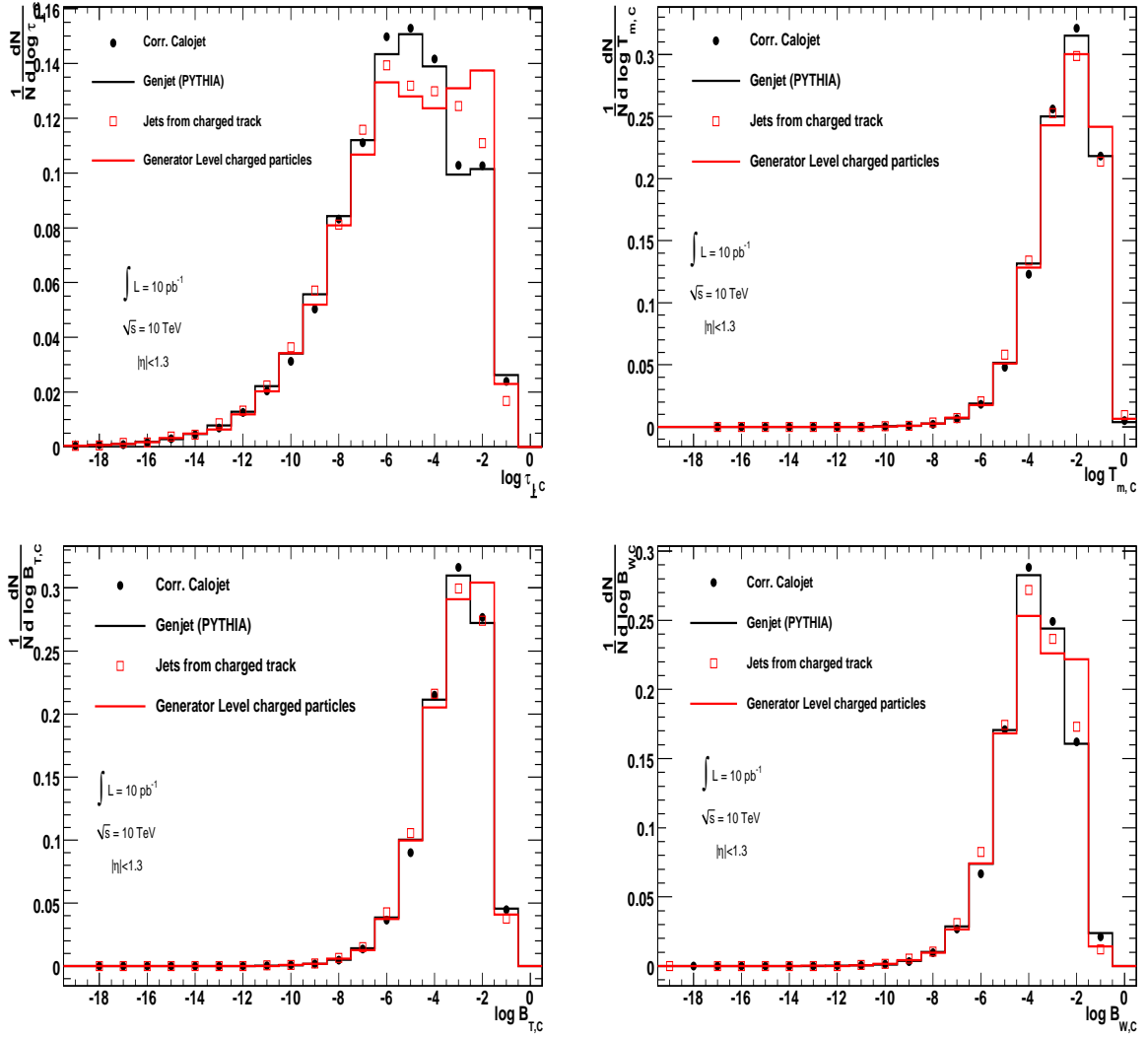


Figure 8.2: Global transverse event shape distributions for particle level and detector level jets. The top left plot shows the distribution for transverse thrust. The top right plot shows the distribution for transverse major. Bottom left and right plots show the distributions for total and wide jet broadenings. The black dots represent distributions obtained using the corrected calorimeter jets as expected to be measured with 10 pb^{-1} . The black lines show distributions obtained using particle level jets. The open red circles show measurements using the jets from charged tracks and the red line shows those from the stable charged particles at the generator level.

8.4 Results

The detector level distributions obtained from corrected CaloJets are unfolded into particle level distributions using a bin-by-bin correction from a comparison of detector level and generator level distributions. Systematic uncertainty in this unfolding process arise due to limited knowledge of the detector correction and is estimated using the same procedure as described in Chapter 7.

Figure 8.4 shows the transverse event shape distributions as expected from a measure-

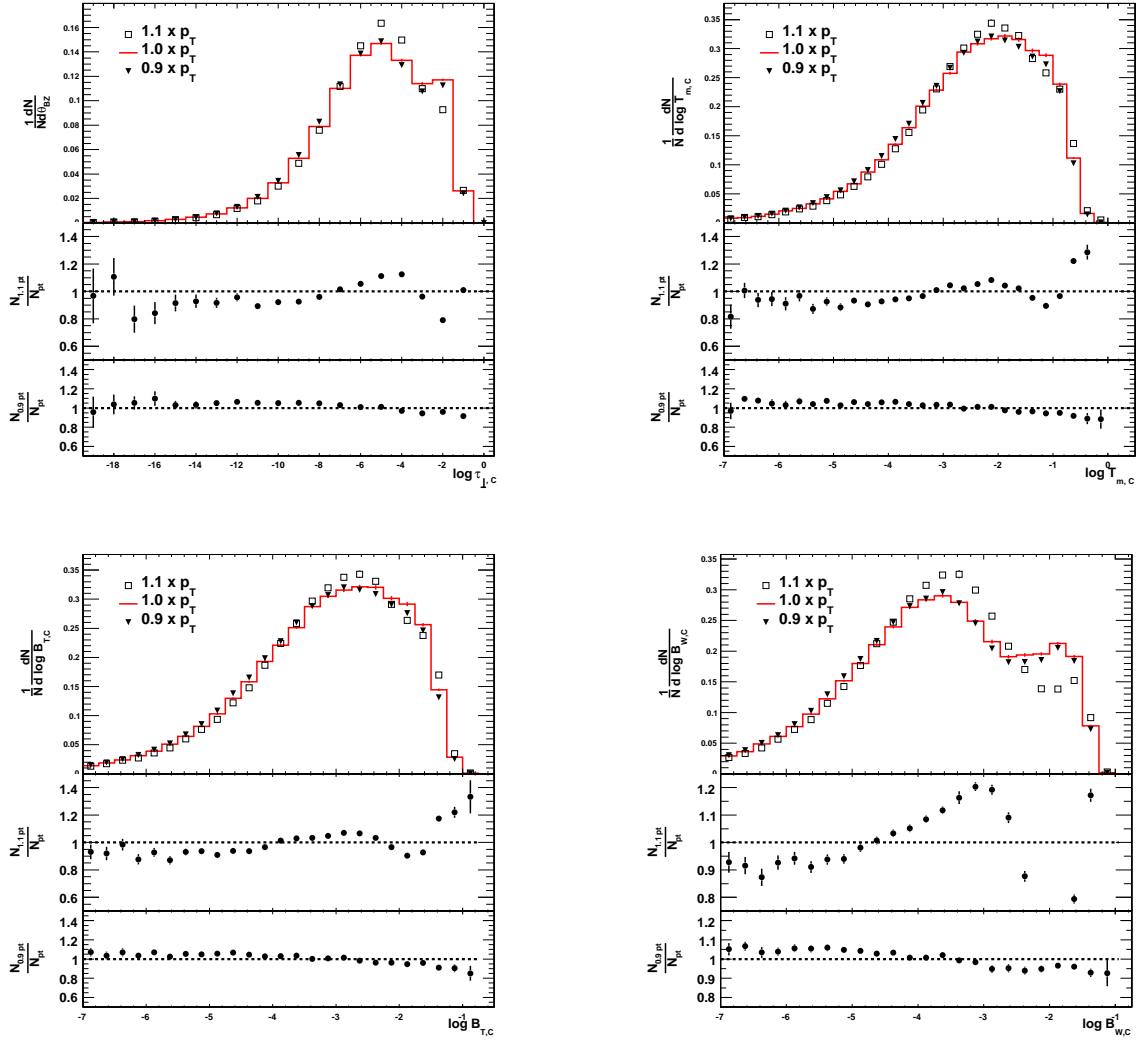


Figure 8.3: The effect of jet energy scale on the event shape distributions. The top left plot shows the distribution for transverse thrust. The top right plot shows the distribution for transverse major. Bottom left and right plots show the distributions for total and wide jet broadenings. Each plot has three parts: the shape distribution with jet energy scale of 1.0, 1.1 and 0.9 and ratio of the distributions when JES is changed by $\pm 10\%$.

ment based on an integrated luminosity of 10 pb^{-1} . The shaded band shows the total uncertainty which is a sum of statistical uncertainty and systematic uncertainty added in quadrature. The systematic uncertainty is the combined uncertainty due to unfolding and due to jet energy scale. The same figure also shows distributions from three different generators: PYTHIA, HERWIG and Madgraph. The expected distributions with total uncertainty show clear sensitivity to distinguish between the different event generators.

Variable	Jet p_T increased by 10%	Jet p_T decreased by -10%	Average systematics
$\log \tau_{\perp,C}$	4.93	3.92	4.61
$\log T_{m,C}$	6.22	4.03	5.26
$\log B_{T,C}$	4.49	3.14	4.02
$\log B_{W,C}$	7.71	2.70	6.55

Table 8.1: RMS (in %) of the ratio of distributions when jet p_T is increased or decreased by 10% with respect to the default distribution.

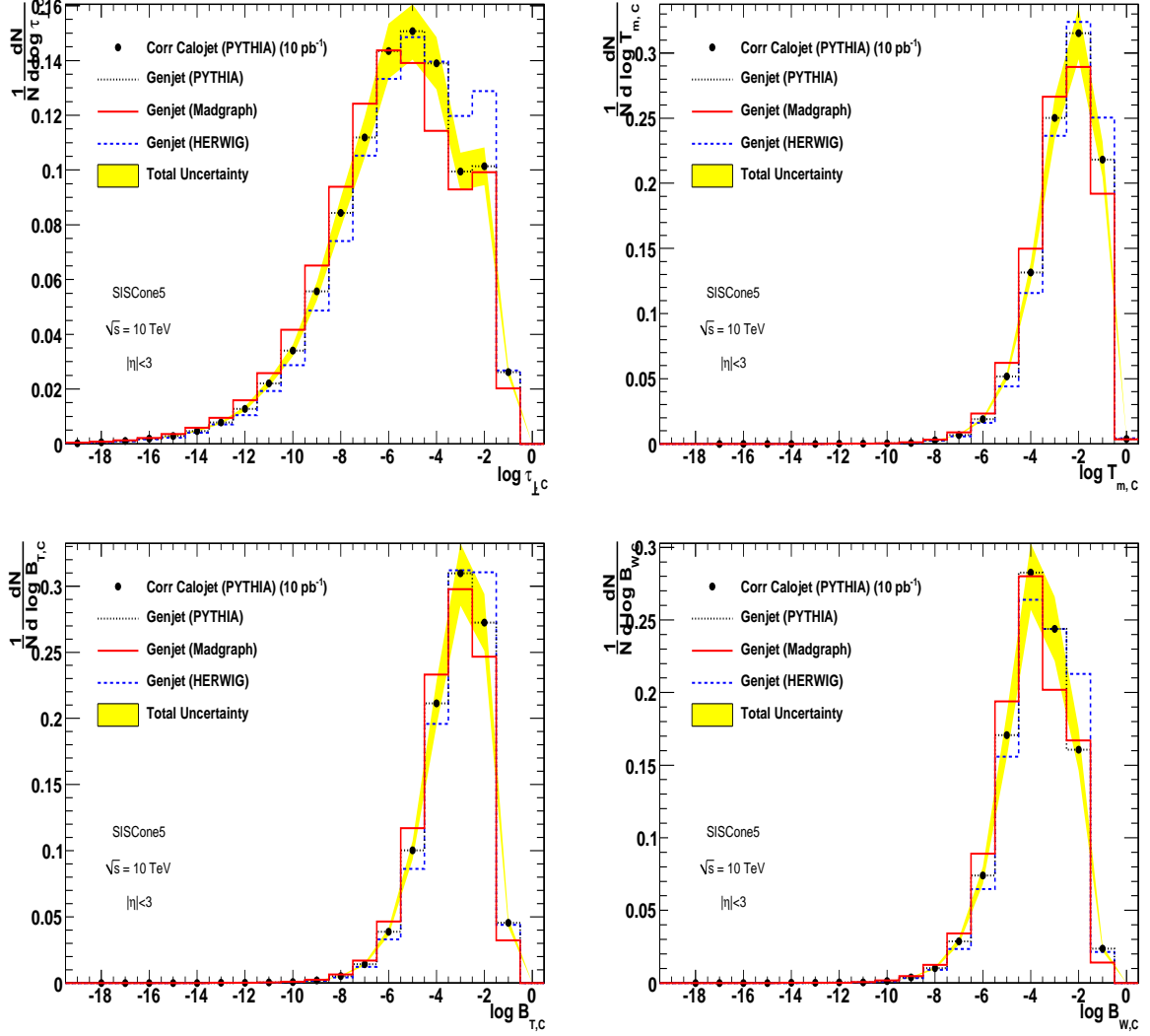


Figure 8.4: Global transverse event shape distributions as they are expected to be measured with an integrated luminosity of 10 pb^{-1} and unfolded to particle level. The distributions are compared to different event generator models. The top left plot shows the distribution for transverse thrust. The top right plot shows the distribution for transverse major. Bottom left and right plots show the distributions for total and wide jet broadenings. The error bars reflect the statistical uncertainty and the yellow bands show the total uncertainty which is a sum of statistical uncertainty and systematic uncertainty (from jet energy scale and from unfolding correction) added in quadrature.

Chapter 9

Conclusion

The performance of the CMS calorimeter system to hadrons is studied with the test beam data taken at the CERN test beam facility area. A detail particle identification is carried out with the help of different beam line counters. Possibility of a gap among the endcap super-crystals is also studied by studying the beam profile. Energy scales for the hadron endcap calorimeter is established using 50 GeV electron beam.

Energy response and resolution of hadrons are measured for the endcap detector of CMS and are compared with similar measurements done with the barrel detector. The endcap detector shows better response and resolution for higher energy beams due to smaller leakage in the system. MIP-fraction is also measured and it shows the same characteristics as in the barrel, namely a small drop off at the high energy end.

For a setup consisting of hadron calorimeter (HCAL) only, the energy resolution is measured to be

$$\frac{\Delta\sigma}{\sigma} = \frac{92\%}{\sqrt{E}} \oplus 3.4\%$$

These measurements are for π^- beams of 30-300 GeV/c at $i\eta$ tower in between 19 and 20.

The energy resolution of the combined calorimeter system with the electromagnetic and hadron calorimeter (HE+EE) with preshower in front is

$$\frac{\Delta\sigma}{\sigma} = \frac{116.9\%}{\sqrt{E}} \oplus 1.4\%$$

Electron runs at various energies from the test beam 2006 are studied. The longitudinal shower profiles of electrons and pions are compared with the stand-alone hadron calorimeter. The calibration constants for the hadron calorimeter obtained with the electrons seem to have a good correlation with those obtained from the muons.

Prospect of studies of global event shape variables as well as multi-jet variables in pp collision at a centre of mass energy of 10 TeV is presented for integrated luminosity of

10 pb^{-1} . Procedure for selecting the data sample, unfolding the data from detector effect and estimation of systematic uncertainties are established. These studies will enable to tune QCD event generators and will distinguish different hadronic models.

A study of inclusive 3-jet and 4-jet events is performed. Several multi-jet topological variables are examined using measured calorimeter jet momenta with corrections as input. These measurements have some dependence to jet algorithms used and Siscone algorithm with $R = 0.5$ is an optimum choice of jet algorithm for these studies. The dominant systematic uncertainties in these measurements will be due to limited knowledge of jet energy scale at the startup. The uncertainty due to jet energy scale is found to be between 3% and 4% for the variables under study. Uncertainty due to unfolding is estimated to be between 2% and 7% whereas the statistical uncertainty is found to be better than 4% for the multijet variables. For the scaled energy of the most energetic jet in 3-jet sample, (x_3) , and the ψ angle, the expected distribution with total uncertainty can distinguish different event generators. The four jet angular variables, the Nachtmann-Reiter angle ($\cos \theta_{NR}$) and the Bengtson-Zerwas angle (θ_{BZ}) have less sensitivity in distinguishing among the event generators.

For the global event shape variables, the expected distributions are compared at the detector level as measured using calorimeters and at the generator level from stable particles. Also measurements using only charged particles at detector level and generator level are compared. Good agreement among all the measurements is seen for all these variables. The expected distributions with total uncertainty for some of the event shape variables show distinguishing capability among different event generators.

Bibliography

- [1] M. Gell-Mann, Acta Phys. Austriaca Suppl. **IX** (1972) 733.
- [2] H. Fritzsch and M. Gell-Mann, 16th International Conference on High Energy Physics, Batavia, 1972.
- [3] H. Fritzsch, M. Gell-Mann and H. Leytwyler, Physics Letters **B47** (1973) 365.
- [4] D. J. Gross and F. Wilczek, Physical Review Letters **30** (1973) 1343.
- [5] D. J. Gross and F. Wilczek, Physical Review **D8** (1973) 3633.
- [6] H. D. Politzer, Physical Review Letters **30** (1973) 1346.
- [7] G. 't Hooft, Nuclear Physics **B33** (1971) 173.
- [8] S. Weinberg, Physical Review Letters **31** (1973) 494.
- [9] Michael E. Peskin and Daniel V. Schroeder, An Introduction to Quantum Field Theory, Addison-Wesley (1995).
- [10] R. K. Ellis, W. J. Stirling and B. R. Webber, QCD and Collider Physics. Cambridge, UK: CUP (1998).
- [11] F. J. Yndurain, The Theory of Quark and Gluon Interactions, 3rd Ed., Springer-Verlag, 1999.
- [12] D. Espriu, Lectures delivered at the XXII Int. Meeting on Fundamental Physics, Jaca, Feb 1994, UB-CM-PF-4/24.
- [13] David J. Gross and Frank Wilczek, Physical Review Letters **30** (1973) 1343; H. David Politzer, Physical Review Letters **30** (1973) 1346.
- [14] S. Bethke, Journal of Physics G: Nuclear and Particle Physics **26** (2000) 27.
- [15] The Coordinated Theoretical-Experimental Project on QCD - CTEQ, <http://www.phys.psu.edu/cteq>.

- [16] MRST Parton Distributions, <https://durpdg.dur.ac.uk/hepdata/mrs.html>.
- [17] The Large Hadron Collider: Conceptual Design, CERN/AC/95-05(LHC), 1995 and LHC Design Report, CERN 2004-003 (2004)
- [18] The CMS Collaboration, Technical Proposal, CERN/LHCC 94-39 (1994).
- [19] The Tracker Project Technical Design Report, CERN/LHCC 98-006(1998) and CMS TDR 5, Addendum CERN LHCC 20-016.
- [20] The Electromagnetic Calorimeter Technical Design Report, CERN/LHCC 97-033, CMS TDR 4 (1997).
- [21] The Hadron Calorimeter Technical Design Report, CERN/LHCC 97-031 (1997).
- [22] S. Abdullin *et al.*, “*Design, performance, and calibration of CMS hadron-barrel calorimeter wedges*”, Journal The European Physical Journal **C55** (2008), 159.
- [23] E. Hernandez *et al.*, “*Fiber sputtering and Painting*”, Radiation Physics and Chemistry **41** (1993) 409.
- [24] B. S. Acharya *et al.*, “*The CMS Outer Hadron Calorimeter*”, CMS NOTE-2006/127.
- [25] G. Baatian *et al.*, Design, Performance, and Calibration of CMS Hadron Endcap Calorimeters, CMS NOTE-2008/010.
- [26] P. Cushman, A. Heering, A. Ronzhin, Nuclear Instrumentation Methods **A442** (2000) 289.
- [27] S. Abdullin *et al.*, “*Design, performance, and calibration of CMS forward calorimeter wedges*”, Journal The European Physical Journal **C53** (2008), 139.
- [28] T. Zimmerman, M. Sarraj, IEEE Transactions on Nuclear Science **43** (1996) 1683.
- [29] T. Zimmerman, J. R. Hoff, J. Solid State Circuits **39** (2004) 895.
- [30] The Magnet Project, Technical Design Report, CERN/LHCC 97-10, CMS TDR 1 (1997).
- [31] The Muon Project, Technical Design Report, CERN/LHCC 97-032, CMS TDR 3 (1997).
- [32] CMS Collaboration, The TRIDAS Project Technical Design Report, Vol. 1: The Trigger Systems, CERN/LHCC 2000-38 (2000). CMS TDR 6.1.
- [33] <https://twiki.cern.ch/twiki/bin/view/CMS/WorkBook>.

- [34] <http://lcgapp.cern.ch/project/simu/HepMC/>.
- [35] S. Agostinelli *et al.*, Nuclear Instruments and Methods **A506** (2003) 250; J. Allison *et al.*, IEEE Transactions on Nuclear Science **53** (2006) 278.
- [36] T. Sjöstrand *et al.*, “*PYTHIA 6.4 Physics and Manual*”, hep-ph/0603175.
- [37] M. Bahr, S. Gieseke, and M. H. Seymour, “*Simulation of multiple partonic interactions in Herwig++*”, Journal of High Energy Physics **07** (2008), hep-ph/0803.076.
- [38] M. L. Mangano *et al.*, “*ALPGEN, a generator for hard multiparton processes in hadronic collisions*”, hep-ph/0206293v2.
- [39] <https://twiki.cern.ch/twiki/bin/view/CMS/MadGraphCMSPage>.
- [40] See, for example, <http://madgraph.phys.ucl.ac.be/>;
<https://twiki.cern.ch/twiki/bin/view/CMS/MadGraphCMSPage>.
- [41] <http://www.hep.phy.cam.ac.uk/theory/webber/MCatNLO/>.
- [42] A. Bassetto, M. Ciafaloni and G. Marchesini, Physics Reports **100** (1983) 201.
- [43] Yu. L. Dokshitzer *et al.*, Review of Modern Physics **60** (1988) 373.
- [44] B. R. Webber, Annual Review of Nuclear and Particle Science **36** (1986) 253.
- [45] D. Amati and G. Veneziano, Physics Letters **B83** (1979) 87.
- [46] Ya. I. Azimov *et al.*, Z. Physik **C27** (1985) 65.
- [47] R. D. Field and S. Wolfram, Nuclear Physics **B213** (1983) 65.
- [48] B. R. Webber, Nuclear Physics **B238** (1984) 492.
- [49] S. G. Gorishny, A. L. Kataev and S. A. Larin , Physics Letters **B212** (1988) 238.
- [50] R. K. Ellis, D. A. Ross and A. E. Terrano, Nuclear Physics **B178** (1981) 421.
- [51] B. R. Webber, Annual Review of Nuclear and Particle Science **36** (1986) 253.
- [52] M. Acciarri *et al.*, Physics Letters **B353** (1995) 145.
- [53] R. Field, R. P. Feynman, Nuclear Physics **B136** (1978) 1.
- [54] B. Anderson *et al.*, Physics Reports **97** (1983) 31.
- [55] G. C. Fox and S. Wolfram, Nuclear Physics **B213** (1983) 65.

- [56] A. B. Kaidalov, K. A. Ter-Martirosyan, Physics Letters **B117** (1982) 247.
- [57] A. Capella, U. Sukhatme, I. C. Tan, J. Tran Thanh Van, Physics Reports **236** (1994) 225.
- [58] R. Demina *et al.*, “*Calorimeter Energy Thresholds for Jet Reconstruction in CMS*”, CMS NOTE-2006/020.
- [59] B. Andersson, G. Gustafson, G. Ingelman, T. Sjöstrand, Physics Reports **97** (1983) 31.
- [60] M. P. Guthrie, R. G. Alsmiller and H. W. Bertini, Nuclear Instruments and Methods **66** (1968) 29.
- [61] H. W. Bertini and P. Guthrie, “*Results from Medium-Energy Intranuclear-Cascade Calculation*”, Nuclear Physics **A169** (1971).
- [62] <http://www.python.org/doc/2.3.5/ref/ref.html>.
- [63] <http://root.cern.ch>.
- [64] C. Buttar *et al.*, Standard Model Handles and Candles Working Group: Tools and Jets Summary Report, arxiv:0803.0678.
- [65] J. E. Huth *et al.*, in Research Directions for the Decade, Proceedings of the Summer Study on High Energy Physics, Snowmass, Colorado, 1990, p. 134.
- [66] S. D. Ellis and D. E. Soper, Physical Review **D48** (1993) 3160.
- [67] S. Catani, Yu. L. Dokshitzer, M. H. Seymour, B. R. Webber, Nuclear Physics **B406** (1993) 187.
- [68] G. P. Salam, “*A Practical Seedless Infrared Safe Cone Algorithm*”, hep-ph/0705.2696.
- [69] P. Schieferdecker *et al.*, “*Performance of the SIScone Jet Clustering Algorithm*”, CMS AN-2008/002.
- [70] R. Harris, K. Kousouris, “*MC Truth L2 and L3 Factorised Jet Corrections at CMS*”, CMS AN-2008/003.
- [71] S. Esen *et al.*, “*Plans for jet energy corrections at CMS*”, CMS AN-2007/055.
- [72] A. Bhatti *et al.* (CDF Collaboration), “*Determination of the Jet Energy Scale at the Collider Detector at Fermilab*”, hep-ex/0510047.

- [73] L. Babukhadia, D. Elvira (D0 Collaboration), “*Method to test the jet energy scale using transverse momentum balance*”, D0 Note 003554, 1998; B.Abbott *et al.*, (D0 Collaboration), Nuclear Instruments and Methods **A424** (1999) 352.
- [74] V. Konopliyanikov *et al.*, “*Jet Calibration using gamma+jet Events in the CMS Detector*”, CMS NOTE-2006/042.
- [75] R. Field *et al.*, “*The underlying event at the LHC*”, CMS NOTE 2006/067.
- [76] S. Agostinelli *et al.*, Nuclear Instruments and Methods **A506** (2003) 250; J. Allison *et al.*, IEEE Transactions on Nuclear Science **53** (2006) 278.
- [77] “*First CMS Results from CRAFT*”, CMS DP-2009/002.
- [78] M. Heinrich, “*Inclusive Jet Cross Section at 10 TeV with CMS*”, CMS AN-2009/034.
- [79] H2 handbook: <https://nahandbook.web.cern.ch/nahandbook/default/h2/>.
- [80] <http://ab-dep-op-sps.web.cern.ch/ab-dep-op-sps/>.
- [81] A. Benaglia *et al.*, “*Intercalibration at 2006 ECAL test beam with the S25 technique*”, CMS DN-2007/002.
- [82] C.M. Kuo *et al.*, “*Performance of CMS ECAL Preshower in testbeam 2007*”, CMS-CR-2008/057.
- [83] S. Abdullin *et al.*, “*The CMS Barrel Calorimeter Response to Particle Beams from 2 to 350 GeV/c*”, European Physics Journal **C60** (2009) 359.
- [84] B. Adeva *et al.*, “*A test of QCD based on 3-jet events from Z^0 decays.*”, Physics Letters **B263**, No.3,4 (1991).
- [85] B. Adeva *et al.*, “*A test of QCD based on 4-jet events from Z^0 decays.*”, Physics Letters **B248**, No.1,2 (1990).
- [86] S. Abachi *et al.*, “*Studies of topological distributions of inclusive three and four jet events in $\bar{p}p$ collisions at $\sqrt{s} = 1800\text{GeV}$ with the D0 detector.*”, Physical Review **D53**, No. 11 (1996) and the references therein.
- [87] F. Abe *et al.*, “*Further Properties of High-Mass Multijet Events at the Fermilab Proton-Antiproton Collider*”, Physical Review **D54** (1996) 4221.
- [88] M. Bengtsson and P.M. Zerwas, Physics Letters **B208** (1988) 306.
- [89] O. Nachtmann and A. Reiter, Z. Physics **C16** (1982) 45.

- [90] J. G. Korner, G. Schierholz and J. Willrodt, Nuclear Physics, **B185** (1981) 365.
- [91] V. Chethuru *et al.*, “*Jet Reconstruction performance at CMS*”, CMS AN-2009/067.
- [92] CMS Collaboration, “*Plans for Jet Energy Corrections at CMS*”, CMS-PAS-JME-007-002.
- [93] See, for example, http://d0server1.fnal.gov/users/strang/web/kt/f_kt.html.
- [94] <https://twiki.cern.ch/twiki/bin/view/CMS/ProductionSummer2008#MadGraph>.
- [95] S. Bose *et al.*, “*QCD studies in CMS with Multijets at $\sqrt{s}=10$ TeV.*”, CMS AN-2009/073.
- [96] S. Catani *et al.*, Physics Letters **B295** (1991) 269.
- [97] Yu L. Dokshitzer *et al.*, Journal of High Energy Physics **01** (1998) 11.
- [98] S. Catani *et al.*, Physics Letters **B263** (1991) 491.
- [99] S. Catani *et al.*, Physics Letters **B272** (1991) 368.
- [100] S. Catani *et al.*, Nuclear Physics **B407** (1993) 3.
- [101] S. Catani *et al.*, Physics Letters **B427** (1998) 377.
- [102] S. Brandt *et al.*, Physics Letters **12** (1964) 57.
- [103] E. Fehri, Physical Review Letters **39** (1977) 1587.
- [104] T. Chandramohan and L. Clavelli, Nuclear Physics **B184** (1981) 365.
- [105] L. Cavelli and D. Wyler, Physics Letters **B103** (1981) 383.
- [106] A. Banfi, G. P. Salam and G. Zanderighi, Journal of High Energy Physics **0408** (2004) 62, [hep-ph/0407287](https://arxiv.org/abs/hep-ph/0407287).

Publications of Suvadeep Bose

SELECTED PUBLICATIONS

- QCD Multijet Studies in CMS at 10 TeV (CMS AN-2009/073, CMS PAS QCD-09-001).
- Combined Endcap Calorimetry Response for Hadrons (Analysis Note in preparation).
- Response of CMS Hadron Calorimeter to Electron Beams, S. Bose, *Pramana - Journal of Physics*, **69**, No.6, (2007).
- Calorimetry Task Force Report, S. Abdullin et al, CMS NOTE-2008/025.
- The CMS Barrel Calorimeter Response to Particle Beams from 2 to 350 GeV/c, S. Abdullin et al, CMS NOTE-2008/034.

CMS PUBLICATIONS

- Design, Performance, and Calibration of the CMS Hadron-Outer Calorimeter, S. Abdullin et al, CMS NOTE-2008/020.
- HCAL participation in Global Run at the end of November 2007 (GREN), S. Abdullin et al, CMS IN-2008/019.
- Study of CMS HCAL response to muons using data collected during Global Run in September, 2007 and Integration Run in October 2007, P. de Barbaro et al, CMS IN-2008/010.